PRINTED MONOPOLE ANTENNAS WITH MULTIPLE BENDS FOR RFID, WLAN AND UWB APPLICATIONS

Jyoti Ranjan Panda

PRINTED MONOPOLE ANTENNAS WITH MULTIPLE BENDS FOR RFID, WLAN AND UWB APPLICATIONS

A

Thesis submitted

for the award of the degree of

DOCTOR OF PHILOSOPHY

By

JYOTI RANJAN PANDA

DEPARTMENT OF ELECTRONICS AND ELECTRICAL ENGINEERING

INDIAN INSTITUTE OF TECHNOLOGY GUWAHATI

GUWAHATI - 781 039, INDIA

FEBRUARY 2012

Certificate

This is to certify that the thesis entitled "**PRINTED MONOPOLE ANTENNAS WITH MULTIPLE BENDS FOR RFID, WLAN AND UWB APPLICATIONS**", submitted by **Jyoti Ranjan Panda** (07610204), a research scholar in the *Department of Electronics and Electrical Engineering, Indian Institute of Technology Guwahati*, for the award of the degree of **Doctor of Philosophy**, is a record of an original research work carried out by him under my supervision and guidance. The thesis has fulfilled all requirements as per the regulations of the institute and in my opinion has reached the standard needed for submission. The results embodied in this thesis have not been submitted to any other University or Institute for the award of any degree or diploma.

Dated:
Guwahati.

Dr. Kshetrimayum Rakhesh Singh
Associate Professor
Dept. of Electronics and Electrical Engg.
Indian Institute of Technology Guwahati
Guwahati - 781 039, India.

To

My dear parents

Birendra Nath Panda and Binodini Panda

for their love and encouragement

&

My wife and son

Rama and Sarthak

for their support and affection

&

My guide

Dr. Kshetrimayum Rakhesh Singh

for his guidance and inspiration

Acknowledgements

First and foremost, I feel it as a great privilege in expressing my deepest and most sincere gratitude to my supervisor Dr. Kshetrimayum Rakhesh Singh, for his excellent guidance throughout my study. His kindness, dedication, hard work and attention to detail have been a great inspiration to me. My heartfelt thanks to you sir for the unlimited support and patience shown to me. I would particularly like to thank him for all his help in patiently and carefully correcting all my manuscripts. I have no doubts that finishing my degree in a proper and timely manner was impossible without his helps, suggestions and advices.

I am also very thankful to my doctoral committee members Professor Dr. Ratnajit Bhattacharjee, Dr. P. R. Sahu and Dr.Aryabartta Sahu for sparing their precious time to evaluate the progress of my work. I express my heartfelt thanks to Dr. Ratnajit Bhattacharjee for providing valuable suggestions on during the progress seminars.

I would also like to thank the Head of the Department Dr. Ratnajit Bhattacharjee and the other faculty members such as Prof. Anil Mahanta for their kind help in carrying out this work. I am also grateful to all the members of the research and technical staff of the department such as Mr. Sanjib Das and Mr. L. N. Sharma without their help I could not have completed this thesis. My special thanks to Mr. Utpal Kumar Sarma for his immense help in fabrication of antennas during the course of my Ph.D work and providing various resources useful for the research work in the high frequency lab of department of EEE of IIT Guwahhati. Apart from this, I would like to thank Mr. Dayananda Goswami for his sincere help in various measurements related to antennas.

I am extremely grateful to Prof. K. J. Vinoy of department of Electrical Communication Engineering (ECE) of Indian Institute of Science (IISc) Bangalore for allowing the anechoic chamber and other allied antenna measurement facilities in his microwave laboratory. I would also like to thank Ms. Hemalatha and Mr. G. Hemanth for their helping hands during antenna measurements. Apart from this my sincere thanks to Mr. Salil Kashyap, a research scholar in department of Electrical Communication Engineering (ECE) of Indian Institute of Science Bangalore for his kind and needful hospitality during my short stayings in the campus of Indian Institute of Science Bangalore. My special thanks to my friends and well wishers in IISc Bangalore such as Harsha, Angshuman, Neeraj, Harikiran, Sarada Prasad and many more for making my staying comfortable and cheerful in IISc Bangalore.

My special thanks to all my friends and well wishers in the department of Electronics and Electrical Engineering, Indian Institute of Technology, Guwahati such as Anka Rao, Ramu, Mahendra Babu, Aditya, Sunil, Usha, Prasadu, Vineel, Rama Chandra, Sachin Kashyap, Sarada Bhai, Himanshuji, Karthikeyanji, Babusenaji, Bhaba, Sumitra, Rajib Panigrahi, Rajib Jana, Sayantan, Samdarshi, Kuntal, Sanjay Mondal, Dol Gobinda, Mandar, Samarji, Pati Sir, Gayadhar, Repabanji, Mukeshji, Murli Manohar, Shivanshu, Deepak Joshi, Brijesh, Ananya, Sheha mam and Ramesh Sir for their kind mental and physical support of some kind during my staying in IIT Guwahati.

My deepest gratitude goes to my family members such as my uncle Prof. S. N. Panda of IIT Kharagpur, my sister Mamatamayee, my nieces Mili, Mini and brother-in-law Prof. P. K. Panigrahi of IIT Kanpur for their continuous love and support throughout my studies. I would like to thank my elder brother Mr. H. R. Panda, sister-in-law Ms. Pritinanda and my niece Surabhi for their love and affection in my life. The opportunities that they have given me and their unlimited sacrifices are the reasons where I am and what I have accomplished so far.

Finally, to my father, Sri Birendra Nath Panda and to my mother, Smt. Binodini Panda, I owe all. No words can really describe my appreciation and gratitude to them for bearing with me for all these years, and without them I would be the lost. I am equally indebted to my in-laws Sri Sudhangshu Ghosh and Smt. Gita Ghosh for their constant support and love. By special thanks to my brother-in-law Dr. Amlan Ghosh for his direct or indirect mental support during my Ph.D in IIT Guwahati. Lastly, thanks to Dr. Rama (Panda) Ghosh and my loving son Sarthak with whom I am ever entangled. I am ever grateful to them for their patience and keep myself on the safer side by taking all the pains on them. I really can not find words to express how much all of them mean to me.

In this short acknowledgement, I may miss the name of some of the people who helped me to make this thesis possible. But I am equally grateful to all of them.

Jyoti Ranjan Panda

Abstract

Printed monopole antenna (PMA) with the microstrip feed line are an important class of broadband antennas. Because of the stripped ground plane on the back side of the substrate, these classes of antennas provide large bandwidth. Dual band operation can be achievable for these classes of antennas by creation of two independent resonating paths in the form of protruding stub in the ground plane and the radiating element printed on the top of the substrate. The major challenge in designing these antennas is the tuning of the protruding stub in the ground plane with the radiating element on the substrate to provide the dual-band operation for RFID, WLAN, etc. These antennas are light weight, low profile, less fragile and easily integrable with the hand held devices.

UWB antennas are wideband antennas (3.1-10.6 GHz), widely used for application in modern wireless hand held devices. Miniaturization is a major challenge for the design of these UWB antennas. Apart from the compact size, consistent omni-directional radiation pattern, appropriate gain characteristics and suitable time domain characteristics are needed for designing a proper UWB antenna. In the UWB frequency region of 3.1-10.6 GHz, many narrowband wireless systems exist such as WiMAX (3.3-3.6 GHz) and WLAN (5-6 GHz), which interferes with the UWB operation. Hence, these narrowband wireless systems' spectrum should be notched up for coexistence of UWB with the other existing narrowband devices.

In our work, we have designed, simulated, fabricated and tested PMAs with multiple bends for applications in RFID, WLAN and UWB systems. Antennas are categorized depending upon the number of bends either in the radiating element or in the protruding strip in the ground plane. In this work, single, double, triple and quadruple bend PMAs for the dual-band WLAN and RFID applications are proposed. It has been observed that our proposed novel PMAs are considerably better than the existing planar antennas in terms of size compactness, bandwidth improvement and gain enhancement for dual-

band RFID/WLAN operations. Besides, rectangular PMA with multiple bends in the feed region with appropriate time and frequency domain characteristics, are proposed for single- and double-notched UWB communications for coexistence of UWB devices with other narrowband devices viz., WIMAX and WLAN.

Keywords: Bend, F-shape, inverted L-strip, monopole antenna, protruding stub, UWB, double notch UWB PMA.

Contents

List of Figures xix

List of Tables xxix

List of Acronyms xxxi

List of Symbols xxxiii

1 Introduction 1

1.1 Introduction . . . 2

1.2 Antenna in wireless system . . . 3

1.3 General antenna classification . . . 4

1.4 Planar antenna . . . 5

1.4.1 Microstrip antenna . . . 6

1.5 Challenges involved in antenna design . . . 7

1.6 Antenna Theory . . . 8

1.6.1 Definition of antenna . . . 8

1.7 Important antenna parameters . . . 9

1.7.1 Frequency bandwidth . . . 9

1.7.2 Directivity and gain . . . 10

1.7.3 Radiation efficiency . . . 11

1.7.4 Radiation pattern . . . 11

1.8 Hertzian dipole . . . 12

1.8.1 Radiation resistance . . . 13

1.8.2 Directivity . . . 13

1.9 Monopole antenna . . . 14

1.10 Methodology to achieve wide operation bandwidth . . . 15

1.10.1 Resonant antennas . . . 15
1.10.2 Quality factor and bandwidth . . . 15
1.11 Fundamental limitations for electrically small antennas . . . 16
1.12 Evolution of planar monopole antenna . . . 19
1.12.1 Theoretical explanation on planar monopole antenna . . . 20
1.12.2 Characteristics of broadband planar monopole antenna . . . 21
1.12.3 "Fat" monopole antennas . . . 22
1.13 Printed monopole antenna (PMA) . . . 24
1.13.1 Printed monopole antenna excitation technique . . . 25
1.14 Design aspects of printed monopole antennas . . . 26
1.15 Motivation . . . 27
1.16 Contribution of the thesis . . . 29
1.17 Organization of the thesis . . . 30
2 PMA structures with single bend 33
2.1 Introduction . . . 34
2.2 F-shaped PMA . . . 35
2.2.1 Antenna design . . . 35
2.2.2 Simulated and measured results on reflection coefficient ($|S_{11}|$) and the parametric study of the proposed antenna . . . 36
2.2.3 Effect of single bend on the proposed antenna performance . . . 38
2.2.4 Gain of the proposed antenna . . . 41
2.2.5 Surface current distribution of proposed antenna . . . 42
2.2.6 Radiation pattern of the proposed antenna . . . 44
2.3 Rectangular PMA with an inverted L-strip in the ground plane . . . 45
2.3.1 Antenna design . . . 45
2.3.2 Simulated and measured results on reflection coefficient ($|S_{11}|$) of the the proposed antenna . . . 46
2.3.3 Effect of single bend on the proposed antenna performance . . . 50
2.3.4 Gain of the proposed antenna . . . 52
2.3.5 Surface current distribution of proposed antenna . . . 55

2.3.6 Radiation pattern of the proposed antenna 57
2.4 Inverted L-shaped PMA with an inverted L-strip in the ground plane 58
2.4.1 Antenna design 58
2.4.2 Simulated and measured results on reflection coefficient ($|S_{11}|$) and the parametric study of the the proposed antenna 59
2.4.3 Effect of single bend on the proposed antenna performance 62
2.4.3.1 Bending analysis on the inverted L-shaped radiating element in the absence of L-strip in ground plane 62
2.4.3.2 Bending analysis on L-strip in ground plane with the presence of inverted L-shaped radiating element 65
2.4.4 Gain of the proposed antenna 67
2.4.5 Surface current distribution of proposed antenna 68
2.4.6 Radiation pattern of the proposed antenna 70
2.5 Summary 70
3 Double bend PMA with an inverted L-strip in the ground plane 73
3.1 Introduction 74
3.2 Inverted L-shaped PMA with an inverted L-strip in the ground plane 75
3.2.1 Antenna design 75
3.3 Simulated and measured results on reflection coefficient ($|S_{11}|$) and the parametric study of the proposed antenna 76
3.4 Effect of double bend on the the proposed antenna performance 84
3.4.1 Bending analysis on reverse L-shaped radiating element with the presence of a square open ended slot in top middle edge of ground plane 84
3.4.2 Bending analysis on reverse L-shaped radiating element with presence of an inverted L-strip and a square open ended slot in top middle edge of ground plane 85
3.4.3 Bending analysis on inverted L-strip in ground plane with presence of a reverse L-shaped radiating element and a square open ended slot in top middle edge of ground plane 88
3.5 Gain of the proposed antenna 91
3.6 Surface current distribution of proposed antenna 93

3.7 Radiation pattern of the proposed antenna 93
3.8 Summary 95

4 Triple bend 9-shaped PMA 97

4.1 Introduction 98
4.2 Antenna design 98
4.3 Simulated and measured results on reflection coefficient ($|S_{11}|$) and the parametric study of the proposed antenna 100
4.4 Effect of triple-bend on the proposed antenna performance 105
4.4.1 Bending analysis on resonating path I with three, two and zero (linear) 90^0 bends in the absence of supporting vertical stub 105
4.4.2 Bending analysis on three and two 90^0 bends in resonating path I in the presence of supporting vertical stub 107
4.5 Gain of the proposed antenna 109
4.6 Surface current distribution of proposed antenna 109
4.7 Radiation pattern of the proposed antenna 111
4.8 Summary 112

5 Quadruple bend PMA with a protruding stub in the ground plane 113

5.1 Introduction 114
5.2 Antenna design 117
5.3 Simulated and measured results on reflection coefficient ($|S_{11}|$) and the parametric study of the proposed antenna 118
5.4 Effect of quadruple-bend on the proposed antenna performance 120
5.4.1 Bending analysis on resonating path I with four, three, two and zero (linear) 90^0 bends in the absence of protruding stub in ground plane 120
5.4.2 Bending analysis on resonating path I with four, three, two and zero (linear) 90^0 bends in the presence of protruding stub in ground plane 124
5.5 Gain of the proposed antenna 125
5.6 Surface current distribution of proposed antenna 125
5.7 Radiation pattern of the proposed antenna 128
5.8 Summary 129

6 Rectangular UWB PMA with multiple bends in the feed region 131

6.1 Introduction . . . 132

6.2 UWB PMA . . . 138

6.2.1 Antenna design . . . 138

6.2.2 Results and discussion . . . 138

6.3 Single notch UWB PMA . . . 141

6.3.1 Antenna design . . . 141

6.3.2 Results and discussion . . . 144

6.4 Double notch UWB PMA . . . 146

6.4.1 Antenna design . . . 146

6.4.2 Results and discussion . . . 148

6.5 Variability of UWB antenna parameters . . . 152

6.5.1 Variability in frequency domain . . . 152

6.5.1.1 Magnitude of transfer function . . . 152

6.5.1.2 Transfer function phase : Group delay . . . 156

6.5.2 Variability in the time domain: Pulse distortion parameters . . . 156

6.5.2.1 Fidelity Factor (F) and stretch ratio (SR) . . . 156

6.5.3 Variability in the space domain . . . 161

6.6 Summary . . . 162

7 Conclusions and future work 165

7.1 Summary of the present work . . . 166

7.2 Conclusions . . . 167

7.3 Suggestions for future work . . . 169

A Antenna Measurement 171

A.1 Antenna Measurement . . . 172

A.1.1 Antenna measurement methodology . . . 172

A.1.1.1 Rohde and Schwarz ZVA 24 vector network analyzer based measurement set up . . . 172

A.1.1.2 Reflection coefficient ($|S_{11}|$) measurement by Rohde and Schwarz ZVA 24 vector network analyzer . . . 173

A.1.2 Agilent PNA (N5230A) based radiation pattern measurement set up 173
A.1.2.1 Anechoic chamber 173
A.1.2.2 Turn table assembly for the far-field radiation pattern measurement . 175
A.1.2.3 Radiation pattern measurement 175
A.1.3 Antenna gain measurement 175

B Electromagnetic Simulation Software IE3D **177**

B.1 Electromagnetic Simulation Software IE3D 178
B.2 IE3D 178
B.3 Basics of method of moments (MoM) 178
B.4 Features of IE3D 181
B.5 Advantages of IE3D 182
B.6 Disadvantages of IE3D 182

Bibliography **183**

List of Publications **201**

List of Figures

1.1 **(a)** A vertical monopole antenna above ground and **(b)** the corresponding center-fed dipole. Shown also are the current variations $I(z')$ over the lengths of both the monopole and the corresponding dipole. 14

1.2 Equivalent circuit of antenna. 16

1.3 Antenna within a sphere of radius r. 18

1.4 Variation of antenna quality factor Q with kr. 18

1.5 **(a)** MSA suspended in air. **(b)** Modified MSA with side feed and **(c)** Planar monopole antenna. 21

1.6 Geometry of straight wire monopole antenna. 23

1.7 Geometry of plate monopole antennas with various configurations. 23

1.8 UWB dipoles with various configurations. 24

1.9 Various geometries of printed monopole antennas. 25

1.10 Various feeding structures to printed monopole antennas. 26

1.11 Different printed monopole antenna design with size reduction technique. 27

2.1 Geometry of the proposed antenna with m=10 mm and n=5.35 mm. 36

2.2 Simulated reflection coefficient ($|S_{11}|$) of proposed antenna. 37

2.3 Simulated reflection coefficient ($|S_{11}|$) of proposed antenna with different constituent structures. 38

2.4 Simulated reflection coefficient ($|S_{11}|$) (dB) graphs, **(a)** m is a variable, n=5.35 mm and **(b)** n is a variable, m=10 mm. 39

2.5 Fabricated prototype of the proposed F-shaped monopole antenna. 39

2.6 Comparison of simulated and measured reflection coefficients ($|S_{11}|$) of the proposed F-shaped monopole antenna for RFID and WLAN applications. 40

2.7 **(a)** Structure of the radiating element with the 90^0 bend resonating path I and **(b)** Structure of the radiating element with the linear resonating path I. 41

2.8 Simulated reflection coefficients ($|S_{11}|$) of the resonant path I with one 90^0 bend and without 90^0 bend (linear). 42

2.9 **(a)** Structure of the radiating element with the 90^0 bend resonating path II and **(b)** Structure of the radiating element with the linear resonating path II. 43

2.10 Simulated reflection coefficients ($|S_{11}|$) of the resonant path II with one 90^0 bend and without 90^0 bend (linear). 44

2.11 **(a)** Comparison of simulated and measured gain (dBi) vs. frequency of the proposed antenna (2.11 GHz-2.77 GHz) and **(b)** Comparison of simulated and measured gain (dBi) vs. frequency of the proposed antenna (4.90 GHz-5.50 GHz). 45

2.12 Direction and magnitude of the surface current distribution for the F-shaped PMA **(a)** at 2.45 GHz and **(b)** at 5.2 GHz. 46

2.13 Measured E-plane (yz-plane) radiation patterns of the proposed antenna at **(a)** 2.45 GHz and **(b)** 5.2 GHz. 46

2.14 Measured H-plane (xy-plane) radiation patterns of the proposed antenna at **(a)** 2.45 GHz and **(b)** 5.2 GHz. 47

2.15 Geometry of the proposed antenna **(a)** Top view and **(b)** Bottom view. 47

2.16 Simulated reflection coefficient ($|S_{11}|$) of proposed antenna. 48

2.17 Geometry of radiating structure with rectangular radiating element having no inverted L-strip in ground plane **(a)** Top view and **(b)** Bottom view. 50

2.18 Geometry of radiating structure with rectangular radiating element having only vertical portion of the inverted L-strip in ground plane **(a)** Top view and **(b)** Bottom view. . . 51

2.19 Comparison of simulated reflection coefficients ($|S_{11}|$) of the proposed antenna with the radiating structures having no inverted L-strip and only vertical portion of the inverted L-strip in ground plane. 51

2.20 Fabricated prototype of the proposed antenna. 52

2.21 Comparison of the simulated and the measured reflection coefficients ($|S_{11}|$) of the proposed antenna. 53

2.22 Geometry of the structure with linear strip in the ground plane of same length as inverted L-strip of the proposed antenna **(a)** Top view and **(b)** Bottom view. 53
2.23 Comparison of simulated reflection coefficients ($|S_{11}|$) of the radiating structures with inverted L-strip in ground plane with rectangular radiating element and linear vertical strip of same length (1-9 GHz range). 54
2.24 Simulated reflection coefficient ($|S_{11}|$) of the radiating structure with a rectangular radiating element and linear vertical strip of same length as its inverted L-strip counterpart in ground plane (1-12 GHz range). 54
2.25 **(a)** Comparison of simulated and measured gain (dBi) vs. frequency of the proposed antenna (2.14 GHz-3.47 GHz) and **(b)** Comparison of simulated and measured gain (dBi) vs. frequency of the proposed antenna (3.98 GHz-7.7 GHz). 55
2.26 Direction and magnitude of the surface current distribution for the rectangular PMA with an inverted L-strip in the ground plane **(a)** at 2.4 GHz and **(b)** at 5.2 GHz. . . . 56
2.27 Measured E-plane (yz-plane) radiation patterns of the proposed antenna at **(a)** 2.4 GHz and **(b)** 5.2 GHz. 57
2.28 Measured H-plane (xy-plane) radiation patterns of the proposed antenna at **(a)** 2.4 GHz and **(b)** 5.2 GHz. 57
2.29 Geometry of the proposed antenna **(a)** Top view and **(b)** Bottom view. 58
2.30 Simulated reflection coefficient ($|S_{11}|$) of proposed antenna. 59
2.31 Geometry of radiating structure with inverted L-shaped radiating element having only vertical portion of inverted L-strip (n=0) in ground plane **(a)** Top view and **(b)** Bottom view. 60
2.32 Comparison of simulated reflection coefficients ($|S_{11}|$) of the proposed antenna, inverted L-shaped radiating structure without inverted L-strip and with only vertical portion of inverted L-strip (n=0) in ground plane. 61
2.33 Simulated reflection coefficient ($|S_{11}|$) (dB) graphs, **(a)** m is a variable, n=11 mm and p=10 mm, **(b)** n is a variable, m=7.5 mm and p=10 mm and **(c)** p is a variable, m=7.5 mm and n=11 mm. 63
2.34 Fabricated prototype of the proposed antenna. 64

2.35 Comparison of the simulated and measured reflection coefficients ($|S_{11}|$) of the proposed antenna. 64
2.36 Geometry of radiating structure with linear vertical strip as the radiating element in the absence of inverted L-strip in ground plane **(a)** Top view and **(b)** Bottom view. . 65
2.37 Geometry of radiating structure with inverted L-shaped radiating element in the absence of inverted L-strip in ground plane **(a)** Top view and **(b)** Bottom view. 65
2.38 Effect of bend on the reflection coefficient ($|S_{11}|$) with one 90^0 bend in radiating element and a linear radiating element with no 90^0 bend of same length in the absence of inverted L-strip in ground plane. 66
2.39 Geometry of radiating structure with linear vertical strip in the ground plane with inverted L-shaped radiating element **(a)** Top view and **(b)** Bottom view. 67
2.40 Comparison of simulated reflection coefficients ($|S_{11}|$) of the radiating structures with inverted L-strip in ground plane and a linear vertical strip of same length in presence of inverted L-shaped radiating element (1-7 GHz range). 67
2.41 Simulated reflection coefficient ($|S_{11}|$) of the radiating structure with a linear vertical strip in the ground plane of same length as inverted L-strip in presence of inverted L-shaped radiating element (1-15 GHz range). 68
2.42 **(a)** Comparison of simulated and measured gain (dBi) vs. frequency of the proposed antenna (2.01 GHz-2.63 GHz) and **(b)** Comparison of simulated and measured gain (dBi) vs. frequency of the proposed antenna (4.82 GHz-6.13 GHz). 69
2.43 Direction and magnitude of the surface current distribution for the inverted L-shaped PMA with an inverted L-strip in the ground plane **(a)** at 2.4 GHz and **(b)** at 5.5 GHz. 70
2.44 Measured E-plane (yz-plane) radiation patterns of the proposed antenna at **(a)** 2.4 GHz and **(b)** 5.5 GHz. 71
2.45 Measured H-plane (xy-plane) radiation patterns of the proposed antenna at **(a)** 2.4 GHz and **(b)** 5.5 GHz. 71

3.1 Geometry of the proposed antenna **(a)** Top view and **(b)** Bottom view. 75
3.2 Simulated reflection coefficient ($|S_{11}|$) of proposed antenna. 76

3.3 Geometry of the structure having reverse L-shaped radiating element with absence of reverse L-strip and open-ended slot in the middle top edge of the ground plane **(a)** Top view and **(b)** Bottom view. 78
3.4 Geometry of the structure having reverse L-shaped radiating element with a vertical strip (n=0) and open-ended slot in the middle top edge of the ground plane **(a)** Top view and **(b)** Bottom view. 79
3.5 Geometry of structure having reverse L-shaped radiating element with reverse L-strip in the ground plane and the absence of open-ended slot in the middle top edge of the ground plane **(a)** Top view and **(b)** Bottom view. 80
3.6 Comparison of simulated reflection coefficients ($|S_{11}|$) of the radiating elements shown in the Fig. 3.3, Fig. 3.11 and Fig 3.4. 80
3.7 Comparison of simulated reflection coefficients ($|S_{11}|$) of the radiating elements shown in the Fig. 3.1 and Fig. 3.5. 81
3.8 Simulated reflection coefficient ($|S_{11}|$) (dB) graphs, **(a)** n is a variable, p=5 mm and **(b)** p is a variable, n=9.5 mm. 82
3.9 Fabricated prototype of the proposed antenna. 82
3.10 Comparison of simulated and measured reflection coefficients ($|S_{11}|$) of the proposed antenna. 83
3.11 Geometry of the structure with two 90^0 bends in radiating element and an open ended slot in the middle top edge of the ground plane **(a)** Top view and **(b)** Bottom view. . 85
3.12 Geometry of the structure with one 90^0 bend in radiating element and an open ended slot in the middle top edge of the ground plane **(a)** Top view and **(b)** Bottom view. . 86
3.13 Geometry of the structure with a linear radiating element and an open ended slot in the middle top edge of the ground plane**(a)** Top view and **(b)** Bottom view. 87
3.14 Comparison of simulated reflection coefficients ($|S_{11}|$) of the radiating elements with two 90^0 bends, one 90^0 bend and a linear structure consisting of a open ended slot in the middle top edge of the ground plane. 87
3.15 Geometry of the structure with one 90^0 bend in radiating element with inverted L-strip and an open ended slot in the middle top edge of the ground plane **(a)** Top view and **(b)** Bottom view. 88

3.16 Geometry of the structure with a linear radiating element with an inverted L-strip and an open ended slot in the middle top edge of the ground plane **(a)** Top view and **(b)** Bottom view. 89

3.17 Comparison of simulated reflection coefficients ($|S_{11}|$) of the radiating elements with two 90^0 bends, one 90^0 bend and a linear structure consisting of inverted L-strip and an open ended slot in the middle top edge of the ground plane. 89

3.18 Geometry of the structure with a vertical strip in the ground plane consisting of reverse L-shaped radiating element and an open ended slot in the middle top edge of the ground plane. 90

3.19 Comparison of simulated reflection coefficients ($|S_{11}|$) of proposed antenna with the radiating structure having a linear vertical strip in ground plane consisting of a reverse L-shaped radiating element and an open ended slot in the middle top edge of the ground plane (1-8.5 GHz range). 91

3.20 Simulated reflection coefficient ($|S_{11}|$) of the radiating structure having a linear vertical strip in ground plane consisting of a reverse L-shaped radiating element and an open ended slot in the middle top edge of the ground plane (1-15 GHz range). 91

3.21 **(a)** Comparison of simulated and measured gain (dBi) vs. frequency of the proposed antenna (2.14 GHz-3.14 GHz) and **(b)** Comparison of simulated and measured gain (dBi) vs. frequency of the proposed antenna (3.4 GHz-8.2 GHz). 92

3.22 Direction and magnitude of the surface current distribution for the inverted L-shaped PMA with an inverted L-strip in the ground plane **(a)** at 2.4 GHz and **(b)** at 5.2 GHz. 94

3.23 Measured E-plane (yz-plane) radiation patterns of the proposed antenna at **(a)** 2.4 GHz and **(b)** 5.2 GHz. 94

3.24 Measured H-plane (xy-plane) radiation patterns of the proposed antenna at **(a)** 2.4 GHz and **(b)** 5.2 GHz. 95

4.1 Geometry of the proposed antenna. 99

4.2 Simulated reflection coefficient ($|S_{11}|$) of proposed antenna. 101

4.3 Geometry of radiating structures with **(a)** with resonating path I only and **(b)** with supporting vertical stub only. 102

4.4 Simulated reflection coefficients ($|S_{11}|$) of the proposed antenna with different constituent structures. . . . 103
4.5 Simulated reflection coefficient ($|S_{11}|$) (dB) graphs, **(a)** L_4 is a variable and **(b)** L_2 is a variable. . . . 104
4.6 Fabricated prototype of the proposed antenna. . . . 104
4.7 Comparison of the simulated and the measured reflection coefficients ($|S_{11}|$) of the proposed antenna. . . . 105
4.8 Geometry of radiating structures with **(a)** only resonating path I having two 90^0 bends and **(b)** linear resonating path I with no 90^0 bend. . . . 106
4.9 Comparison of simulated reflection coefficients ($|S_{11}|$) of the radiating structures with the presence of only resonating path I having three 90^0 bends, two 90^0 bends and linear resonating path (no 90^0 bend). . . . 107
4.10 Geometry of radiating element with two 90^0 bends in the resonating path I with supporting vertical stub. . . . 108
4.11 Comparison of simulated reflection coefficients ($|S_{11}|$) of proposed antenna (three 90^0 bends in resonating path I and supporting vertical stub) and two 90^0 bends in the resonating path I with supporting vertical stub. . . . 109
4.12 **(a)** Comparison of simulated and measured gain (dBi) vs. frequency of the proposed antenna (2.18 GHz-2.93 GHz) and **(b)** Comparison of simulated and measured gain (dBi) vs. frequency of the proposed antenna (4.46 GHz-6.30 GHz). . . . 110
4.13 Direction and magnitude of the surface current distribution for triple bend 9-shaped PMA **(a)** at 2.45 GHz and **(b)** at 5.2 GHz. . . . 111
4.14 Measured E-plane (yz-plane) radiation patterns of the proposed antenna at **(a)** 2.45 GHz and **(b)** 5.2 GHz. . . . 112
4.15 Measured H-plane (xy-plane) radiation patterns of the proposed antenna at **(a)** 2.45 GHz and **(b)** 5.2 GHz. . . . 112

5.1 Geometry of the proposed antenna with M = 8 mm, N = 12 mm and P = 4.8 mm. . . . 117
5.2 Simulated reflection coefficient ($|S_{11}|$) of the proposed antenna. . . . 118
5.3 Simulated reflection coefficients ($|S_{11}|$) of the antenna with and without protruding stub in the ground plane. . . . 119

5.4 Simulated reflection coefficient ($|S_{11}|$) (dB) graphs, **(a)** M is a variable, N= 12 mm, P =4.8 mm, **(b)** N is a variable, M=8 mm, P=4.8 mm and **(c)** P is a variable, M=8 mm, N=12 mm. 121

5.5 Fabricated folded strip monopole antenna with a protruding stub prototype (a) Top view and (b) Bottom view. 122

5.6 Comparison of the simulated and measured reflection coefficients ($|S_{11}|$) (dB) of the proposed dual-band monopole antenna for WLAN and RFID applications. 122

5.7 Geometry of radiating element in the absence of vertical stub in the ground plane with **(a)** four 90^0 bends, **(b)** three 90^0 bends, **(c)** two 90^0 bends and **(d)** zero 90^0 bend. . . 123

5.8 Comparison of simulated reflection coefficients ($|S_{11}|$) with four, three, two and zero (linear) 90^0 bends in resonating path I in the absence of vertical stub in ground plane. 124

5.9 Geometry of radiating element in the presence of vertical stub in the ground plane with **(a)** three 90^0 bends, **(b)** two 90^0 bends and **(c)** zero 90^0 bend. 126

5.10 Comparison of simulated reflection coefficients ($|S_{11}|$) with four, three, two and zero (linear) 90^0 bends in resonating path I in the presence of vertical stub in ground plane. 127

5.11 Measured gain (dBi) vs. frequency of the proposed antenna. 127

5.12 Direction and magnitude of the surface current distribution for quadruple bend PMA with a protruding stub in the ground plane **(a)** at 2.4 GHz and **(b)** at 5.8 GHz. . . . 128

5.13 Measured E-plane (yz-plane) radiation patterns of the proposed antenna at **(a)** 2.4 GHz and **(b)** 5.8 GHz. 129

5.14 Measured H-plane (xy-plane) radiation patterns of the proposed antenna at **(a)** 2.4 GHz and **(b)** 5.8 GHz. 129

6.1 FCC mask for UWB indoor communications. 133

6.2 Geometry of antenna 1 (UWB PMA). 139

6.3 Geometry of radiating UWB antennas with **(a)** zero step and **(b)** one step in the stair-cased structures at the bottom corners of the rectangular radiating element. . . . 140

6.4 Comparison of VSWR graphs of radiating UWB antennas with zero step, one step and two steps in the stair-cased structures at the bottom corners of the rectangular radiating element. 140

6.5 Fabricated prototype of the UWB PMA (antenna 1) **(a)** Top View **(b)** Bottom View. 141

6.6 Comparison of simulated and measured VSWR of antenna 1. 141
6.7 Comparison of simulated and measured gain (dBi) vs. frequency of antenna 1. 142
6.8 Geometry of antenna 2 (single notch UWB PMA). 143
6.9 Fabricated prototype of the single notch UWB PMA (antenna 2) **(a)** Top View **(b)** Bottom View. 143
6.10 Measured and simulated VSWR of antenna 2, compared to antenna 1. 145
6.11 Effect of length (N) on the VSWR of the antenna 2. 145
6.12 Simulated and measured gain (dBi) of antenna 2, compared with the measured gain of antenna 1. 146
6.13 Geometry of antenna 3 (Double notch UWB PMA). 147
6.14 Fabricated prototype of the double notch UWB PMA (antenna 3) **(a)** Top View **(b)** Bottom View. 147
6.15 Simulated and measured VSWR of antenna 3, compared to antenna 1. 149
6.16 Simulated and measured gain (dBi) of antenna 3, compared with the measured gain of antenna 1. 149
6.17 Comparison between the simulated and measured input resistance of antenna 3. 150
6.18 Comparison between the simulated and measured input reactance of antenna 3. 150
6.19 Direction and magnitude of the surface current distribution for double notch UWB PMA (antenna 3) **(a)** at 3.4 GHz and **(b)** at 5.5 GHz. 151
6.20 Measured E-plane (yz-plane) radiation patterns of double notch UWB PMA (antenna 3) at **(a)** 4.5 GHz, **(b)** 7.5 GHz, **(c)** 9.5 GHz and **(d)** 12 GHz. 152
6.21 Measured H-plane (xy-plane) radiation patterns of double notch UWB PMA (antenna 3) at **(a)** 4.5 GHz, **(b)** 7.5 GHz, **(c)** 9.5 GHz and **(d)** 12 GHz. 153
6.22 A transmit-receive antenna system. 154
6.23 Measured transfer function ($|S_{21}|$) (face-to-face) of antenna 1, antenna 2 and antenna 3. 155
6.24 Measured group delay of antenna 1, antenna 2 and antenna 3. 157
6.25 Antenna input signal (5^{th} derivative of Gaussian pulse) with single pulse. 158
6.26 Power spectral density (dBm/MHz) of FCC spectral mask for indoor UWB communication system and power spectral density (dBm/MHz) of antenna input signal (5^{th} derivative of Gaussian pulse). 158

6.27 Experimental set-up for time domain transmission and reception characteristics for antenna 3 (face-to-face). 159

6.28 Experimental set-up for time domain transmission and reception characteristics for antenna 3 (side by side). 160

6.29 Measured received signals of antenna 3 **(a)** transmitted fifth derivative of Gaussian pulse, **(b)** face-to-face (θ=0^0), and **(c)** side-by-side (θ=0^0). 160

6.30 Measured received signals of antenna 3 stationed face-to-face for **(a)** θ=30^0 **(b)** θ=60^0 and **(c)** θ=90^0. 163

6.31 Measured received signals of antenna 3 stationed side-by-side for **(a)** θ=30^0 **(b)** θ=60^0 and **(c)** θ=90^0. 163

A.1 Front face of the Rohde and Schwarz ZVA 24 vector network analyzer. 172

A.2 Radiation pattern measurement set up. 174

A.3 Photographs of anechoic chamber used for the measurement of radiation pattern for proposed antennas in Microwave Laboratory of department of Electrical Communication Engineering, Indian Institute of Science, Bangalore, INDIA. 174

B.1 An incident field E_i is applied to the metallic structure S. 179

List of Tables

1.1 **Frequency bands assigned for modern wireless communication system** . . . 3

1.2 **Relationship between Monopole and Dipole Antenna** 15

2.1 **Comparative study for the proposed antenna with the existing antennas** . . 52

2.2 **Comparative study for the proposed antenna with the existing antennas** . . 62

3.1 **Comparative study for the proposed antenna with the existing antennas** . . 83

5.1 **Technical specifications for RFID systems** 116

6.1 **UWB Specifications** 134

A.1 **Some specifications of the Rohde and Schwarz ZVA 24 vector network analyzer** 173

List of Acronyms

ABW	Absolute Bandwidth
CPW	Coplanar Waveguide
DBMA	Dual-band Monopole Antenna
DCS	Digital communication system
DPO	Digital Phosphor Oscillator
DVB	Digital Video Broadcasting
FCC	Federal Communication Commission
FBW	Fractional Bandwidth
GPS	Global positioning system
GSM	Global system for mobile
HIPERLAN	High Performance Radio Local Area Network
IEEE	Institute of Electrical and Electronics Engineer
IF	Intermediate Frequency
IMT	International Mobile Telecommunications
ISM	Industrial Scientific Medical
ISI	Inter Symbol Interference
MIC	Microwave Integrated Circuit
MMIC	Monolithic Microwave Integrated Circuit
MSA	Microstrip Antenna
PDA	Personal Digital Assistants
PCB	Printed Circuit Board
PCS	Personal Communication System
PHS	Personal Handy-Phone System
PMA	Printed Monopole Antenna

RFID	Radio Frequency Identification
SMA	Sub Miniature A
UHF	Ultra High Frequency
UMTS	Universal Mobile Telecommunication System
UWB	Ultra-Wide Band
VSWR	Voltage Standing Wave Ratio
WB	Wireless Broadband
WiMAX	Worldwide Inter-operability for Microwave Access
WLAN	Wireless Local Area Networks

List of Symbols

$\overrightarrow{A}$	Magnetic vector potential
D	Directivity
D_0	Maximum directivity
e_{cd}	Conduction and dielectric efficiency or radiation efficiency
$\overrightarrow{E}$	Electric field intensity, V/m
η	Intrinsic impedance of the medium (377 $\approx 120\pi$ Ohms for free space)
f_L	Lower edge bandwidth
f_H	Upper edge bandwidth
f_0	Resonant frequency
G_0	Maximum gain
$\overrightarrow{H}$	Magnetic field intensity, A/m
k	Wave number(m^{-1})
λ	Wavelength
μ	Permeability of free space ($4\pi\times10^{-7}$ H/m)
Ω	Resistance
P_{in}	Total input power
P_{rad}	Total radiated power
Q	Quality factor
$Q_{lossless}$	Lossless quality factor
R_r	Radiation resistance
R_L	Load resistance
U	Radiation intensity
U_0	Radiation intensity of isotropic source
U_{max}	Maximum radiation intensity

W_{av}	Average power density
Z_w	Wave impedance
Z_{in}	Input impedance

1

Introduction

Contents

1.1 Introduction 2
1.2 Antenna in wireless system 3
1.3 General antenna classification 4
1.4 Planar antenna 5
1.5 Challenges involved in antenna design 7
1.6 Antenna Theory 8
1.7 Important antenna parameters 9
1.8 Hertzian dipole 12
1.9 Monopole antenna 14
1.10 Methodology to achieve wide operation bandwidth 15
1.11 Fundamental limitations for electrically small antennas 16
1.12 Evolution of planar monopole antenna 19
1.13 Printed monopole antenna (PMA) 24
1.14 Design aspects of printed monopole antennas 26
1.15 Motivation 27
1.16 Contribution of the thesis 29
1.17 Organization of the thesis 30

1.1 Introduction

James Clerk Maxwell predicted the existence of electromagnetic waves in 1873 [1], which is the beginning of the wireless communication engineering. He proved that the light is a continuously varying electromagnetic wave with time and at other wavelengths, the electromagnetic radiation is possible. Heinrich Hertz in the year 1888 demonstrated that the electromagnetic waves are existed physically with the help of first spark gap generator.

Guglielmo Marconi first demonstrated the phenomenon of wireless telegraph to an English telegraph office in the year 1896 [2]. Sir Jagadish Chandra Bose (1858-1937), a highly talented Indian genius widely recognized as the first scientist, who demonstrated the phenomenon of wireless transmission of electromagnetic waves with the help of horn antenna [3] between the periods of 1894-1900. In this way, both Marconi and J.C Bose opened the new scientific and technical field of wireless communication. In the years 1901, Marconi first transmitted three-dot Morse codes of the letter "S" over the distance of three kilometers [4]. Fifty vertical wires were used as the transmitting antenna in the form of fan connected to the ground through the spark transmitter. The receiving antenna was supported by a flying kite which was a 200m wire. This was the beginning of antenna technology. In 1921, the short-wave radio was developed by which the radio transmission to the other side of the world was made possible [5]. Frequency modulation (FM) was first demonstrated by the Edwin Armstrong in 1933 and in 1940, an FM-mobile-radio system for the US state police was designed by Daniel Nobel [6], professor of electrical engineering at University of Connecticut. Global System for Mobile (GSM) was formed in the year 1982 which was the beginning of the modern wireless communication engineering. Around 1990, the release of the first GSM specification and the L-band digital radio demonstration were the major events which creates the widespread research interests in the wireless communication system. The first GSM call was made in Finland in the year 1991 and six years after, the IEEE 802.11 standard was came into existence which is known as Wi-Fi [7]. In 2000, Bluetooth special interest group was formed and Eriksson Company first released the Bluetooth products [8]. The first Bluetooth product was a wireless handset and phone adaptor. The research in wireless communication systems was spreaded rapidly in the last ten years which provided numerous technical solutions in the digital and wireless communication domain and made the life simpler. Wireless technology is generating enormous appeal for sophisticated data and voice services such as Wi-Fi, 3G along with GSM, code division multiple access (CDMA) and UMTS [9]. An overview of the frequency bands assigned for

Table 1.1: Frequency bands assigned for modern wireless communication system

System	Full Description	Band of Frequency (MHz)
GSM-900	Global System for mobile communication	880-960
GPS	Global Position Systems	1208-1248, 1556-1595
DCS-1800	Digital Communication System	1710-1795
PCS-1900	Personal Communication System	1850-1990
PHS	Personal Handy-Phone Systems	1905-1920
UMTS	Universal Mobile Telecommunications Systems	1290-2170
Wi-Bro	Wireless Broadband	2300-2390
ISM	Industrial, Scientific and Medical	2400-2484, 5150-5350, 5725-5825
DVB-H	Digital Video Broadcasting	470-890
RFID	Radio Frequency Identification Systems	30-2400
UWB	Ultra Wide Band	3100-10600

modern wireless communication system is summarized in Table 1.1.

1.2 Antenna in wireless system

Antenna is an integral as well as a critical component of any wireless communication system. Truly speaking antenna acts as a transducer between the free space and guided wave. According to the IEEE standards definition for the antenna defines the antenna as "a means for radiating or receiving radio waves" [10]. All sorts of antennas operate on the basic principle of electromagnetic theory. The actual word antenna is derived from the Latin word "antemna", which become antenna in English. The term antenna was first used by Marconi in the lecture delivered by him in the year 1890 [11].

After James Clerk Maxwell postulated and unified the theory of electromagnetism, the evolution of antenna begins in rapid manner. Initially the shape of antenna was wire type radiating elements in the year 1940, which can be operated up to some ultra high frequency (UHF). But the beginning of the World War II propelled the development of antenna research in a marvelous way. During that period, the antenna technology was developed with elements such as reflectors, apertures and waveguides [12]. The development of microwave sources such as magnetron and klystron accelerated the emergence of antenna and microwave communication.

Computational techniques for the calculation of various parameters of the electromagnetic waves developed during World War II. Simultaneously the evolution of computer architectures enhances the

computing capability of complex numerical methods that allowed the ease of analysis for the complex antenna system [13].

During the middle of the nineteenth century, drastic development occurred in the antenna technology as the impedance bandwidth is enlarged to 40:1 or more. These wideband antennas are known as the frequency independent antennas, whose geometrics are specified by angles instead of linear dimensions. The important application of these frequency independent antennas includes TV reception, lenses, feed for reflectors, point to point communication, etc.

Nearly twenty years later, patch antenna were introduced which are used in many applications which are used in many applications till date. These patch antennas are easy to fabricate compared to earlier antenna design and configuration. These patch antennas can provide easy integration with many compact and hand-held devices and various antenna characteristics of these antennas such as radiation pattern, gain, etc can be controlled electronically. In recent years, millimeter wave antennas has gone through many transformations and now-a-days these antennas can be integrated in many small devices in which the passive and active components can be combined with the radiating elements in one component unit. Adaptive arrays also known as the smart antennas were introduced in the recent years, where signal processing algorithms can be incorporated and simultaneously embedded with the antennas. These new era antennas can be easily integrable with the advanced digital systems [14].

1.3 General antenna classification

Antennas can be classified into six broad categories. They are (1) Wire antenna, (2) Array antennas, (3) Aperture antennas, (4) Lens antenna, (5) Reflector antenna, and (6) Printed antennas.

Wire antennas are used as transmitting as well as receiving antenna on the short wave, medium wave and long wave bands and are found application in aircrafts, ships, buildings, automobiles and so on. Dipole helix and loop antennas can be included in the category of the wire antenna.

Aperture antennas have some sort of openings through which the electromagnetic waves are transmitted or received. Examples of aperture antennas include slots, waveguides, horns, reflectors and lenses. Aperture antennas are commonly used in aircraft and spacecraft applications. The aperture can be flush mounted with the surface of the vehicle and the opening can be covered with a dielectric which allows the electromagnetic energy to pass through.

Lens antenna can convert spherical waves into flat plane waves. This antenna uses a microwave lens, which are simpler to an optical lens to strengthen the spherical wave-fronts. These antennas are used for outdoor as well as indoor applications such as point-to-point, point-to-multipoint links, radio astronomy radars, systems including collision avoiding devices and satellite communication.

Reflector antennas are used to concentrate flux of electromagnetic energy (EM) radiated/received or to change its direction. Usually they are parabolic in nature. Advantages of the reflector antennas have high gain and directivity. Reflector antennas are used in radio telescopes and satellite communication. Array antennas [15, 16, 17] are modern antennas developed in the last three decades which includes adaptive arrays capable of beam-forming.

In comparison to the above described antennas, printed antennas are inexpensive and easy to fabricate. On the printed circuit board (PCB), they are compact in size and can accommodate on the planar and non-planar surfaces and compatible with the monolithic microwave integrated circuits (MMIC) designs. The most well known and printed antenna is microstrip antenna.

1.4 Planar antenna

Planar antennas have completely revolutionized the application of microwave antennas in wireless communication systems. Planar antennas are compact and can be easily integrable in the hand-held devices such as mobile phones and personal digital assistants (PDAs) [18, 19]. For accommodation of these planar antennas within the hand-held devices, the size of the planar antennas must be compact and mechanically strong. So the microstrip antennas and printed monopole antennas (PMA) are the appropriate candidate for application in the wireless and ultra-wide-band (UWB) communication systems. For the application of wireless local area networks (WLAN), printed antennas are very much appropriate. Easy integration of these antennas is possible on the PCB for the reduction on the packaging cost.

Printed antennas are originated from the development in the research of microstrip, coplanar waveguide (CPW), slot lines etc [20, 21]. The first printed antennas were used in mid nineteen seventies even though the explanation of the origin of the radiation from these antennas was proposed in early 1950. The key advantages of the printed antennas are

- Easy fabrication technique using PCB.
- Small overall dimensions and light weight.

- Integrable to antenna array systems.
- Easy integration with MMIC devices and other electronic components.

1.4.1 Microstrip antenna

Microstrip patch antenna in its simplest form comprise of a metal radiating patch on one side of the dielectric substrate, which have a full metal ground plane on the other side. In the microstrip antenna (MSA)[89], a feeding structure is needed to excite the metal radiating and in general, a microstrip transmission line of 50-Ω is used to feed the MSA. But there are many other feeding mechanisms existed to excite the radiating element and notable among them are coaxial feed or probe feed, aperture coupled microstrip feed and coplanar waveguide (CPW) feed. Effective radiation from the patch is possible if the length of the patch would be a half guided wavelength size at the resonant frequency. Fringing occurs between the ground plane and the patch edge, which is responsible for the radiation from the patch. A small degree of directivity can be possible as the fringing region acts as a two-element array.

Several advantages can be obtainable from microstrp antennas compared to traditional microwave antennas and therefore the microstrip antennas can be used over the broad frequency range from few MHz to several GHz. Some of the typical advantages of the microstrip antennas are listed below.

- Low volume and light weight.
- Fabrication cost is very low.
- Easy integrable with the microwave integrated circuit (MIC).
- Dual-frequency and dual-polarization operations are possible.
- Feed-lines and matching networks can be easily fabricated.
- Mechanically strong and can be easily mounted on the hard surfaces.

But along with the above advantages microstrip antenna suffers from many disadvantages also and notable among them are

- Narrow bandwidth.
- Low gain.

- Low efficiency.
- Large Ohmic loss.
- Extraneous radiation from junctions and feeds.
- Complex feed structure for high frequency arrays.
- Excitation of surface wave.
- Less capability to handle the power.

In microstrip antennas, the reason for narrow bandwidth and low efficiency is due to the large quality factor (Q). By increasing the thickness of the substrate, the Q can be reduced. But by increasing the thickness of the substrate, surface waves will be generated by consuming a big fraction of the total power delivered by the source. Due to the surface wave, unwanted power loss occurs, since the scattering takes place at the dielectric bends which causes the degradation of antenna performance [22].

The radiating patches of microstrip antenna can take different shapes such as rectangular, square, circular, elliptical, triangular, concentric circular etc.

1.5 Challenges involved in antenna design

The modern era wireless communication system is advancing enormously that all the digital wireless services such as Bluetooth and WLAN etc can be integrated inside the small communication wireless gadgets and hand held devices such as mobile phones. Hence antenna design is a big challenge in the present era. Another biggest challenge in antenna design involves the placement of antenna inside the small hand held devices so that the antenna can accommodate suitably inside the gadgets. To meet this challenge, multi-band antenna design is needed with consistent radiation pattern, appropriate gain and efficiency over the wide frequency band.

Small antennas with sufficient bandwidth, appropriate gain and less sensitive to the outer environment are needed to do the miniaturization of the modern hand held communication device. But the antenna size, bandwidth, quality factor and radiation efficiency are interrelated and the miniaturization has its theoretical limitation to achieve maximum gain and efficiency of the radiator.

1.6 Antenna Theory

Monopole antennas are the most widely used broadband antennas in the modern wireless communication domain. Due to their some of the excellent features such as broader bandwidth, omnidirectional radiation pattern, appropriate gain characteristics, ease of fabrication, mechanically strong etc, they are most popular among the antenna fraternity. Apart from this, monopole antennas are the most basic and primitive category of antennas which have been widely used since the Italian inventor Guglielmo Marconi sent and received first radio signal in Italy in 1895. The structure of monopole antenna is consist of a straight wire vertically mounted above a ground plane and provides horizontal radiation pattern and vertical polarization. The thin wire monopole antenna can provide wider bandwidth by modifying their geometry such as folding, loading or thickening of the straight wire which is the radiating element. Typical monopole antenna design includes various loading elements, conical or skeletal conical, cage etc [23-26]. Apart from these bandwidth enhancement techniques, planar elements have been used in place of wire elements of the monopoles to broaden the impedance bandwidth [27-32].

The main aim of this thesis is to design antennas which can be suitable for the future wireless and UWB applications. Before proceeding to the antenna design procedure, it is important to have some acquaintance with the general antenna basics and concepts. There are some antennas terminologies which are always have to be considered while designing the antenna. At the same time, the primary requirements for the wireless and UWB antenna are discussed. Apart from this, some typical approaches for achieving the wide operation bandwidth are presented.

1.6.1 Definition of antenna

The IEEE standard Definitions of Terms for Antennas (IEEE Std 145-1983) defines the antenna or aerial as a means for radiating or receiving radio waves. So, the antenna acts as a transitional structure between free-space and a guiding device. The guiding device or the transmission line may take the form of a coaxial line or a hollow pipe (waveguide) or a microstrip, and it is used to transport electromagnetic energy from the transmitting source to the antenna (when the antenna is used in transmitting mode), or from the antenna to the receiver (when the antenna is used in receiving mode).

The main function of an antenna is to accentuate or optimize the radiation energy in particular direction and block the unwanted radiation energy in other direction at a particular frequency in

advanced wireless systems. So, apart from the transitional device, the antenna must serve as a directional element. Hence in order to meet the specific requirements, the antenna must take the various physical geometries. As a result the antenna may be a straight conducting wire, a patch, an aperture, a lens, a reflector, an assembly of elements (arrays) and so on. A proper design of antenna can improve the overall system performance and relax the system requirements.

1.7 Important antenna parameters

To elaborate the functional performance of an antenna, definitions of various antenna parameters are needed. In practice, there are commonly used antenna parameters including frequency bandwidth, directivity, gain, radiation pattern, input impedance and so on[89].

1.7.1 Frequency bandwidth

Frequency bandwidth is the range of frequencies with respect to some characteristics within which the performance of antenna conforms to a specified standard. In other words, on the either side of the center frequency, the bandwidth can be considered as the range of frequencies where the antenna characteristics are within the acceptable value of those at the center frequency. Generally, the antenna should have the reflection coefficient less than -10 dB over its frequency bandwidth in wireless communication. The frequency bandwidth of an antenna is generally expressed as either absolute bandwidth (ABW) or fractional bandwidth (FBW). If f_L and f_H are the lower edge and upper edge the antenna bandwidth respectively, then the ABW is defined as the difference of f_H and f_L. The FBW is defined as the percentage of the frequency difference over the center frequency as given in equation 1.1 and 1.2.

$$ABW = (f_H - f_L) \tag{1.1}$$

$$FBW = \frac{2(f_H - f_L)}{(f_H + f_L)} \times 100 \tag{1.2}$$

In case of broadband antennas, the bandwidth can be expressed as the ratio of the upper edge and lower edge frequencies, where the antenna performance is acceptable as shown in the equation 1.3.

$$BW = \frac{f_H}{f_L} \tag{1.3}$$

1.7.2 Directivity and gain

The directivity of an antenna is defined as the ratio of the radiation intensity in a given direction from the antenna to the radiation intensity averaged over all directions which is equivalent to the radiation intensity of an isotropic antenna. The average radiation intensity is equal to the total power radiated by the antenna divided by 4π. If the direction is not specified, the direction of maximum radiation intensity is implied. The directivity of a nonisotropic source is equal to the ratio of its radiation intensity in a given direction over that of an isotropic source. We can express this relation by the following equation as

$$D = \frac{U}{U_0} = \frac{4\pi U}{P_{rad}} \tag{1.4}$$

If the direction is not specified, it implies the direction of maximum radiation intensity (maximum directivity) expressed as

$$D_{\max} = D_0 = \frac{U_{\max}}{U_0} = \frac{4\pi U_{\max}}{P_{rad}} \tag{1.5}$$

where D is the directivity (dimensionless), D_0 is the maximum directivity (dimensionless), U is radiation intensity (W/unit solid angle), U_{max} is the maximum radiation intensity (W/unit solid angle), U_0 is the radiation intensity of isotropic source (W/unit solid angle), P_{rad} is the total radiated power (W). It is quite clear from the above equations, that for an isotropic source, the directivity is unity since U, Umax, and U_0 are equal to each other.

Absolute gain of an antenna (in a given direction) is defined as the ratio of the intensity, in a given direction, to the radiation intensity that would be obtained if the power accepted by the antenna were radiated isotropically. The radiation intensity corresponding to the isotropically radiated power is equal to the power accepted (input) by the antenna divided by 4π. This can be expressed by the following equation

$$Gain = 4\pi \frac{U(\theta, \phi)}{P_{in}} \tag{1.6}$$

where $U(\theta, \phi)$ is the radiation intensity, P_{in} is the total input (accepted) power. In most cases we deal with relative gain, which is defined as the ratio of the power gain in a given direction to the power gain of a isotropic antenna in its referenced direction. The power input must be the same for both the

antennas. The reference antenna is usually a dipole, horn, or any other antenna whose gain can be calculated or it is known. In most cases, however, the reference antenna is a lossless isotropic source. When the direction is not mentioned, the power gain is usually taken in the direction of maximum radiation.

1.7.3 Radiation efficiency

The antenna radiation efficiency or the conduction-dielectric efficiency e_{cd} is defined as the ratio of the power delivered to the radiation resistance R_r to the power delivered to R_r and R_L. Thus the radiation efficiency can be written as

$$e_{cd} = [\frac{R_r}{R_r + R_L}] \tag{1.7}$$

The antenna radiation efficiency is a dimensionless quantity. The maximum gain G_0 is related to directivity D_0 by

$$G_0 = e_{cd} D_0 \tag{1.8}$$

1.7.4 Radiation pattern

The antenna radiation pattern is defined as a mathematical representation or graphical representation of the radiation properties of the antenna as a function of space coordinates. In most cases, it is determined in the far-field region and is represented as a function of the directional coordinates. Radiation properties include power flux density, radiation intensity, field strength, directivity, phase or polarization. Usually, the pattern describes the normalized field (power) values with respect to the maximum values. The radiation property of most concern is the two- or three-dimensional spatial distribution of radiated energy as a function of the observer's position along a path or surface of constant radius. A trace of the received power at a constant radius is called the power pattern. A graph of the spatial variation of the electric (or magnetic) field along a constant radius is called an amplitude field pattern. In practice, the three-dimensional pattern is sometimes required and can be constructed in a series of two-dimensional patterns. However, for most practical applications, a few plots of the pattern as a function of θ for some particular values of ϕ, plus a few plots as a function of ϕ for some particular values of θ will provide most of the useful information needed, where θ and ϕ represent the two axes in a spherical coordinate system. The three common radiation patterns of

great importance are as follows:

- An isotropic radiator is defined as a hypothetical lossless antenna having equal radiation in all directions. It is only an ideal case and cannot be physically realizable, but it is often taken as a reference for expressing the directive properties of actual antennas.
- A directional antenna is the antenna having the property of radiating or receiving electromagnetic waves more effectively in some directions than in others. This term is usually applicable to an antenna whose maximum directivity is significantly greater than that of a half-wave dipole.
- An omnidirectional antenna is the one having an essentially nondirectional pattern in a given plane and a directional pattern in any orthogonal plane. So omnidirectional radiation pattern can be considered as a special case of directional radiation pattern.

1.8 Hertzian dipole

An infinitesimally small current element is called a Hertzian dipole. The Hertzian dipole is a dipole of length dl which is much smaller than the wavelength λ of the excited wave, i.e. dl $<<\lambda$(dl $< (\lambda/50)$). Apart from this, it is very thin and its radius "a" is also much smaller than the wavelength λ. Electrical size of an antenna is the physical dimension of the antenna defined relative to wavelength. Electrically small antennas are small relative to wavelength whereas electrically large antennas are large relative to wavelength. Hertz dipole is not of much practical use but it is the basic building block of any kind of antennas.

In the far field region where $kr \gg 1$, the E- and H-field can be expressed as[89]

$$\begin{aligned} E_\theta &\approx j\eta \frac{kI_0 dl \sin\theta}{4\pi r} e^{-jkr} \\ E_r &\approx E_\phi = H_r = H_\theta = 0 \\ H_\phi &\approx j \frac{kI_0 dl \sin\theta}{4\pi r} e^{-jkr} \end{aligned} \tag{1.9}$$

The wave impedance Z_w is defined as the ratio of E_θ and H_ϕ and expressed as

$$Z_w = \frac{E_\theta}{H_\phi} \approx \eta \tag{1.10}$$

where Z_w is the wave impedance, k is wave number and η is the intrinsic impedance of the medium ($377 \approx 120\pi$ Ohms for free space).

The E-and H- field components are orthogonal to each other in the far field region, transverse to the radial direction of propagation and vary with the inversely proportional to r and r variations are separable from θ and ϕ.

1.8.1 Radiation resistance

The real part of the input impedance is denoted as the radiation resistance for a lossless antenna. Performing the integration of the Poynting vector over a closed surface, the total radiated power P_{rad} by the source can be found out. The radiation resistance can be evaluated from the real part of P_{rad} which is given below

$$P_{rad} = \frac{1}{2}\mathrm{Re}\int (\overrightarrow{E} \times \overrightarrow{H}*)ds = \eta(\frac{\pi}{3})|\frac{I_0 dl}{\lambda}|^2 = \frac{1}{2}|I_0|^2 R_r \tag{1.11}$$

$$R_r = \eta(\frac{2\pi}{3})|\frac{dl}{\lambda}|^2 = 80\pi^2|\frac{dl}{\lambda}|^2 \tag{1.12}$$

Hence from the above relationship it is quite clear that R_r is dependent on dl and the wavelength λ.

1.8.2 Directivity

The power radiated by a Hertzian dipole is directional in nature. The average power density W_{av} of the source can be evaluated as

$$W_{av} = \frac{1}{2}\mathrm{Re}[\overrightarrow{E} \times \overrightarrow{H}*] = \frac{1}{2}|E_\theta|^2\overrightarrow{r} = \frac{\eta}{2}|\frac{kI_0 dl}{4\pi}|^2\frac{\sin^2\theta}{r^2}\overrightarrow{r} \tag{1.13}$$

The radiation intensity U which is associated with the average power density W_{av} is given by

$$U = r^2 W_{av} = \frac{\eta}{2}|\frac{kI_0 dl}{4\pi}|^2\sin^2\theta = \frac{r^2}{2\eta}|E_\theta(r,\theta,\phi)|^2 \tag{1.14}$$

The maximum value of U occurs at $\theta = \pi\ /2$ and is equals to

$$U_{\max} = \frac{\eta}{2}|\frac{kI_0 dl}{4\pi}|^2 \tag{1.15}$$

Hence the directivity of the Hertzian dipole is reduced to

$$D_0 = \frac{4\pi U_{\max}}{P_{rad}} = 1.5 \tag{1.16}$$

1.9 Monopole antenna

Monopole antenna in its simplest form can be considered as the antenna erected orthogonally above an infinite ground plane as shown in Fig. 1.1(a) whose length is one half the length of the corresponding double length center-fed dipole antenna shown in Fig. 1.1(b).

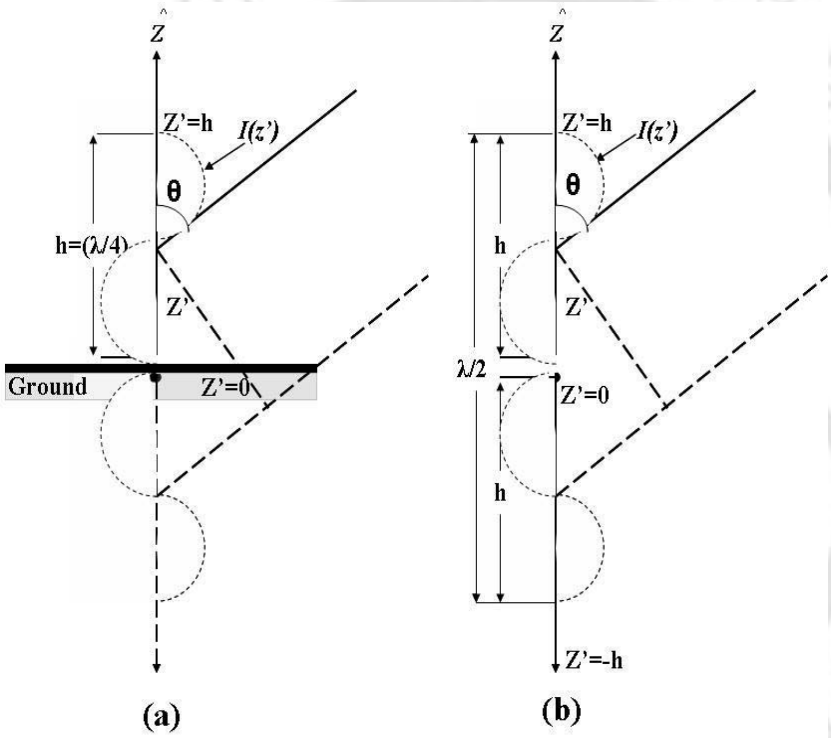

Figure 1.1: **(a)** A vertical monopole antenna above ground and **(b)** the corresponding center-fed dipole. Shown also are the current variations $I(z')$ over the lengths of both the monopole and the corresponding dipole.

The vertical monopole antenna of height h forms a standing wave pattern for the current distribution when $I(z')$ is fed at the center of the monopole antenna can be expressed as

$$I(z') = \frac{I(0)}{\sin(kh)} \sin k(h - z') \tag{1.17}$$

where $I(0)$ is the current at the center of the monopole antenna i.e. at z=0 and the range for z' is $0 \leq z' \leq h$. The creation of the standing wave pattern in the monopole antenna is due to the image of the monopole created by the ground plane having a current distribution identical to the lower arm of the dipole antenna. So the monopole antenna looks as a dipole antenna fed at the center position for

Table 1.2: Relationship between Monopole and Dipole Antenna

	Monopole Above Ground of Length=h	**Corresponding Dipole of Twice Length L=2h**
Radiation Pattern	Same as that for the dipole but only for angle $0 \leq \theta \leq 60^0$	
Feed-point resistance R_a	$R_{a(Monopole)}$=0.5 $R_{a(Dipole)}(2h)$	$R_{a(Dipole)}$: function of length L=2h (Fig. 1.1)
Feed-point reactance X_a	$X_{a(Monopole)}$=0.5 $X_{a(Dipole)}(2h)$	$X_{a(Dipole)}$: function of length L=2h (Fig. 1.1)
Directivity D_a	$D_{a(Monopole)}$=0.5×2$D_{a(Dipole)}(2h)$	$D_{a(Dipole)}$: function of length L=2h

the upper half of the space. The fields generated by the monopole antenna can not penetrate the high conductivity ground plane. So all the radiations from the monopole antenna are confined to the upper half space creating the power density for any angle θ is two times higher than the power density of the dipole antenna radiating same amount of power. Hence the directivity and gain of the monopole antenna are twice that of the double length dipole antenna. Table 1.2 listed the relationship of a monopole antenna of length h above the ground and a corresponding dipole antenna of length L=2h.

For the monopole antenna, the feed-point reactance X_a depends on the conductor radius a, where the feed-point resistance Ra is relatively independent of the conductor radius a for the thin antennas ($a \quad \lambda \leq 1$) [33].

1.10 Methodology to achieve wide operation bandwidth

The most important parameter of any broadband antenna is operating bandwidth. For different types of antennas, various methods have been adopted for enhancement of the bandwidth of antenna.

1.10.1 Resonant antennas

Straight wire dipole, quarter wave monopole and microstrip antennas are the resonant antennas and operate at a single resonance mode at a time. The operating bandwidth is dependent on the antenna quality factor Q and radiation efficiency e_{cd}.

1.10.2 Quality factor and bandwidth

The quality factor Q of an antenna is the measure of loss in the resonant circuit as antenna is a resonating device and it is defined as the $2\pi f$ times the average energy stored to the Ohmic energy

loss per second. The quality factor can be calculated through the equivalent circuit of an antenna shown in the Fig. 1.2.

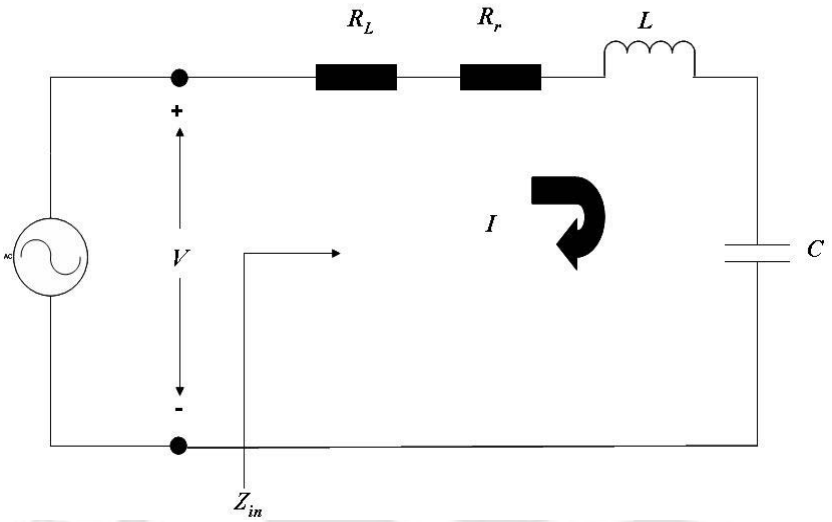

Figure 1.2: Equivalent circuit of antenna.

At resonant frequency f_0 $(2\pi f_0 = 1/\sqrt{LC})$

$$Q = 2\pi f_0 \frac{\frac{1}{4}|I|^2 L + \frac{1}{4}|I|^2 \frac{1}{(2\pi f_0)^2 C}}{\frac{1}{2}|I|^2 (R_r + R_L)} = \frac{2\pi f_0 L}{R_r + R_L} = \frac{1}{2\pi f_0 (R_r + R_L) C} = \frac{1}{2\pi f_0 R_r C} \cdot \frac{R_r}{R_r + R_L} = Q_{lossless} . e_{cd} \tag{1.18}$$

where $Q_{lossless}$ is the quality factor when the antenna is assumed to be lossless, i.e. R_L=0; e_{cd} is the antenna radiation efficiency. Equation 1.18 symbolizes the direct proportionality of the quality factor Q to the antenna radiation efficiency e_{cd}.

The FBW can be expressed as

$$FBW = 2\frac{\Delta f_H}{f_0} = \frac{1}{Q} \tag{1.19}$$

where FBW is the fractional bandwidth of the antenna which varies inversely with the quality factor Q.

1.11 Fundamental limitations for electrically small antennas

First, L. J Chu in his landmark work in 1948 [34], investigated the fundamental limitations for electrically small antennas. Subsequently in the year 1960, R. F. Harrington [35] also independently

postulated the fundamental limitations for electrically small antennas, so together they are called Chu-Harrington criterion for electrically small antennas. In 1964, R. E. Collin and S. Rothschild evaluated the quality factor of the antenna [36] by subtracting the energy density associated with the power flow from the total energy density. In 1975, Harord. A. Wheeler provided the definition of electrical small antenna [37]. In his paper, he described an electrically small antenna is one whose size is a small fraction of wavelength. In 1981, R.C. Hansen in his paper [38] postulated four fundamental limitations in antennas in areas of (a) electrically small antennas, (b) super-directive antennas, (c) super-resolution antennas and (d) high-gain antennas. Electrically small antennas are analyzed with the help of spherical mode theory having the antenna placed and enclosed in a virtual sphere, the quality factor of electrically small antennas were derived and found that the Q varies inversely as the cube of radius of sphere in radian wavelength. In the year 1996, James. S. McLean [39] reexamined thoroughly the fundamental limits on the radiation Q of electrically small antennas and found that Chu-Harrington's criterion the electrical small antennas are accurate. After this, many researches tried to provide more accurate and modified expression for Q [40-43], but the expression of Q for the electrically small antennas provided by the Chu and Harrington still holds good for the electrically small antennas.

The definition of electrically small antennas reveals that the electrically small antenna is the one who's largest dimension $2r$ satisfies $kr < 1$, where k is the wave number and equal to $2\pi/\lambda$. This derivation for the limits on the electrically small antennas is evaluated by assuming that the whole of the antenna structure (with largest linear dimension of $2r$) and feeding structure and oscillator are all enclosed within a virtual sphere of radius r [89] as shown in Fig. 1.3.

When $kr < 1$, the quality factor Q of a small antenna can be expressed as

$$Q = \frac{1 + 2(kr)^2}{(kr)^3[1 + (kr)^2]}.e_{cd} \tag{1.20}$$

The variation of Q with kr for different antenna radiation efficiencies are plotted in Fig. 1.4.

Fig. 1.4 and equation 1.20 depict the relationship between the quality factor Q and the antenna size as well as the radiation efficiency. From Fig. 1.4, it is quite clear that the size of the antenna drops considerably as the Q rises rapidly, which relates the lowest available Q to the largest dimension of the electrically small antennas. Since the FBW of any antenna is inversely proportional to Q, although the increase of Q reduces the size if the antenna but the bandwidth of the antenna becomes narrower.

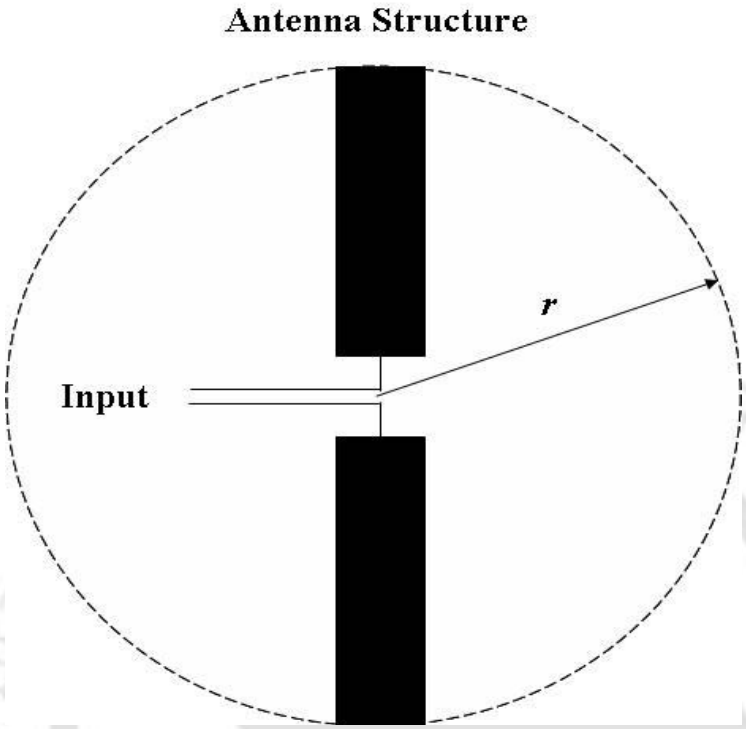

Figure 1.3: Antenna within a sphere of radius r.

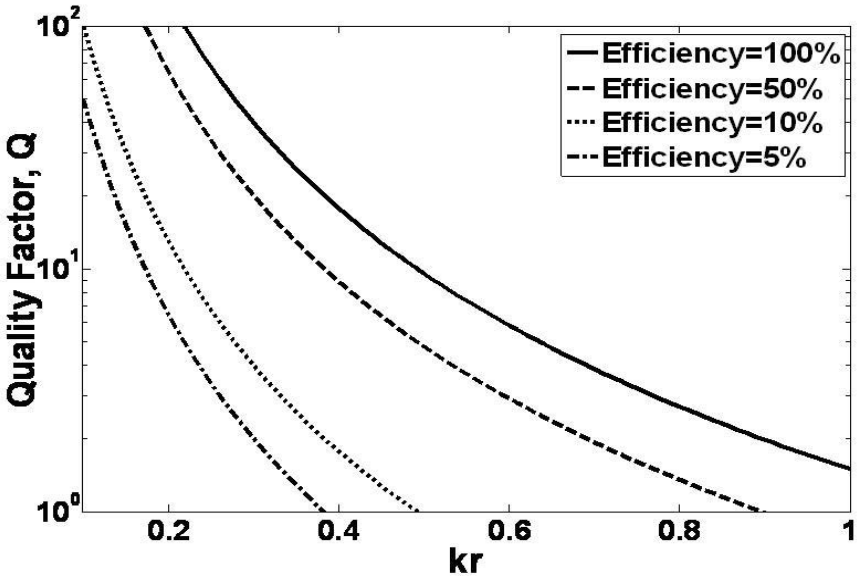

Figure 1.4: Variation of antenna quality factor Q with kr.

So the antenna size, quality factor, bandwidth and radiation efficiency are closely interrelated and there is absolutely no freedom to independently optimize each one. Hence there exists always a trade off between them to obtain an optimal antenna performance.

1.12 Evolution of planar monopole antenna

Antenna design in modern wireless communication system is placing great demands in many aspects. Modern communication system in this era functions simultaneously in two or three frequency bands [53]. Hence appropriate multi-band antennas should be designed to meet the modern era communication requirements. These include cellular system, wireless LAN, satellite navigation system and combination of these systems.

One of the most widely employed antennas for application in wireless communication system is monopole antenna. The most prominent and first member of this family is the quarter-wave monopole antenna above a perfectly conducting ground plane. The impedance bandwidth attainable for the monopole antenna with quarter-wavelength length is dependent on the radius of the cylindrical radiating element and the bandwidth increases with the increase of the radius of the cylindrical radiating element. The fractional bandwidth (FBW) (10dB reflection coefficient) in the frequency range of 1-6 GHz for the length to radius factor of 20 and 100 is approximately 25% and 16% [44]. To enhance the impedance bandwidth of the monopole antenna with less cost and simplest methodology is to replace the cylindrical radiating element with a planar radiating element, which results in a planar monopole antenna. Mainke and Gundlach in the text book written by them in German in 1968 explained that the planar monopole antenna is a special case of cylindrical and conical monopoles. In the year 1976, Dubost and Zisler [45] described in more detail regarding the planar monopole antennas. N. P Agrawall and G. Kumar in the year 1998, studied extensively on the broadband planar monopole antenna and published a revolutionary research paper [46], which completely opens up the new research area on the planar monopole antenna. In their landmark paper in 1998, they proposed a mathematical expression for accurately determining the frequency corresponding to the lower edge of the impedance BW for the planar monopole antennas, especially circular and elliptical disc monopole.

The planar monopole is situated at a distance of h above the ground plane [47]. The replacement of planar radiating element of different shapes in place of the cylindrical wire element increases the radiating surface area of the monopoles, imparts huge effect on the bandwidth of the monopole antenna. As a result, the bandwidth of the planar monopole antenna increases considerably. Different size and shape of the planar radiating element such as circular, elliptical, square, rectangular, triangular, pentagonal and hexagonal have been analyzed and have seen that the planar monopole antennas with the above radiating elements provide broad bandwidth. Among all the planar radiating elements of

different shapes, the circular monopoles [48, 49] and the elliptical monopoles [46] fed along the semi major axis provide maximum bandwidth. Planar monopoles provide extreme wide bandwidth with appropriate radiation pattern after proper optimization in the shape and size of the radiating element. Planar monopole antennas exhibit maximum flexibility in reconfigurable radio system [44] by radiating over radio terminal's entire frequency range. Planar monopole antennas can be designed to cover the frequency range from GSM900, through GSM1800/PCS1900, IMT-2000, the 2.45 GHz and 5.8 GHz ISM band and also including UWB (3.1 GHz to 10.6 GHz).

In other way, the evolution of broadband planar monopole antennas can also be explained by realizing that the broadband planar monopole antennas are a special case of microstrip antenna (MSA) or modified MSA. The usual configuration of MSA is incapable of producing multi octave bandwidth because the MSA is a purely mono resonance structure when operated at its dominant mode. The bandwidth of the MSA can be enhanced by either increasing the height of the substrate or decreasing the value of the dielectric constant of the substrate. If the MSA with the rectangular patch is fed by a co-axial feed with air as the substrate and a perpendicular ground plane, it results the effective dielectric constant of the substrate as one and the considerable increase of the height h. Both these factors will yield large BW.

1.12.1 Theoretical explanation on planar monopole antenna

With thick substrate and low dielectric constant for MSA, the bandwidth enhancement of around 5% to 15% is obtained. The efficiency of the MSA degrades considerably when the thickness of the substrate is increased to a very high value and apart from this the level of cross polarization is increased substantially. The probe height is also increased with the increase of the substrate thickness. The probe inductance increases with the increase of the probe length as a result the input impedance become too inductive to achieve proper impedance matching. This configuration is shown in Fig. 1.5(a). The length of the probe as the large probe inductance can be reduced considerably when the patch is fed through the periphery of the MSA with the shorter probe length of length p as shown in Fig. 1.5(b). Additional ground plane is necessary when the patch is fed along the periphery. If the height h were very large, the bottom ground plane would have negligible effect and hence can be removed. This arrangement of the broadband MSA is similar to that of the monopole as shown in the Fig. 1.5(c) [46, 48-50]. Very large impedance bandwidth can be achievable by the planar disc monopoles which can be explained in the following two ways.

- The area of the radiating element of planar monopole antennas can be equated to the equivalent cylindrical monopole antenna with large effective diameter. A monopole antenna in general consists of a thin vertical radiating element over a ground plane whose bandwidth is improved with the increase in its diameter [51].

- The planar monopole antennas can be considered as the MSA with very thick air substrate hence have the high impedance bandwidth. For the radiating elements of various shapes and sizes, the higher bandwidth is a result of suitable overlap of various higher order modes and these modes generally undergo smaller impedance variation. The shape and size of the planar radiating elements can be thoroughly optimized to bring all the activated modes within VSWR=2 circle in the Smith chart, resulting to a very high impedance bandwidth. In this way, the bandwidth of the planar monopole antennas is enhanced considerably.

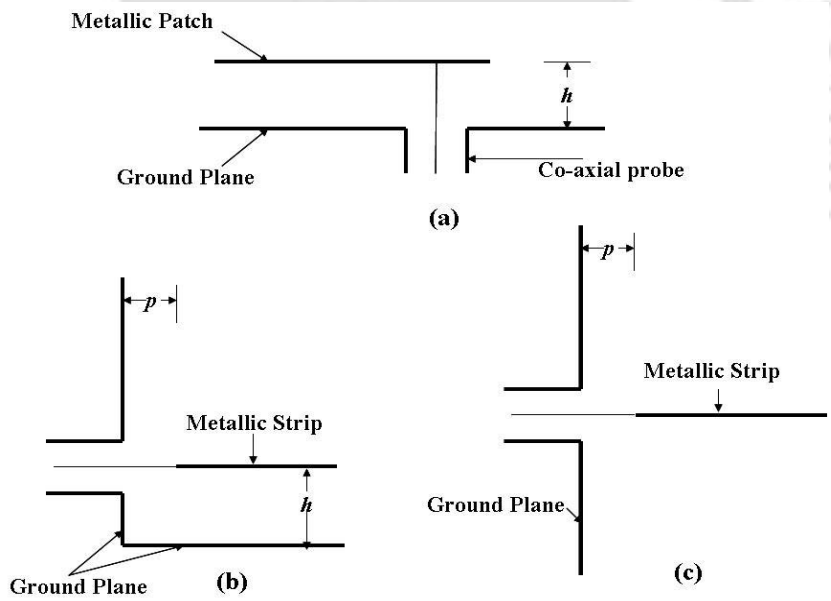

Figure 1.5: **(a)** MSA suspended in air. **(b)** Modified MSA with side feed and **(c)** Planar monopole antenna.

Hence the planar disc monopole antennas are the special case of MSA with infinite air substrate in which the horizontal ground plane is considered to be located at infinity.

1.12.2 Characteristics of broadband planar monopole antenna

Broadband planar monopole antennas are proven themselves as superior radiators as they provide very wide bandwidth over a huge band of frequencies. Because of the excellent radiating capabilities,

they are finding their place in numerous applications. Some of the characteristics of the planar monopole antennas are listed below

- Planar monopole antennas can attain compact size, acceptable radiation efficiency and linear phase response [52].
- Easy to fabricate and low manufacturing cost.
- Planar monopole antenna posses omni-directional radiation pattern for all operation bands and capable of multi-band operation also [53].
- Stable monopole radiation patterns over an extremely wide frequency range [54].
- Provide maximum flexibility in configurable radios [55].
- Planar monopole antennas can be capable of providing very large impedance bandwidth. For example 80% impedance bandwidths are achieved for planar monopole antennas for various shapes and sizes [50, 56].
- With the implementation of the band-notched characteristics in its wide operation bandwidth, planar monopole antennas can provide the interference immunity and can co-exist with other various other narrow band wireless systems [52].

1.12.3 "Fat" monopole antennas

Fig. 1.6 shows the traditional monopole antenna configuration which consists of a cylindrical wire connected vertically through the feeding line over the ground plane. The cylindrical wire acts as a radiating element. This is the most primitive antenna structure and widely used antenna in wireless communication system because of it's simple structure, low cost and omni-directional radiation pattern.

But at the -10 dB reflection coefficient, the bandwidth of the straight wire monopole antenna is around 10% to 20% depending upon the radius to length ratio of the monopole. But it is seen that the bandwidth increases with the increase of radius to length ratio. This means when the radius to length ratio increase, the surface for the radiation increases as a result various operating mode apart from the fundamental modes are activated. These different modes overlaps suitably and hence provide wide operation bandwidth. This indicates that "fatter" radiating elements will lead to broader

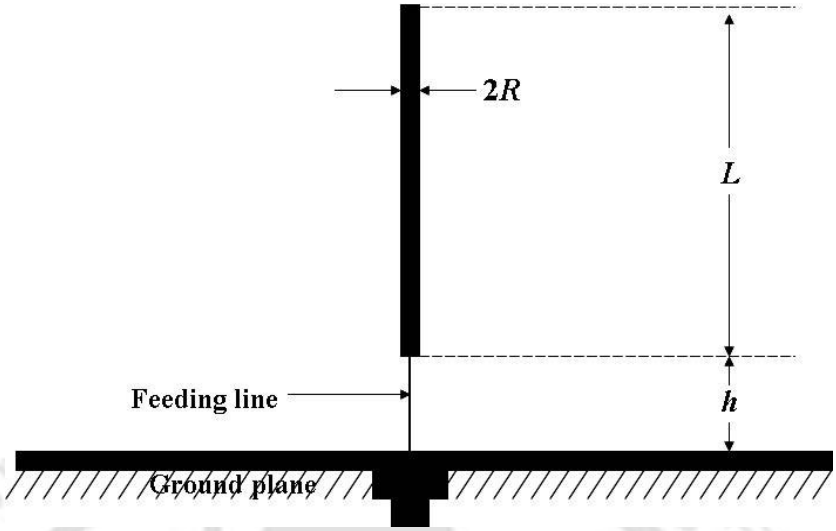

Figure 1.6: Geometry of straight wire monopole antenna.

bandwidth because the current area radiation resistance increases [57]. But when the radius of the radiating element with respect to length of the feed line is too large, the impedance mismatch occurs and bandwidth is degraded.

Hence to achieve the wider bandwidth, the wire element of monopole antenna is replaced with planar radiating elements in terms of thin plates of different sizes and shapes which are obviously much "fatter". These plates take various configurations such as a square [44, 58], circle [46], triangle [59], trapezoid [60], "Bishop Hat" [61] and so on [62, 63] is shown in Fig. 1.7.

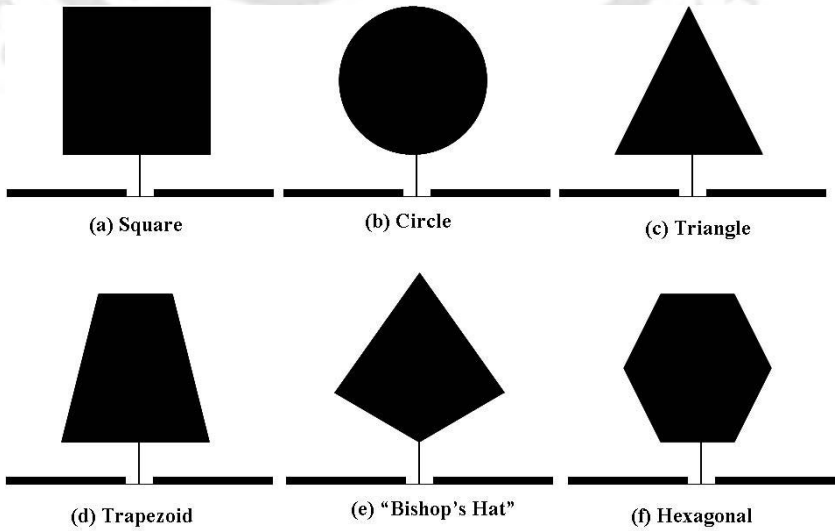

Figure 1.7: Geometry of plate monopole antennas with various configurations.

In the course of time, several novel methods are adopted and proposed to improve the antenna

bandwidth such as using a beveling plate [64, 65], a double feed [66] or an asymmetrical feed arrangement [67], a trident shaped feeding strip [68] and so on. For satisfactory radiation pattern stability, a second orthogonal element is also added in[69, 70].

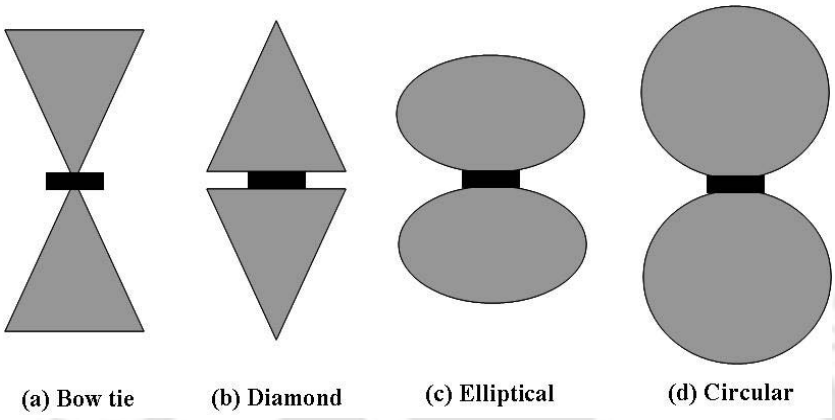

Figure 1.8: UWB dipoles with various configurations.

Monopole antennas are derived from dipole antenna by eliminating one element and driving the remaining element against the ground plane. Hence it is obvious that the "fat" dipoles such as circular disc dipole [71], elliptical disc dipole [72], diamond dipole [73] and bow tie antenna [74] can also exhibit UWB characteristics. These UWB dipoles are shown in Fig. 1.8.

1.13 Printed monopole antenna (PMA)

In case of planar monopole antennas, the radiating structure is planar but the whole of the monopole antenna structure is not planar as the radiating element is situated orthogonally above the ground plane. Hence because of the non-planar structure of whole antenna, these types of antennas though provide high operation bandwidth, they are not suitable for integration with printed circuit boards (PCB) or microwave monolithic integrated circuits (MMIC). This drawback of non planar structure of planar antennas limits its application in modern wireless portable hand-held communication devices.

Hence to derive a planar version of whole of the monopole antenna structure, the feeding structure and the radiating element should be printed on the same side of the substrate material. When the feeding structure and the radiating element are printed on the same side of the substrate then these types of monopole antennas are known as the printed monopole antenna (PMA). According to the structure of feeding elements of the PMA, they can be mainly classified into two categories. One is

microstrip line feeding structure [75-80] and other is coplanar waveguide (CPW) feeding structure [81-86]. Printed monopole antennas have the same features as that of the planar monopole antennas but the structure is different. PMAs are also broadband antennas with moderate gain and omni-directional radiation pattern and can be used for GSM900, GSM1800/PCS1900, IMT-2000, 2.45 GHz, 5.8 GHz ISM band and UWB (3.1 GHz to 10.6 GHz) systems. Because of these advantageous features, printed monopole antennas are highly popular in the wireless communication fraternity [87, 88]. The various geometries of the monopole antennas are shown in the Fig. 1.9.

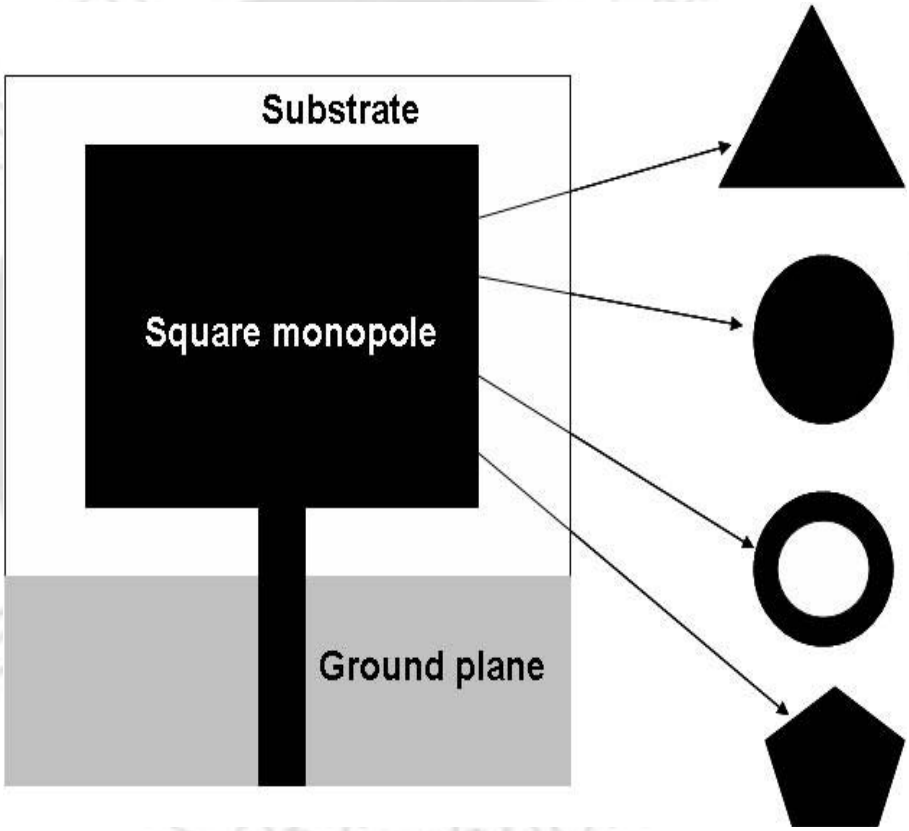

Figure 1.9: Various geometries of printed monopole antennas.

1.13.1 Printed monopole antenna excitation technique

There are many kinds of feeding techniques which are used to feed and excite the printed monopole antennas. They are microstrip line feed and coplanar waveguide feed [90]. In case of microstrip feed line technique, a microstrip feed-line is directly connected to the radiating element. Here, the microstrip line and patch are etched on the same side of the substrate and other side of the substrate, the half etched ground plane is printed below the substrate to provide the proper impedance matching. In

this way, the whole structure is highly planar and can be easily integrable with the RF circuit boards. The other feeding structure is known as the coplanar waveguide (CPW) structure. In this feeding mechanism the ground plane, feeding microstrip transmission line and the radiating element are in the same side of the substrate. The structures of the different feeding technique to the printed antennas are shown in the Fig. 1.10.

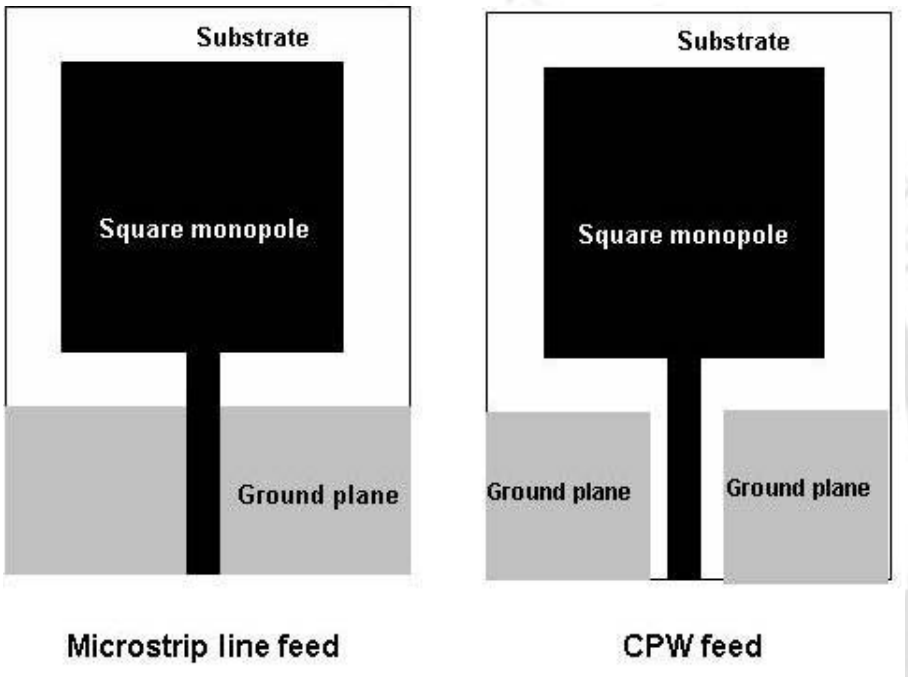

Figure 1.10: Various feeding structures to printed monopole antennas.

1.14 Design aspects of printed monopole antennas

In the present era literature, numerous printed monopole antenna designs are available ranging from ultra wide band monopole antenna, multi-band monopole antenna and single band monopole antenna. The basic structure for the printed monopole antenna is a radiating element which resonates with one-quarter wavelength of the required resonant frequency. The resonating element in the form of metallic conductor which is printed on the substrate. Size is an important and very critical issue for the design of any printed monopole antenna. Many size reduction techniques are available in the literature for the printed monopole antennas such as wrapping, folding and bending [91, 92, 93]. These techniques reduce the size of the printed monopole antennas to a greater extent. Fig. 1.11 shows the design of some of the printed monopole antennas in which the size reduction techniques have been adopted.

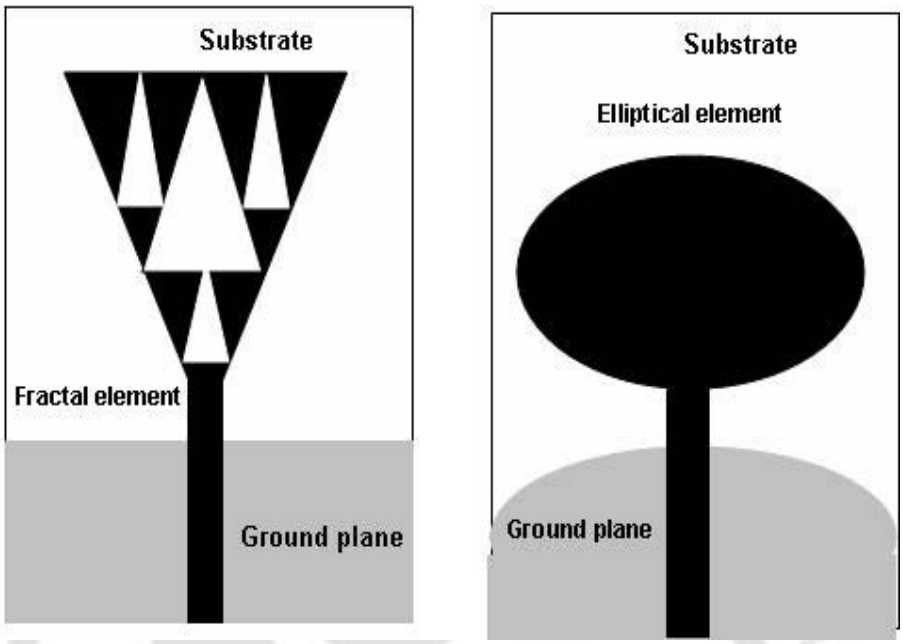

Figure 1.11: Different printed monopole antenna design with size reduction technique.

In many of the multi-band printed monopole antennas, two different current paths are existed which excite two different modes for the operation in the multi-frequency region. This excitation technique involves the loading of a meander line, which generates a resonance at 900 MHz with an inverted-L geometry having resonance occurred at 1.8 GHz [94, 95].

1.15 Motivation

With the widespread development of mobile and wireless communication system, there are huge demands for both data and voice services. Rapid advancement of the modern wireless communication industry enables all the communication systems such as Bluetooth, WLAN, etc to be embedded on one hand held devices. In future, mobile devices will be enabled with all the wireless protocols.

The most important challenge in the antenna design is to accommodate antennas in the small space provided by the mobile devices. In order to solve this challenge, planar multi-band antennas should be designed with compact size. Along with the compact size, the planar multi-band antennas should have consistent radiation pattern and sufficient gain over the wide frequency band.

In low power wireless communication devices, planar multi-band antennas have widespread applications in wireless systems. Multi-band antennas with directional and omni-directional radiation pattern play a vital role in modern wireless communication system. There are many narrow band

wireless applications such as WLAN, WiMAX, RFID, etc. Hence, for narrowband applications in multiple frequencies, excellent choice is the multi-band antennas.

PMA with microstrip feeding structure are also an important class of broadband antennas. Because of the stripped ground plane on the back side of the substrate, these classes of antennas provide large bandwidth. In the literatures till now, the dual-band operation of the PMAs are achieved by creating two independent resonant paths from the main radiating element. But not much research has been carried out so far for the dual-band characteristics of PMAs by erecting strips of different shapes from the ground plane. Dual band operation is achievable for these classes of antennas by creation of two independent resonating paths in the form of protruding stub in the ground plane and also through the radiating element printed on the substrate fed with microstrip feed-line. The major challenge in designing these antennas is the tuning of the protruding stub in the ground plane with the radiating element on the substrate to provide dual-band operation for RFID, WLAN, etc. These antennas are light weight, low profile, less fragile and easily integrable in the hand held devices.

UWB antennas are wideband antennas (3.1-10.6 GHz) widely used for application in modern wireless hand held devices. Miniaturization is a major challenge for design of the UWB antennas. Apart from compact size, consistent omni directional radiation pattern, appropriate flat gain characteristics and suitable time domain response are needed for designing proper UWB antenna. In the UWB band range of 3.1-10.6 GHz, many narrowband wireless system co-exist such as WiMAX (3.3-3.6 GHz) and WLAN (5-6 GHz), which interferes with the UWB operation. Hence, these narrow band wireless systems should be notched up for the uninterrupted operation of UWB. So, different resonant structures at the center notch frequencies are embedded for creating notches to mitigate the potential interference with the narrowband system. This put a great challenge for the UWB notch antenna design as the resonant structures should notch out the exact interference band and should not affect the necessary usable UWB band.

Hence, finally, because of these stringent challenges of these various planar printed multi-band and planar UWB notch antennas in terms of design and fabrication, deep motivation is generated to design and fabricate some of the novel, new compact planar multi-band and UWB antennas so that it can be useful in the contemporary modern wireless communication domain.

1.16 Contribution of the thesis

In this thesis, an extensive study on the performance of PMA with multiple bends has been carried out for application in wireless systems such as RFID, WLAN and UWB. It has been concluded that bends in the PMAs are a versatile and effective way of achieving dual-band antenna performance with size miniaturization. In order to achieve dual-band antenna performance L-strip can be introduced in the ground plane of the PMA. Another way of obtaining the dual-band antenna performance is to introduce two resonating paths in the PMA such as PMA with two arms or branches like that of the F-shaped PMA. Bends could also be introduced in the feed region of the PMA to obtain UWB antenna performance. L-strip open circuited stubs connected microstrip feed-line gives rise to band-notch characteristics in the UWB antenna. Some of the contributions of the thesis are:

(i) With the advancement in software defined radio, we may require a single device which can work for any applications. A new F-shaped dual-band PMA for RFID and WLAN application is proposed. The proposed antenna attains 12.5 percent size reduction, 43.16 percent bandwidth improvement and 3.10 percent average gain enhancement as compared to contemporary dual band PMAs [116].

(ii) A rectangular PMA with an inverted L-strip in the ground plane is proposed for dual-band WLAN applications. This novel antenna attains 50.75 percent size reduction, 76.88 percent average bandwidth improvement and 15.17 percent average gain enhancement when compared to contemporary dual-band PMAs [113].

(iii) A compact PMA with an inverted L-shaped radiating element and an inverted L-strip in the ground plane for application in dual-band WLAN systems is proposed. This new antenna achieves 73.33 percent size reduction, 45.71 percent average bandwidth enhancement and 53.6 percent average gain improvement when compared to contemporary dual-band PMAs [121].

(iv) A novel compact double-bend PMA with an inverted L-strip in the ground plane is proposed for dual-band WLAN applications. This new antenna attains 5.71 percent size reduction, 64.53 percent average bandwidth improvement when compared to contemporary dual-band PMAs [133] but the improvement of gain is not considerable when compared to above PMA.

(v) A new 9-shaped dual-band PMA for RFID and WLAN application is proposed. Size reduction

of 18.57 percent, average bandwidth improvement of 37.08 percent and 16.45 percent average gain enhancement are achieved when compared to antenna [114].

(vi) A simple microstrip fed folded strip monopole antenna (FSMA) with a protruding stub in the ground plane for simultaneous applications in the WLAN and RFID is presented. This new antenna attains 8.25 percent size reduction, 57.95 percent average bandwidth improvement and 16.19 percent average gain enhancement when compared to contemporary dual-band PMAs [141].

(vii) A compact double notch UWB PMA is proposed. Two open circuited stubs at two sides of the microstrip feed line achieves the dual band notch characteristics. This antenna achieves a size reduction of 47.5 percent and gain enhancement of 9 percent when compared with the contemporary double notch UWB PMAs [182].

1.17 Organization of the thesis

The thesis is divided into seven chapters.

Chapter one gives a brief review of the state-of-art of PMAs for dual-band wireless and UWB applications. This also includes the introduction of current trends in the PMA design for wireless application. Apart from this, chapter one covered fundamentals regarding basic antenna theory and primary requirement for the dual-band (WLAN and RFID) and UWB printed antennas for wireless communication.

Chapter two includes the different design of the single bend compact PMAs for dual-band WLAN and RFID applications. It also includes the measured results of the fabricated prototype of the dual-band printed monopole antennas.

Chapter three focuses on the double bend microstrip line fed compact PMA for dual-band WLAN application. The antenna is designed properly, simulated, fabricated and measured.

Chapter four contains the design aspects of triple bend 9-shaped PMA. All the simulated and measured results are included in this chapter.

Chapter five will deal with the quadruple bend PMA with a protruding stub in the ground plane.

Chapter six deals with the design aspects of the double notch UWB PMA to mitigate the potential interference of UWB system with narrow band wireless systems. The double notch UWB PMA is suitably designed, simulated, fabricated and measured. The measured results are in good agreement

with the simulated results. Apart from this, time domain characteristic of the double notch UWB PMA is experimentally evaluated.

Conclusion from thesis research work and scope for future research are discussed in Chapter seven.

2

PMA structures with single bend

Contents

2.1 Introduction 34
2.2 F-shaped PMA 35
2.3 Rectangular PMA with an inverted L-strip in the ground plane 45
2.4 Inverted L-shaped PMA with an inverted L-strip in the ground plane . 58
2.5 Summary 70

2.1 Introduction

The rapid development of modern wireless communication systems has caused wide interests in designing wide-band and multi-band antennas; especially for the wireless communication system and wireless local area network (WLAN). Wireless local area networks (WLAN), as a viable, cost effective and high data connectivity solution, have been getting more and more attention. There are three operation bands in the IEEE 802.11 WLAN standards, 2.4 GHz (2.4-2.484 GHz), 5.2 GHz (5.15-5.35 GHz) and 5.8 GHz (5.725-5.825 GHz). Antenna is a very important device for any wireless communication systems. Printed monopole antennas (PMAs) are good candidates for dual-band applications because they are low profile and low cost, easy to fabricate, low and easy to integrate with microwave and monolithic integrated circuits (MMIC). Also the omni-directional radiation characteristics of monopole antennas make them suitable for indoor applications. In published literature, many configurations of antennas with dual-band operating characteristics have been reported for WLAN applications [96-100], such as G-shaped monopole [96, 97], split-ring monopole [98], E-shaped and meander line monopole [99, 100], and so on. However, among these designs, most of them are either large in size or complex in structure for practical applications. Therefore, it is desirable to design dual-band printed monopole antennas with small size and simple structure for 2.4/5.2/5.8 GHz WLAN applications.

The radio frequency identification (RFID) in recent years has received wide spread attention for application in many services such as tracking objects, identifying objects in the manufacturing and supply chain management systems as well as material flow systems [101]. An RFID system basically comprise of a read/write mechanism and a tag (transponder). In other words, RFID system consists of a data processing system, transponder (tags), antennas and readers [102]. The encoded data is transferred between the tag and read/write device by means of electromagnetic waves at the assigned bands of 125 KHz, 13.56 MHz, 869 MHz, 902-928 MHz, 2.45 GHz and 5.8 GHz [103]. The tag, which holds the antenna and a microchip transmitter, must be low cost, less fragile, low profile and generally of small size for the convenient use in the RFID system. Therefore an efficient antenna with high gain, omnidirectionality, and wide impedance bandwidth but with a planar structure becomes necessary for application in RFID domain. Many antenna design for the RFID application has been reported including coplanar waveguide (CPW) fed folded slot [104], the aperture coupled structures [105], meander line structures [106], etc. Apart from the above RFID antenna designs, several RFID antenna designs are proposed [107-109] in the literature. Compact printed monopole antennas are

indispensable for the application in WLAN and RFID applications. Along with the compact size, the antenna should be low cost, light weight, less fragile, low profile and finally, the fabrication methodology should be simple.

Based on the background of structures of various dual-band antennas for application in WLAN/RFID systems, this chapter describes the three compact dual-band PMAs for application in WLAN/RFID applications. The most common feature related to these three antennas is the structure of antennas which consists of only one bend either in the prime radiating element or in the protruding stub in the ground plane. The first antenna in this chapter consists of an F-shaped radiating element for RFID/WLAN applications. The second antenna consists of a rectangular radiating element and an inverted L-strip in the ground plane. The structure of third antenna consists of an inverted L-shaped radiating element with an inverted L-strip in the ground plane for application in WLAN systems. All the antennas are compact and fed by microstrip transmission line.

2.2 F-shaped PMA

2.2.1 Antenna design

Fig. 2.1 shows the printed F-shaped dual-band monopole antenna for RFID and WLAN applications. The F-shaped radiating element has only one bend in each of the two resonating paths of the proposed antenna. Hence this antenna belongs to the catogory of single bend PMA. The F-shaped monopole antenna is printed on the FR4 substrate of relative permittivity 4.4 and the thickness 1.6 mm. The shape of the antenna element is like an English letter "F" without the conductor backed ground plane. A 50-Ω microstrip line is used for the excitation. The strip width of F-shaped monopole antenna is 3 mm, same as that of the width of the microstrip line. The remaining design dimensions are shown in the Fig. 2.1.

The F-shaped element provides two different resonant paths I and II. The length of the resonant path I is L_1=24.5 mm and the length of the resonant path II is L_2=15.35 mm. The resonant path L_1 is chosen $\sim 0.25\lambda_1$ at the resonant frequency of 2.45 GHz and the resonant path L_2 is chosen $\sim 0.25\lambda_2$ at the resonant frequency of 5.2 GHz. By properly varying the lengths L_1 and L_2, we can fix the antenna resonance at 2.45 GHz and 5.2 GHz respectively. The overall adjustments of the geometrical parameters are done for the improvement of impedance bandwidth in the 2.45 GHz and 5.2 GHz bands.

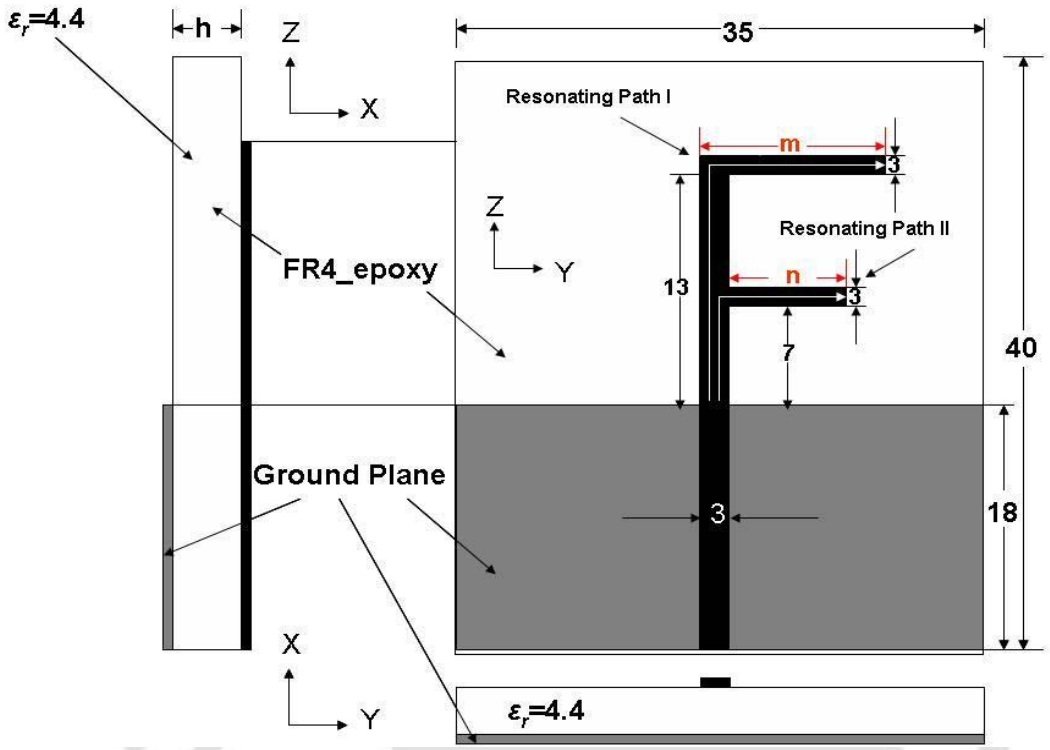

Figure 2.1: Geometry of the proposed antenna with m=10 mm and n=5.35 mm.

2.2.2 Simulated and measured results on reflection coefficient ($|S_{11}|$) and the parametric study of the proposed antenna

Fig. 2.2 shows the simulated reflection coefficient ($|S_{11}|$) graph of the proposed antenna. From the graph it is clear that the proposed antenna resonates at two center resonant frequencies of f_1=2.44 GHz with reflection coefficient value of -12.10 dB and f_2=5.18 GHz with the reflection coefficient value of -26.85 dB. The band at the center frequency of f_1=2.44 GHz extends from 2.11 GHz to 2.77 GHz with the percentage bandwidth of 27.049. Similarly the band at the center frequency of f_2=5.18 GHz stretches from 4.90 GHz to 5.5 GHz with the percentage bandwidth of 11.538. The band at the center frequency of f_1=2.44 GHz can be used for the application of RFID systems and the band at the center frequency of f_2=5.18 GHz can be used in the frequency domain of WLAN systems.

Fig. 2.3 depicts the simulated reflection coefficient ($|S_{11}|$) of the proposed antenna with the different constituent structures. When only resonant path I is present shown in the Fig. 2.7(a), the structure resonates at the center frequency of 2.40 GHz (f_x=2.40 GHz) and another resonance occurs at the center frequency of 6.52 GHz (f_y=6.52 GHz), which is approximately the third harmonic of f_x (f_y ~$3f_x$). When only resonant path II is present shown in the Fig. 2.9(a), the structure resonates

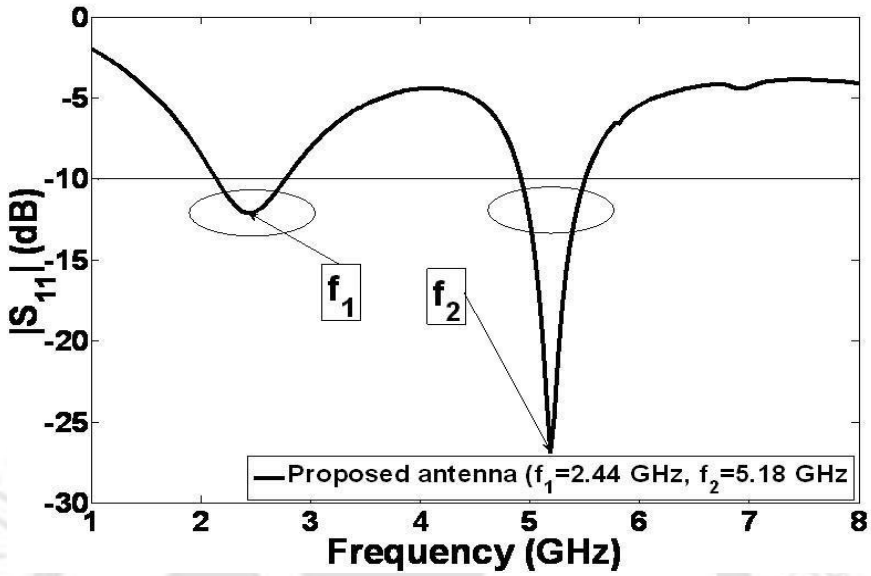

Figure 2.2: Simulated reflection coefficient ($|S_{11}|$) of proposed antenna.

with the center frequency of 3.74 GHz (f_z=3.74 GHz). But when the two resonant paths are present simultaneously, the proposed antenna resonates at two resonant center frequencies such as f_1=2.44 GHz and f_2=5.18 GHz. When the two resonant paths are present together, the resonance at the higher frequency occurs at f_2=5.18 GHz. That means, the resonance at the higher frequency f_2=5.18 GHz is approximately the average of f_y and f_z. The average of f_y and f_z is found out to be 5.13 GHz, which is very close to f_2=5.18 GHz. The first resonant frequency (f_x/f_1) is almost constant at around 2.40/2.44 GHz irrespective of the presence of either resonant path I only or the presence of two resonant paths simultaneously.

Fig 2.4(a) shows the reflection coefficient for successive values of the upper arm length m of the F-shaped radiating element when the other parameter such as n (= 5.35 mm) remain constant. From the graph, one can experience that when m increases from 6 mm to 14 mm, the first resonant frequency (f_1) moves towards left, which means that the first resonance frequency (f_1) decreases with the increase of the length m. On the other hand, the second resonant frequency (f_2) is also decreases with the increase of m, which means that the second resonant frequency (f_2) moves towards left.

Fig 2.4(b) shows the reflection coefficient for successive values of the lower arm length n of the F-shaped radiating element when the other parameter such as m (= 10 mm) remain constant. From the graph, it can be seen that when n increases from 1.35 mm to 9.35 mm, very little shifting of first

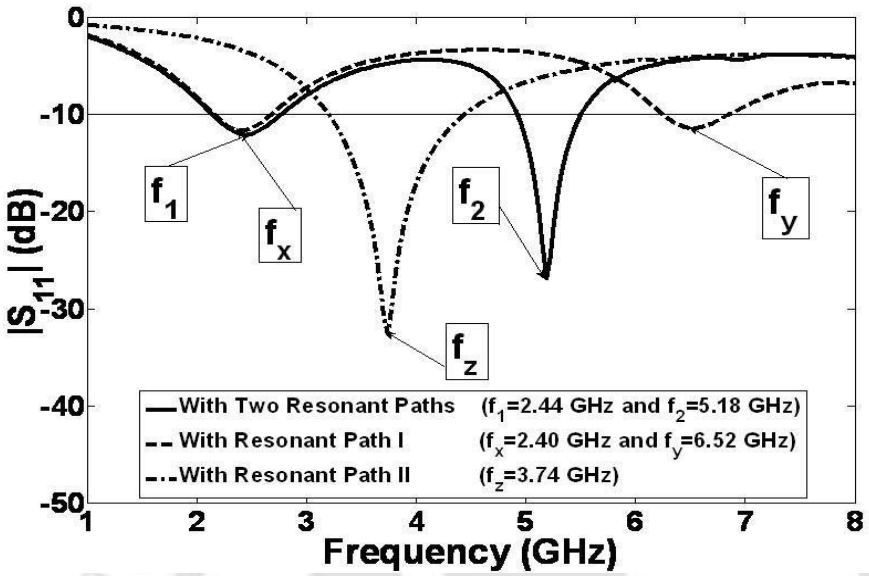

Figure 2.3: Simulated reflection coefficient ($|S_{11}|$) of proposed antenna with different constituent structures.

resonant frequency (f_1) occurs. On the other hand the second resonant frequency (f_2) moves towards left, which means that the second resonant frequency (f_2) decreases with the increase of the length of the lower arm length n of the F-shaped radiating element. The shifting of (f_1) towards left is less rapid as compared to shifting of (f_2) towards left. As n increases, (f_2) deceases rapidly as compared to (f_1). Hence the first resonant frequency (f_1) is almost independent of the variation of n, the length of the lower arm of the F-shaped radiating element.

Fig. 2.5 shows the photograph of the fabricated prototype of the proposed F-shaped monopole antenna for RFID and WLAN applications and Fig. 2.6 depicts the comparison of the simulated and measured reflection coefficients ($|S_{11}|$) of the proposed antenna. The reflection coefficient measurement was done using the Rohde and Schwarz ZVA24 vector network analyzer. With the measurement, the first resonance occurs at 2.44 GHz at the reflection coefficient value of -27.17 dB having the percentage bandwidth of 22.49 percent and the second resonance occurs at 5.25 GHz at the reflection coefficient value of -49.58 dB possessing percentage bandwidth of 6.24 percent.

2.2.3 Effect of single bend on the proposed antenna performance

In the proposed F-shaped PMA, the two 90^0 single bends exist in two different resonating paths. In the planar microwave circuit domain, these 90^0 bends are known as the discontinuity. These discontinuities in the microstrip structures are caused by the sudden change in the geometry of the

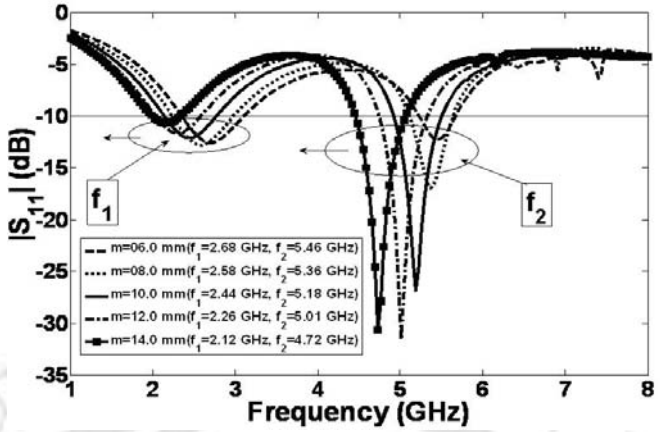

(a)

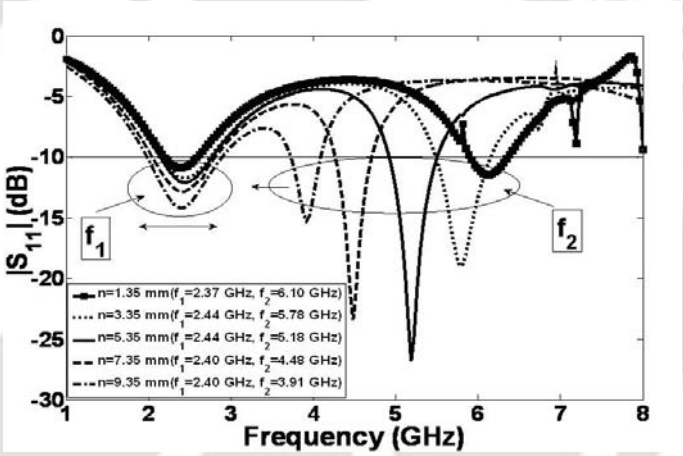

(b)

Figure 2.4: Simulated reflection coefficient ($|S_{11}|$) (dB) graphs, **(a)** m is a variable, n=5.35 mm and **(b)** n is a variable, m=10 mm.

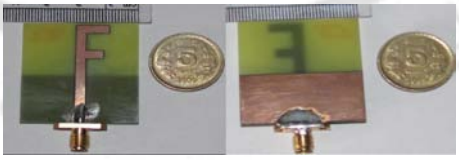

Figure 2.5: Fabricated prototype of the proposed F-shaped monopole antenna.

strip conductor. As a result electric, magnetic and current distributions are modified around the corners of 90^0 bend. In case of PMA, the 90^0 bends in the radiating elements alters the occurring of the resonance frequency. Analysis on the bending in the radiating element of the proposed F-shaped PMA is carried out. First with the resonating path I only in the radiating element, the structure simulated is shown in the Fig. 2.7(a). The resonating path I is meant for providing resonance at 2.45

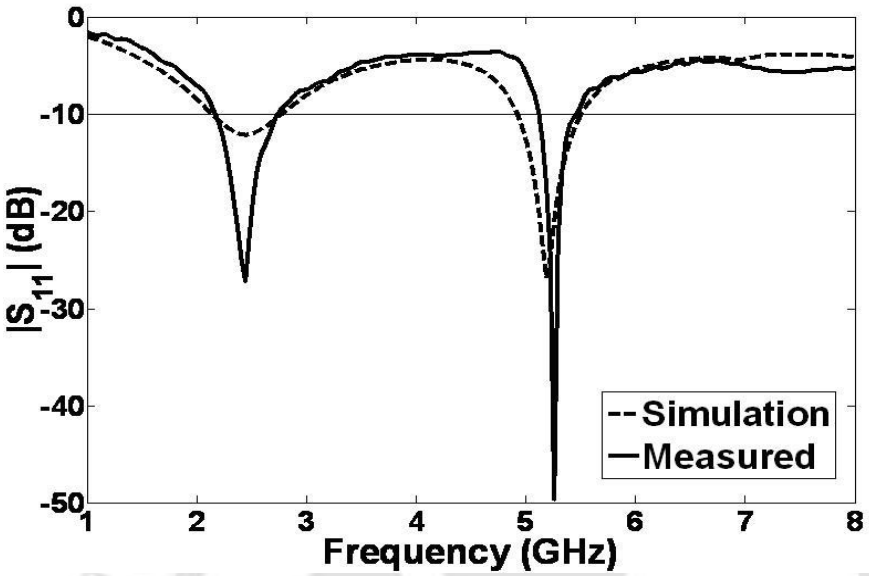

Figure 2.6: Comparison of simulated and measured reflection coefficients ($|S_{11}|$) of the proposed F-shaped monopole antenna for RFID and WLAN applications.

GHz, which is $\sim 0.25\lambda_1$ (L_1=24.5 mm) at 2.45 GHz. The radiating structure provides two resonances at f_x=2.40 GHz and f_y=6.52 GHz. The second resonant frequency f_y is approximately the third harmonic of f_x ($f_y \sim 3f_x$), which is shown in the Fig. 2.8.

Now the 90^0 bend of the first resonant path is unfolded and the radiating element becomes a straight line of same length as the resonating path I or in other words the radiating element becomes linear shown in the Fig. 2.7(b). In this condition, the radiating structure is simulated. After simulation it is found that the radiating structure also provides two resonances at f_{xL}=2.30 GHz and f_{yL}=5.99 GHz, shown in the Fig. 2.8. The second resonant frequency f_{yL} is approximately the third harmonic of f_{xL} ($f_{yL} \sim 3f_{xL}$).

Similarly the bending analysis is performed for the case of resonant path II which is meant for providing resonance at 5.2 GHz, which is $\sim 0.25\lambda_2$ (L_2=15.35 mm) at 5.2 GHz when the resonant path I is absent shown in Fig. 2.9(a). With one single 90^0 bend in the resonating path II, the structure resonated at f_z=3.74 GHz with the reflection coefficient ($|S_{11}|$) value of -32.60 dB.

Now the single 90^0 bend in the resonating path II is unfolded and is made linear (L_2=15.35 mm) which is shown in Fig. 2.9(b) and the structure is simulated. After simulation it is found that the linear resonating structure resonates at f_{zL}=3.56 GHz with the reflection coefficient ($|S_{11}|$) value of -16.32 dB, which is shown in the Fig. 2.10.

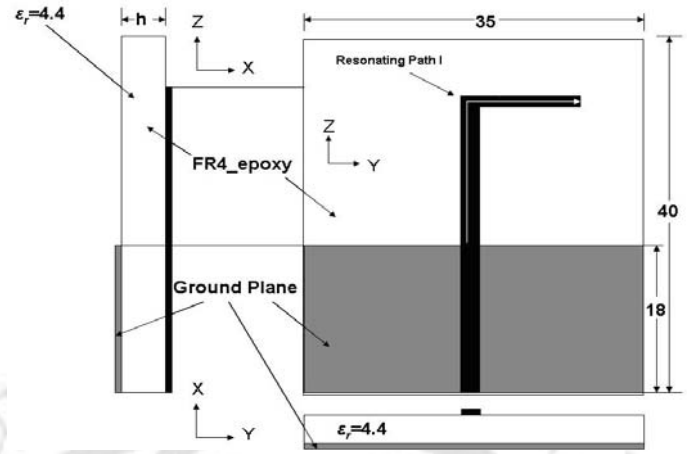

(a)

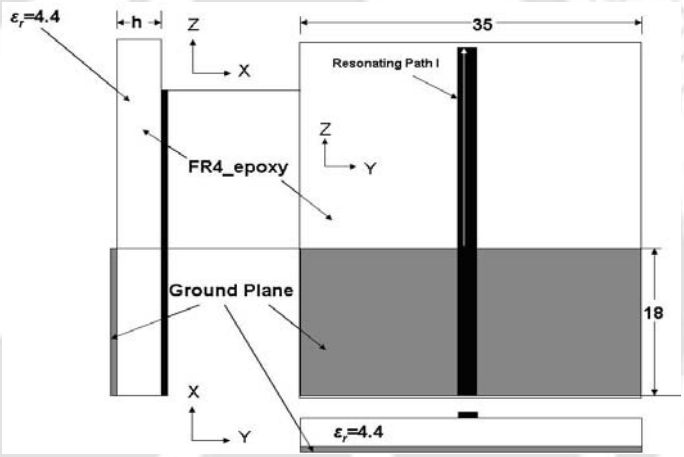

(b)

Figure 2.7: **(a)** Structure of the radiating element with the 90^0 bend resonating path I and **(b)** Structure of the radiating element with the linear resonating path I.

From the analysis, it is found that the 90^0 bending shifts the center of the resonant frequency to a higher frequency when compared with the linear resonating case [110]. But in the higher frequency range, apart from shifting the center of the resonating frequency to a higher value with 90^0 bending as compared to the linear case, the bending also strengthens the resonating characteristic of the radiating structures.

2.2.4 Gain of the proposed antenna

Fig. 2.11 (a) and (b) shows comparison of simulated and measured gain (dBi) vs. frequency of the proposed antenna in 2.11 GHz-2.77 GHz and 4.90 GHz-5.50 GHz band range. The simulated gain at 2.45 GHz is 1.87 dBi and the measured gain at 2.45 GHz is 1.88 dBi. Similarly simulated

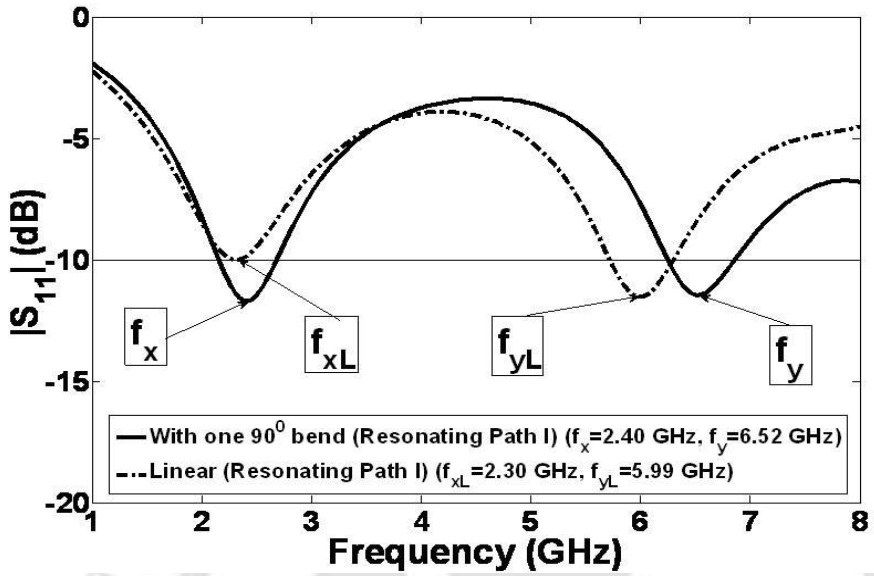

Figure 2.8: Simulated reflection coefficients ($|S_{11}|$) of the resonant path I with one 90^0 bend and without 90^0 bend (linear).

gain at 5.2 GHz is 2.89 dBi and the measured gain at 5.2 GHz is 2.90 dBi. The proposed antenna provides sufficient and appropriate gain required for the operation in the RFID (2.45 GHz) and WLAN (5.15-5.35 GHZ) bands.

2.2.5 Surface current distribution of proposed antenna

At 2.45 GHz, the magnitude of the current density is high in the microstrip fed-line and the ground plane just behind the microstrip feed-line. Apart from this the magnitude of the current density is moderate on the upper arm of the F-shaped radiating element. The direction of current in the microstrip feed-line is upward in direction. In the upper arm of the F-shaped radiating element, the direction of current is retuning in nature and in the lower arm of the F-shaped radiating element is entering in nature. The current in both the arms are unidirectional and continuous in nature and no cancellation of current occurs in any of the radiating element. Because of this the two arms of the F-shaped radiating element resonate in the respective frequency bands for which they are designed. The direction and magnitude of the surface current density are shown in the Fig. 2.12 (a)

At 5.2 GHz, the direction of current density is just opposite to that of at 2.45 GHz. The current in the upper arm of the F-shaped radiating element is entering in nature and current in the lower arm of the F-shaped radiating element is returning in nature. The magnitude of the current density

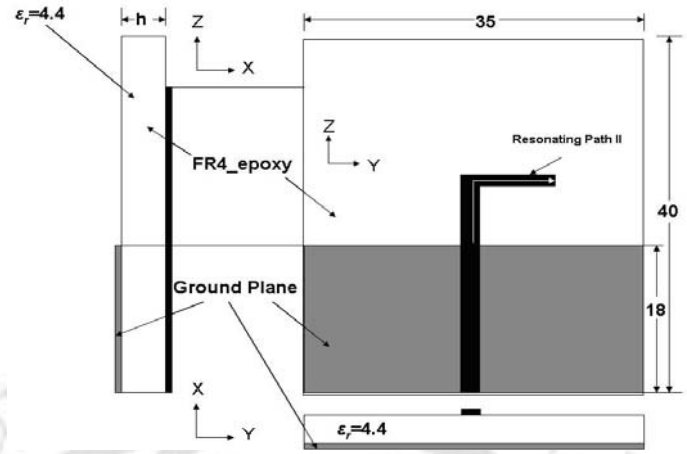

(a)

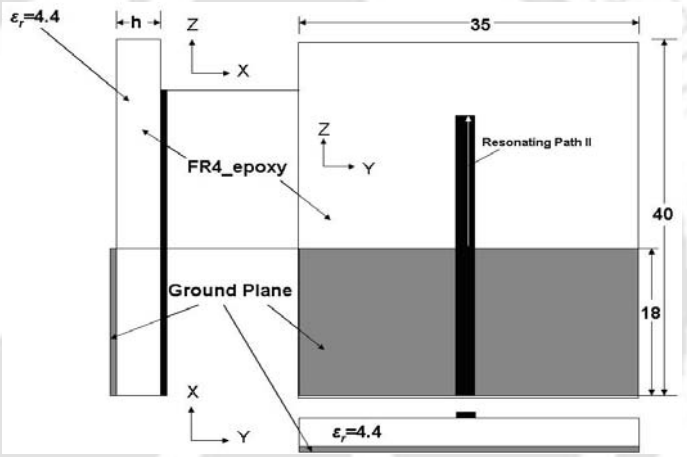

(b)

Figure 2.9: **(a)** Structure of the radiating element with the 90^0 bend resonating path II and **(b)** Structure of the radiating element with the linear resonating path II.

is high on the upper as well as in the lower arm of the F-shaped radiating element. In the edges of the F-shaped radiating element, the current density is also very high. As the current density at the edges of the F-shaped radiating element is very high, effective scattering of the field components happens. As there is more scattering occurs, the effective radiation is also occurs at 5.2 GHz. Hence a proper resonance occurs at 5.2 GHz. At the tip of the upper arm and lower arm of the F-shaped element the current density is low but at the beginning of the radiation paths, the current density is relatively high. That is nearly a quarter wave variations along the resonant path of the monopole which corresponds to the resonant frequency. Hence antenna radiates effectively at 5.2 GHz as well as 2.45 GHz and provides a strong resonance at 5.2 GHz. The direction and magnitude of the surface current density are shown in the Fig. 2.12 (b). The surface current distributions are generated by

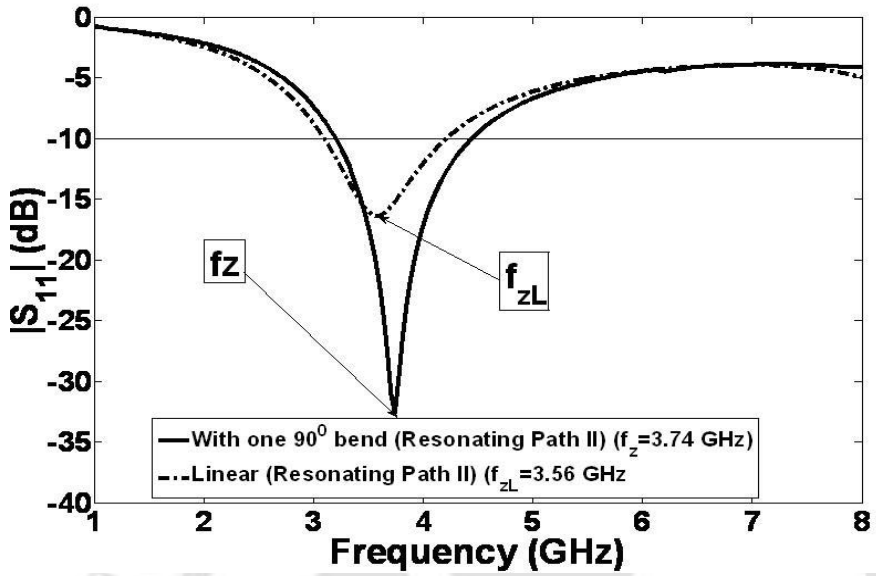

Figure 2.10: Simulated reflection coefficients ($|S_{11}|$) of the resonant path II with one 90^0 bend and without 90^0 bend (linear).

using the electromagnetic simulation software HFSS V.14 [194].

2.2.6 Radiation pattern of the proposed antenna

The measured co- and cross-polarized E-plane (yz-plane) and H-plane (xy-plane) radiation patterns of the F-shaped monopole antenna at 2.45 and 5.2 GHz are shown in the Fig. 2.13 and Fig. 2.14 respectively. It can be observed that E-plane radiation pattern is of the shape "8" in the two frequencies. At 5.2 GHz, the shape of the E-plane radiation pattern is slightly distorted. The H-plane radiation pattern on the other hand is purely omni-directional pattern at the two frequencies i.e. at 2.45 and 5.2 GHz. At 2.45 GHz and 5.2 GHz, the E-plane cross-polar radiation pattern is in between -20 and -30 dB. At 2.45 GHz and 5.2 GHz, the H-plane cross polarization level is also in between -20 and -30 dB approximately. This F-shaped monopole antenna demonstrates a consistent radiation pattern in the desired bands of frequencies. This antenna has good radiation pattern in both E- and H- planes at both the frequencies 2.45 GHz and 5.2 GHz.

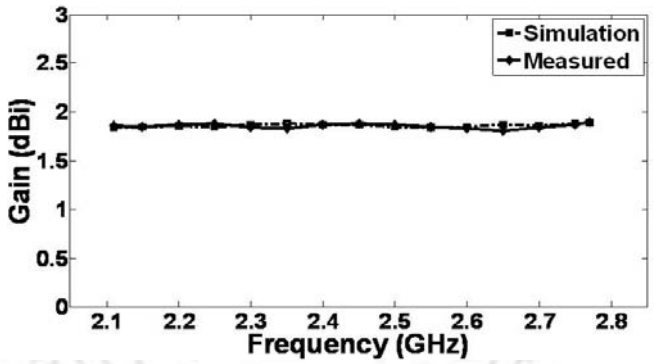

(a)

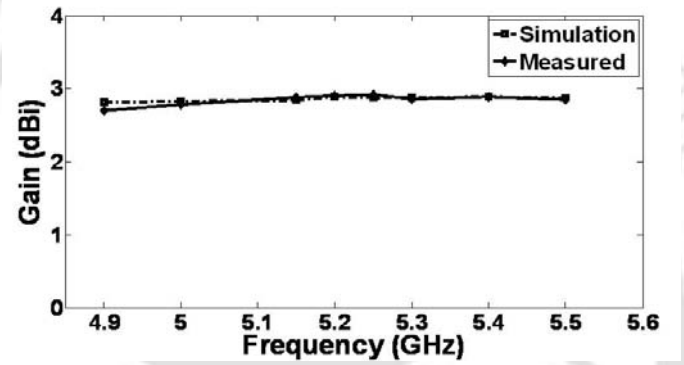

(b)

Figure 2.11: **(a)** Comparison of simulated and measured gain (dBi) vs. frequency of the proposed antenna (2.11 GHz-2.77 GHz) and **(b)** Comparison of simulated and measured gain (dBi) vs. frequency of the proposed antenna (4.90 GHz-5.50 GHz).

2.3 Rectangular PMA with an inverted L-strip in the ground plane

2.3.1 Antenna design

Fig. 2.15 shows the geometry of the proposed antenna. This antenna is fabricated on a FR4 epoxy substrate with dielectric constant of 4.4 and thickness of 1.6 mm. The antenna is fed by a microstrip line of width 3 mm. In the proposed antenna, the rectangular patch printed on the substrate serves as the radiating element. On the ground plane an inverted L-strip is protruded out from the left side of the ground plane. All the design dimensions are shown in Fig. 2.15. The proposed antenna has only one bend in the inverted L-strip protruded from the ground plane. Thats why this antenna belongs to the class of single bend PMA. The first resonance path is the inverted L-strip in the ground plane whose length is $0.212\lambda_1$ at 2.4 GHz and the other higher resonances are combinely produced by rectangular radiating element and inverted L-strip in ground plane.

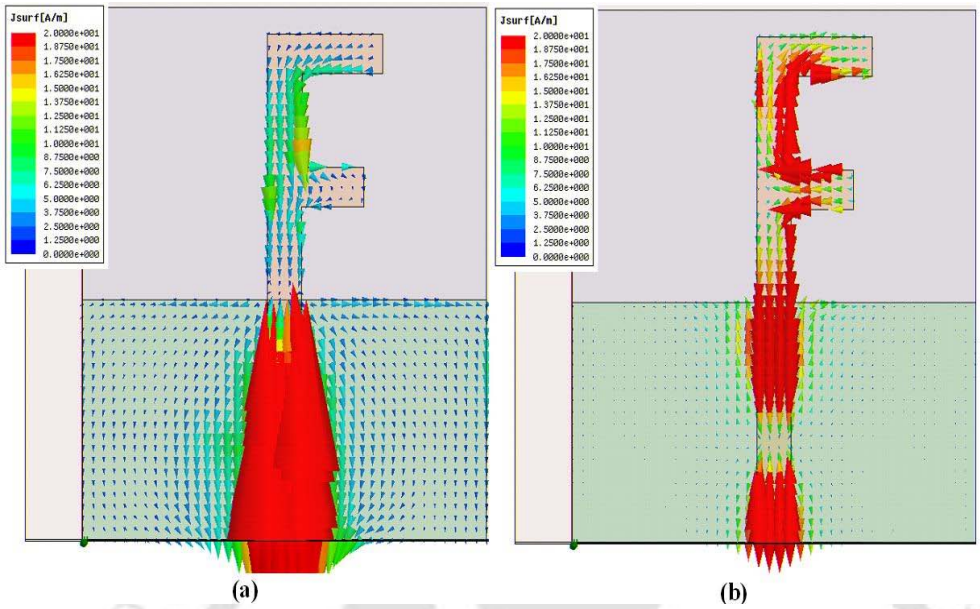

Figure 2.12: Direction and magnitude of the surface current distribution for the F-shaped PMA **(a)** at 2.45 GHz and **(b)** at 5.2 GHz.

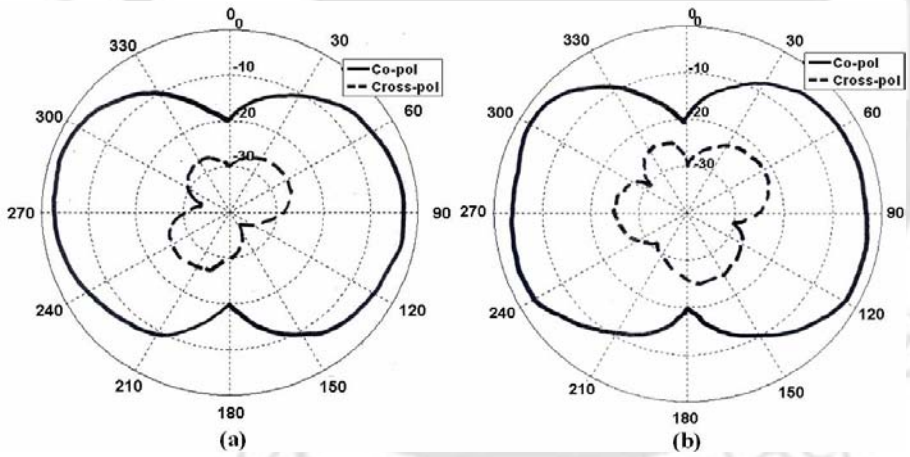

Figure 2.13: Measured E-plane (yz-plane) radiation patterns of the proposed antenna at **(a)** 2.45 GHz and **(b)** 5.2 GHz.

2.3.2 Simulated and measured results on reflection coefficient ($|S_{11}|$) of the the proposed antenna

Fig. 2.16 shows the simulated reflection coefficient ($|S_{11}|$) of the proposed antenna. The first resonance occurs at f_1=2.48 GHz with the reflection coefficient value of -34.71 dB. The band extends from 2.14 GHz to 3.47 GHz. The percentage bandwidth in this band region is 47.71. The WLAN's 2.4-2.484 GHz band is completely immersed in this band of 2.14 GHz to 3.47 GHz. The second band extends from 3.98 GHz to 7.70 GHz with two resonances at f_2=4.54 GHz (reflection coefficient value

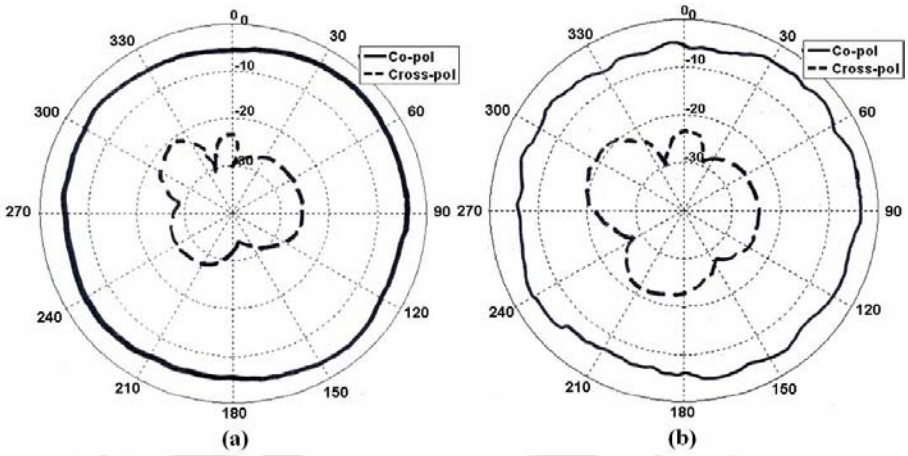

Figure 2.14: Measured H-plane (xy-plane) radiation patterns of the proposed antenna at **(a)** 2.45 GHz and **(b)** 5.2 GHz.

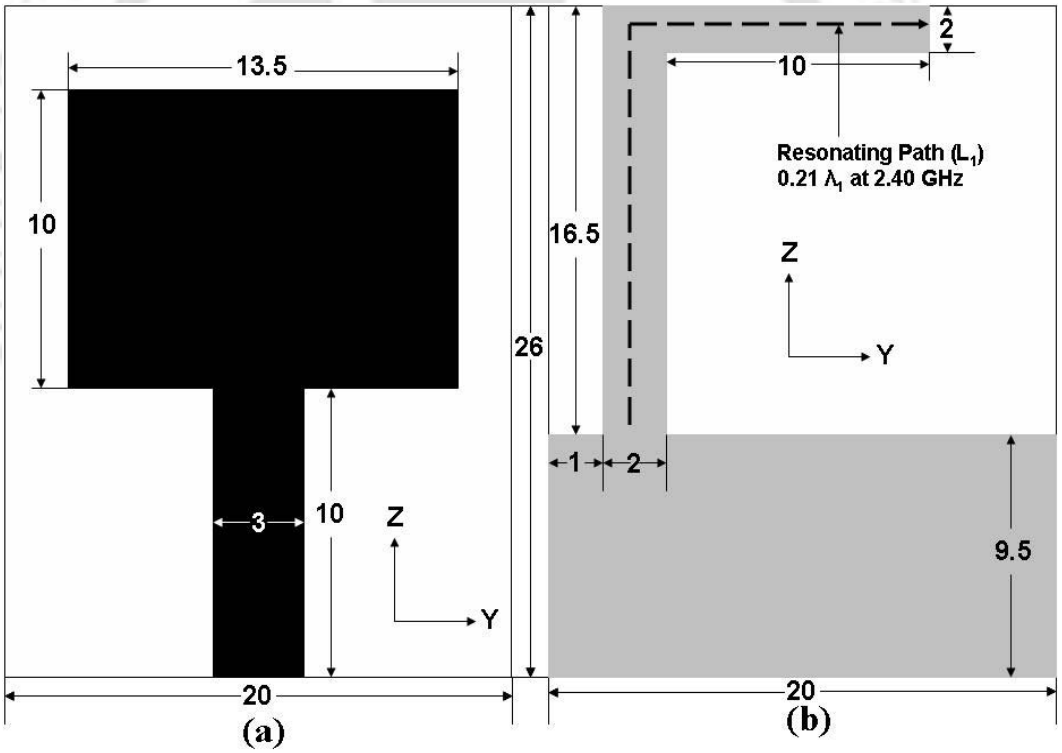

Figure 2.15: Geometry of the proposed antenna **(a)** Top view and **(b)** Bottom view.

of -34.82 dB) and f_3=6.91 GHz (reflection coefficient value of -32.00 dB) respectively. Due these two resonances, a huge band is obtained with the percentage bandwidth of 63.69. The entire WLAN band which extends from 5.15-5.35 GHz and 5.725-5.825 GHz can be suitably accommodated in this band from 3.98 GHz to 7.70 GHz.

When there is no inverted L-strip in the ground plane, the antenna has only rectangular radiating

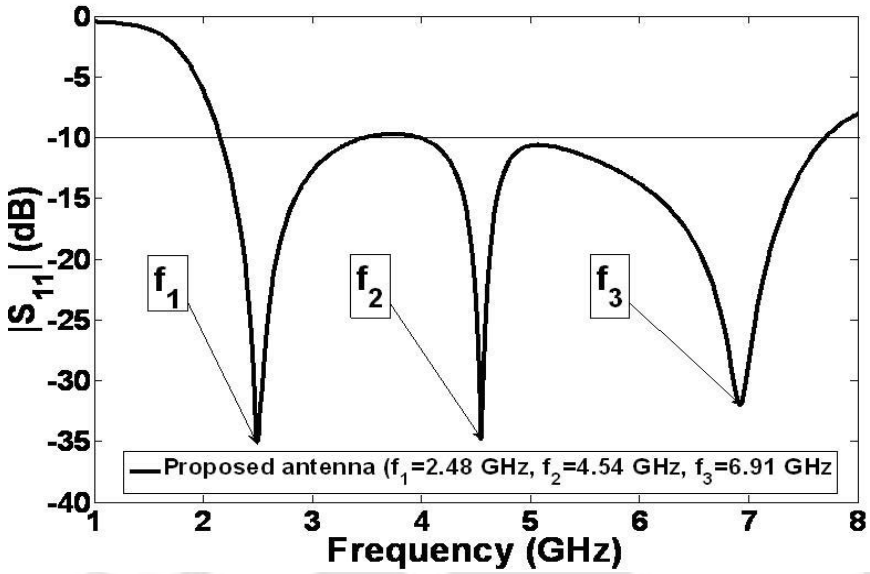

Figure 2.16: Simulated reflection coefficient ($|S_{11}|$) of proposed antenna.

element shown in the Fig. 2.17. In this situation the antenna weakly resonates only at f_a=6.35 GHz with the reflection coefficient value of -19.43 dB shown in the Fig. 2.19. In this case, the band extends from f_{low}=4.47 GHz to 8.19 GHz with the percentage bandwidth of 58.76. The mathematical expression for the f_{low} was first derived by K. P. Ray [111]. For any printed monopole antenna, the resonant frequency can be approximately calculated by equating its area (area of rectangular radiating element) to that of an equivalent cylindrical monopole antenna [48] of equivalent height equal to the length of monopole L and equivalent radius r. The theoretical expression for the $f_{low(th)}$ of the rectangular printed monopole antenna is given by

$$f_{low(th)} = \frac{7.2}{(L + r + p) \times k} GHz \tag{2.1}$$

where

L=Length of the monopole (cm) =1 cm

r=Radius of equivalent cylindrical monopole antenna (cm)=(W/2π)=(1.35/2π)=0.21485 cm

p=Length of the feed-gap (cm) = 0.05 cm

k= 1.15 [112]

Putting all the numerical in the above equation, the $f_{low(th)}$ is found out to be 4.95 GHz. But on

simulation, this value is found out to be f_{low}=4.47 GHz.

When only vertical portion of the inverted L-strip(16.5 mm=0.1738λ at 3.16 GHz) is protruded out from the ground plane without 90^0 bend shown in the Fig. 2.18, two weak resonances are visible in the reflection coefficient ($|S_{11}|$) graph in Fig. 2.19. One resonance occurred at f_b=3.16 GHz with the reflection coefficient value of -15.76 dB and other resonance occurred at f_c=6.01 GHz with the reflection coefficient value of -14.61 dB. The band at center frequency of f_b=3.16 GHz extends from 2.80 GHz to 4.12 GHz with the percentage bandwidth of 38.15 and the band at center frequency of f_c=6.01 GHz extends from f_{low1}=5.04 GHz to 8.58 GHz with the percentage bandwidth of 51.98. In this case the the f_{low1} shifted ahead to 5.04 GHz as compared to the case when only rectangular element is present (f_{low}=4.47 GHz).

But when the 90^0 bend is introduced in the vertical protruding stub in the ground plane, the proposed antenna with the rectangular radiating element provides two huge bands from 2.14 GHz to 3.47 GHz (resonance occurred with center frequency of f_1=2.48 GHz) having the percentage bandwidth of 47.71 and the second band is a huge band from f_{low2}=3.98 GHz to 7.70 GHz (two resonances having the center frequencies of f_2=4.54 GHz and f_3=6.91 GHz) with the percentage bandwidth of 63.69. The f_{low2}=3.98 GHz is shifted back as compared to previous case because the presence of a third resonance at f_3=6.91 GHz. The third resonance frequency f_3=6.91 GHz is approximately the third harmonic of the first resonant frequency f_1=2.48 GHz ($f_3 \sim 3f_1$). It is also clear that the rectangular radiating element is responsible for providing only the second resonant frequency at f_2=4.54 GHz. The inverted L-strip provides one resonance with the center frequency of f_1=2.48 GHz and the other resonance at f_3=6.91 GHz, which is approximately the third harmonic of the first resonant frequency f_1=2.48 GHz ($f_3 \sim 3f_1$).

Hence because of inverted L-strip in the ground plane, deep resonances with two huge bands are exhibited by the proposed antenna which can be appropriately applicable in the WLAN systems. Because of the electromagnetic coupling between the inverted L-strip in the ground plane and rectangular radiating element on the substrate, large bands with deep resonances are possible in the proposed antenna.

Table 2.1 explains in the tabular form the comparative study performed on the proposed antenna with the existing antennas for application in WLAN system in the literatures regarding size, band, percentage bandwidth and gain. The proposed antenna is considerably better in many aspects as

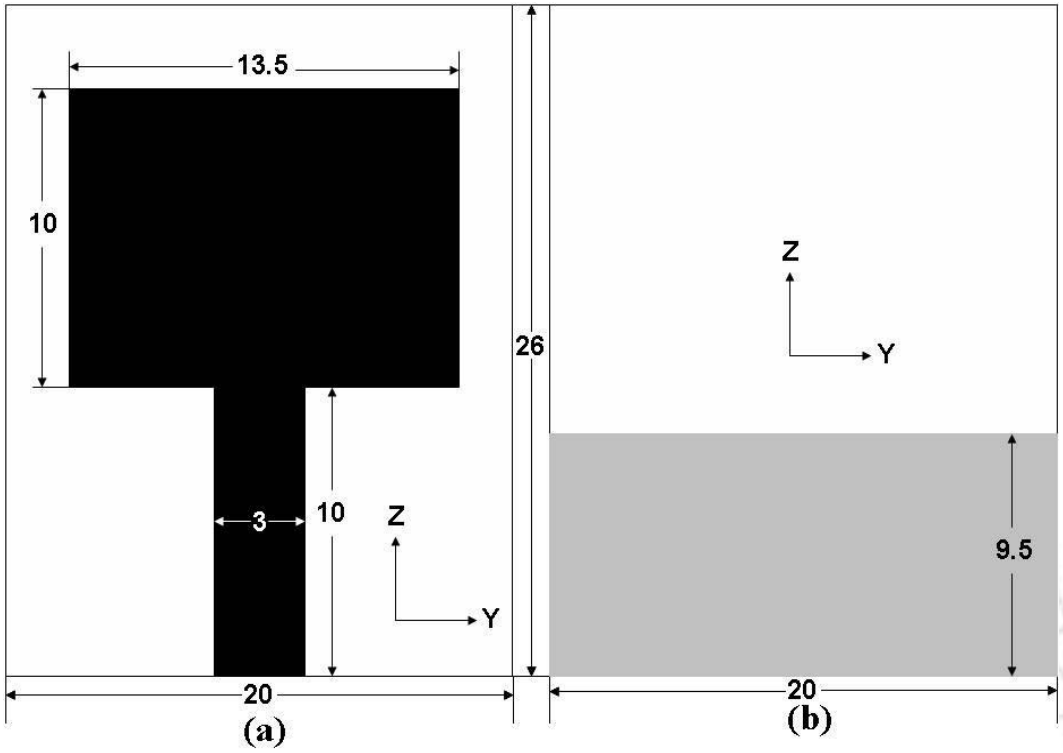

Figure 2.17: Geometry of radiating structure with rectangular radiating element having no inverted L-strip in ground plane **(a)** Top view and **(b)** Bottom view.

compared to the existing antennas in the literature.

Fig. 2.20 shows the fabricated prototype of the proposed antenna. The reflection coefficient ($|S_{11}|$) of the proposed antenna is measured with the help of Rohde and Schwarz ZVA24 vector network analyzer. Fig. 2.21 shows the comparison of simulated and measured reflection coefficient ($|S_{11}|$) of the proposed antenna. From the graph, it is clear that there is close matching between the simulated and measured results.

2.3.3 Effect of single bend on the proposed antenna performance

The effect of 90^0 bend in the inverted L-strip (resonating path L_1 at 2.4 GHz) of the ground plane is carried out. When the inverted L-strip is present with the rectangular radiating element (proposed antenna), three resonances occurred at f_1=2.48 GHz, f_2=4.54 GHz and f_3=6.91 GHz. The inverted L-strip in ground plane is responsible for providing two resonances i.e. at f_1=2.48 GHz and f_3=6.91 GHz, where f_3 is approximately the third harmonic of f_1 ($f_3 \sim 3f_1$). The second resonance is provided by the rectangular radiating element at f_2=4.54 GHz.

Now the total length of the L-strip is unfolded and is made a straight vertical strip of same length

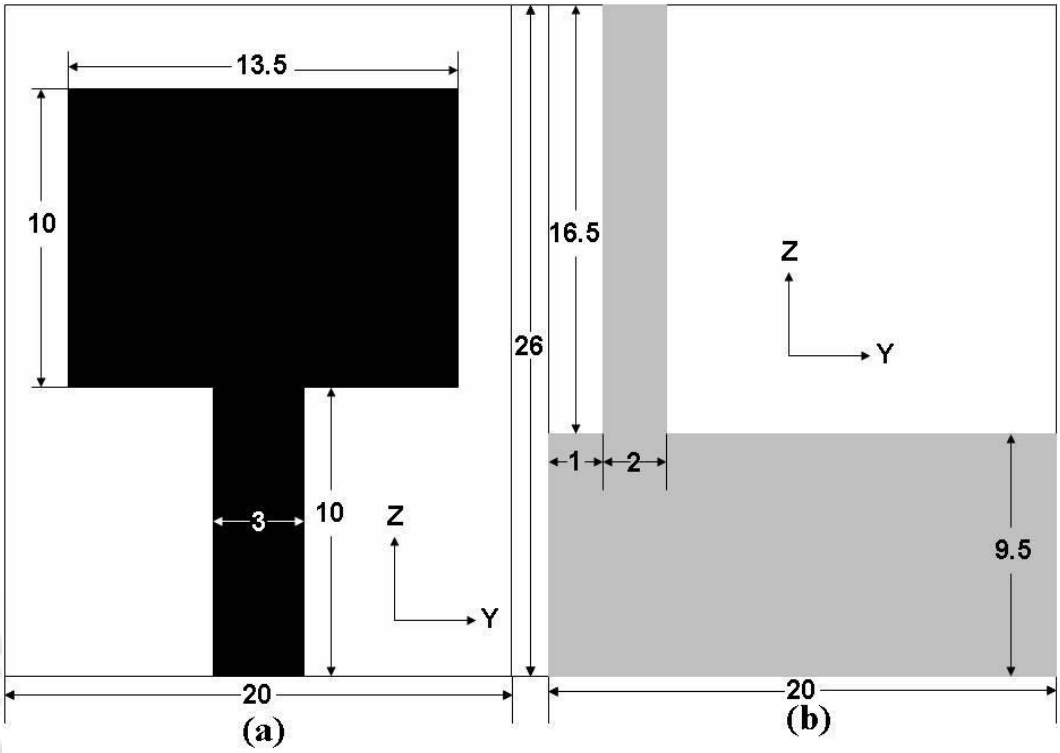

Figure 2.18: Geometry of radiating structure with rectangular radiating element having only vertical portion of the inverted L-strip in ground plane **(a)** Top view and **(b)** Bottom view.

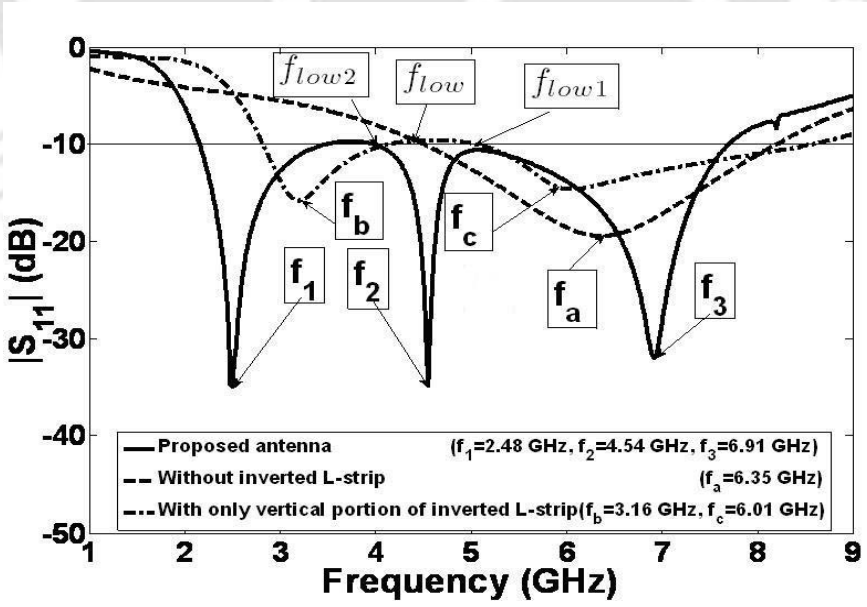

Figure 2.19: Comparison of simulated reflection coefficients ($|S_{11}|$) of the proposed antenna with the radiating structures having no inverted L-strip and only vertical portion of the inverted L-strip in ground plane.

as 90^0 bend L-strip as shown in the Fig. 2.22 and the structure is simulated. Two resonances are visible in the reflection coefficient ($|S_{11}|$) as shown in the Fig. 2.23. The first resonance $f_{1Linear}$ occurs

Table 2.1: Comparative study for the proposed antenna with the existing antennas

	Size (mm^2)	**Band 1 (GHz)**	**Band 2 (GHz)**	**% BW at Band 1**	**% BW at Band 2**	**Gain (dBi)**
This work	20×26=520	(2.14-3.47)	(3.98-7.70)	47.41	63.69	1.83-3.51 and 3.35-3.95
[113]	22×48=1056	(2.30-2.55)	(5.10-5.95)	10.30	15.38	1.00-1.40 and 3.80-4.20
[114]	40×35=1400	(2.38-2.52)	(4.86-6.87)	05.71	34.27	2.20-2.70 and 2.00-3.00
[115]	40×38=1520	(2.28-2.70)	(4.52-6.28)	16.90	32.60	-0.50-0.50 and 1.50-2.00
[116]	40×40=1600	(2.40-2.50)	(5.10-6.10)	04.08	17.85	0.30 and 4.80
[117]	109.03×77.88=8491.25	(2.40-2.52)	(4.94-5.72)	04.87	14.63	4.00

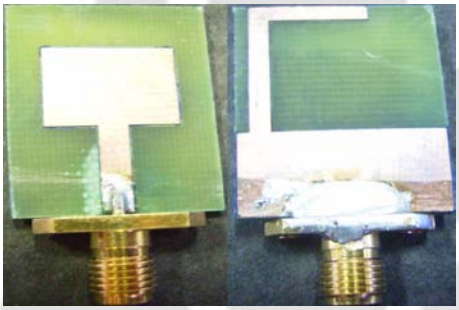

Figure 2.20: Fabricated prototype of the proposed antenna.

at 3.54 GHz and the second resonance occurs at $f_{2Linear}$=6.61 GHz. The $f_{1Linear}$=3.54 GHz is right shifted version of f_1 when strip is 90^0 bend (L-strip) and $f_{2Linear}$=6.61 GHz is also the right shifted version of f_2 when strip is 90^0 bend (L-strip). The third resonance $f_{3Linear}$ has occurred at 10.78 GHz, which should be the third harmonic of $f_{1Linear}$ ($f_{3Linear}$ ~$3f_{1Linear}$) shown in the Fig. 2.24. From the above analysis it is clear that a 90^0 bend reduces the resonant frequency as compared to a straight vertical strip in the ground plane of same length.

2.3.4 Gain of the proposed antenna

The simulated gain in the range of 2.14 GHz-3.47 GHz varies from 1.76 dBi to 3.4 dBi. The value of simulated gain at 2.48 GHz is 2.4 dBi. Similarly, the simulated gain in the range of 3.98 GHz-7.7 GHz varies from 3.3 dBi to 3.8 dBi. The value of simulated gains at 5.2 GHz and 5.8 GHz are 3.41 dBi and 3.45 dBi respectively.

The measured gain in the range of 2.14 GHz-3.47 GHz varies from 1.83 dBi to 3.51 dBi. The value

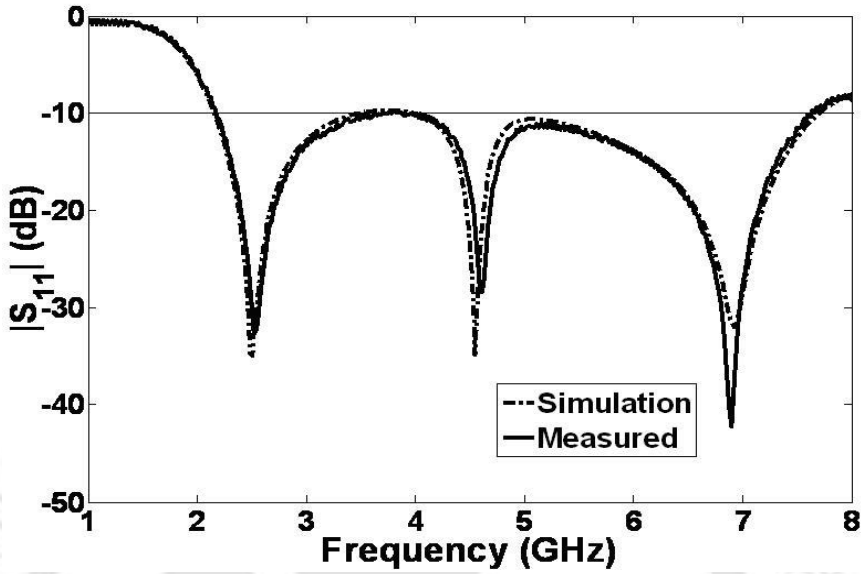

Figure 2.21: Comparison of the simulated and the measured reflection coefficients ($|S_{11}|$) of the proposed antenna.

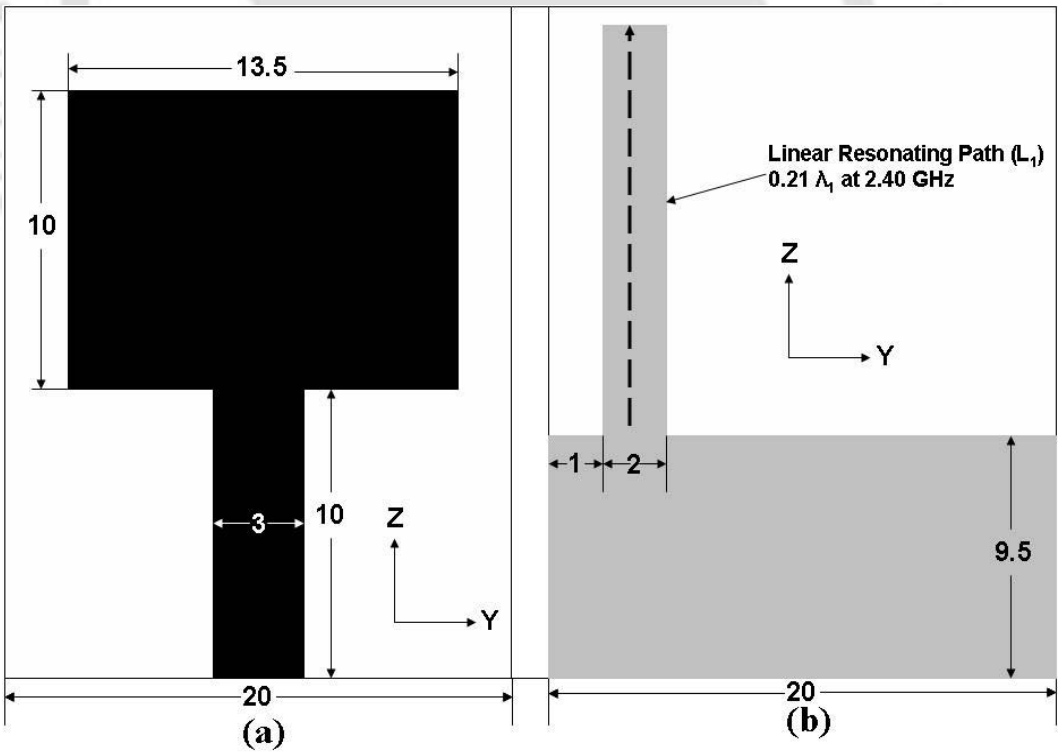

Figure 2.22: Geometry of the structure with linear strip in the ground plane of same length as inverted L-strip of the proposed antenna **(a)** Top view and **(b)** Bottom view.

of measured gain at 2.48 GHz is 2.35 dBi, which is sufficient for the operation in WLAN 2.4-2.484 GHz system satisfactorily. Similarly, the measured gain in the range of 3.98 GHz-7.7 GHz varies from

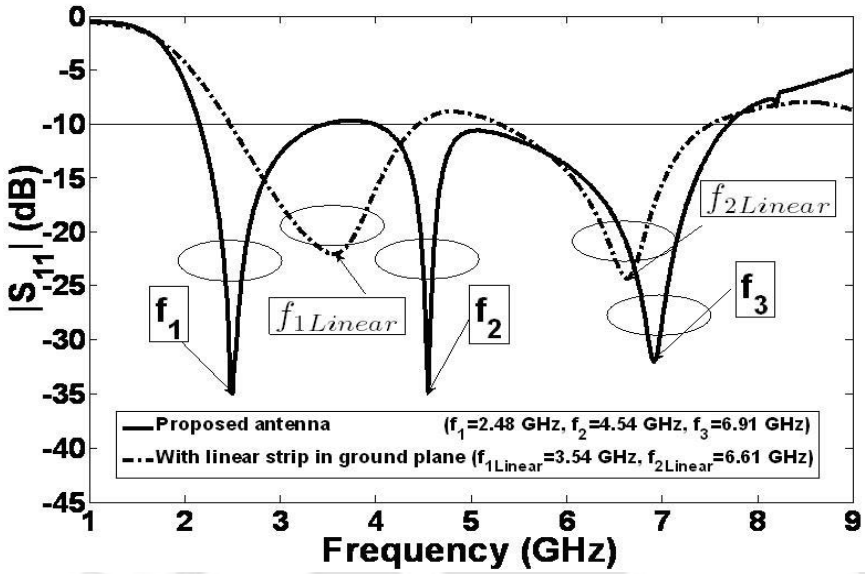

Figure 2.23: Comparison of simulated reflection coefficients ($|S_{11}|$) of the radiating structures with inverted L-strip in ground plane with rectangular radiating element and linear vertical strip of same length (1-9 GHz range).

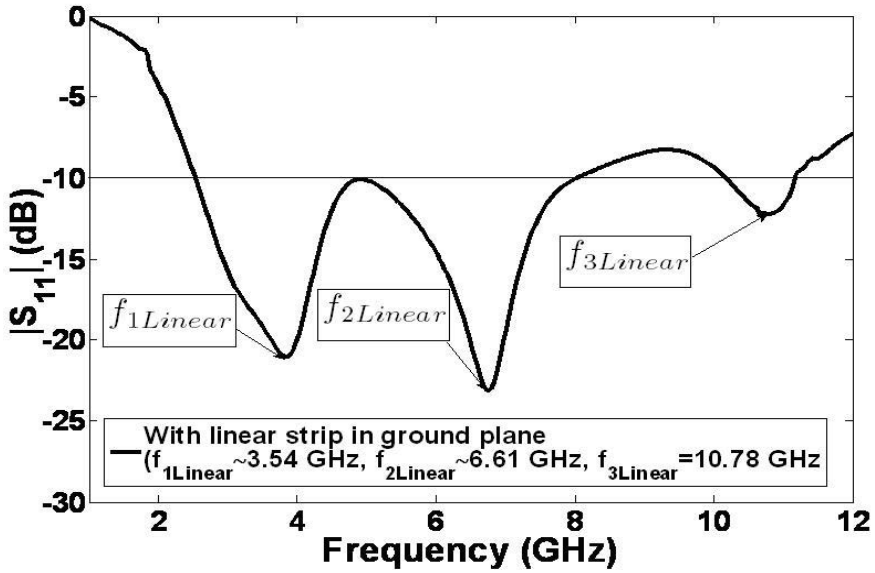

Figure 2.24: Simulated reflection coefficient ($|S_{11}|$) of the radiating structure with a rectangular radiating element and linear vertical strip of same length as its inverted L-strip counterpart in ground plane (1-12 GHz range).

3.35 dBi to 3.95 dBi. The value of measured gains at 5.2 GHz and 5.8 GHz are 3.67 dBi and 3.78 dBi respectively, which is sufficient for the operation in 5.15 GHz-5.35 GHz and 5.725 GHz-5.825 GHz WLAN system satisfactorily. Fig 2.25 shows comparison of simulated and measured gain (dBi) vs.

frequency of the proposed antenna in 2.14 GHz-3.47 GHz and 3.98 GHz-7.7 GHz range.

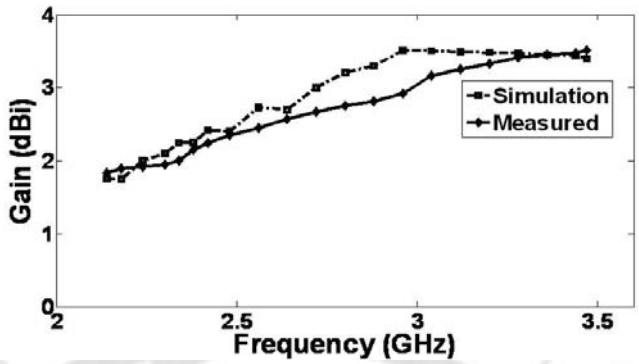

(a)

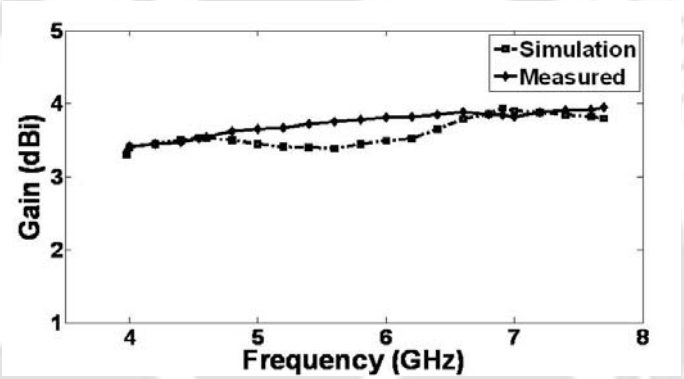

(b)

Figure 2.25: (a) Comparison of simulated and measured gain (dBi) vs. frequency of the proposed antenna (2.14 GHz-3.47 GHz) and **(b)** Comparison of simulated and measured gain (dBi) vs. frequency of the proposed antenna (3.98 GHz-7.7 GHz).

2.3.5 Surface current distribution of proposed antenna

At 2.4 GHz, the magnitude of the surface current is high on the microstrip feed-line, ground plane (just behind the microstrip feed-line). Apart from this, the magnitude of current density is moderate on the rectangular radiating element and very high in the vertical part of the inverted L-shaped strip on the ground plane. The magnitude of the surface current density is high in the lower left side of the rectangular ground plane. The ground plane provides the return path for the current. The current is continuous with high value of the surface current density and moves in the upward direction in the inverted L-shaped strip in the ground plane at 2.4 GHz. On the other hand the current density on the rectangular element is moderate. Since there is moderate current density in the rectangular radiating element and on the ground plane itself, antenna radiates and provides the resonances in 2.14 GHz/3.47 GHz band and 3.98 GHz/7.7 GHz band.

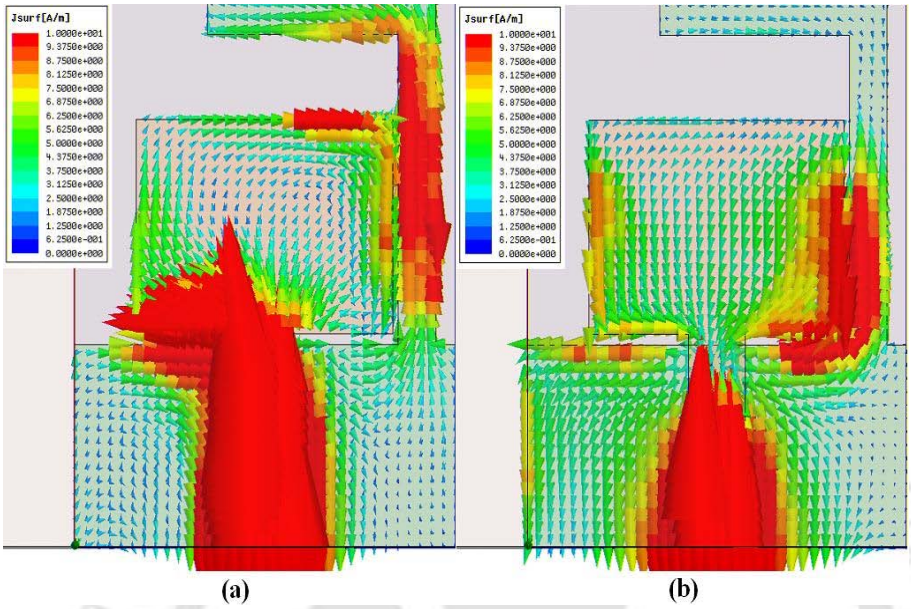

Figure 2.26: Direction and magnitude of the surface current distribution for the rectangular PMA with an inverted L-strip in the ground plane **(a)** at 2.4 GHz and **(b)** at 5.2 GHz.

At 5.2 GHz, the magnitude of the current density is very high on the lower side of the inverted L-shaped strip i.e. in the region where inverted L-shaped strip is protruded out from the ground plane. In the tip of the inverted L-shaped strip the current density is very low. Hence a maximum of current density occurs at the bottom of the inverted L-shaped strip and a minimum of current density occurs at the tip of the inverted L-shaped strip. That is nearly a quarter wave variations along the length of the strip monopole which corresponds to the resonant frequency. Hence antenna radiates effectively at 2.4 GHz and provides a strong resonance. Apart from this very high current density is visible in the ground plane near to the feed-line. On the rectangular radiating element the current density is sufficiently high as compared to that of 2.4 GHz case. There is considerable current density on two vertical side of the radiating element. Since in all the antenna structures such as the ground plane, microstrip feed-line, rectangular radiating element and the inverted L-shaped strip in the ground plane the current density is sufficiently high which is responsible for the proposed antenna to radiate and resonate effectively and strongly in 2.14 GHz/3.47 GHz band and 3.98 GHz/7.7 GHz band. Fig. 2.26 (a) and Fig. 2.26 (b) depicts the magnitude of the surface current density at 2.4 GHz and 5.2 GHz respectively.

2.3.6 Radiation pattern of the proposed antenna

The measured normalized co-polarized and cross-polarized E-plane (yz-plane) and H-plane (xy-plane) radiation patterns of the proposed monopole antenna at 2.4 GHz and 5.2 GHz are shown in the Fig. 2.27 and Fig. 2.28 respectively. It can be observed that the co-polar E-plane radiation pattern is of the shape of "8" at 2.4 GHz and 5.2 GHz approximately. At 2.4 GHz and 5.2 GHz, the E-plane cross-polar radiation patterns are in between -20 and -30 dB. The co-polar H-plane radiation pattern on the other hand is purely omni-directional at the two frequencies i.e. at 2.4 GHz and 5.2 GHz. At 2.4 GHz, the H-plane cross-polar radiation pattern is approximately -20 dB and the H-plane cross polarization level is in between -20 and -30 dB at 5.2 GHz.

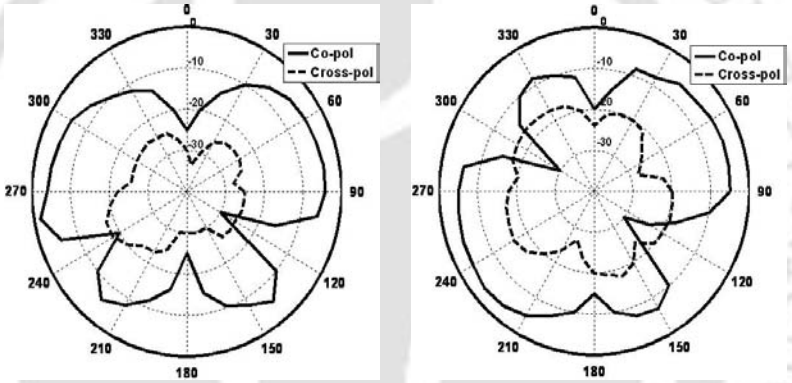

(a) (b)

Figure 2.27: Measured E-plane (yz-plane) radiation patterns of the proposed antenna at **(a)** 2.4 GHz and **(b)** 5.2 GHz.

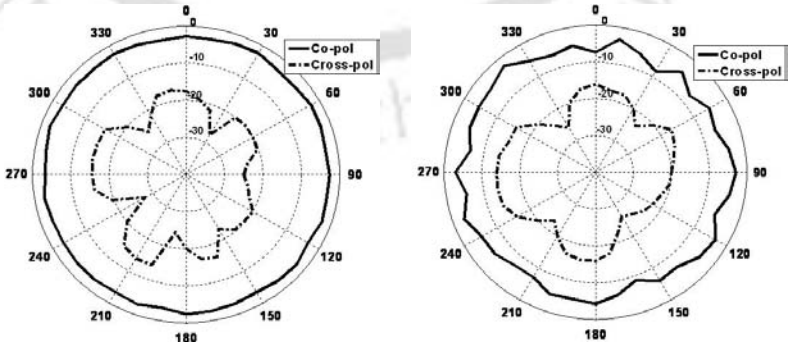

(a) (b)

Figure 2.28: Measured H-plane (xy-plane) radiation patterns of the proposed antenna at **(a)** 2.4 GHz and **(b)** 5.2 GHz.

2.4 Inverted L-shaped PMA with an inverted L-strip in the ground plane

2.4.1 Antenna design

Fig. 2.29 shows the geometry of the proposed antenna. This antenna is fabricated on a FR4 epoxy substrate with dielectric constant of 4.4 and thickness of 1.6 mm. The antenna is fed by the microstrip line of width 3 mm. The upper part of the microstrip feed-line is orthogonally bent towards left constituting an inverted L-shaped radiating element of the proposed antenna. On the ground plane, an inverted L-strip is protruded out from the right side of the ground plane. The proposed antenna belongs to the class of single bend PMA as there is only one bend in the inverted L-shaped radiating element and also in the inverted L-strip in the ground plane. All the design dimensions are shown in the Fig. 2.29 with some variables for the purpose of parametric study. The length of the variables of the proposed antenna are m=7.5 mm, n=11.0 mm and p=10.00 mm. Two resonant paths are created in the proposed antenna structure for dual band operation. The first resonance path is in the inverted L-strip in the ground plane whose length is $0.17\lambda_1$ at 2.40 GHz and the second resonance path is the microstrip feed-line orthogonally bent towards left constituting the radiating element whose length is $0.215\lambda_2$ at 5.61 GHz.

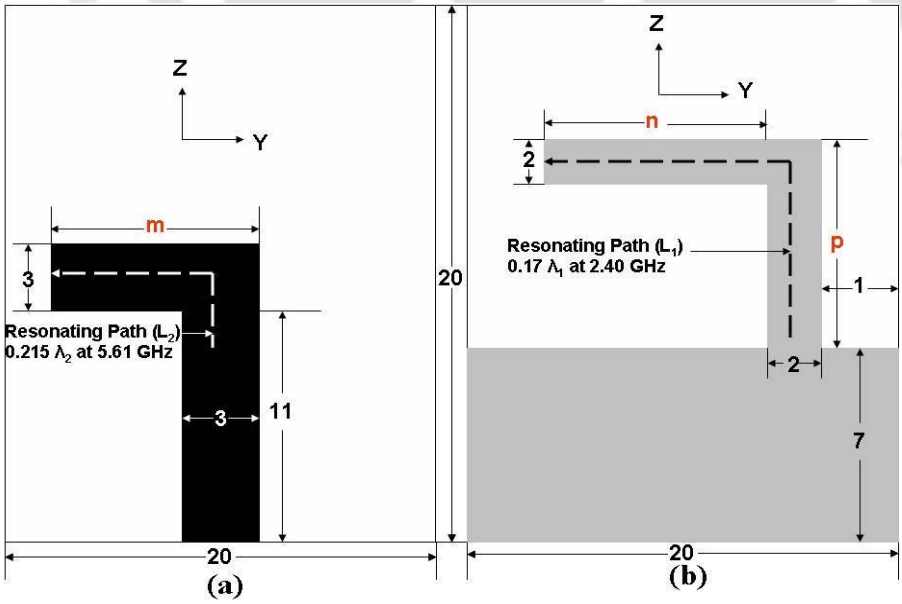

Figure 2.29: Geometry of the proposed antenna **(a)** Top view and **(b)** Bottom view.

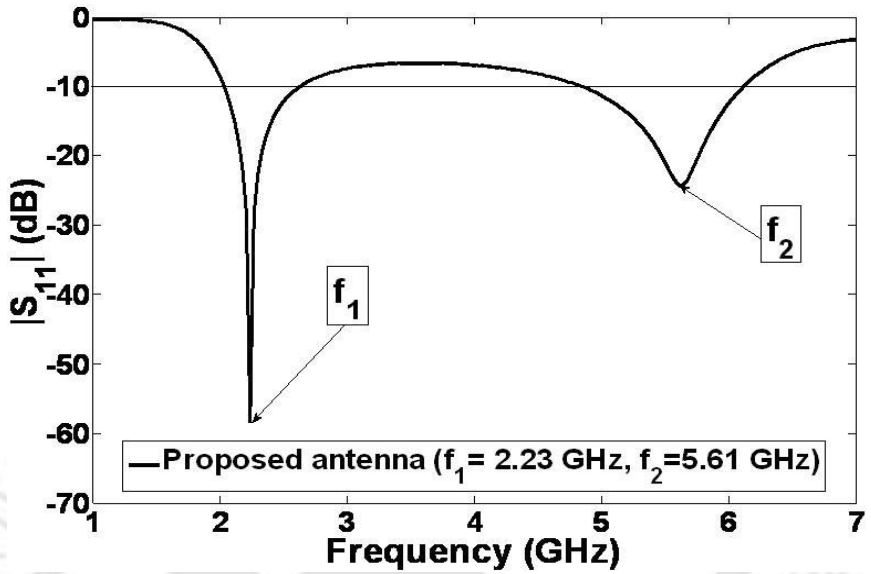

Figure 2.30: Simulated reflection coefficient ($|S_{11}|$) of proposed antenna.

2.4.2 Simulated and measured results on reflection coefficient ($|S_{11}|$) and the parametric study of the the proposed antenna

Fig. 2.30 shows the simulated reflection coefficient ($|S_{11}|$) of the proposed antenna. The first resonance occurs at f_1=2.23 GHz with the reflection coefficient value of -58.20 dB. The band extends from 2.01 GHz to 2.63 GHz. The percentage bandwidth in this band region is 26.72. The WLAN's 2.4-2.485 GHz band is completely immersed in this band of 2.01 GHz to 2.63 GHz. The second band extends from 4.82 GHz to 6.13 GHz with the peak of the resonance occurs at f_2=5.61 GHz with the reflection coefficient value of -24.22 dB. The percentage bandwidth in this band region is 23.92. The entire WLAN band which extends from 5.15-5.35 GHz and 5.725-5.825 GHZ can be suitably accommodated in this band from 4.82 GHz to 6.13 GHz.

When there is only inverted L-shaped radiating element and no inverted L-strip in the ground plane shown in the Fig. 2.37, antenna resonates only with the center frequency of f_{1b}=5.82 GHz with the reflection coefficient ($|S_{11}|$) value of -44.28 dB. In this case the resonance band extends from 4.97 GHz to 6.71 GHz. When a vertical portion of inverted L-strip (n=0) without 90^0 bend of length p=10 mm shown in the Fig. 2.31 is protruded from the right side of the ground plane, the antenna weakly resonates at $f_{n=0}$=3.65 GHz having the reflection coefficient value of -13.25 dB with resonance at the higher frequency region is completely vanished as shown in the Fig. 2.32.

But when a 90^0 horizontal bend is introduced in the protruded stub in the ground plane, con-

siderable changes has occurred the reflection coefficient ($|S_{11}|$) of the antenna. One more resonance is occurring at the higher frequency region having the center resonance frequency at f_2=5.61 GHz transforming the antenna resonance characteristic from single band resonance to dual band resonance. Two prominent bands are created. The first resonance occurs at f_1=2.23 GHz with the reflection coefficient value of -58.20 dB. The band extends from 2.01 GHz to 2.63 GHz. The percentage bandwidth in this band region is 26.72. The second band extends from 4.82 GHz to 6.13 GHz with the peak of the resonance occurs at f_2=5.61 GHz with the reflection coefficient value of -24.22 dB. The percentage bandwidth in this band region is 23.92. This scenario is shown in the Fig. 2.32. Hence with the introduction of inverted L-strip in the ground plane, the antenna becomes dual-band antenna.

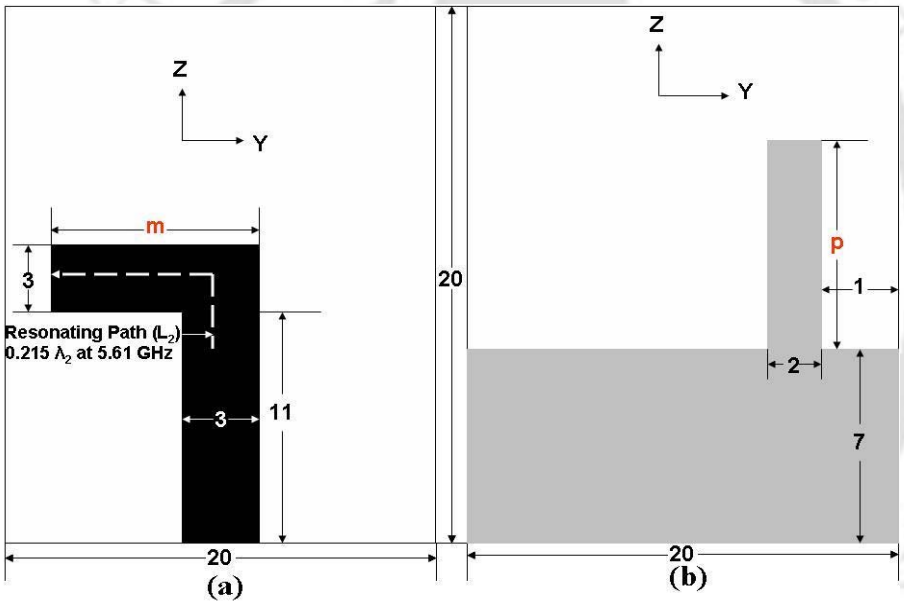

Figure 2.31: Geometry of radiating structure with inverted L-shaped radiating element having only vertical portion of inverted L-strip (n=0) in ground plane **(a)** Top view and **(b)** Bottom view.

Fig. 2.33(a) shows the reflection coefficient for successive values of the length m of the bend arm of the inverted L-shaped radiating element when the other parameters such as n (=11 mm) and p (=10 mm) are kept constant. From the graph, it is clearly visible that when m increases from 5.5 mm to 9.5 mm, the first resonant frequency (f_1) moves towards left, which means that the first resonant frequency (f_1) decreases with the increase of the length m. That means when m increases from 5.5 mm to 9.5 mm, f_1 deceases from 2.35 GHz to 2.14 GHz, which is 8.93% shift in the frequency towards left. On the other hand, the second resonant frequency (f_2) shifts rapidly towards left with the increase of length of m. In other words the second resonant frequency (f_2) decreases rapidly from 6.42 GHz to

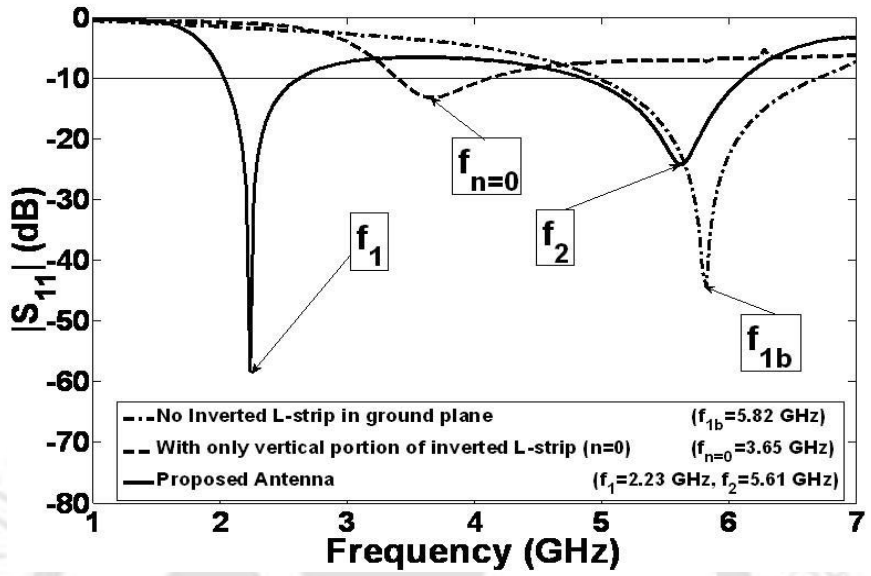

Figure 2.32: Comparison of simulated reflection coefficients ($|S_{11}|$) of the proposed antenna, inverted L-shaped radiating structure without inverted L-strip and with only vertical portion of inverted L-strip (n=0) in ground plane.

4.76 GHz when the length m increases from 5.5 mm to 9.5 mm, which is 25% shift in the frequency towards left.

Fig. 2.33(b) shows the reflection coefficient for successive values of the length n of the bend arm of the inverted L-strip in the ground plane when the other parameters such as m (=7.5 mm) and p (=10 mm) are kept constant. From the graph, it can be seen that when n increases from 9 mm to 13 mm, the first resonant frequency (f_1) moves towards left, which means that the first resonant frequency (f_1) decreases from 2.32 GHz to 2.11 GHz, which is 9.05% shift in the frequency towards left with the increase of the length of length n. On the other hand, the second resonant frequency (f_2) rapidly shifts towards left with the increase of length of n. In other words the second resonant frequency (f_2) decreases rapidly from 5.94 GHz to 5.28 GHz, which is 11.11% shift in the frequency towards left when the length n increases from 9 mm to 13 mm.

Fig 2.33(c) shows the reflection coefficient for successive values of the length p of the inverted L-strip in the ground plane when the other parameters such as m (= 7.5 mm) and n (= 11 mm) remain constant. From the graph, one can experience that when p increases from 8 mm to 12 mm, the first resonant frequency (f_1) moves towards right, which means that the first resonance frequency (f_1) increases from 2.08 GHz to 2.44 GHz, which is 14.75% shift in the frequency towards right with the

Table 2.2: Comparative study for the proposed antenna with the existing antennas

	Size (mm^2)	**Band 1 (GHz)**	**Band 2 (GHz)**	**% BW at Band 1**	**% BW at Band 2**	**Gain (dBi)**
This work	20×20=400	(2.01-2.63)	(4.82-6.13)	26.72	23.92	1.11-1.51 and 2.60-2.80
[118]	32×16=512	(2.25-2.54)	(4.85-7.21)	12.02	39.06	2.50-3.00 and 3.20-5.20
[119]	24×35=875	(2.30-3.85)	(5.10-7.14)	21.40	32.80	2.25-2.62 and 4.00-5.00
[120]	34×34=1156	(2.44-2.55)	(4.45-5.35)	4.4	3.1	1.50-1.80 and 2.51-2.65
[121]	50×30=1500	(2.30-2.50)	(4.90-5.90)	08.33	18.51	1.5 and 0.3
[122]	50×60=3000	(2.26-2.91)	(5.10-5.35)	25.14	04.78	0.8 and 0.4

increase of the length p. But when the length p is 8 mm there is no resonance in the first resonance frequency f_1. On the other hand, the second resonant frequency (f_2) rapidly decreases from 5.97 GHz to 5.28 GHz (11.55% shift in the frequency towards left) with the increase of p, which means that the second resonant frequency (f_2) moves towards left when p increases from 8 mm to 12 mm.

Table 2.2 explains in the tabular form the comparative study performed on the proposed antenna with the existing antennas for application in WLAN system in the literatures regarding size, band, percentage bandwidth and gain. The proposed antenna is considerably better in many aspects as compared to the existing antennas in the literature.

Fig. 2.34 shows the fabricated prototype of the proposed antenna. The reflection coefficient ($|S_{11}|$) of the proposed antenna is measured with the help of Rohde and Schwarz ZVA24 vector network analyzer. Fig. 2.35 shows the comparison of simulated and measured reflection coefficient ($|S_{11}|$) of the proposed antenna. From the graph, it is clear that there is close matching between the simulated and measured results.

2.4.3 Effect of single bend on the proposed antenna performance

2.4.3.1 Bending analysis on the inverted L-shaped radiating element in the absence of L-strip in ground plane

When there is no 90^0 bend in the radiating element means the radiating element is linear whose length is $0.215\lambda_2$ at 5.61 GHz which is equivalent to the length of the inverted L-shaped radiating element at 5.61 GHz, the radiating structure resonates with the center frequency of f_{0b}=5.46 GHz

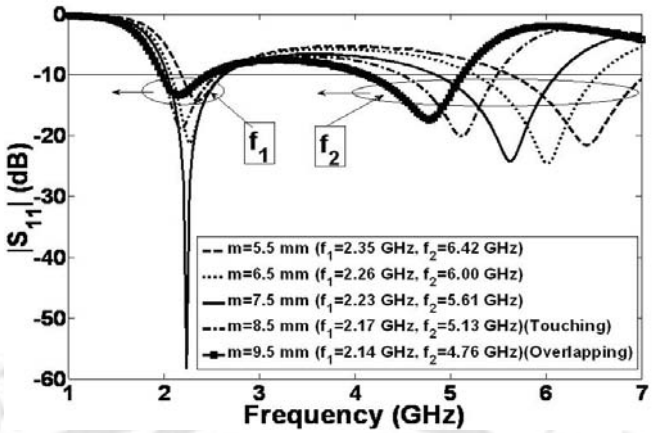

(a)

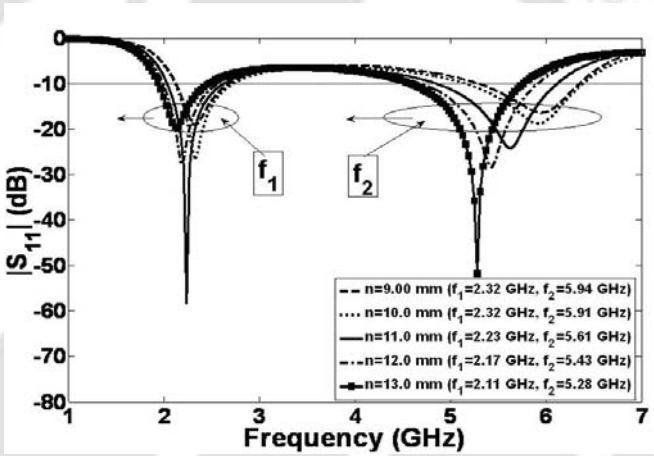

(b)

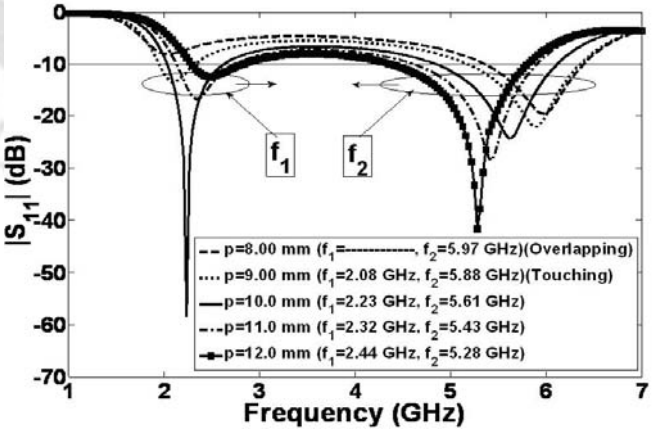

(c)

Figure 2.33: Simulated reflection coefficient ($|S_{11}|$) (dB) graphs, **(a)** m is a variable, n=11 mm and p=10 mm, **(b)** n is a variable, m=7.5 mm and p=10 mm and **(c)** p is a variable, m=7.5 mm and n=11 mm.

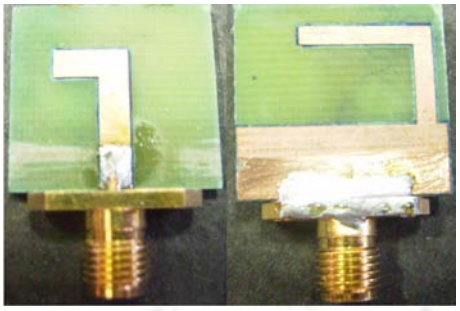

Figure 2.34: Fabricated prototype of the proposed antenna.

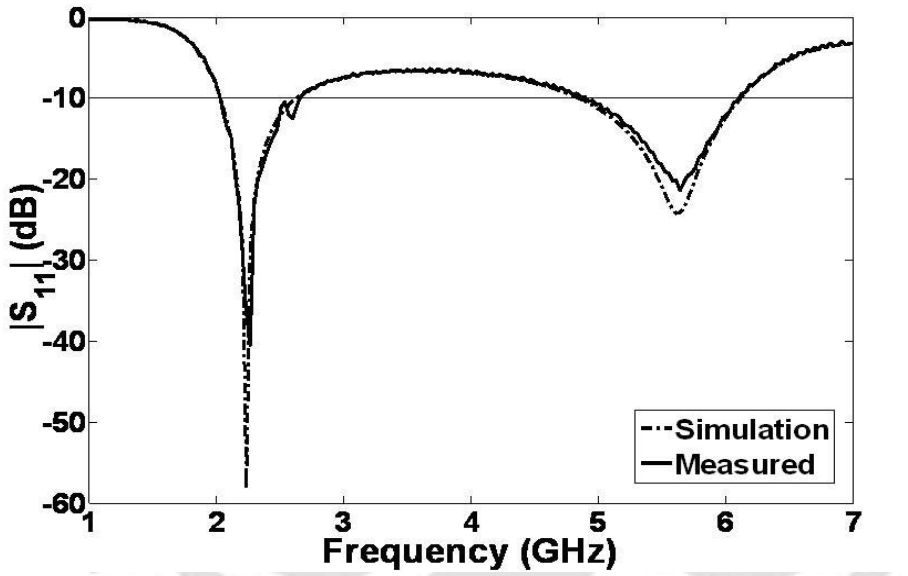

Figure 2.35: Comparison of the simulated and measured reflection coefficients ($|S_{11}|$) of the proposed antenna.

having the reflection coefficient value of -13.83 dB shown in Fig. 2.38. At the same time there is no inverted L-strip in the ground plane and the structure is shown in the Fig. 2.36.

But in the present condition when a 90^0 bend is introduced in the radiating element and the structure is shown in the Fig. 2.37, a strong resonance occurs at f_{1b}=5.82 GHz with the reflection coefficient value of -44.28 dB shown in the Fig. 2.38. Hence the introduction of a single 90^0 bend in the radiating element not only shifts the resonant frequency to the higher value [110] but also helps in strong resonance.

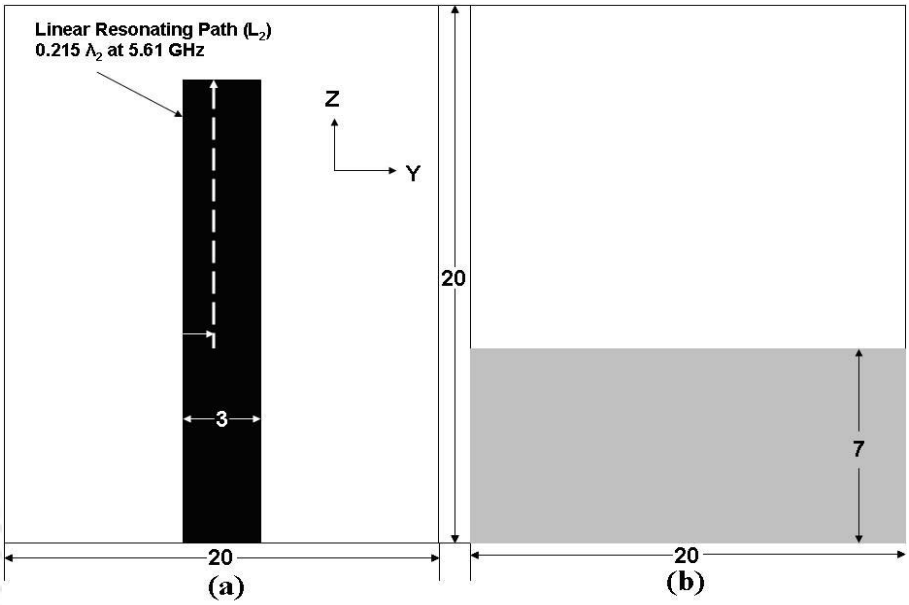

Figure 2.36: Geometry of radiating structure with linear vertical strip as the radiating element in the absence of inverted L-strip in ground plane **(a)** Top view and **(b)** Bottom view.

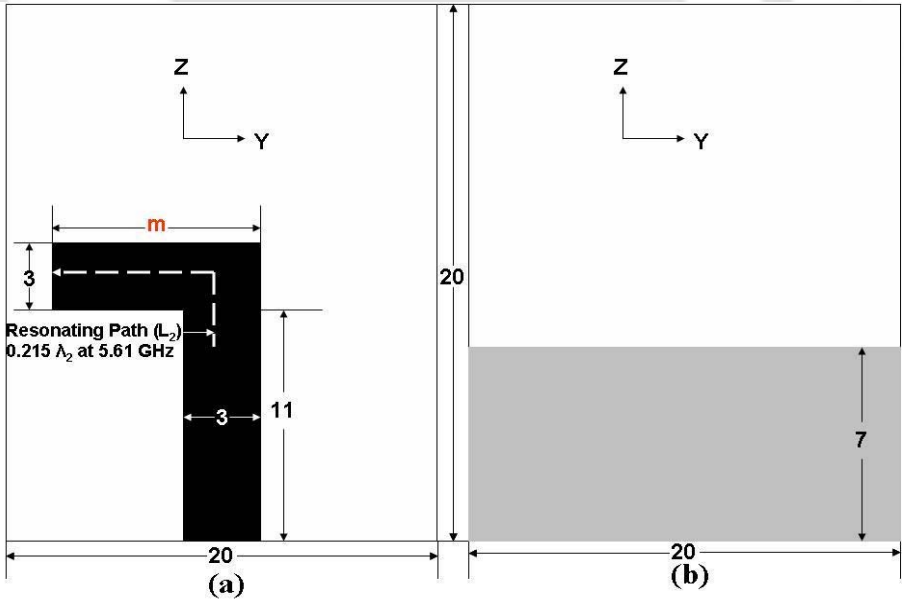

Figure 2.37: Geometry of radiating structure with inverted L-shaped radiating element in the absence of inverted L-strip in ground plane **(a)** Top view and **(b)** Bottom view.

2.4.3.2 Bending analysis on L-strip in ground plane with the presence of inverted L-shaped radiating element

Now the bending analysis is performed on the protruded inverted L-strip (resonating path L_1=0.17λ_1 at 2.40 GHz) in the ground plane. When there is inverted L-strip with one 90^0 bend in the ground

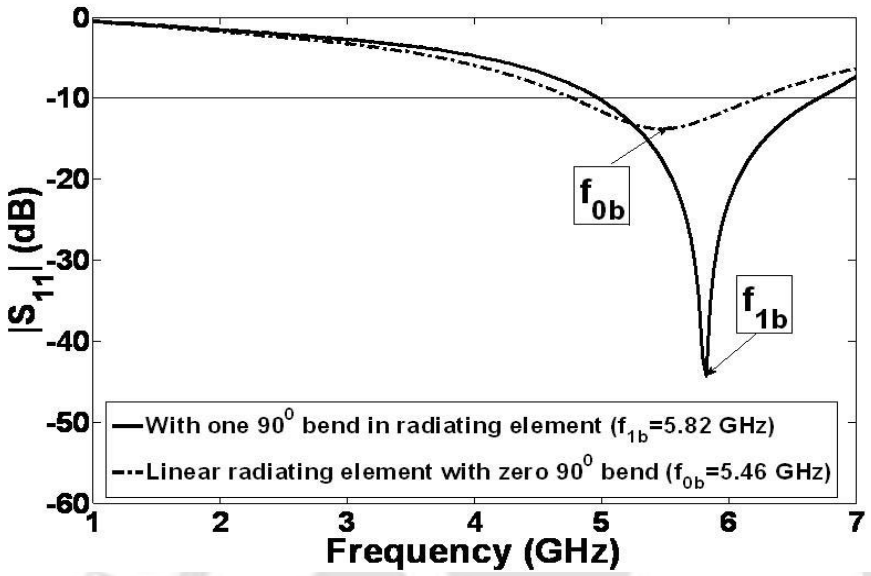

Figure 2.38: Effect of bend on the reflection coefficient ($|S_{11}|$) with one 90^0 bend in radiating element and a linear radiating element with no 90^0 bend of same length in the absence of inverted L-strip in ground plane.

plane along with the inverted L-shaped radiating element (proposed antenna), the antenna resonates at two resonant frequencies i.e. atf_1 =2.23 GHz and f_2=5.61 GHz.

Now the inverted L-strip in the ground plane is unfolded and is made linear of same length as the 90^0 bend inverted L-strip, which is shown in the Fig. 2.37 and the structure is simulated. The simulated reflection coefficient graph is shown in the Fig. 2.40. There is one resonance $f_{1Linear}$ =4.01 GHz is visible in the graph. The other resonance occur at $f_{2Linear}$=12.28 GHz shown in the Fig. 2.41.

The bending analysis is performed for the both the cases of inverted L-shaped radiating element (L-strip is absent in ground plane) and inverted L-strip in the ground plane with the presence of inverted L-shaped radiating element. When bending analysis is performed on the inverted L-shaped radiating element, the resonating frequency is shifted to a slightly higher value with 90^0 bend radiating element as compared its linear counterpart of same length. Apart from this, with bending in the inverted L-shaped radiating element the resonance becomes stronger than the linear case. But when bending analysis is performed on the inverted L-strip in the ground plane with the presence of inverted L-shaped radiating element, the resonating frequencies are shifted to much higher value with linear strip in the ground plane as compared to its 90^0 bend inverted L-strip counterpart of same length. Hence, it is possible to decrease the size of the resonator to a great extent.

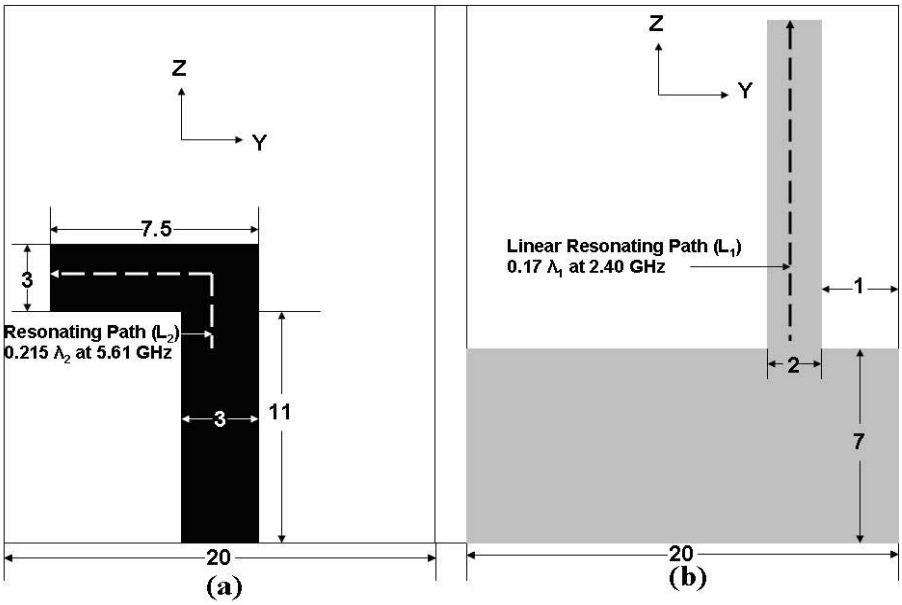

Figure 2.39: Geometry of radiating structure with linear vertical strip in the ground plane with inverted L-shaped radiating element **(a)** Top view and **(b)** Bottom view.

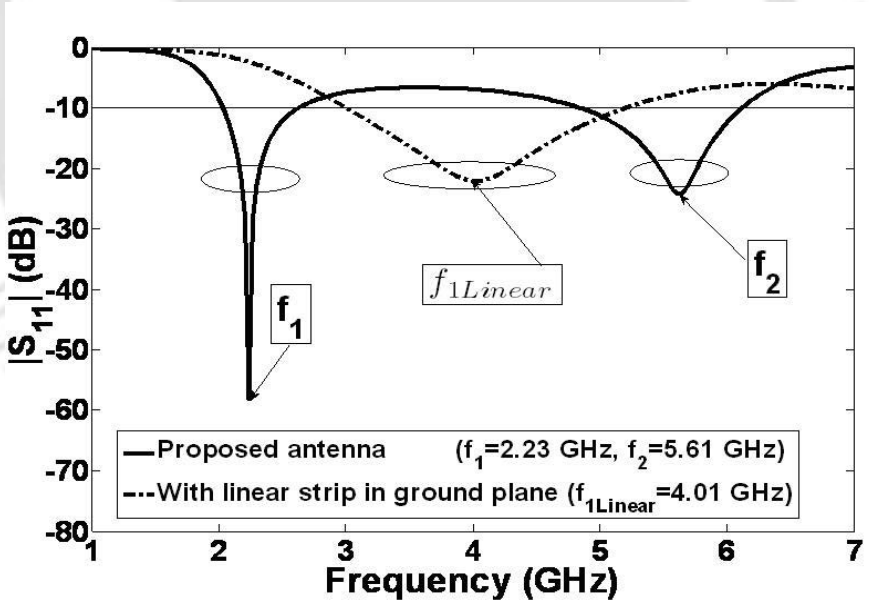

Figure 2.40: Comparison of simulated reflection coefficients ($|S_{11}|$) of the radiating structures with inverted L-strip in ground plane and a linear vertical strip of same length in presence of inverted L-shaped radiating element (1-7 GHz range).

2.4.4 Gain of the proposed antenna

The simulated gain in the range of 2.01 GHz-2.63 GHz varies from 1.05 dBi to 1.45 dBi. The value of simulated gain at 2.41 GHz is 1.22 dBi. Similarly, the simulated gain in the range of 4.82 GHz-6.13

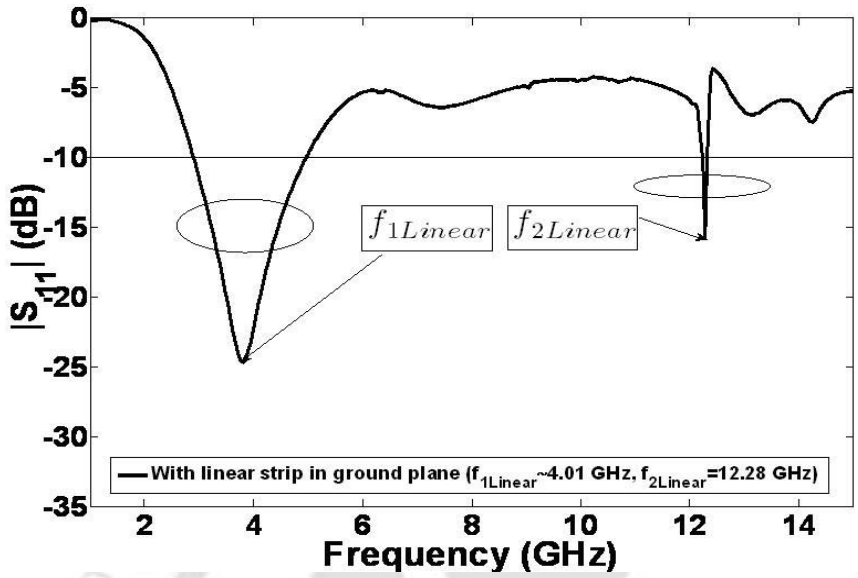

Figure 2.41: Simulated reflection coefficient ($|S_{11}|$) of the radiating structure with a linear vertical strip in the ground plane of same length as inverted L-strip in presence of inverted L-shaped radiating element (1-15 GHz range).

GHz varies from 2.5 dBi to 2.76 dBi. The value of simulated gains at 5.2 GHz and 5.8 GHz are 2.76 dBi and 3.02 dBi respectively.

The measured gain in the range of 2.01 GHz-2.63 GHz varies from 1.11 dBi to 1.51 dBi. The value of measured gain at 2.41 GHz is 1.31 dBi, which is sufficient for the operation in WLAN 2.4-2.484 GHz system satisfactorily. Similarly the measured gain in the range of 4.82 GHz-6.13 GHz varies from 2.6 dBi to 2.8 dBi. The value of measured gains at 5.2 GHz and 5.8 GHz are 2.95 dBi and 3.15 dBi respectively, which is sufficient for the operation in 5.15 GHz-5.35 GHz and 5.725 GHz-5.825 GHz WLAN system satisfactorily. Fig 2.42 shows comparison of simulated and measured gain (dBi) vs. frequency of the proposed antenna in 2.01 GHz-2.63 GHz and 4.82 GHz-6.13 GHz range.

2.4.5 Surface current distribution of proposed antenna

At 2.4 GHz, the magnitude of the current density is high at the edges of the microstrip feed-line, in the ground plane just behind the microstrip feed-line. The magnitude of the current density is very high in the bottom portion as well as in the edges of the inverted L-shaped radiating element. On the other hand the magnitude of the current density in the inverted L-shaped strip in the ground plane is low as compared to the inverted L-shaped radiating element. The direction of the current density is downward on the vertical portion of the inverted L-strip in the ground plane. Hence the net magnitude

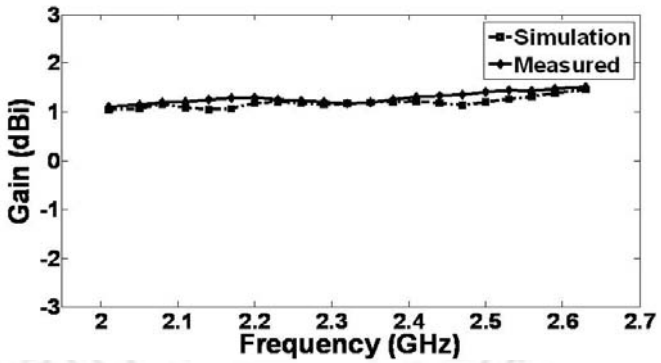

(a)

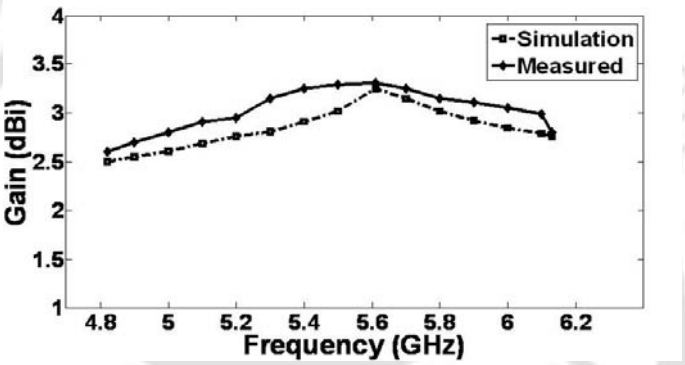

(b)

Figure 2.42: (a) Comparison of simulated and measured gain (dBi) vs. frequency of the proposed antenna (2.01 GHz-2.63 GHz) and **(b)** Comparison of simulated and measured gain (dBi) vs. frequency of the proposed antenna (4.82 GHz-6.13 GHz).

of current density is more in the inverted L-shaped radiating element. Regarding the direction of the surface current, the current moves continuously upward in the inverted L-shaped radiating element. No current cancellation occurs in the radiating element. As the sufficient current density is present in the radiating element, effective radiation occurs in both the frequency bands of 2-3 GHz and 5-6 GHz.

At 5.5 GHz, the magnitude of the current density is high in the corner of 90^0 bend and the edges of the horizontal portion of the inverted L-shaped strip in the ground plane. Apart from this, very high current density is visible on the microstrip feed-line and in the ground plane just behind the microstrip feed-line. The current density is also moderate on the edges of the inverted L-shaped radiating element. The direction of the current in the inverted L-shaped strip in the ground plane is continuously upward and the magnitude of the current is also high on the edges of the inverted L-shaped strip which is designed to produce resonance at 2.4 GHz. Since sufficient current density in two of the radiating elements and no current cancellation occurs in any of the radiating elements,

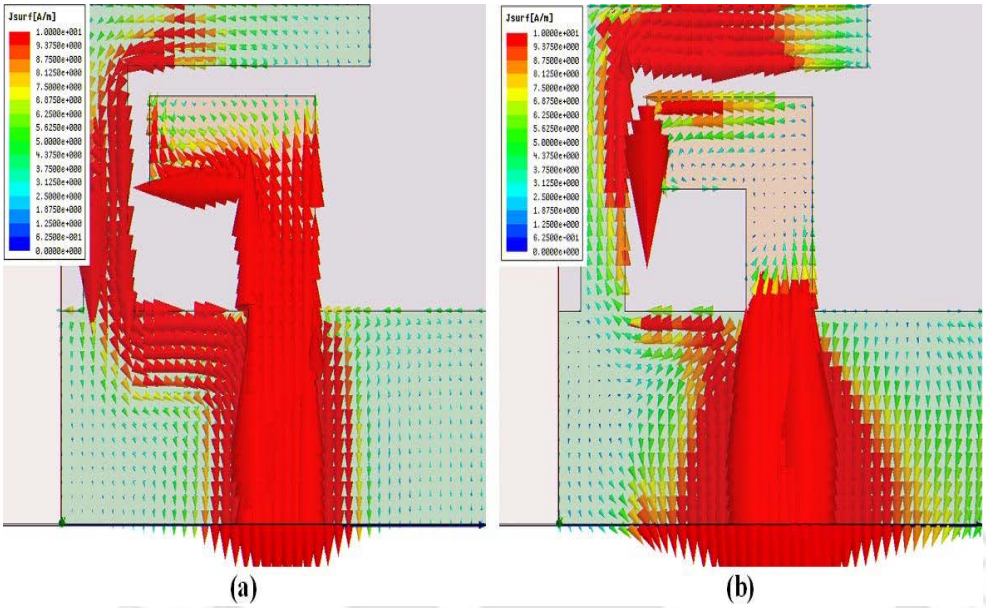

Figure 2.43: Direction and magnitude of the surface current distribution for the inverted L-shaped PMA with an inverted L-strip in the ground plane **(a)** at 2.4 GHz and **(b)** at 5.5 GHz.

effective radiation occurs in both the frequency bands of 2-3 GHz and 5-6 GHz. The magnitude of the current density in 2.4 GHz and 5.5 GHz is shown in the Fig. 2.43 (a) and Fig. 2.43 (b).

2.4.6 Radiation pattern of the proposed antenna

The measured normalized co-polarized and cross-polarized E-plane (yz-plane) and H-plane (xy-plane) radiation patterns of the proposed monopole antenna at 2.4 GHz and 5.5 GHz are shown in the Fig. 2.44 and Fig. 2.45 respectively. It can be observed that the co-polar E-plane radiation pattern is of the shape "8" at 2.4 GHz and 5.5 GHz approximately. At 2.4 GHz and 5.5 GHz, the E-plane cross-polar radiation patterns are in between -20 and -30 dB. The co-polar H-plane radiation pattern on the other hand is purely omni-directional at the two frequencies i.e. at 2.4 GHz and 5.5 GHz. At 2.4 GHz, the H-plane cross-polar radiation pattern is approximately -20 dB and the H-plane cross polarization level is in between -20 and -30 dB at 5.5 GHz. This antenna is much more compact in size than the previous two antennas.

2.5 Summary

In this chapter three new single bend compact and simple PMAs are presented. The first antenna is a microstrip line fed monopole antenna in which the radiating element is F-shape. Two resonating

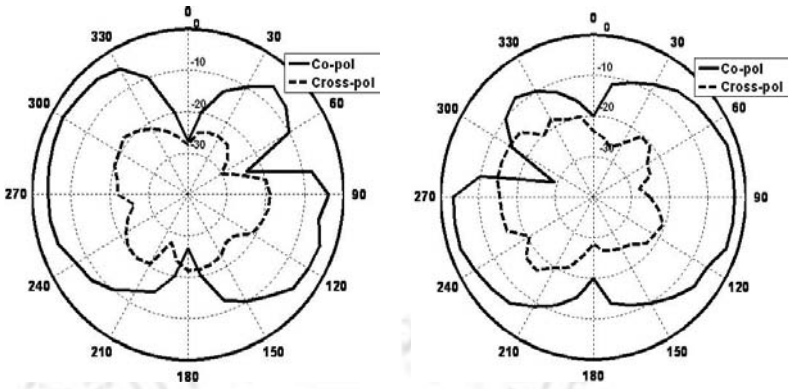

(a) (b)

Figure 2.44: Measured E-plane (yz-plane) radiation patterns of the proposed antenna at **(a)** 2.4 GHz and **(b)** 5.5 GHz.

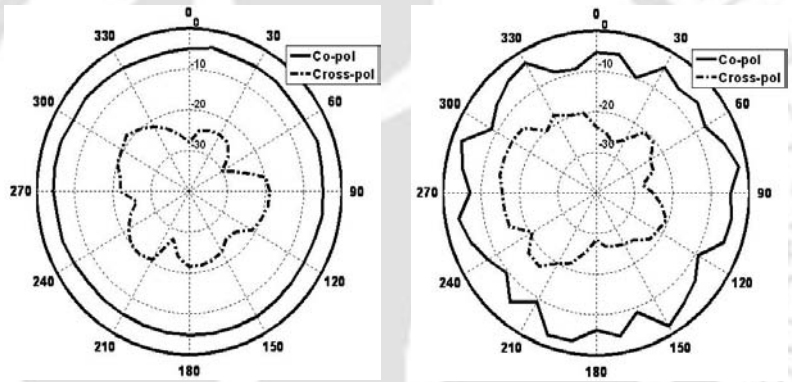

(a) (b)

Figure 2.45: Measured H-plane (xy-plane) radiation patterns of the proposed antenna at **(a)** 2.4 GHz and **(b)** 5.5 GHz.

paths are created to provide two simultaneous resonances in RFID and WLAN domain. The antenna is relatively compact and simple in structure. The proposed antenna shows consistent radiation pattern and appropriate gain characteristic. The proposed antenna attains 12.5 percent size reduction, 43.16 percent bandwidth improvement and 3.10 percent average gain enhancement as compared to contemporary dual band PMAs [116].

The second printed monopole antenna has a rectangular radiating element and a protruding inverted L-strip on the ground plane. The inverted L-strip provides the resonating path for the resonance at the low frequency region and higher frequency region. The rectangular radiating element provides resonance in the middle frequency region providing a huge bandwidth. The proposed antenna is a dual-band monopole antenna with sufficient bandwidth in which the whole of the WLAN application

band can be easily accommodated. Apart from this, the proposed antenna has appropriate gain and radiation characteristics for the application in WLAN domain. This proposed antenna attains 50.75 percent size reduction, 76.88 percent average bandwidth improvement and 15.17 percent average gain enhancement when compared to contemporary dual-band PMAs [113].

The third antenna is the smallest in comparison to other two antennas. In this antenna, the upper part of the microstrip feed-line is orthogonally bent towards left constituting an inverted L-shaped radiating element of the proposed antenna. On the ground plane an inverted L-strip is protruded out from the right side of the ground plane. In this way two resonant paths are generated to provide the simultaneous resonances at the two frequencies so that this proposed antenna can be applicable in WLAN application domain. This new antenna achieves 73.33 percent size reduction, 45.71 percent average bandwidth enhancement and 53.6 percent average gain improvement when compared to contemporary dual-band PMAs [121].

Hence, finally it can be concluded that the printed single bend monopole antennas with microstrip feeding structures are excellent category of broadband antennas. Dual band operation can be achievable for these classes of antennas by creation of two independent resonating paths in the form of protruding stub in the ground plane and also through the radiating element printed on the substrate.

3

Double bend PMA with an inverted L-strip in the ground plane

Contents

3.1 Introduction 74
3.2 Inverted L-shaped PMA with an inverted L-strip in the ground plane . 75
3.3 Simulated and measured results on reflection coefficient ($|S_{11}|$) and the parametric study of the proposed antenna 76
3.4 Effect of double bend on the the proposed antenna performance 84
3.5 Gain of the proposed antenna 91
3.6 Surface current distribution of proposed antenna 93
3.7 Radiation pattern of the proposed antenna 93
3.8 Summary 95

3.1 Introduction

Microstrip-line fed PMAs are attractive antennas for application in modern wireless communication system due to its many advantages such as low cost, light weight, ease of fabrication, and easily mountable in many hand held devices. There are many PMAs available in the literature. Some of these antennas are explained below.

In [123], the antenna has a rectangular radiating element fed by microstrip feed-line and a trapezoidal strip is printed on the back side of the antenna for WLAN/WiMAX application. In [124], the antenna has a rectangular strip ring with double meander line and a top loaded vertical strip for the dual-band wireless application. The antenna in [125] has a step size slot in the rectangular radiating element and a open ended slot in the top middle edge of the ground plane. The antenna comprise of a simple trapezoidal patch [126] with stepped impedance in the two lower bottom corner of the patch. In the ground plane, two double open-ended U-shaped slots are created for wireless applications. In [127], the antenna is fed by the microstrip feed line and the antenna has the meandered radiating element with two shorting sleeves on the two sides of the ground plane. Antenna loaded with an annular concentric split ring [128] slot for the application in dual-band wireless application. In [129], the antenna has a pair of symmetric resonators and a beveled planar radiator for application in wireless domain. The antenna in [130] has a modified fork-shaped strip for the multi-band wireless application. In [131], the antenna comprise of three branches of paw-shaped strip for the WLAN/WiMAX application. In [132], the antenna is fed by microstrip line and consists of a circular ring, a Y-shape like strip and defected ground structure for application in WLAN/WiMAX.

All the above described antennas are microstrip-line fed PMAs for application in wireless domain such as WLAN (2.4(2.4-2.484 GHz)/5.2(5.15-5.35 GHz)/5.8(5.725-5.825 GHz)) and WiMAX (2.5-2.69 GHz and 3.4-3.69 GHz) operating bands. Size is very crucial parameter for the design of PMAs for wireless applications. The newly proposed antenna is compact in size as compared to the existing microstrip-line fed PMAs and considerable bandwidth and gain enhancement are achieved. The proposed antenna has the two bends in the radiating element. Hence, this antenna belongs to the category of double bend PMA. Because of small size and large bandwidth in the WLAN domain of operation, this newly proposed antenna may find suitable applications in modern wireless communication systems.

3.2 Inverted L-shaped PMA with an inverted L-strip in the ground plane

3.2.1 Antenna design

Fig. 3.1 shows the geometry of the proposed antenna. The antenna is fabricated on the FR4 epoxy substrate with dielectric constant of 4.4 and thickness 1.6 mm. The antenna is fed by the microstrip line with the width of 3 mm. The upper part of the microstrip feed-line is extended as a reverse L-shape constituting the radiating element of the proposed antenna. On the ground plane, an inverted L-strip is protruded out from the right side of the ground plane. An open ended square slot is created on the middle top edge of the ground plane for the enhancement of the bandwidth of the proposed antenna. The proposed antenna has the two bends in the radiating element. Hence, this antenna belongs to the category of double bend PMA. The first resonating path (L_1) is in the inverted L-strip in the ground plane whose length is $0.188\lambda_1$ at 2.4 GHz and the second resonating path (L_2) is the microstrip feed-line extended as a reverse L-shape whose length is $0.25\lambda_2$ at 5.2 GHz. All the design parameters are shown the Fig. 3.1 with some variables for the purpose of parametric study. The length of the variables of the proposed antenna are n=9.50 mm and p=5.00 mm.

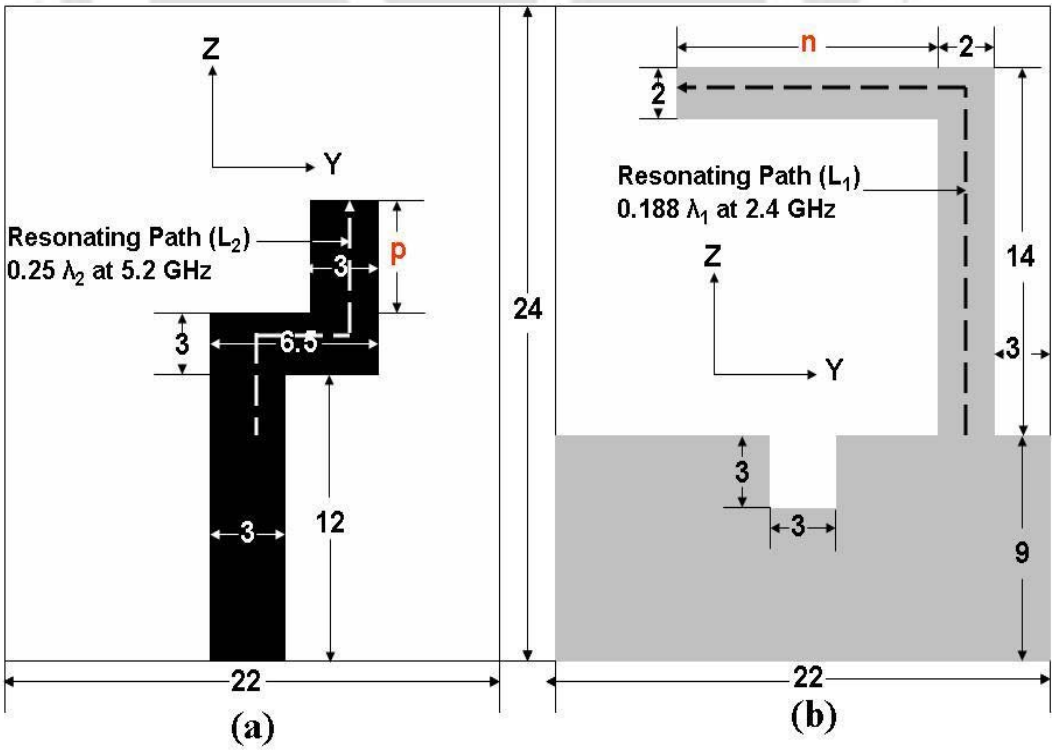

Figure 3.1: Geometry of the proposed antenna **(a)** Top view and **(b)** Bottom view.

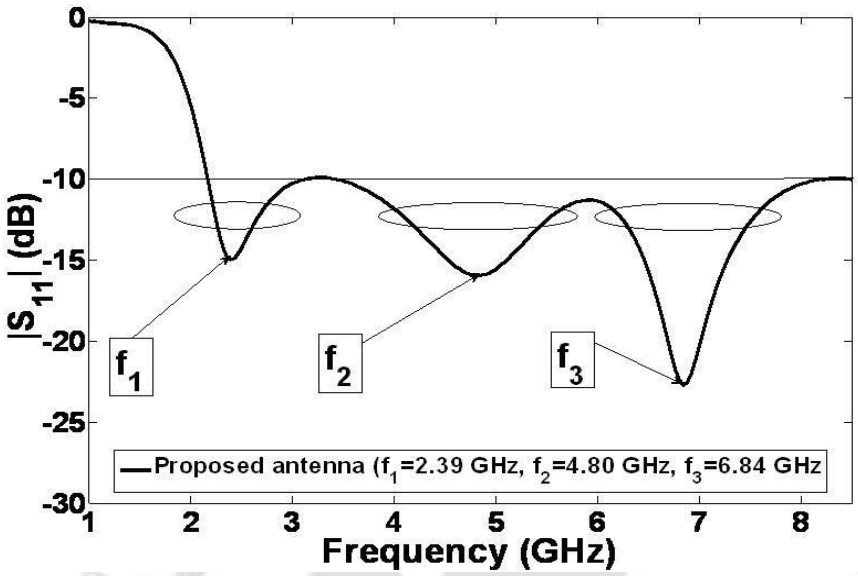

Figure 3.2: Simulated reflection coefficient ($|S_{11}|$) of proposed antenna.

3.3 Simulated and measured results on reflection coefficient ($|S_{11}|$) and the parametric study of the proposed antenna

Simulated reflection coefficient ($|S_{11}|$) of proposed antenna is shown in the Fig. 3.2. The first resonance occurs at f_1=2.39 GHz with the reflection coefficient value of -14.98 dB. The band extends from 2.14 GHz to 3.14 GHz. The percentage bandwidth in this band region is 37.87. The WLAN's 2.4-2.484 GHz band is completely immersed in this band of 2.14 GHz to 3.14 GHz. Apart from this, the WiMAX band from 2.5 GHz to 2.69 GHz can be accommodated in the band range of 2.14 GHz to 3.14 GHz. The second band extends from 3.40 GHz to 8.21 GHz with two resonances at f_2=4.80 GHz (reflection coefficient value of -15.96 dB) and f_3=6.84 GHz (reflection coefficient value of -22.71 dB). Due to these two resonances, a huge band is obtained with the percentage bandwidth of 82.85. The entire WLAN band which extends from 5.15-5.35 GHz and 5.725-5.825 GHZ can be suitably accommodated in this band from 3.40 GHz to 8.21 GHz. WiMAX's other operating band from 3.4 GHz to 3.69 GHz can be easily operate in the band from 3.40 GHz to 8.21 GHz.

When there is no open-ended slot and no inverted L-strip in the ground plane shown in the Fig. 3.3, antenna with only reverse L-shaped radiating element resonates at the center frequency of f_a=5.22 GHz having the reflection coefficient ($|S_{11}|$) value of -24.60 dB shown in the Fig. 3.6. In this case the resonance band extends from 4.35 GHz to 6.19 GHz with percentage bandwidth of 34.91.

When an open ended slot is introduced in the middle top edge of the ground plane and no inverted L-strip in the ground plane shown in the Fig. 3.11, the antenna with reverse L-shaped radiating element resonates with the center frequency of f_{r2b}=5.03 GHz with the reflection coefficient ($|S_{11}|$) value of -34.47 dB shown in the Fig. 3.6. The band extends from 4.14 GHz to 6.14 GHz with the percentage bandwidth of 38.91. Hence, the center of the resonant frequency shifts towards left i.e. the center of the resonant frequency deceases with the introduction of the open ended slot in the middle top edge of the ground plane. Apart from this, the open ended slot in the middle top edge of the ground plane enhances the bandwidth from 34.91 in previous case to 38.91 in the present case.

Now a vertical stub with of length 14 mm (n=0 mm) is protruded out from the right side of the ground plane without 90^0 bending as shown in the Fig. 3.4. At the same time, the open ended slot is present in the middle top edge of the ground plane and the reverse L-shaped radiating structure serves as the radiating element. In this situation, the antenna resonates with the center frequency of f_b=4.12 GHz having the reflection coefficient ($|S_{11}|$) value of -31.34 dB shown in the Fig. 3.6. The length of the vertical stub of length 14 mm is 0.192λ at 4.12 GHz. The band extends from 3.29 GHz to 5.32 GHz having the percentage bandwidth of 47.15. Hence, with the open ended slot and the vertical protruding stub, the center of the resonant frequency shifts towards left rapidly in comparison with the previous case. Apart from this, the percentage bandwidth is also enhanced from 38.91 in the previous case to 47.15 in the present case.

Now the open ended slot is removed from the middle top edge of the ground plane and a 90^0 bend is erected towards left of the vertical protruding stub in the ground plane shown in the Fig. 3.5. This structure in the ground plane is known as the "inverted L-strip". Considerable changes have occurred in the reflection coefficient ($|S_{11}|$) of the antenna. Two prominent bands are created. First band extends from 2.16 GHz to 2.79 GHz (percentage bandwidth=25.45) having the center resonance frequency occurs at f_x=2.39 GHz with the reflection coefficient ($|S_{11}|$) value of -15.14 dB. The second band extends from 4.62 GHz to 7.50 GHz (percentage bandwidth=47.52) with two resonances at f_y=5.29 GHz and f_z=7.03 GHz as shown in the Fig. 3.7.

When all the three structures such as reverse L-shaped radiating element, L-strip in the ground plane and the open ended slot in the middle top edge of the ground plane just behind the microstrip feed-line are present altogether shown in the Fig. 3.1 which is the proposed antenna, remarkable bandwidth enhancement in the two bands is achieved. The percentage bandwidth of the first band

improved from 25.45 to 37.87. The first band extends from 2.14 GHz to 3.14 GHz (percentage bandwidth=37.87) with the center frequency occurred at f_1=2.39 GHz with the reflection coefficient ($|S_{11}|$) value of -14.98 dB. Now the bandwidth of the second band extends from 3.40 GHz to 8.21 GHz with the percentage bandwidth of 82.85. In this band, two clear resonances are visible at f_2=4.80 GHz and f_3=6.84 GHz with the reflection coefficient ($|S_{11}|$) values of -15.96 dB and -22.71 dB respectively.

Due to the presence of the open-ended slot in the middle top edge of the ground plane the bandwidth has improved from 47.52 to 82.82 as depicted in Fig. 3.7. The reason for the huge bandwidth improvement is due to the proper impedance matching between the feed-line and the radiating element in the frequency range of 3.40 GHz to 8.21 GHz.

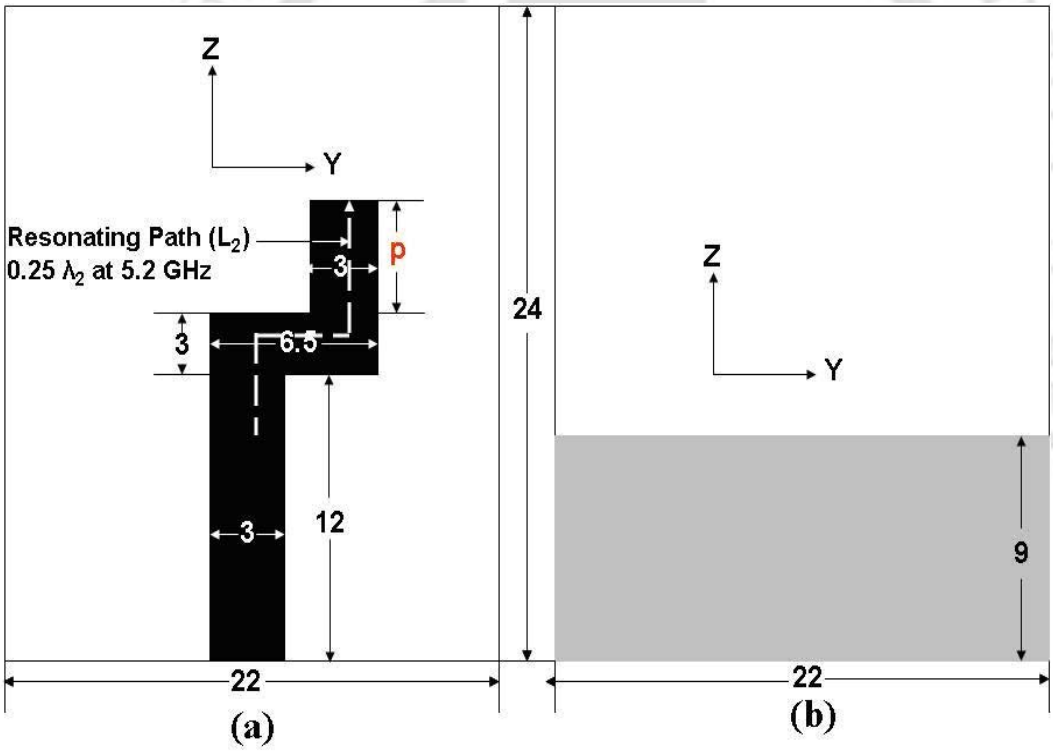

Figure 3.3: Geometry of the structure having reverse L-shaped radiating element with absence of reverse L-strip and open-ended slot in the middle top edge of the ground plane **(a)** Top view and **(b)** Bottom view.

Fig. 3.8 shows the parametric studies performed by varying the lengths of different components of the proposed antenna. In fig 3.8(a), the length n of the upper arm of the inverted L-strip on the ground plane is varied when all the other parameters are kept constant. When the length n is increased from 7.5 mm to 11.5 mm, the first resonance frequency (f_1) moved towards left from 2.80 GHz to 2.01 GHz, which is 28.14% resonant frequency shift towards left. In other words the f_1 decreases with the increase of length n. On the other hand, the third resonance frequency (f_3) also decreases from 7.29

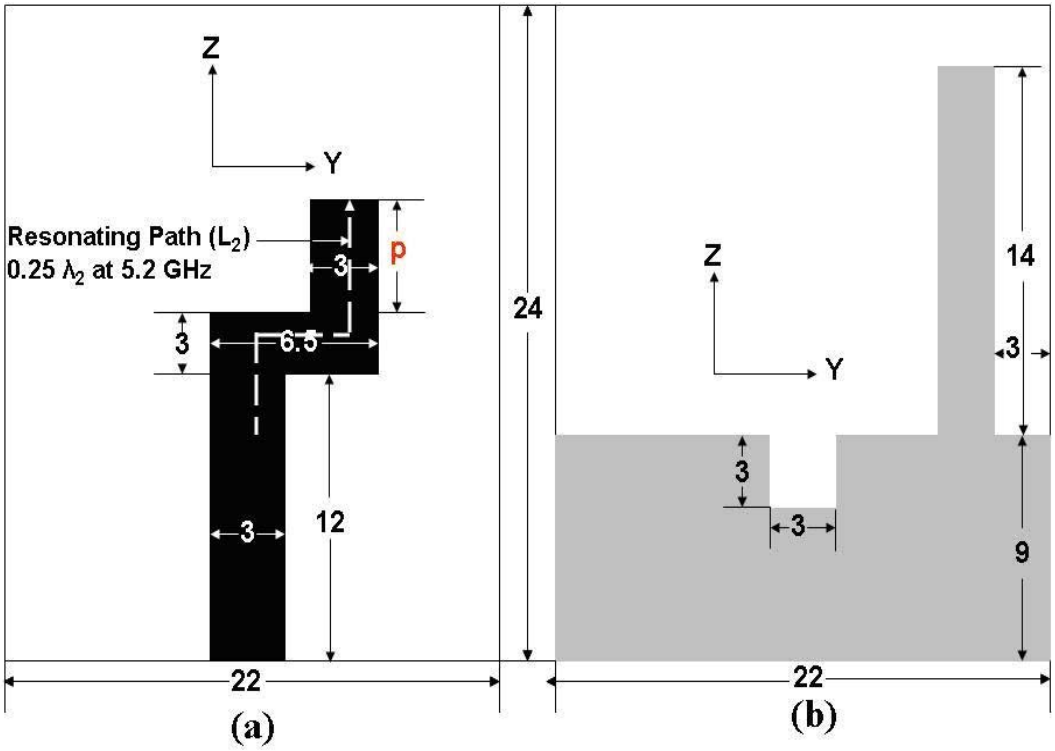

Figure 3.4: Geometry of the structure having reverse L-shaped radiating element with a vertical strip (n=0) and open-ended slot in the middle top edge of the ground plane **(a)** Top view and **(b)** Bottom view.

GHz to 6.23 GHz with the increase of length n from 7.5 mm to 11.5 mm, which is 14.54% shift of resonant frequency towards left. But the middle activated resonance frequency f_2 moves towards right with the increase of length n. That means the second resonance frequency increases from 4.56 GHz to 5.14 GHz, which is 9.53% resonant frequency shift towards right with the increase of length n. As this resonance frequency is situated in between the first and third resonance frequency, the movement of the middle resonance frequency is effected by the movement of resonance frequencies of f_1 and f_3.

Fig. 3.8(b) shows the variation upper vertical length p of the reverse L-shaped radiating element when all the other parameters are kept constant. When the length p is increased from 3 mm to 7 mm, the first resonance frequency (f_1) moved towards left from 2.54 GHz at p=4 mm to 1.94 GHz at p=7 mm, which is 23.62% resonant frequency shift towards left. In other words the f_1 decreases with the increase of length p. But when p=3 mm, there is no resonance. As the p increases, the strong resonances are building up from 2.54 GHz to 1.94 GHz. On the other hand, the second resonance frequency (f_2) also decreases from 5.10 GHz at p=3 mm to 4.73 GHz at p=6 mm, which is 7.25% resonant frequency shift towards left. But when p=7 mm, the performance is degraded as there is no

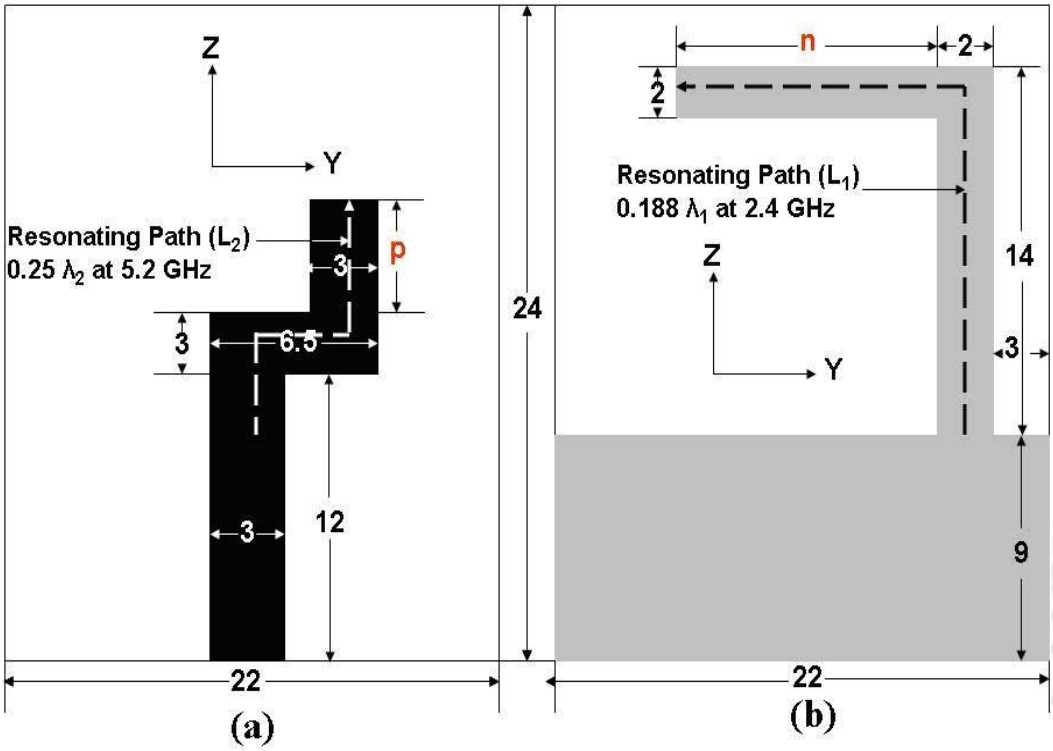

Figure 3.5: Geometry of structure having reverse L-shaped radiating element with reverse L-strip in the ground plane and the absence of open-ended slot in the middle top edge of the ground plane **(a)** Top view and **(b)** Bottom view.

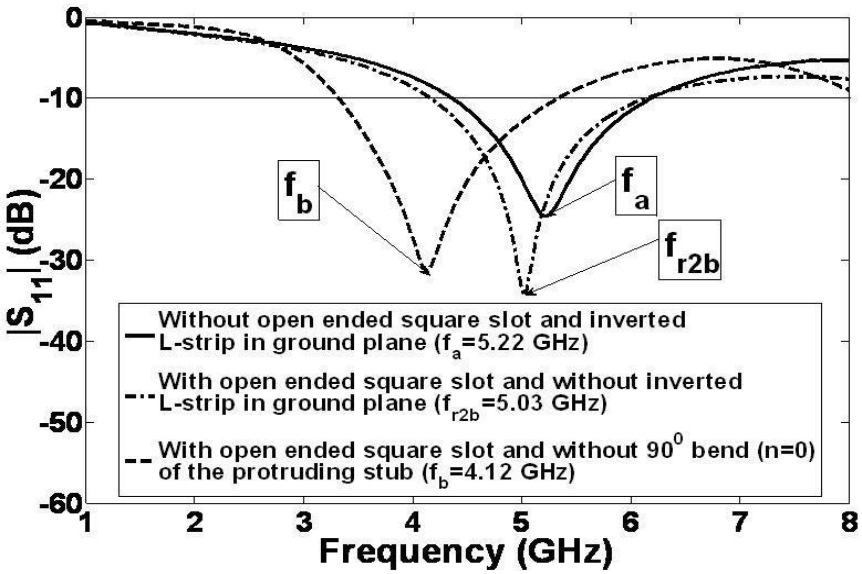

Figure 3.6: Comparison of simulated reflection coefficients ($|S_{11}|$) of the radiating elements shown in the Fig. 3.3, Fig. 3.11 and Fig 3.4.

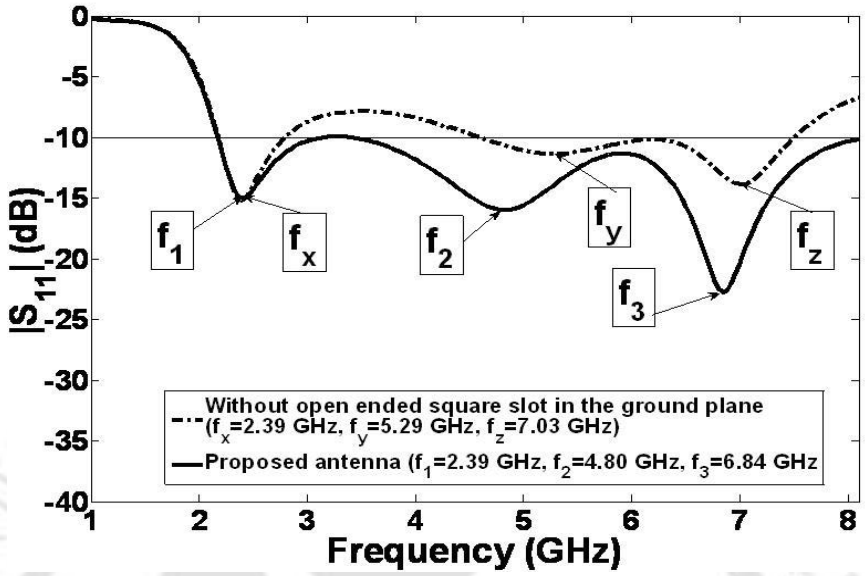

Figure 3.7: Comparison of simulated reflection coefficients ($|S_{11}|$) of the radiating elements shown in the Fig. 3.1 and Fig. 3.5.

resonance at p=7 mm. But the third resonance frequency f_3 moves towards right with the increase of length p from 6.72 GHz to 6.91 GHz, which is 2.74% shift in resonant frequency towards right. That means the third resonance frequency increases with the increase of length p.

When there is no open ended slot in the middle top edge of the ground there also occurs three resonances at f_x=2.39 GHz, f_y=5.29 GHz and f_z=7.03 GHz. But the second band extends from 4.62 GHz to 7.50 GHz (percentage bandwidth=47.52) with two resonances at f_y=5.29 GHz and f_z=7.03 GHz. But on the introduction of a square open ended slot with width and height of 3 mm, the second bandwidth is improved considerably and the bandwidth of the second band extends from 3.40 GHz to 8.21 GHz with the percentage bandwidth of 82.85 with two resonances at f_2=4.80 GHz and f_3=6.84 GHz.

Table 3.1 explains in the tabular form the comparative study performed on the proposed antenna with the existing antennas for application in WLAN system in the literatures regarding size, band, percentage bandwidth and gain. The proposed antenna is considerably better in many aspects as compared to the existing antennas in the literature.

Fig. 3.9 shows the fabricated prototype of the proposed antenna. The reflection coefficient ($|S_{11}|$) of the proposed antenna is measured with the help of Rohde and Schwarz ZVA24 vector network analyzer. Fig. 3.10 shows the comparison of simulated and measured reflection coefficients ($|S_{11}|$) of

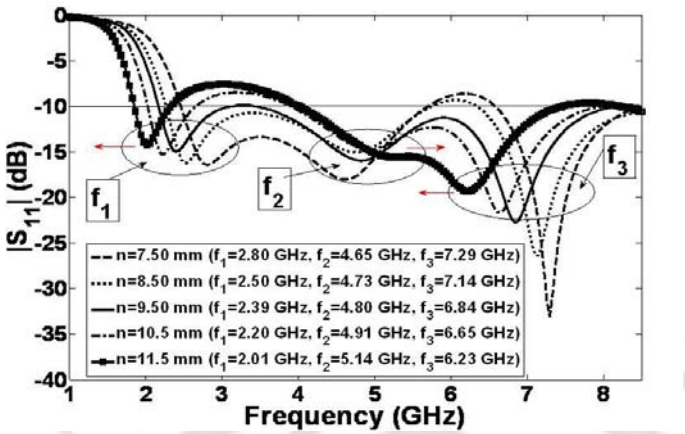

(a)

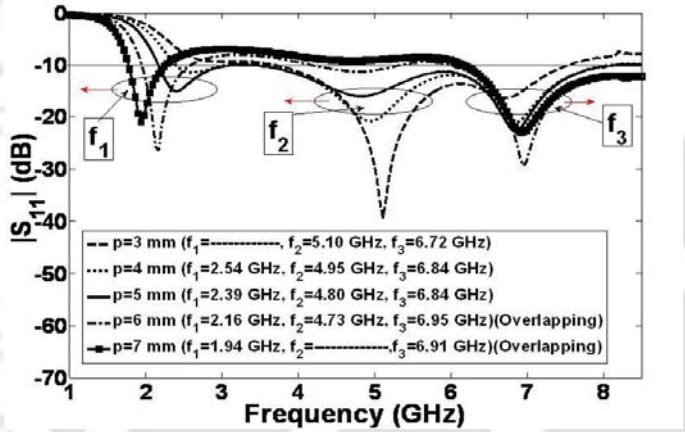

(b)

Figure 3.8: Simulated reflection coefficient ($|S_{11}|$) (dB) graphs, **(a)** n is a variable, p=5 mm and **(b)** p is a variable, n=9.5 mm.

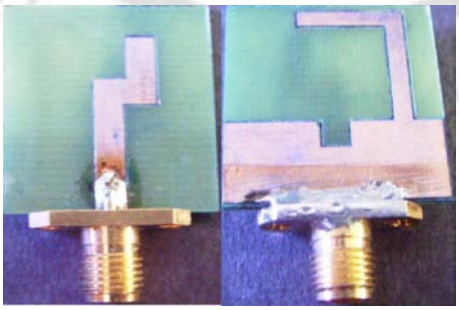

Figure 3.9: Fabricated prototype of the proposed antenna.

the proposed antenna. From the graph, it is clear that there is close matching between the simulated and measured results.

Table 3.1: Comparative study for the proposed antenna with the existing antennas

	Size (mm^2)	Band 1 (GHz)	Band 2 (GHz)	% BW at Band 1	% BW at Band 2	Gain (dBi)
This work	22×24=528	(2.14-3.14)	(3.40-8.21)	37.87	82.85	1.39-3.20 and 1.88-3.15
[133]	28×20=560	(2.36-2.58)	(4.53-6.38)	08.90	33.91	2.03 and 3.04
[134]	15×40=600	(2.25-2.46)	(4.40-7.38)	09.20	50.70	1.25-1.35 and 3.50-4.50
[135]	24×25=600	(2.06-2.43)	(3.73-7.86)	16.48	71.26	1.66 and 4.59
[136]	50×15=750	(2.38-2.53)	(4.28-6.03)	06.42	32.00	1.75-2.06 and 3.13-3.76
[137]	25.5×28.5=812.25	(2.07-2.45)	(4.15-8.73)	17.00	79.00	1.50-2.80 and 2.00-6.20
[138]	22×45=990	(2.10-2.65)	(5.15-6.10)	23.15	16.88	2.00 and 3.40-4.00
[139]	32×34=1088	(2.32-3.03)	(4.77-6.33)	26.54	28.10	2.70-3.30 and 1.90-5.10
[140]	40×45=1800	(2.34-2.54)	(4.87-5.98)	08.42	20.43	1.80-2.50 and 4.20-5.00
[141]	37×51.55=1907.35	(2.28-2.62)	(4.52-6.00)	13.87	28.13	2.50-3.10 and 2.50-4.10
[142]	54×52=2808	(1.80-2.53)	(6.04-4.94)	33.71	20.03	3.40-4.00 and 8.60-9.20

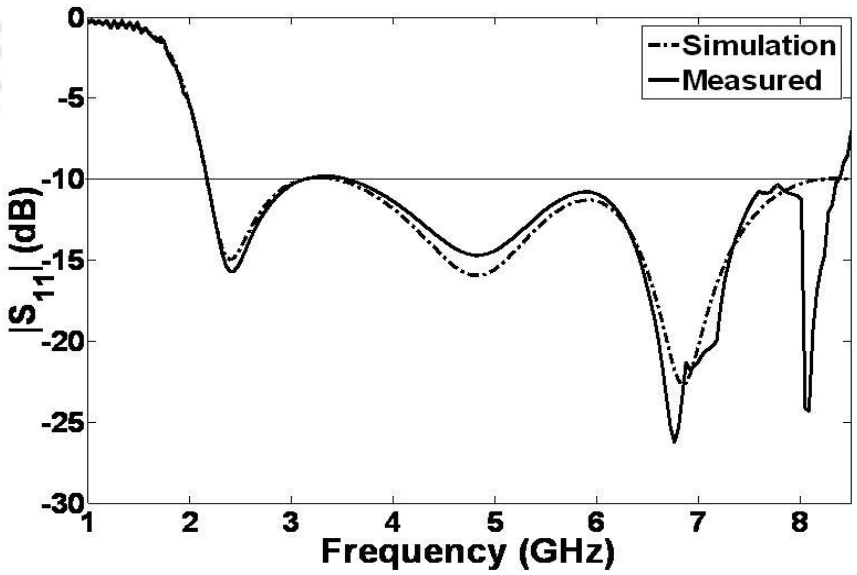

Figure 3.10: Comparison of simulated and measured reflection coefficients ($|S_{11}|$) of the proposed antenna.

3.4 Effect of double bend on the the proposed antenna performance

3.4.1 Bending analysis on reverse L-shaped radiating element with the presence of a square open ended slot in top middle edge of ground plane

Bending analysis is performed on the reverse L-shaped radiating element which consists of two 90^0 bends. At the same time no L-strip is present in the ground plane. An open ended slot is present in the middle top edge of the ground plane for the purpose of bandwidth enhancement.

In the first case, reverse L-shaped radiating element with two 90^0 bends is simulated which is the second resonating path (L_2) ($0.25\lambda_2$) at 5.2 GHz. The structure is shown in the Fig. 3.11. After simulation, it is found that the structure resonates at f_{r2b}=5.03 GHz with the reflection coefficient value of -34.47 dB. The reflection coefficient graph is shown in the Fig. 3.14.

For the second case, the second 90^0 bend is unfolded and the structure is shown in the Fig. 3.12. After simulation, the reflection coefficient graph shows one resonance at f_{r1b}=4.76 GHz with the reflection coefficient value of -12.99 dB is shown in the Fig. 3.14. From the graph, it is clear that with one bend, the resonant frequency is decreased or shifted left of the resonant frequency for the case of two 90^0 bends of same length.

In the third case, the single 90^0 bend is unfolded and the radiating element is made linear of same length ($0.25\lambda_2$ at 5.2 GHz) as that of the two 90^0 bend radiating element, which is shown in the Fig. 3.13. The structure is simulated. After simulation, it is found that the linear structure resonates at f_{rL}=4.50 GHz with the reflection coefficient value of -16.19 dB which is shown in the Fig. 3.14. From the graph, it is clear that the resonating frequency for the case of linear structure is decreased or shifted left of the resonating frequency occurred for the case of single 90^0 bend structure.

Hence, from the above bending analysis it is clear that, with the increase of 90^0 bend bends in the radiating element, the resonating frequency of the subsequent bends increases [110] or shift towards right in the reflection coefficient graph. Apart from this, the bending enhances the resonance quality of the resonating structure by providing deep resonances and also helps in tuning the resonant frequency in the desired application range.

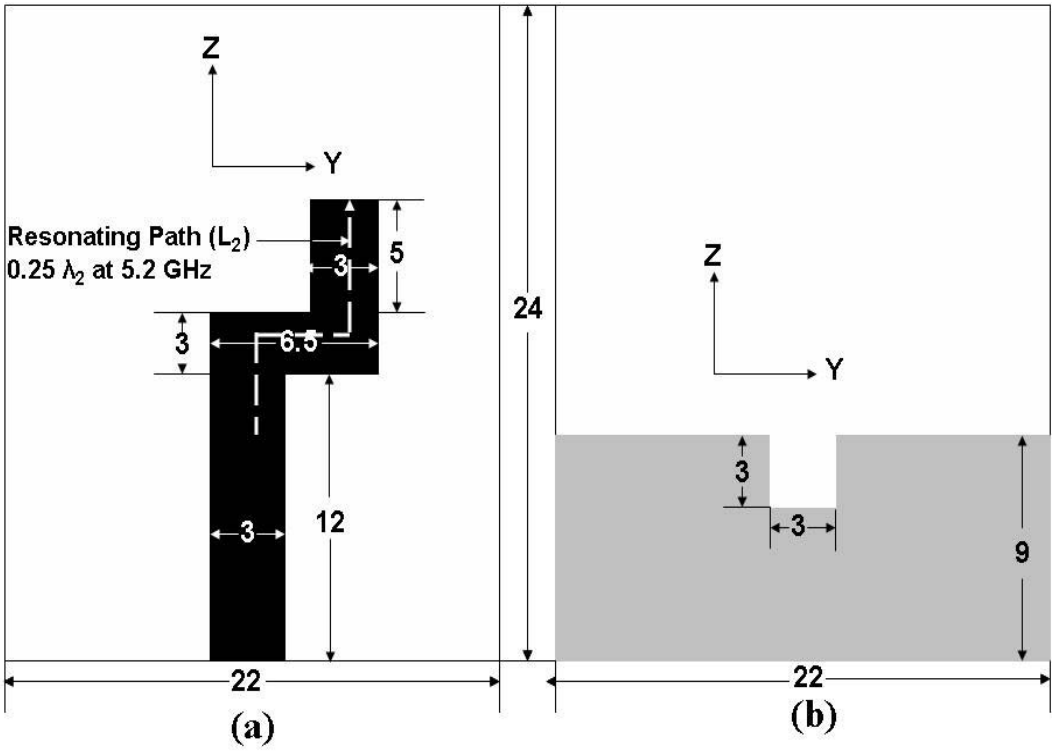

Figure 3.11: Geometry of the structure with two 90^0 bends in radiating element and an open ended slot in the middle top edge of the ground plane **(a)** Top view and **(b)** Bottom view.

3.4.2 Bending analysis on reverse L-shaped radiating element with presence of an inverted L-strip and a square open ended slot in top middle edge of ground plane

Bending analysis is performed on the reverse L-shaped radiating element with the presence of inverted L-strip in the ground plane and an open ended square slot on the tip middle edge of the ground plane.

First case is the proposed antenna in which two 90^0 bends are present in the reverse L-shaped radiating element and there exists an inverted L-strip along with an open ended square slot in the top middle edge of the ground plane which is nothing but the proposed antenna. The radiating element is the second resonating path which is $0.25\lambda_2$ at 5.2 GHz. On simulation, three resonances are visible in the graph shown in the Fig. 3.17 with the center frequencies of f_1=2.39 GHz, f_2=4.80 GHz and f_3=6.84 GHz as resonances at f_2 and f_3 are merged together to provide a huge band from 3.40 GHz to 8.21 GHz.

In the second case, one 90^0 bend is unfolded in the radiating element keeping the same resonating length ($0.25\lambda_2$ at 5.2 GHz) as previous case and the structure is shown in the Fig. 3.15. On simulation

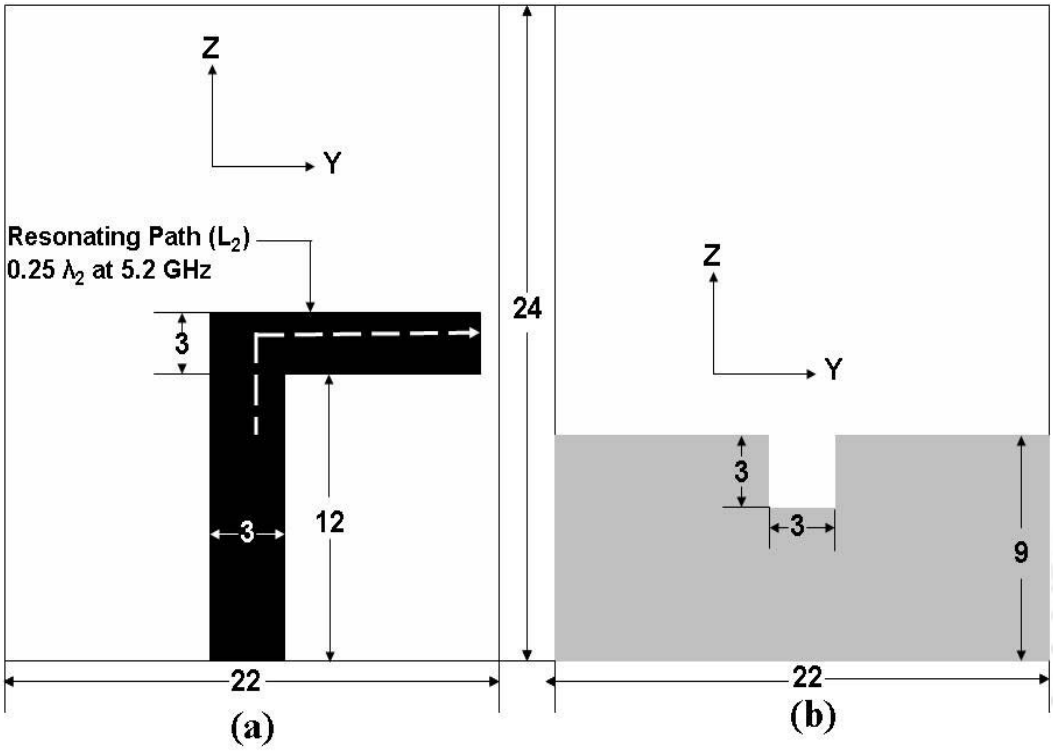

Figure 3.12: Geometry of the structure with one 90^0 bend in radiating element and an open ended slot in the middle top edge of the ground plane **(a)** Top view and **(b)** Bottom view.

two resonances are visible with the center frequencies of f_L=4.20 GHz and f_M=6.72 GHz which is shown in the Fig. 3.17. There is no first resonance at the lower frequency region but a small resonance tendency is visible (at f_K) in the reflection coefficient ($|S_{11}|$) shown in the Fig. 3.17. In this case, both the resonant frequencies of f_L and f_M are reduced or shifted to left with comparison of the first case consisting of two 90^0 bends in the radiating element.

In the third case, one 90^0 bend in the radiating element of the previous case is unfolded to a linear radiating element of same resonating length ($0.25\lambda_2$ at 5.2 GHz) as before which is shown in the Fig. 3.16 and all other structures in the ground plane are same as before. In this condition after simulation, the structure resonates only at f_R=6.72 GHz, which is same as previous case as shown in the Fig. 3.17. The occurrence of the third resonance frequency is remain unaltered as compared to previous case with one 90^0 bend in the radiating element. There is no resonance at f_P and f_Q region but some resonance tendencies are visible at f_P and f_Q region.

Hence, from the above analysis it is clear that less 90^0 bend in the radiating element produces lower resonant frequencies as compared to its more 90^0 bend resonating element counterpart. Apart from

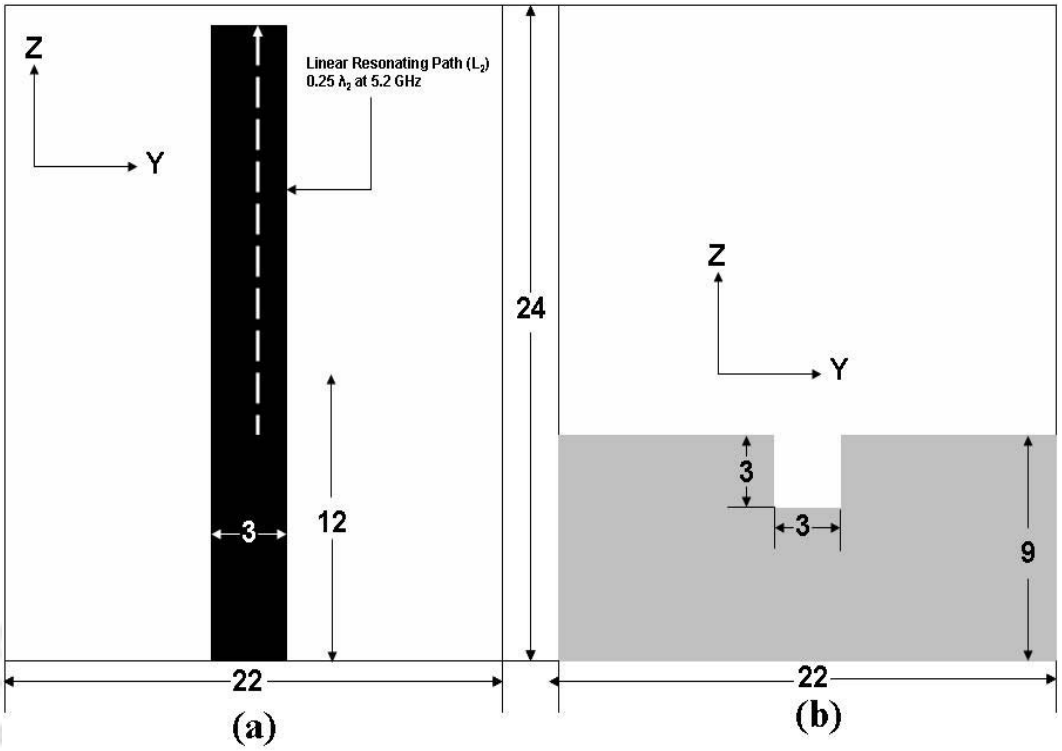

Figure 3.13: Geometry of the structure with a linear radiating element and an open ended slot in the middle top edge of the ground plane**(a)** Top view and **(b)** Bottom view.

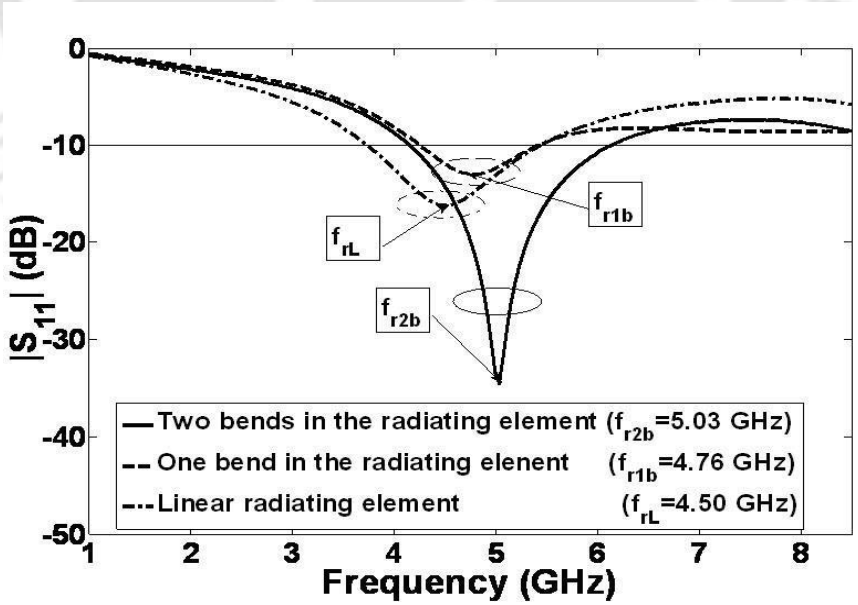

Figure 3.14: Comparison of simulated reflection coefficients ($|S_{11}|$) of the radiating elements with two 90^0 bends, one 90^0 bend and a linear structure consisting of a open ended slot in the middle top edge of the ground plane.

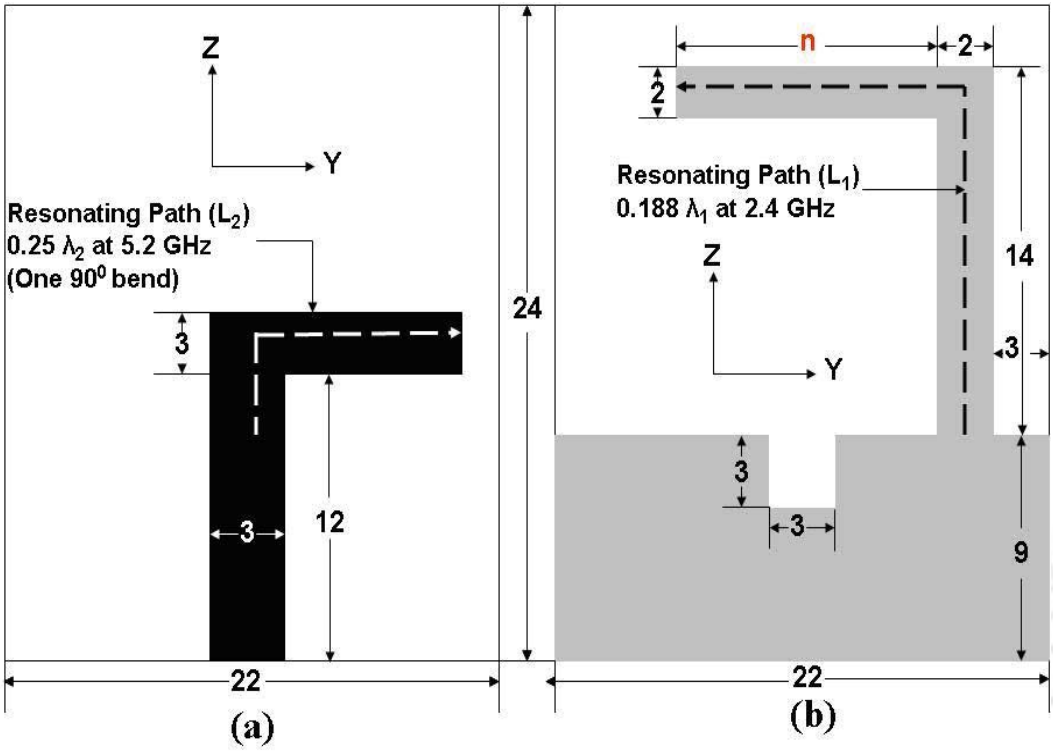

Figure 3.15: Geometry of the structure with one 90^0 bend in radiating element with inverted L-strip and an open ended slot in the middle top edge of the ground plane **(a)** Top view and **(b)** Bottom view.

this it is apparent that the more 90^0 bends in the radiating element improve the antenna resonating characteristics and also bandwidth requirement in the desired frequency range.

3.4.3 Bending analysis on inverted L-strip in ground plane with presence of a reverse L-shaped radiating element and a square open ended slot in top middle edge of ground plane

Now the bending analysis is performed on the protruded L-strip (resonating path L_1=0.188λ_1 at 2.40 GHz) in the ground plane. When there is L-strip with one 90^0 bend in the ground plane along with the reverse L-shaped radiating element (proposed antenna), the antenna resonates at three resonant frequencies i.e. atf_1 =2.39 GHz, f_2=4.80 GHz and f_3=6.84 GHz

Now the L-strip in the ground plane is unfolded and is made linear of same length as the L-strip, which is shown in the Fig. 3.18 and the structure is simulated. The simulated reflection coefficient graph is shown in the Fig. 3.19. There is one resonance $f_{1Linear}$ =4.46 GHz is visible in the graph. The $f_{1Linear}$=4.46 GHz is right shifted version of f_1=2.39 GHz when strip is 90^0 bend (L-strip). Similarly other two resonant frequencies are shifted considerably right of f_2 and f_3 and occurred at $f_{2Linear}$

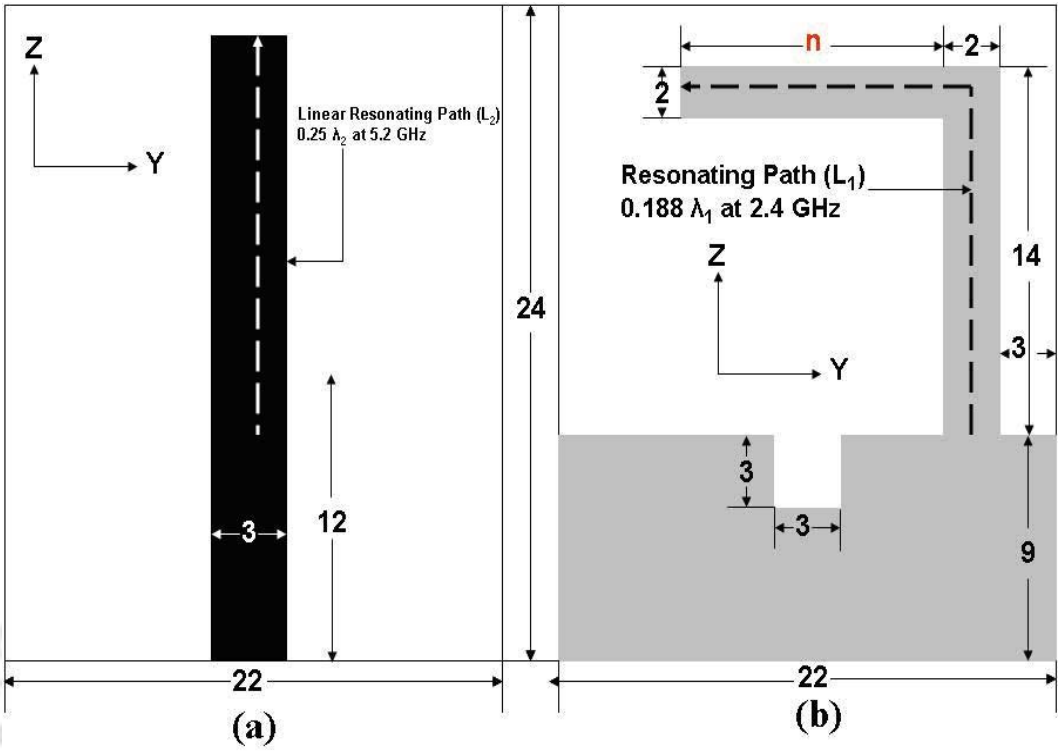

Figure 3.16: Geometry of the structure with a linear radiating element with an inverted L-strip and an open ended slot in the middle top edge of the ground plane **(a)** Top view and **(b)** Bottom view.

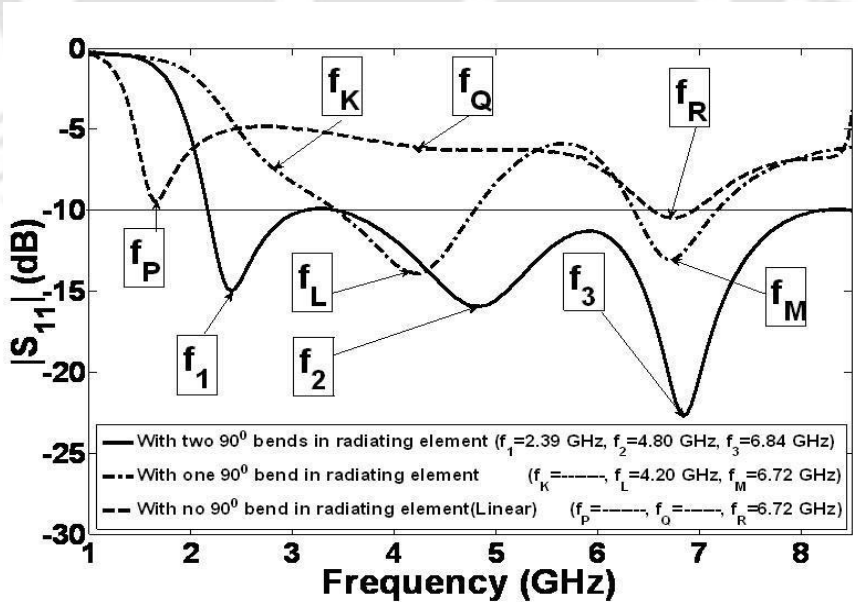

Figure 3.17: Comparison of simulated reflection coefficients ($|S_{11}|$) of the radiating elements with two 90^0 bends, one 90^0 bend and a linear structure consisting of inverted L-strip and an open ended slot in the middle top edge of the ground plane.

=9.47 GHz and $f_{3Linear}$ =14.11 GHz, which is shown in the Fig. 3.20.

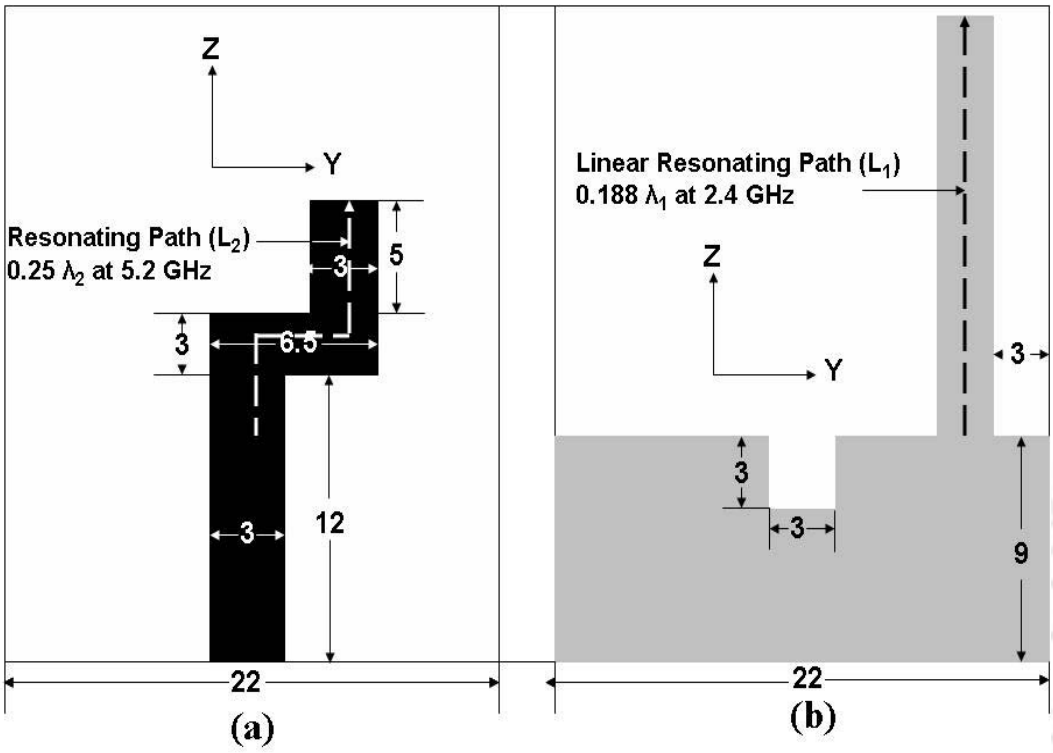

Figure 3.18: Geometry of the structure with a vertical strip in the ground plane consisting of reverse L-shaped radiating element and an open ended slot in the middle top edge of the ground plane.

The bending analysis is performed for both the cases of reverse L-shaped radiating element (two 90^0 bends) with an open ended slot in the middle top edge of the ground plane (L-strip is absent in ground plane) and L-strip in the ground plane with the presence of reverse L-shaped radiating element with an open ended slot in the middle top edge of the ground plane. From the study, it is clear that the bending put opposite effect on the resonating frequency in radiating element and L-strip in the ground plane. When bending analysis is performed on the reverse L-shaped radiating element only with two 90^0 bends, the resonating frequency is shifted to a higher value as compared with one 90^0 bend in radiating element and its linear counterpart of same length. Apart from this, with bending in the radiating element, the resonance becomes stronger than the linear case. But when bending analysis is performed on the L-strip in the ground plane with the presence of reverse L-shaped radiating element, the resonating frequencies are shifted to considerably higher values with linear strip in the ground plane as compared to its 90^0 bend L-strip counterpart of same length.

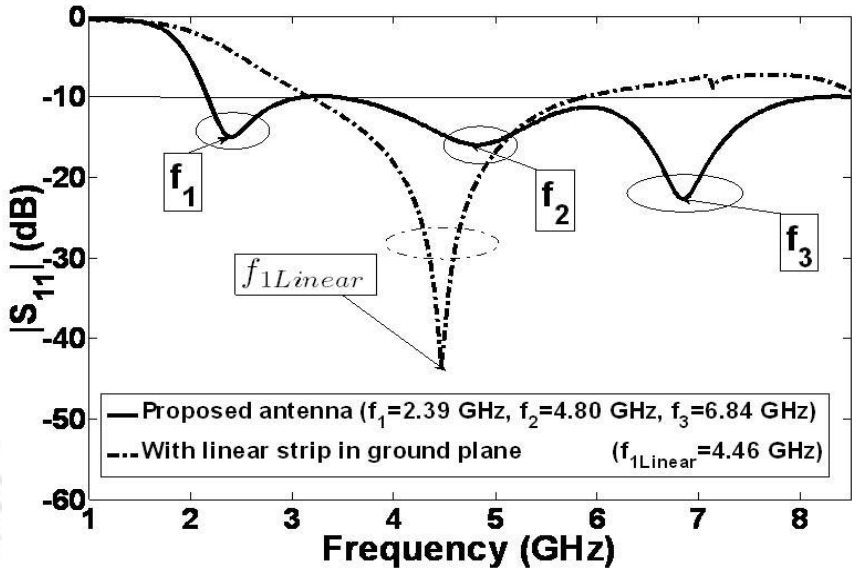

Figure 3.19: Comparison of simulated reflection coefficients ($|S_{11}|$) of proposed antenna with the radiating structure having a linear vertical strip in ground plane consisting of a reverse L-shaped radiating element and an open ended slot in the middle top edge of the ground plane (1-8.5 GHz range).

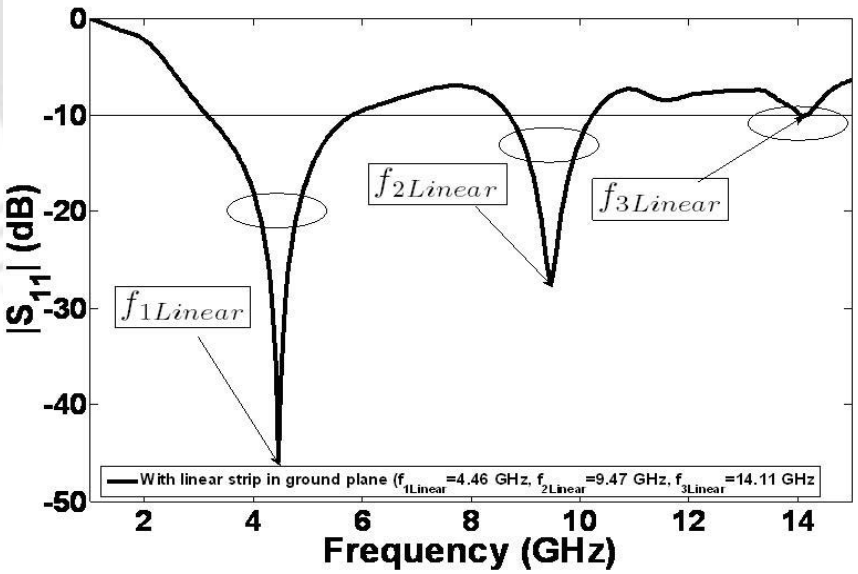

Figure 3.20: Simulated reflection coefficient ($|S_{11}|$) of the radiating structure having a linear vertical strip in ground plane consisting of a reverse L-shaped radiating element and an open ended slot in the middle top edge of the ground plane (1-15 GHz range).

3.5 Gain of the proposed antenna

The simulated gain in the range of 2.14 GHz-3.14 GHz varies from 1.33 dBi to 3.10 dBi. The value of simulated gain at 2.39 GHz is 1.88 dBi. Similarly, the simulated gain in the range of 3.40 GHz-8.21

GHz varies from 1.75 dBi to 3.15 dBi. The value of simulated gain at 5.2 GHz and 5.8 GHz are 3.35 dBi and 3.00 dBi respectively.

The measured gain in the range of 2.14 GHz-3.14 GHz varies from 1.39 dBi to 3.2 dBi. The value of measured gain at 2.39 GHz is 1.75 dBi, which is sufficient for the operation in WLAN 2.4-2.484 GHz system satisfactorily. Similarly, the measured gain in the range of 3.40 GHz-8.21 GHz varies from 1.88 dBi to 3.15 dBi. The value of measured gains at 5.2 GHz and 5.8 GHz are 3.37 dBi and 3.05 respectively, which is sufficient for the operation in 5.15 GHz-5.35 GHz and 5.725 GHz-5.825 GHz WLAN system satisfactorily. Fig. 3.21 shows comparison of simulated and measured gain (dBi) vs. frequency of the proposed antenna in 2.14 GHz-3.14 GHz and 3.4 GHz-8.2 GHz range.

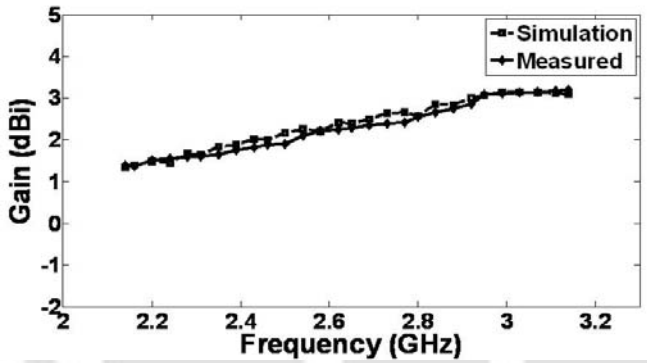

(a)

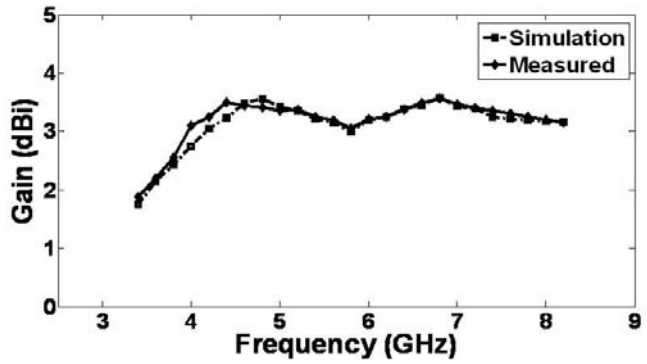

(b)

Figure 3.21: **(a)** Comparison of simulated and measured gain (dBi) vs. frequency of the proposed antenna (2.14 GHz-3.14 GHz) and **(b)** Comparison of simulated and measured gain (dBi) vs. frequency of the proposed antenna (3.4 GHz-8.2 GHz).

3.6 Surface current distribution of proposed antenna

At 2.4 GHz, the current direction is upward in the reverse L-shaped radiating element. The magnitude of surface current density is high at the bottom region of the microstrip feed-line and at the lower edges of the reverse L-shaped radiating element. As usual the ground plane provides the return path of the surface current. Since the high current density is present on the reverse L-shaped radiating element, it radiates effectively as the impedance matching is proper and provides the huge bandwidth from 3.40 GHz to 8.21 GHz. Apart from this the presence of the open ended square slot on the middle top edge of the ground plane provides the extra current path for return of the surface current and helps in proper impedance matching. The reverse L-shaped radiating element is designed for radiation in 5.2 GHz. But at the same time current density is moderate on the inverted L-shaped strip on the ground plane. Since the current density is moderate on the inverted L-shaped radiating element, moderate resonance occurred at 2.4 GHz band. As the current density is low on the inverted L-shaped strip in the ground plane, the strong radiation and resonance is due to the reverse L-shaped radiating element. The magnitude of the surface current density at 2.4 GHz is shown in Fig. 3.22 (a).

At 5.2 GHz, the scenario is different from that at 2.4 GHz. Current flow from top to bottom on the reverse L-shaped radiating element. But at 5.2 GHz, the density of the surface current is relatively high in horizontal portion of the inverted L-shaped strip in the ground plane. As the current density is relatively sufficient in both the reverse L-shaped radiating element and inverted L-shaped strip in the ground plane, strong resonances occur in both the 2.4 GHz band region and 5.2 GHz band region. Apart from this the presence of the open ended square slot on the middle top edge of the ground plane provides the extra current path for return of the surface current and helps in proper impedance matching. Very high current flows on the edges of the open ended square slot on the middle top edge of the ground plane. This might be the reason for enhancement of the bandwidth and proper impedance matching when the open ended stub is present on the middle top edge of the ground plane. Fig. 3.22 (a) and Fig 3.22 (b) shows the magnitude of the surface current density at 2.4 GHz and 5.8 GHz respectively.

3.7 Radiation pattern of the proposed antenna

The measured normalized co-polarized and cross-polarized E-plane (yz-plane) and H-plane (xy-plane) radiation patterns of the proposed monopole antenna at 2.4 GHz and 5.2 GHz are shown in the

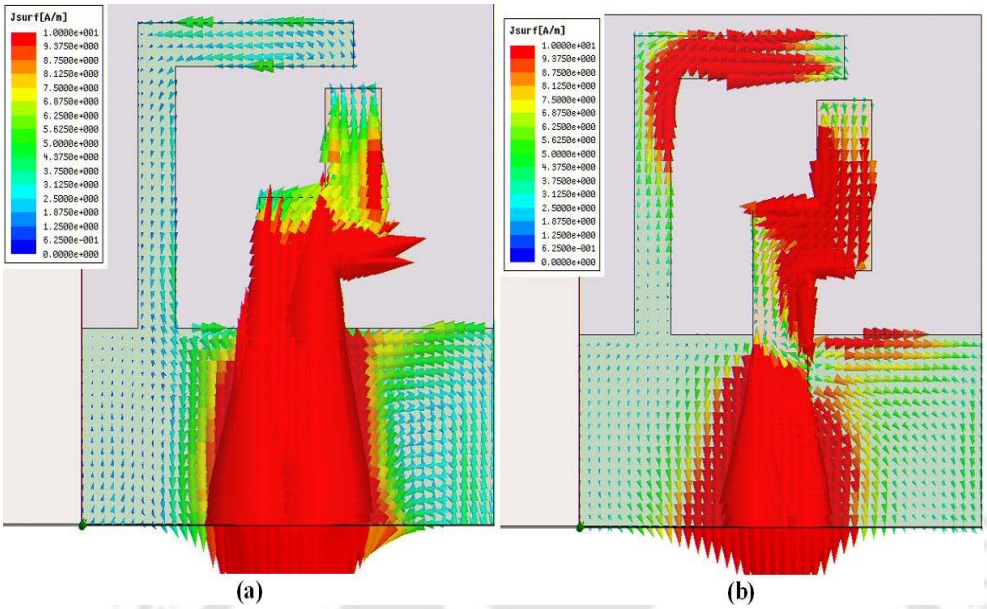

Figure 3.22: Direction and magnitude of the surface current distribution for the inverted L-shaped PMA with an inverted L-strip in the ground plane **(a)** at 2.4 GHz and **(b)** at 5.2 GHz.

Fig. 3.23 and Fig. 3.24 respectively. It can be observed that the co-polar E-plane radiation pattern is of the shape of "8" at 2.4 GHz and 5.2 GHz approximately. At 2.4 GHz and 5.2 GHz, the E-plane cross-polar radiation patterns are in between -20 and -30 dB. The co-polar H-plane radiation pattern on the other hand is purely omni-directional at the two frequencies i.e. at 2.4 GHz and 5.2 GHz. At 2.4 GHz, the H-plane cross-polar radiation pattern is approximately -20 dB and H-plane cross polarization level is in between -20 and -30 dB at 5.2 GHz.

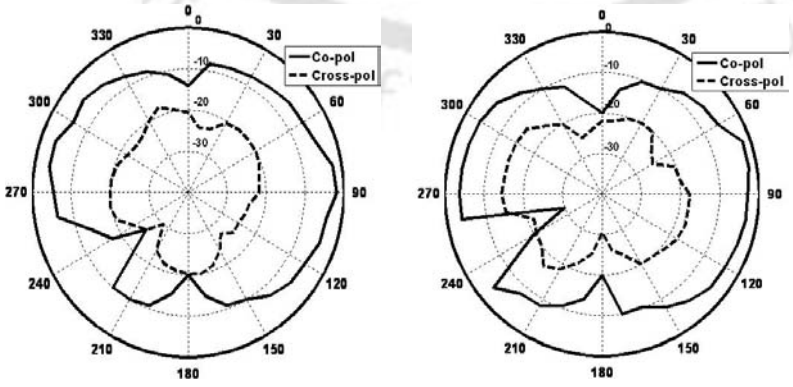

Figure 3.23: Measured E-plane (yz-plane) radiation patterns of the proposed antenna at **(a)** 2.4 GHz and **(b)** 5.2 GHz.

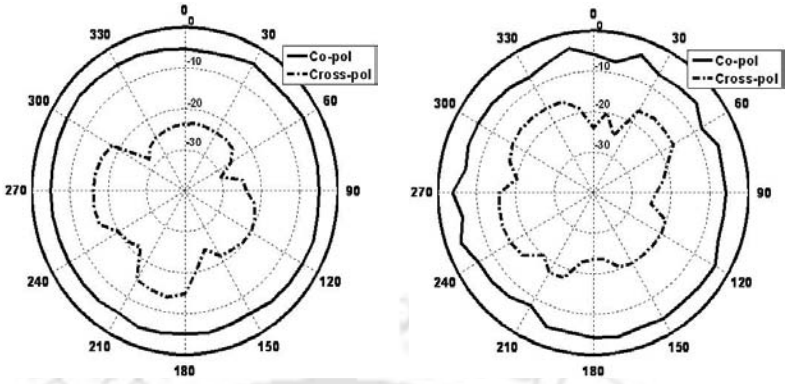

(a) (b)

Figure 3.24: Measured H-plane (xy-plane) radiation patterns of the proposed antenna at **(a)** 2.4 GHz and **(b)** 5.2 GHz.

3.8 Summary

In this chapter, a new double bend compact and simple PMA is presented. The geometry of the antenna comprises of a reverse L-shaped radiating element and an inverted L-strip is protruding out from the right side of the ground plane. Two resonant paths are created so that that proposed antenna can resonate at two simultaneous resonant frequencies for the application in WLAN application. The proposed antenna provides the considerable bandwidths so that the antenna can be suitably used in the wireless domain. The proposed antenna is a dual-band monopole antenna with sufficient bandwidth in which the whole of the WLAN application band can be easily accommodated. Apart from this, the proposed antenna has appropriate gain and radiation characteristics for the application in WLAN domain. This new antenna attains 5.71 percent size reduction, 64.53 percent average bandwidth improvement when compared to contemporary dual-band PMAs [133] but the improvement of gain is not considerable when compared to above PMA.

4

Triple bend 9-shaped PMA

Contents

4.1 Introduction 98
4.2 Antenna design 98
4.3 Simulated and measured results on reflection coefficient ($|S_{11}|$) and the parametric study of the proposed antenna 100
4.4 Effect of triple-bend on the proposed antenna performance 105
4.5 Gain of the proposed antenna 109
4.6 Surface current distribution of proposed antenna 109
4.7 Radiation pattern of the proposed antenna 111
4.8 Summary 112

4.1 Introduction

Compact printed monopole antennas are indispensable candidates for applications in WLAN, UWB and RFID. Along with the small size, the antenna should preferably be low cost, light weight, less fragile and low profile. Besides, the fabrication methodology should be simple. Many compact printed monopole antennas are reported in the literature for wireless applications. Notable structures among them are: CPW-fed dual frequency monopole antenna [143], dual band CPW-fed strip-sleeve monopole antenna [144], CPW fed L-shaped slot planar monopole antenna for triple band operation [145], internal planar monopole antenna for mobile phones [146], dual-band planar branched monopole antenna [147], etc. Similarly, many compact printed antennas for RFID application at 5.8 GHz are available in the literature such as CPW-fed dual folded strip [148]. In [149], a dual band monopole antenna with stagger-tuned arm was proposed, where the antenna resonates at 2.45 GHz and 5.8 GHz, which was solely meant for the application in WLAN domain. Our intention here is to design a compact monopole antenna, which can be used simultaneously for WLAN as well as RFID (2.4 to 2.4835 GHz) systems.

In this chapter, a new compact, 9-shaped dual-band printed monopole antenna is presented for RFID and WLAN. The geometry of this proposed antenna has three bends in its radiating element. Hence this proposed antenna belongs to the category of triple bend PMA. This antenna simultaneously resonates at 2.54 GHz and 5.13 GHz, which are the operating frequency bands for RFID and WLAN systems respectively. It allows us to use a single antenna for both the RFID and WLAN systems. The antenna is constructed on a non-conductor backed dielectric. 9-shaped strip is printed on one side of it, which is fed by a microstrip line. The dual-band performance can be easily obtained for this type of antenna by fine-tuning the lengths of the 9-shaped strip.

4.2 Antenna design

Fig. 4.1 shows the geometry of the proposed 9-shaped printed monopole antenna for RFID and WLAN applications. The shape of the radiating element of the proposed monopole antenna looks like an English number “Nine”. That’s why the name of the proposed antenna is “9-shaped antenna”. The 9-shaped monopole antenna is printed on a FR4 substrate of relative permittivity 4.4 and thickness 1.6 mm as shown in Fig. 4.1. A 50-Ω microstrip line is used for the excitation. The strip width of the 9-shaped monopole antenna is 3.06 mm, same as that of the width of the microstrip feed line.

The proposed antenna has 9-shaped resonating element which is responsible for the two resonances around 2.51 GHz and 5.18 GHz respectively. The final optimized dimensions of the antenna through EM simulations are L_1=1 mm, L_2=5.4 mm, L_3=10 mm, L_4=7 mm, w_e=3.06 mm, L_k=14 mm and L_{gnd}=12 mm. The dimensions ($W \times L$) of the substrate are 30 mm and 38 mm respectively. The proposed 9-shaped monopole antenna was simulated using the IE3D full wave simulator [191].

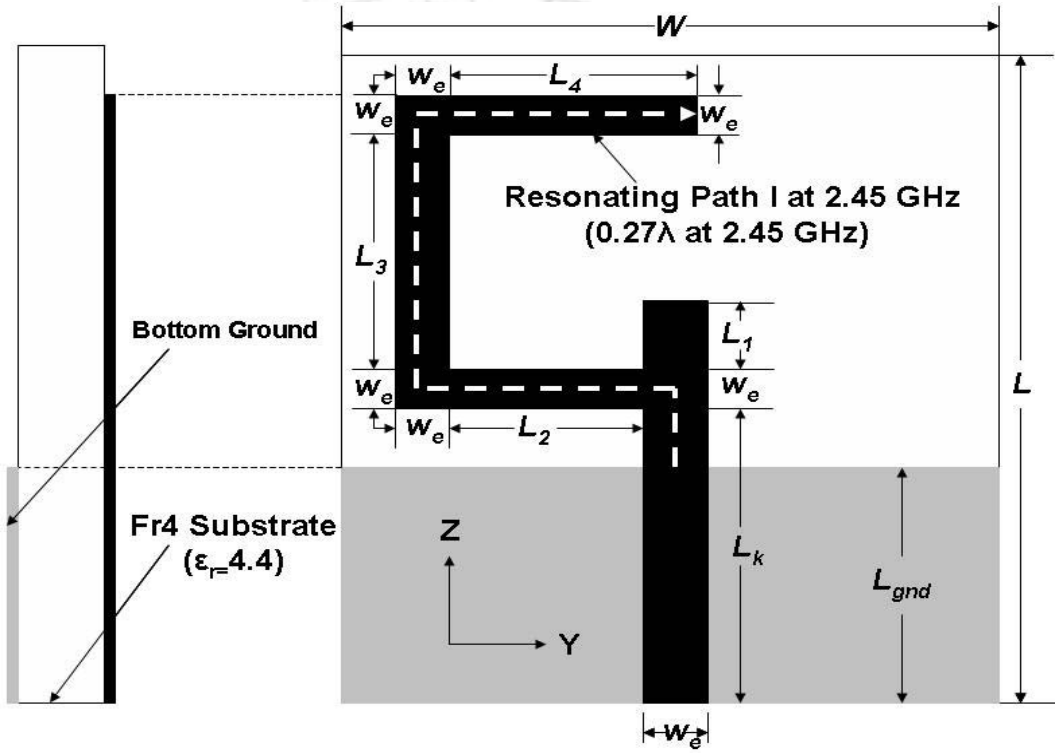

Figure 4.1: Geometry of the proposed antenna.

For a printed monopole antenna, the theoretical lower cut off frequency at the first resonant frequency can be approximately calculated by equating its area (in this case a folded 9-shaped printed monopole) to that of an equivalent cylindrical monopole antenna[48] of equivalent height L_c and equivalent radius r_c as follows:

$$f_{1low(th)} = \{\frac{7.2}{L_c + r_c + p}\}GHz \tag{4.1}$$

where

$$L_c = \{L_2 + L_3 + L_4 + (2 \times w_e)\} \tag{4.2}$$

$$r_c = \frac{w_e \times \{L_1 + L_2 + L_3 + L_4 + (4 \times w_e)\}}{2\pi \times \{L_2 + L_3 + L_4 + (2 \times w_e)\}} \tag{4.3}$$

$$p = L_k - L_{gnd} \tag{4.4}$$

In equation 4.1 all the parameters such as L_c, r_c and p are in cm. Applying all the design parameters in equation 4.2, 4.3 and 4.4, the values of L_c, r_c and p are found out to be L_c=2.852 cm, r_c=0.06085 cm and p=0.2 cm. Putting all these numerical values in equation 4.1, the $f_{1low(th)}$ is found out to be $f_{1low(th)}$=2.313 GHz. Hence by simulation the first lower cut off frequency at the first resonant frequency is f_{1low}=2.17 GHz, which is close to the $f_{1low(th)}$=2.313 GHz. The first resonance frequency occurs at f_1=2.54 GHz. The second resonant frequency f_2 should be a multiple of the first resonant frequency. Without the element of length L_1 (vertical stub), the radiating element giving the first (f_x) and second (f_y) resonant frequencies at f_x=2.43 GHz and f_y=4.86 GHz respectively shown in the Fig. 4.4. f_y is found out to be exactly the second harmonic of f_x (f_y=2f_x). On inclusion of vertical stub of length L_1 in the radiating element, the second resonant frequency (f_2) is obtained at f_2=5.13 GHz. Thus this small vertical stub of length L_1 is shifting the second resonant frequency from f_y=4.86 GHz to f_2=5.13 GHz. By properly varying the dimensions of the antenna, we can fix the antenna resonance at 2.45 GHz and 5.2 GHz respectively. The overall adjustments of the geometrical parameters are done for the improvement of impedance bandwidth in the 2.45 GHz and 5.2 GHz band.

4.3 Simulated and measured results on reflection coefficient ($|S_{11}|$) and the parametric study of the proposed antenna

The simulated reflection coefficient ($|S_{11}|$) of the proposed antenna is shown in the Fig. 4.2. The first resonance (f_1) occurs at 2.54 GHz with the reflection coefficient value of -15.02 dB. The band extends from 2.18 GHz to 2.93 GHz. The percentage bandwidth in this band region is 29.35. In this band, the RFID system (2.45 GHz) can be operated suitably. The second band extends from 4.46 GHz to 6.30 GHz with the peak of the resonance (f_2) occurs at 5.13 GHz with the reflection coefficient value of -24.87 dB. The percentage bandwidth in this band region is 34.20. The entire WLAN band which extends from 5.15-5.35 GHz and 5.725-5.825 GHZ can be suitably accommodated in this band from 4.46 GHz to 6.30 GHz.

The resonant characteristics of the proposed antenna can be analyzed by considering the presence of one resonating path in the 9-shaped radiating element and a supporting vertical stub for the fine tuning of the resonance at the higher frequency region. The length of the only resonating path is ((L_k-L_{gnd})+(w_e/2)+(w_e/2)+L_2+(w_e/2)+(w_e/2)+L_3+(w_e/2)+ (w_e/2)+L_4)=((14-12)+1.53+1.53+5.4+1.53 +1.53+10+1.53+1.53+7)=33.58 mm, which is approximately 0.27λ at 2.45 GHz. When the first resonanting path is only present (shown in the Fig. 4.3(a)), the structure weakly resonates at the center

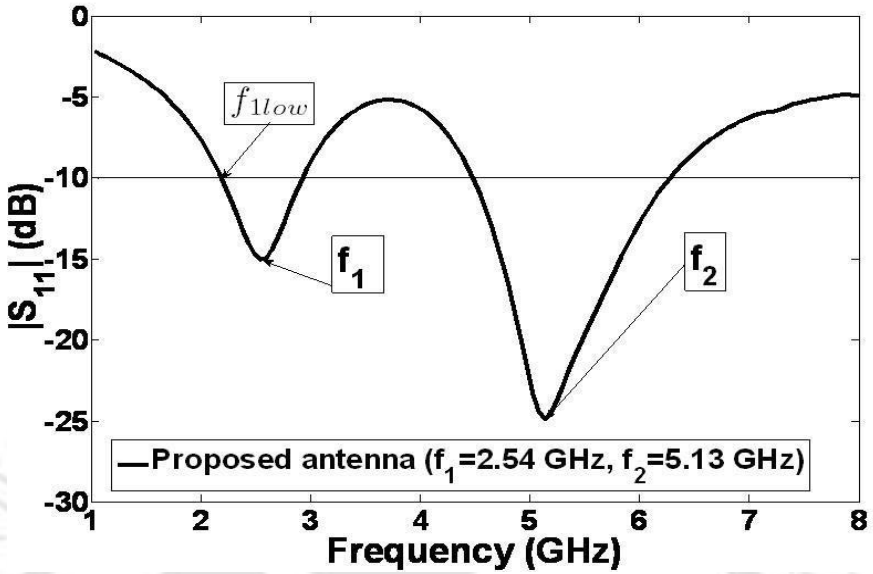

Figure 4.2: Simulated reflection coefficient ($|S_{11}|$) of proposed antenna.

frequency of f_x=2.43 GHz with the reflection coefficient value of -10.40 dB and at the center frequency of f_y=4.86 GHz with the reflection coefficient value of -17.22 dB, which is exactly the second harmonic of f_x (f_y=2f_x). When the vertical stub is only present(shown in the Fig. 4.3(b)), the structure exhibits no resonance in the lower frequency region, but resonance occur in the higher frequency region at the center frequency of f_z=6.81 GHz with the reflection coefficient value of -17.91 dB. But when the resonating path and the vertical stub are both present simultaneously that means the structure of the proposed antenna, the antenna strongly resonates at f_1=2.54 GHz and f_2=5.13 GHz as compared to previous two cases. Hence the presence of vertical stub not only supports the strong resonances in the two frequency regions (lower and higher) in the proposed antenna but also fine tunes the resonant frequency at higher frequency range (f_2=5.13 GHz) according to the desired frequency range for application in WLAN. Now with the two structures (resonant part and supporting vertical stub), the proposed antenna resonates with the center frequency of f_1=2.54 GHz having the reflection coefficient value of -15.02 dB and with the center frequency of f_2=5.13 GHz having the reflection coefficient value of -24.87 dB. The situations described above are depicted in the Fig. 4.4.

Fig. 4.5(a) shows the reflection coefficient for successive values of L_4 of the radiating element when the other parameter such as L_1 (=1.0 mm) remain constant. From the graph, one can experience that when L_4 increases from 3 mm to 11 mm, the first resonant frequency (f_1) moves towards left, which

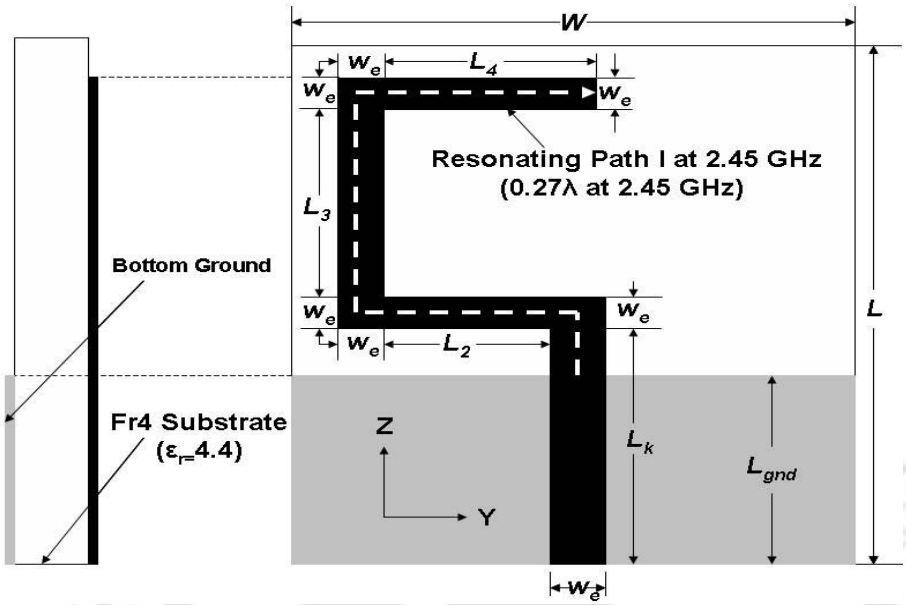

(a)

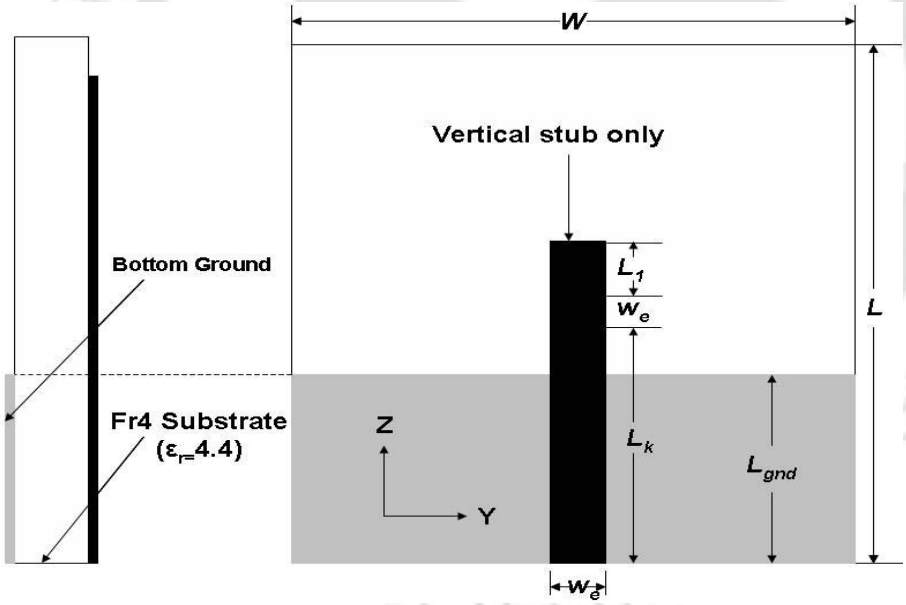

(b)

Figure 4.3: Geometry of radiating structures with **(a)** with resonating path I only and **(b)** with supporting vertical stub only.

means that the first resonance frequency (f_1) decreases from 2.86 GHz to 2.27 GHz with the increase of the length L_4, which is 20.62% shift of resonance frequency towards left. On the other hand, the second resonant frequency (f_2) is also decreased from 5.62 GHz to 4.59 GHz with the increase of L_4, which means that the second resonant frequency (f_2) moves towards left, which is 18.32% shift of resonance frequency towards left.

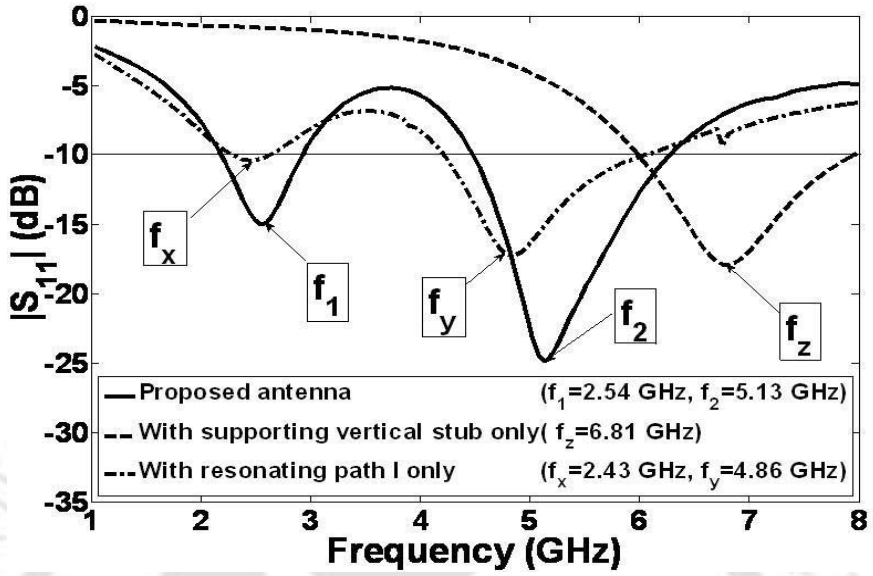

Figure 4.4: Simulated reflection coefficients ($|S_{11}|$) of the proposed antenna with different constituent structures.

Fig. 4.5(b) shows the reflection coefficient for successive values of vertical stub L_1 when the other parameter such as L_4 (= 7 mm) remain constant. From the graph, it can be seen that when L_1 increases from 0.5 mm to 4 mm, very little shifting of first resonant frequency (f_1) occurs, which is much less than the shifting of the second resonant frequency (f_2). This means the first resonance f_1 is unaffected with the increase of L_1 and remain static at its position at 2.54 GHz. But when the L_1 is increased from 0.5 mm to 4.0 mm the second resonant frequency (f_2) decreases from 5.19 GHz to 4.86 GHz, which is 6.35% resonance frequency shift towards left.

Fig. 4.6 shows the photograph of the fabricated prototype of the proposed 9-shaped monopole antenna for 2.45 GHz (RFID) and 5.2 GHz (WLAN) applications. Fig. 4.7 shows the comparison of the simulated and measured reflection coefficients ($|S_{11}|$). The reflection coefficient measurement was done using the Rohde and Schwarz ZVA24 vector network analyzer. From the graph, it is quite clear that there is reasonably good agreement between the measured and the simulated reflection coefficients. The first simulated resonance frequency (f_1) occurs at 2.54 GHz at the reflection coefficient value of -15.02 dB with the percentage bandwidth of 29.35 (2.18 GHz to 2.93 GHz). The second simulated resonance frequency (f_2) occurs at 5.13 GHz at the reflection coefficient value of -24.87 dB with the percentage bandwidth of 34.20 (4.46 GHz to 6.30 GHz). Similarly, the first resonance occurs at 2.46 GHz having a measured reflection coefficient value of -24.57 dB with percentage bandwidth of 15.56

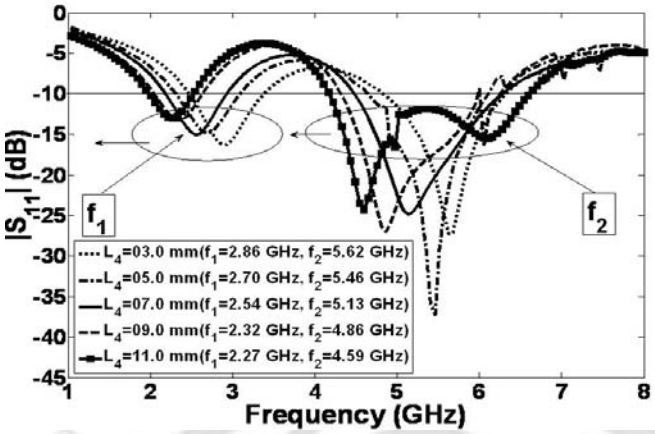

(a)

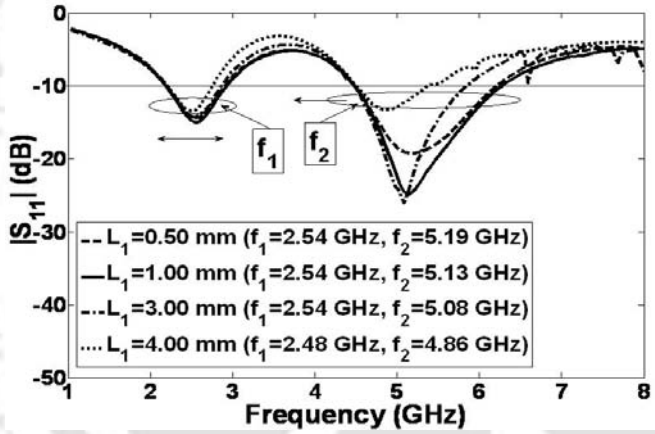

(b)

Figure 4.5: Simulated reflection coefficient ($|S_{11}|$) (dB) graphs, **(a)** L_4 is a variable and **(b)** L_2 is a variable.

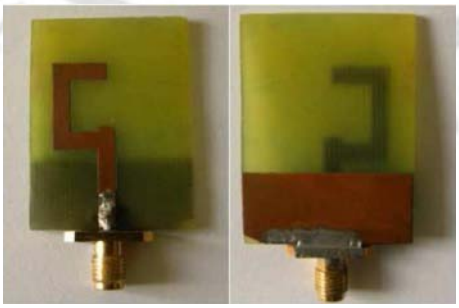

Figure 4.6: Fabricated prototype of the proposed antenna.

(2.31 GHz to 2.70 GHz) and the second resonance occurs at 5.22 GHz having a measured reflection coefficient value of -14.08 dB with percentage bandwidth of 42.27 (4.03 GHz to 6.19 GHz).

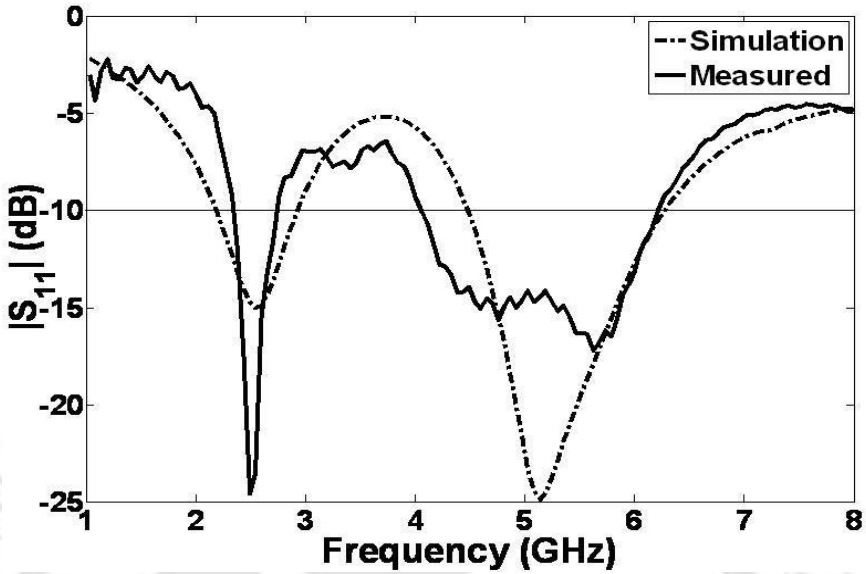

Figure 4.7: Comparison of the simulated and the measured reflection coefficients ($|S_{11}|$) of the proposed antenna.

4.4 Effect of triple-bend on the proposed antenna performance

4.4.1 Bending analysis on resonating path I with three, two and zero (linear) 90^0 bends in the absence of supporting vertical stub

Bending analysis is performed on the resonating path I when there are three 90^0 bends, two 90^0 bends and no 90^0 bend i.e. the linear resonating path I in the absence of the supporting vertical stub. In all the cases, the length of the resonating path I is 33.58 mm which is 0.27λ at 2.45 GHz.

In the first case when there is three 90^0 bends in the resonating path I shown in the Fig. 4.3(a), the radiating structure resonates at the center frequency of f_x=2.43 GHz with the reflection coefficient ($|S_{11}|$) value of -10.40 dB which is shown in the Fig. 4.9.

In the second case where there are two 90^0 bends in the resonating path I shown in the Fig. 4.8(a), there is no performance from the resonating path I but there is a tendency of resonance is visible in the Fig. 4.9 at 2.38 GHz, which on sake of analysis can be denoted as f_{x2}.

Similarly in the third case when there is no bend in the radiating element I i.e. the structure of radiating element is linear shown in the Fig. 4.8(b), there is also no performance from the linear resonating path I but there is a tendency of resonance is visible in the Fig. 4.9 at 1.94 GHz, which on sake of analysis can be denoted as f_{x0}.

Hence from the bending analysis performed on the resonating path I with three 90^0 bends, two 90^0

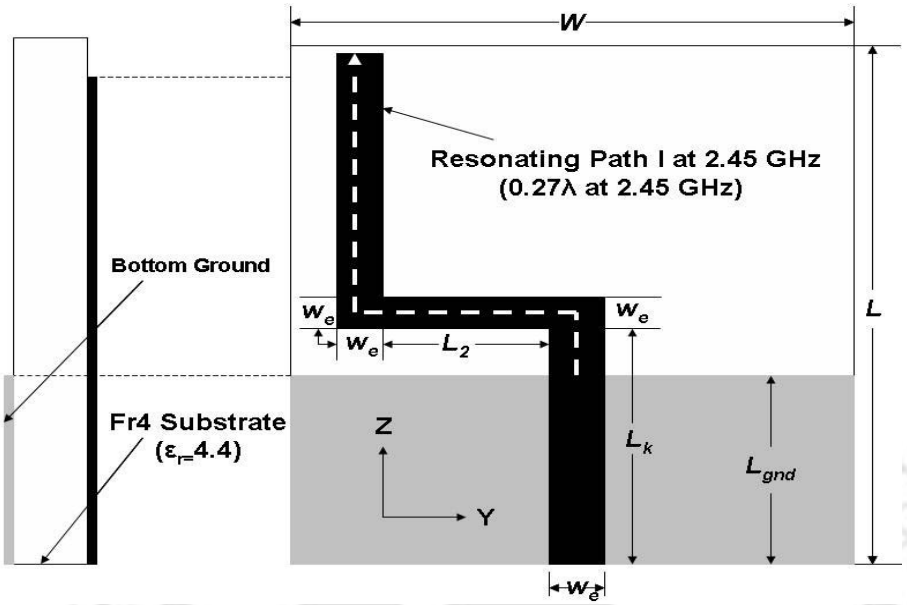

(a)

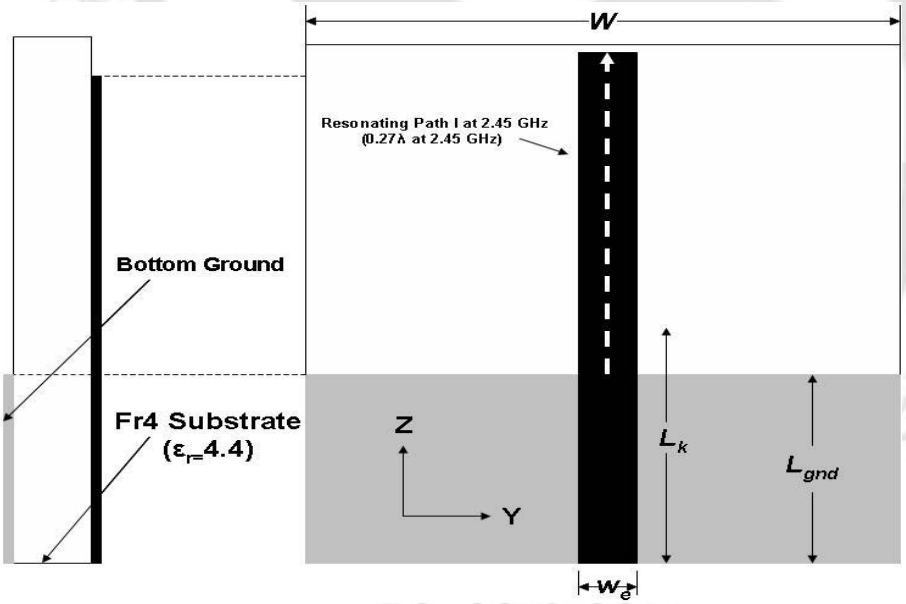

(b)

Figure 4.8: Geometry of radiating structures with **(a)** only resonating path I having two 90^0 bends and **(b)** linear resonating path I with no 90^0 bend.

bends and zero 90^0 bend i.e. the linear resonating path I in the absence of the supporting vertical stub, it is quite clear that the more the number of bends in the resonating path, deeper is the resonance at the desired frequency band of interest. This is clear from Fig. 4.9 that with three 90^0 bends, good performance is shown by the resonating path I as compared to two 90^0 bends and zero 90^0 bend i.e. the linear resonating path I in the absence of the supporting vertical stub. Apart from this, the

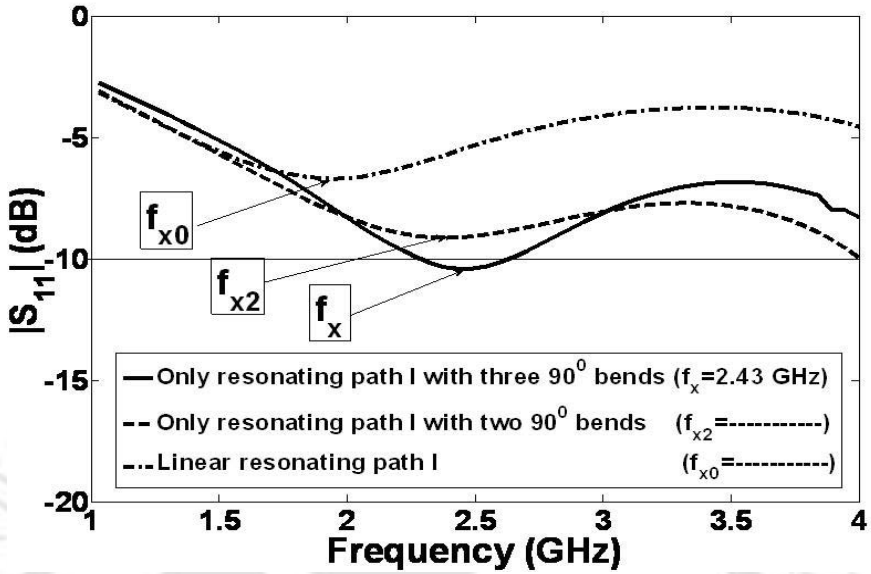

Figure 4.9: Comparison of simulated reflection coefficients ($|S_{11}|$) of the radiating structures with the presence of only resonating path I having three 90^0 bends, two 90^0 bends and linear resonating path (no 90^0 bend).

resonance frequency shifts towards right of the reflection coefficient graph ($|S_{11}|$) i.e. the resonant frequency increases as the number of bends increase from zero to three in the resonant path I [110].

4.4.2 Bending analysis on three and two 90^0 bends in resonating path I in the presence of supporting vertical stub

Now the bending analysis is performed on the resonating path I with two 90^0 bends with the presence of the supporting vertical stub and is compared with the performance in the resonating frequency with the proposed antenna consisting of three 90^0 bends in resonating path I with the presence of the supporting vertical stub. The length of the resonating path I is same as 33.58 mm which is 0.27λ at 2.45 GHz.

For the proposed antenna with three 90^0 bends in resonating path I with the presence of the supporting vertical stub, the first resonance frequency occurs at f_1=2.54 GHz with the reflection coefficient ($|S_{11}|$) value of -15.02 dB. The second resonance frequency occurs at f_2=5.13 GHz with the with the reflection coefficient ($|S_{11}|$) value of -24.87 dB.

But when one of the 90^0 bend is infolded in resonating path I, The number of 90^0 bends in the resonating path reduces to two shown in the Fig. 4.10. In this condition, with the presence of supporting vertical stub, when the structure is simulated, the structure resonates in the higher frequency of f_{22b}=4.86 GHz with the reflection coefficient ($|S_{11}|$) value of -26.37 dB. But there is no

performance in the lower frequency region but there is a tendency of resonance is visible in the Fig. 4.11 at 2.38 GHz, which on sake of analysis can be denoted as f_{12b}.

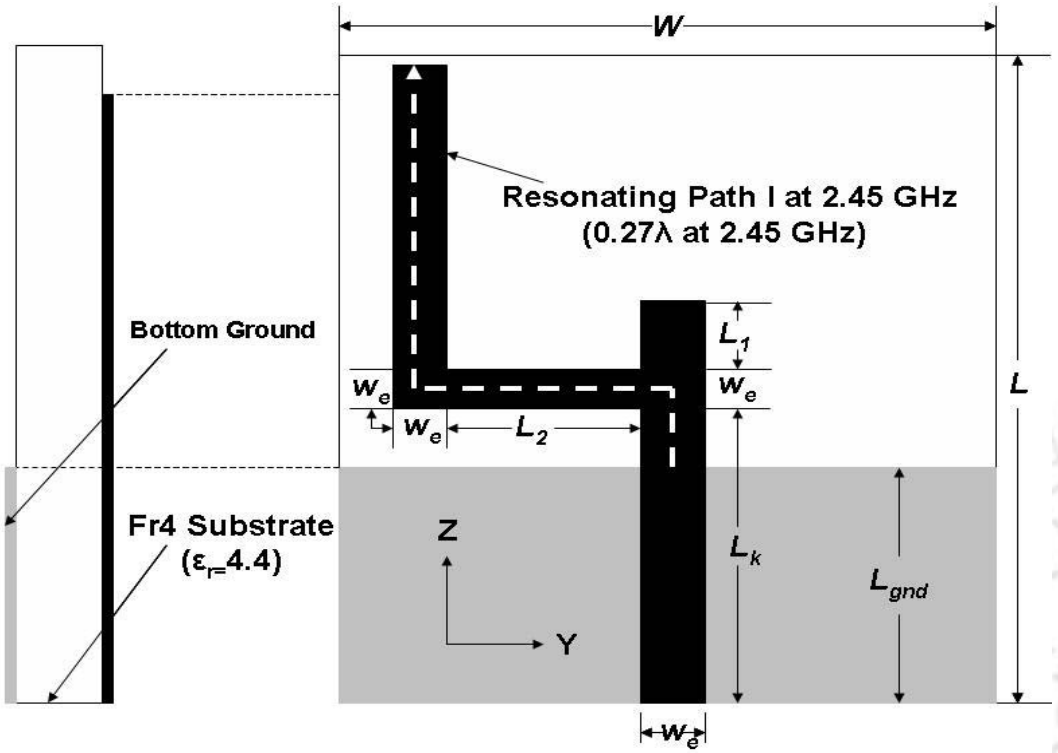

Figure 4.10: Geometry of radiating element with two 90^0 bends in the resonating path I with supporting vertical stub.

Hence from the above bending analysis on the resonating path I containing three 90^0 bends with the supporting vertical stub (proposed antenna) and the resonating path I containing two 90^0 bends with supporting vertical stub, it is clear that with the less number of 90^0 bends (two) in the resonating path I along with the supporting vertical stub, the required resonances at the desired frequency bands do not take place. There is no resonance occurring at the lower frequency range and at the higher frequency range, the resonance is not occurring in the required frequency range.

On the other hand, when the numbers of 90^0 bends are increased to three in the resonating path I with the supporting vertical stub (proposed antenna), required and sufficient resonances are occurring in the desired frequency bands. Apart from this, the depth of the resonances and the bandwidths in the respective frequency bands have improved considerably. Another observation is that during the above bending analysis, the more numbers of bends in the resonating path I, more is the shift in the resonance frequencies towards the right [110].

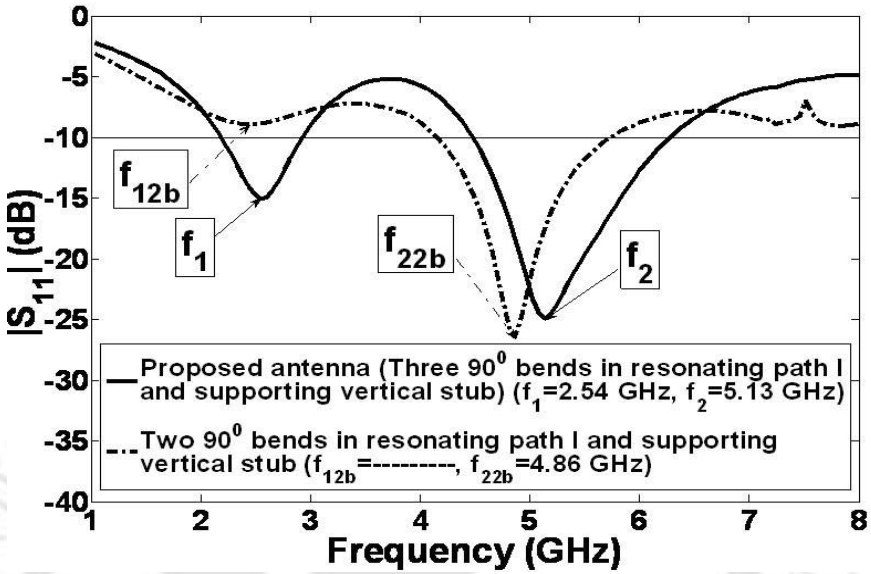

Figure 4.11: Comparison of simulated reflection coefficients ($|S_{11}|$) of proposed antenna (three 90^0 bends in resonating path I and supporting vertical stub) and two 90^0 bends in the resonating path I with supporting vertical stub.

4.5 Gain of the proposed antenna

The simulated gain in the range of 2.18 GHz-2.93 GHz varies from 2.60 dBi to 2.70 dBi. The value of simulated gain at 2.45 GHz is 2.78 dBi. Similarly, the simulated gain in the range of 4.46 GHz-6.30 GHz varies from 3.1 dBi to 3.22 dBi. The value of simulated gain at 5.2 GHz is 3.29 dBi.

The measured gain in the range of 2.18 GHz-2.93 GHz varies from 2.56 dBi to 2.60 dBi. The value of measured gain at 2.45 GHz is 2.79 dBi, which is sufficient for the operation in RFID (2.45 GHz) system satisfactorily. Similarly the measured gain in the range of 4.46 GHz-6.30 GHz varies from 3.15 dBi to 3.2 dBi. The value of measured gain at 5.2 GHz is 3.33 dBi, which is sufficient for the operation in 5.15 GHz-5.35 GHz WLAN system satisfactorily. Fig. 4.12 shows comparison of simulated and measured gain (dBi) vs. frequency of the proposed antenna in 2.18 GHz-2.70 GHz and 4.40 GHz-6.30 GHz range.

4.6 Surface current distribution of proposed antenna

At 2.45 GHz, the magnitude of the surface current in the L_4 branch is less and the current is returning in nature. The same situation is visible in the L_3 branch. The current flows from top to bottom in this branch i.e. the current is returning in nature. In the L_2 branch, the current is

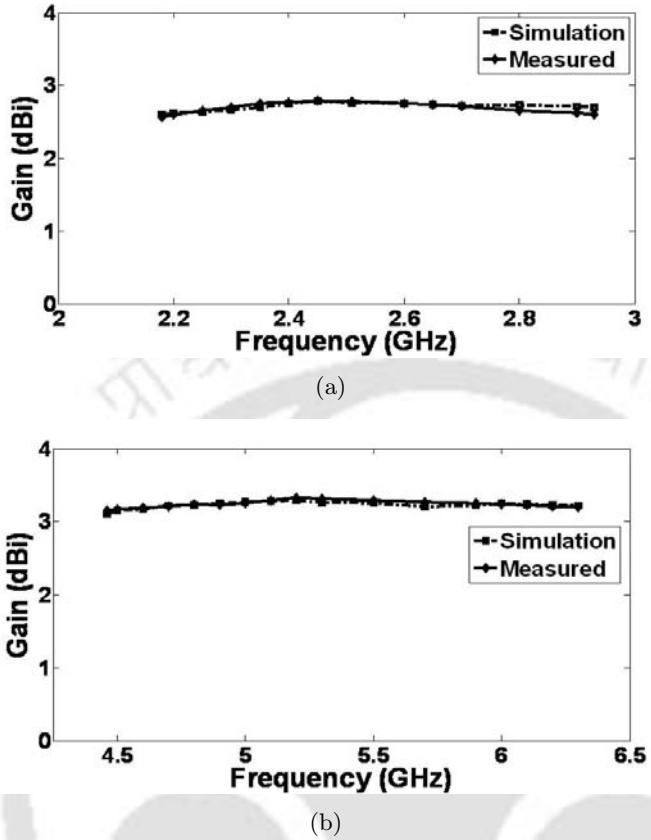

Figure 4.12: **(a)** Comparison of simulated and measured gain (dBi) vs. frequency of the proposed antenna (2.18 GHz-2.93 GHz) and **(b)** Comparison of simulated and measured gain (dBi) vs. frequency of the proposed antenna (4.46 GHz-6.30 GHz).

moving from right to left direction and the magnitude of the surface current is high in this branch. The magnitude of the surface current is high in the feed-line region. The surface currant distribution scenario at 2.45 GHz is shown in Fig. 4.13 (a).

Similarly at 5.2 GHz, the magnitude of the surface current in the L_4 branch is high and the current is forward moving in nature. The same situation is visible in the L_3 branch. The current flows from bottom to top in this branch i.e. the current is forward moving in nature. The magnitude of the surface current is high in the right edge of the L_3 branch. In the L_2 branch, the magnitude of the current distribution is high, but the current is returning in nature i.e. the current moves from right to left in this branch which is depicted in the Fig. 4.13 (b). As known, the electromagnetic coupling effect controlled the two excited resonant frequencies at 2.45 GHz and 5.2 GHz between the (L_c+L_k) element and (L_1+L_k) element. Fig. 4.13 shows the magnitude of the surface current of the proposed 9-shaped antenna at 2.45 GHz and 5.2 GHz.

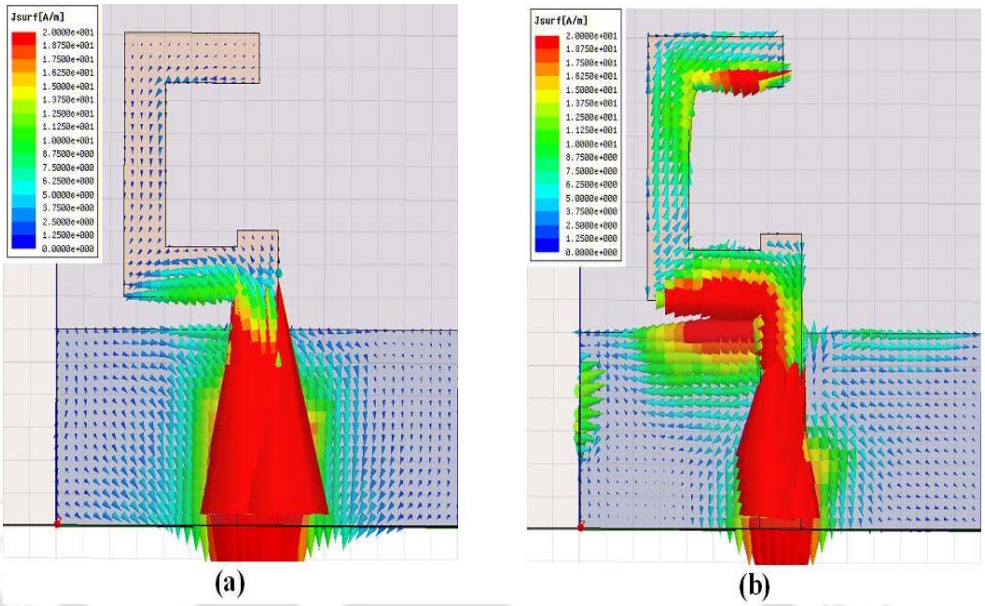

Figure 4.13: Direction and magnitude of the surface current distribution for triple bend 9-shaped PMA **(a)** at 2.45 GHz and **(b)** at 5.2 GHz.

4.7 Radiation pattern of the proposed antenna

The measured normalized co-polarized and cross-polarized E-plane (yz-plane) and H-plane (xy-plane) radiation patterns of the 9-shaped monopole antenna at 2.45 GHz and 5.2 GHz are shown in the Fig. 4.14 and Fig. 4.15 respectively. It can be observed that the co-polar E-plane radiation pattern is of the shape of "8" at 2.45 GHz and 5.2 GHz. At 2.45 GHz, the E-plane cross-polar radiation pattern is in between -10 and -20 dB. At 5.2 GHz the shape of the co-polar E-plane radiation pattern is slightly distorted in the bottom right hand side portion. The co-polar H-plane radiation pattern on the other hand is purely omni-directional at the two frequencies i.e. at 2.45 GHz and 5.2 GHz. Unlike at 2.45 GHz, the H-plane cross-polar radiation pattern is approximately at around -10 dB or more precisely the H-plane cross polarization level is in between -10 and -20 dB at 5.2 GHz. Hence, this 9-shaped monopole antenna demonstrates a consistent radiation pattern in the desired band of frequencies. As visible from the E-plane radiation patterns at 2.45 GHz and 5.2 GHz, the cross polarization fields are quite higher. Hence many bends are advantageous in terms of antenna performance but may lose the polarization purity in some directions.

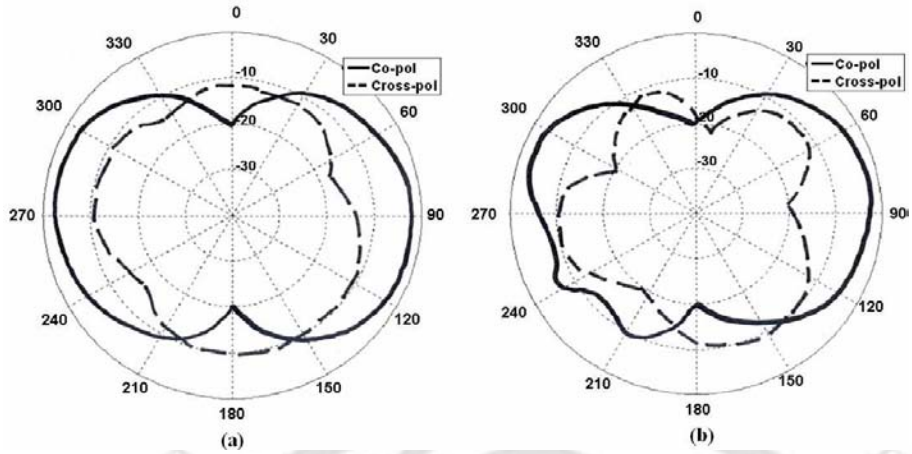

Figure 4.14: Measured E-plane (yz-plane) radiation patterns of the proposed antenna at **(a)** 2.45 GHz and **(b)** 5.2 GHz.

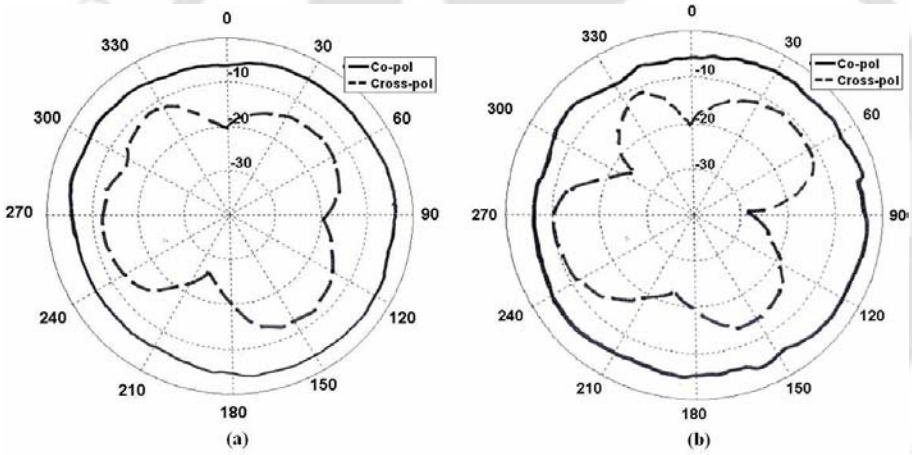

Figure 4.15: Measured H-plane (xy-plane) radiation patterns of the proposed antenna at **(a)** 2.45 GHz and **(b)** 5.2 GHz.

4.8 Summary

In this chapter, a new triple bend compact and simple PMAs is presented. The shape of the radiating element of the third antenna is 9-shaped and this also fed by microstrip line. This antenna also resonates in the RFID and WLAN frequency range. This antenna is compact and simple in nature. This antenna is fabricated and all the antenna parameters are measured. This antenna shows appropriate gain characteristic and consistent radiation pattern in the required band of interest. Size reduction of 18.57 percent, average bandwidth improvement of 37.08 percent and 16.45 percent average gain enhancement are achieved when compared to antenna reported in [114].

5

Quadruple bend PMA with a protruding stub in the ground plane

Contents

5.1 Introduction 114
5.2 Antenna design 117
5.3 Simulated and measured results on reflection coefficient ($|S_{11}|$) and the parametric study of the proposed antenna 118
5.4 Effect of quadruple-bend on the proposed antenna performance 120
5.5 Gain of the proposed antenna 125
5.6 Surface current distribution of proposed antenna 125
5.7 Radiation pattern of the proposed antenna 128
5.8 Summary 129

5.1 Introduction

For wireless identification, the Radio Frequency Identification (RFID) is a powerful emerging technology and need efficient antennas for application that uses RFID technology. A RFID system is a wireless communication system in which we can identify an object and can know the information associated with that object, without having any physical contact with it. The RFID technology can be used in many applications like distribution industry, delivery service control, library management, parking control, and patient supervision in hospitals. Due to the rapid growth in the radio frequency technology, we are able to manufacture RFID tag antennas of very small sizes in different forms like cards, labels, and coins.

The RFID has been allotted different frequency ranges in different countries. Mostly it is operated in five frequency ranges: low frequency (125 kHz, 135 kHz), high frequency (13.56 MHz), amateur band (433.92 MHz), ultra high frequency (860 to 960 MHz), and microwave frequency (2.45 GHz). Each frequency range has different abilities to receive signals across distances and to penetrate through opaque materials such as metals, sodium, graphite, and different liquids. Therefore RFID systems have different applications in different frequency ranges. Many international organizations are carrying out proceedings on RFID applications. Meanwhile studies for RFID have been carried out at the UID centre in Japan and ETSI in Europe.

A RFID system mainly consists of a RFID tag antenna and a RFID reader antenna. The RFID tag antenna is attached to an object. The object information is made available to the chip of the RFID tag. Now this information of the object to which the tag is attached is transmitted from the tag antenna to the reader antenna by RF communication. Finally the information is sent from the reader antenna to a server, where the processing of this information is done.

As the reader antenna comes nearer to the region of tag antenna, it transmits an electromagnetic signal to the tag, and the tag gets activated by that energy of the continuous wave signal. Now the activated tag transmits back to the reader, the information of the object to which the tag is attached. Now this tag information available in the reader section can be finally fed to a network which processes this information, so that tag acts as a sensor.

Each RFID tag is composed of a chip and an antenna. The chip contains an electronic product code (EPC), which is the unique identification code of the tag. The reader is composed of RF circuits, a modulator/demodulator, a time processing module, and a protocol processor. The accuracy of the

reader depends on the surrounding environment.

The RFID system can be classified into active and passive RFID systems on the basis of existence and absence of a battery source in the tag section. An active tag has an internal power supply source inside it to supply power to the tag's circuitry and a transmitter to send signals to the reader. So strong signals can be generated with the help of the battery and thus an active tag can provide a large readable range. A passive tag, which does not have an internal power supply inside it, gets activated only when RF power is received from the reader. A rectifier circuit is also needed in the case of a passive tag in order to convert ac power received from the reader into dc power to activate the tag's circuitry. The passive tag gets activated only when the reader is at a minimum distance from the tag so that the dc power obtained by the tag circuitry is above a certain specific threshold. Thus the maximum readable range of a passive tag is very less when compared to that of an active tag. The criterion on which an active or a passive tag is selected is mainly dependant on the application in which we are using the RFID system. An active tag because of the presence of power supply has long readable ranges, but at the same time they are very expensive. So the active tags are mainly used in the applications which require relatively small number of tags having long readable ranges. The passive tags have the advantages like light weight, low cost, and ability to be used for a very long time. But the passive tags have the drawbacks such as short read range and high power consumption in the reader. One typical application in which passive tags are used is in the airports where these passive tags are attached to the luggage and are used in checking out their departure and arrival.

In the RFID system, the reader antenna should have a high gain, in order to have a long read range so that it can detect the tag antenna located at a very long distance. However in some other applications, it is not desirable to have a long read range, since in those applications, the reader cannot distinguish tags between users since it will detect tags from different users at the same time. So the Table 5.1 shows the typical technical specification needed for the smooth operation of RFID system.

Over the last decade wireless communication systems have developed rapidly. It is also becoming more and more popular now-a-days. PMAs are valuable and important component for applications in wireless communication systems such as wireless local area network (WLAN), ultra-wideband (UWB) and radio frequency identification (RFID). PMAs are good candidates for dual-band applications, as they exhibit low profile, easy fabrication, low cost, and easy integration. Also, the omni-directional radiation characteristics of monopole antenna make them very suitable for indoor applications. Many

Table 5.1: Technical specifications for RFID systems

Operating frequencies	2.45 GHz and 5.8 GHz
Occupied channel bandwidth	2400 to 2483.5 MHz and 5725 to 5875.0 MHz
Peak electric field strength	Less than 20 dB above the average value
Data rates	100 Kbps to 1 Mbps
Maximum EIRP	+36 dBm in a system with at least 75 channels and +27 dBm in a system with 15 to 74 channels
Radiation pattern	Omni directional
Dimension of antenna	Less than 70 mm (Excluding the ground plane)
Operating temperature	-40^0C to 80^0C
Input impedance	50-Ω
Read range	0 to 100 meters
Operating humidity	95 % non-condensing

compact PMAs were fabricated for wireless applications and reported in the literature [150-156]. Most of these antennas are designed for applications either in WLAN [150-154] or worldwide interoperability for microwave access (WiMAX) [155, 156]. In recent literature [157-165], many different kinds of antennas are fabricated and proposed for dual- or multi-band applications.

In this chapter, a new printed microstrip fed folded strip monopole antenna (FSMA) with a protruding stub in the ground plane for simultaneous applications in the WLAN and RFID is presented. The geometry of this proposed antenna has four 90^0 bends in its radiating element. Hence this proposed antenna belongs to the category of quadruple bend PMA. There are two resonant paths in the proposed antenna, one in the folded strip and the other in the protruding stub in the ground plane. It supports two resonances at 2.4 GHz and 5.81 GHz, which are the center frequencies of the WLAN and RFID respectively. The proposed antenna can be used in the ISM (2.4/2.5 GHz with the center frequency of 2.45 GHz), and Zigbee operating band as the operating regions for ISM and Zigbee falls under the resonating band of proposed antenna. The antenna is constructed by a non-conductor backed folded strip with a microstrip feedline. The dual-band performance can be easily obtained for this type of antenna by fine-tuning the lengths of the two resonant paths in the folded strip and the protruding stub in the ground plane.

5.2 Antenna design

The dual-band monopole antenna (DBMA) with a microstrip fed folded strip and a protruding stub in the ground plane is printed on the FR4 substrate of relative permittivity 4.4 and thickness 1.6 mm as shown in the Fig. 5.1. A 50-Ω microstrip line is used for the excitation. The folded strip width and protruding stub width of the proposed DBMA is 3 mm, same as that of the width of the microstrip line. The remaining design dimensions are given in Fig. 5.1.

Two resonance paths are clearly visible in the proposed antenna, one in the folded strip (L_α) of the radiating element and the other (L_β= N) in the protruding stub of the ground plane. The length of the resonanting path in the folded strip is L_α= 29.8 mm, which is $0.23\lambda_1$ at the first resonant frequency of 2.4 GHz (f_1= 2.4 GHz). Similarly, the length of the second resonanting path in the protruding stub of the ground plane is L_α= N = 12 mm, which is $0.23\lambda_2$ at the second resonance frequency of 5.8 GHz (f_2 = 5.8 GHz). By properly varying the lengths L_α and L_β, we can fix the antenna resonance at 2.4 GHz and 5.8 GHz, respectively. The overall adjustments of the geometrical dimensions are done for the improvement of impedance bandwidth in the 2.4 GHz and 5.8 GHz bands. The full wave simulator IE3D [191] is used to simulate the proposed antenna.

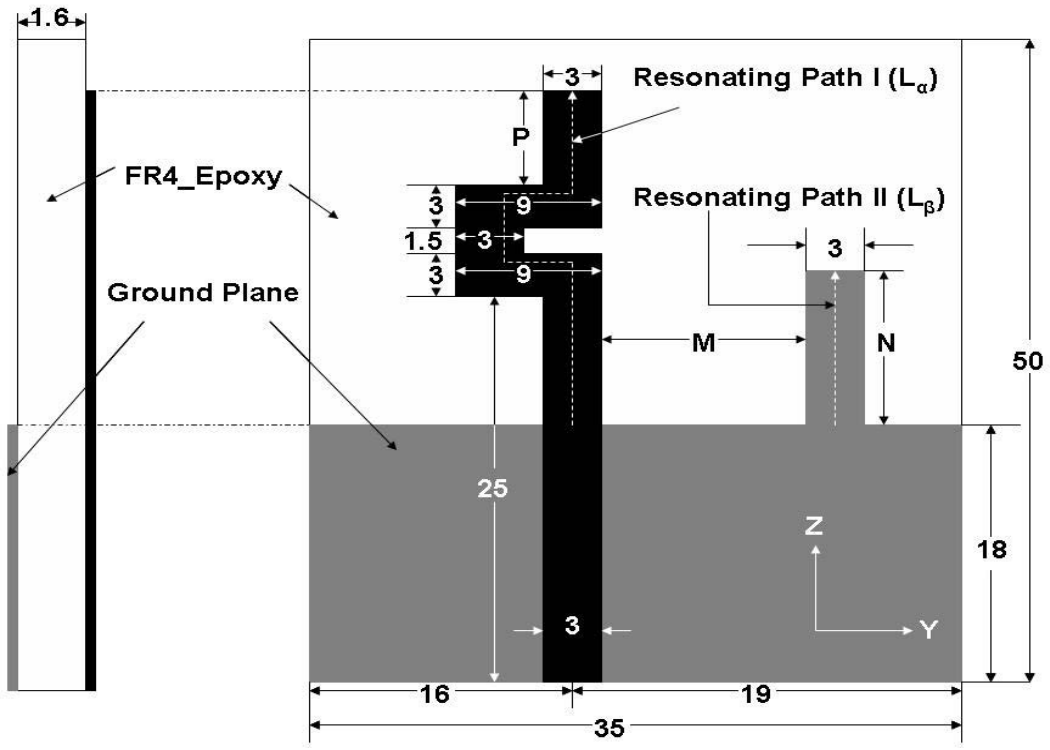

Figure 5.1: Geometry of the proposed antenna with M = 8 mm, N = 12 mm and P = 4.8 mm.

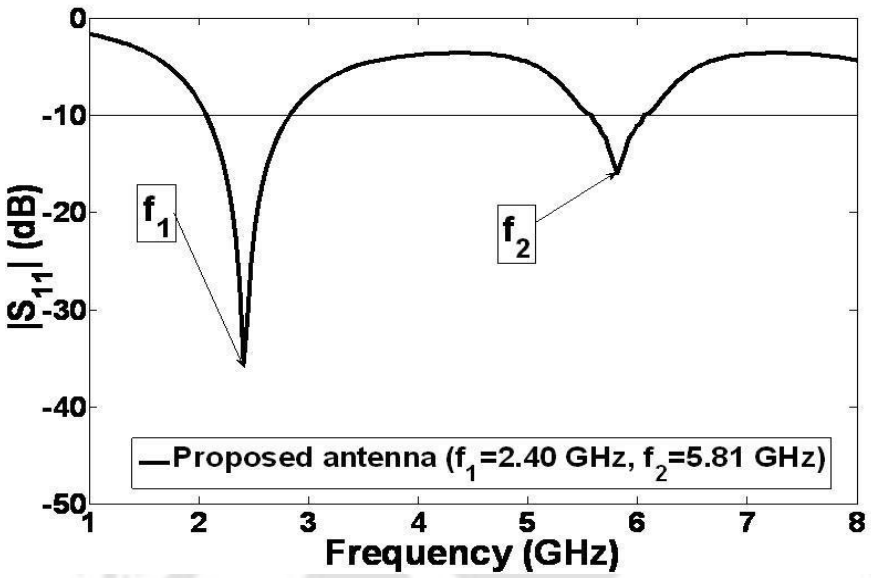

Figure 5.2: Simulated reflection coefficient ($|S_{11}|$) of the proposed antenna.

5.3 Simulated and measured results on reflection coefficient ($|S_{11}|$) and the parametric study of the proposed antenna

Fig. 5.2 shows the simulated reflection coefficient ($|S_{11}|$) of the proposed antenna. The first resonance occurs at f_1=2.40 GHz with the reflection coefficient value of -35.48 dB. The band extends from 2.06 GHz to 2.82 GHz. The percentage bandwidth in this band region is 31.14. The WLAN's 2.4-2.485 GHz band is completely immersed in this band of 2.06 GHz to 2.82 GHz. The second band extends from 5.57 GHz to 6.08 GHz with the peak of the resonance occurs at f_2=5.81 GHz with the reflection coefficient value of -15.91 dB. The percentage bandwidth in this band region is 8.75. The entire RFID band which extends from 5.725-5.875 GHz can be suitably accommodated in this band from 5.57 GHz to 6.08 GHz.

When there is no protruding stub in the ground plane and only folded strip is present as the radiating element shown in the Fig. 5.7(a), the structure weakly resonates only with the center frequency of f_x=2.58 GHz with the reflection coefficient value of -13.75 dB. But when a vertical protruding stub is erected from the ground plane, the scenario has changed drastically. Two resonances occurred which transformed the radiating structure in the dual-band operation mode. In the lower frequency region, a strong resonance occurred with the center frequency of f_1=2.40 GHz. A moderate resonance is visible in the higher frequency region with the center frequency region at f_2=5.81 GHz. The presence

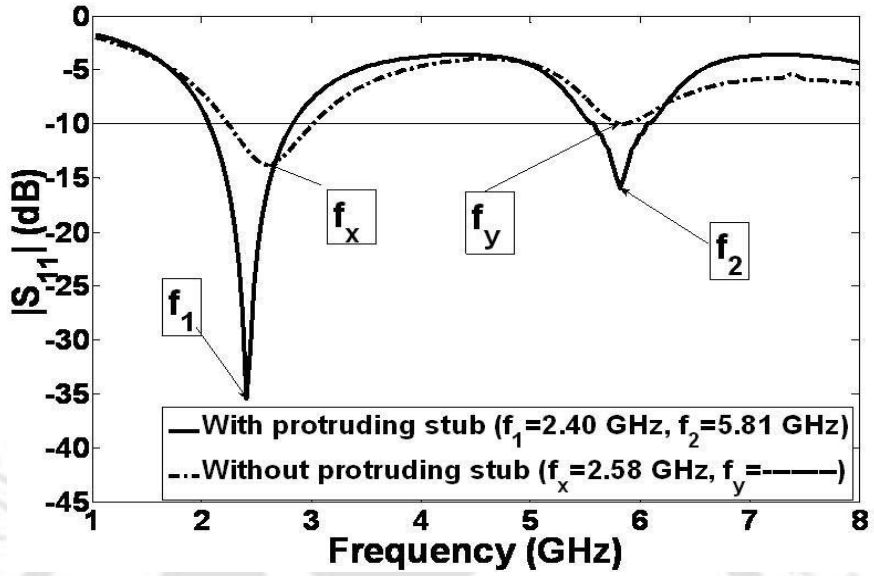

Figure 5.3: Simulated reflection coefficients ($|S_{11}|$) of the antenna with and without protruding stub in the ground plane.

of the protruding stub in the ground plane not only strengthens the resonating characteristics of the proposed antenna, but also provides another resonance at the higher frequency region makes the antenna a dual-band antenna which can be simultaneously applicable in the WLAN and RFID domain, shown in the Fig. 5.3. The reason for the strong resonance by the protruding stub may be due to the electromagnetic coupling effect between the folded-strip radiating element and the protruding stub in the ground plane.

Fig. 5.4(a) shows the reflection coefficient for successive values of the distance M between the folded strip of the radiating element and the protruding stub in the ground plane when the other parameters such as N (= 12 mm) and P (= 4.8 mm) are kept constant. From the graph, it is clearly visible that when M increases from 4 mm to 12 mm, the first resonant frequency (f_1) moves towards left, which means that the first resonant frequency (f_1) decreases from 2.54 GHz to 2.30 GHz, which is 9.44% resonant frequency shift towards left with the increase of the distance M. On the other hand, the second resonant frequency (f_2) almost remains static at 5.8 GHz, but the performance degrades at M = 10 mm and 12 mm.

Fig. 5.4(b) shows the reflection coefficient for successive values of the length N of the protruding stub in the ground plane when the other parameters such as M (= 8 mm) and P (= 4.8 mm) remain constant. From the graph, it can be seen that when N increases from 8 mm to 16 mm, the first resonant

frequency (f_1) moves towards left, which means that the first resonant frequency (f_1) decreases rapidly from 2.58 GHz to 2.26 GHz, which is 12.40% shift in the resonant frequency towards left with the increase in the length of the protruding stub N. On the other hand, very little shifting of second resonant frequency (f_2) occurs, which is less than the shifting of the first resonant frequency (f_1). Hence the second resonant frequency (f_2) is almost independent of the variation of N, the length of the protruding stub.

Fig. 5.4(c) shows the reflection coefficient for successive values of the length P of the radiating element (means also the total length of the folded strip ($L_1 = L_\alpha$)) when the other parameters such as M (= 8 mm) and N (= 12 mm) remain constant. From the graph, one can experience that when P increases from 0.8 mm to 8.8 mm, the first resonant frequency (f_1) moves towards left, which means that the first resonance frequency (f_1) decreases from 2.65 GHz to 2.16 GHz, which is 18.49% shift in the resonant frequency towards left with the increase of the length P. On the other hand, the second resonant frequency (f_2) is also decreased from 6.06 GHz to 5.43 GHz, which is 10.39% shift in the resonant frequency towards left with the increase of P, but the performance degrades at P = 8.8 mm.

Fig. 5.5 shows the fabricated prototype of the proposed antenna for WLAN and RFID applications at 2.4 and 5.81 GHz. Fig. 5.6 shows the comparison of the simulated and measured graphs of the reflection coefficient ($|S_{11}|$) (dB) of the proposed antenna. The reflection coefficient measurement was performed using Rohde and Schwarz ZVA24 vector network analyzer. From the graph, it is clear that there is reasonably good agreement between the measured and simulated reflection coefficients ($|S_{11}|$) (dB). With the measurement, the first resonance occurs at 2.4 GHz having the reflection coefficient value of -40.48 dB with percentage fractional bandwidth (FBW) of 32.99 (2.05 GHz to 2.86 GHz), and the second resonance occurs at 5.81 GHz having the reflection coefficient value of -20.21 dB with percentage FBW of 10.11 (5.55 GHz to 6.14 GHz). Hence, from the experimental results, it is clear that the fabricated prototype can be used for the dual band WLAN and RFID applications around 2.4 GHz and 5.8 GHz.

5.4 Effect of quadruple-bend on the proposed antenna performance

5.4.1 Bending analysis on resonating path I with four, three, two and zero (linear) 90^0 bends in the absence of protruding stub in ground plane

Bending analysis is performed on the resonating path I (L_α) with four, three, two and zero (linear) 90^0 bends in the absence of protruding stub in the ground plane. The length of the resonant path is

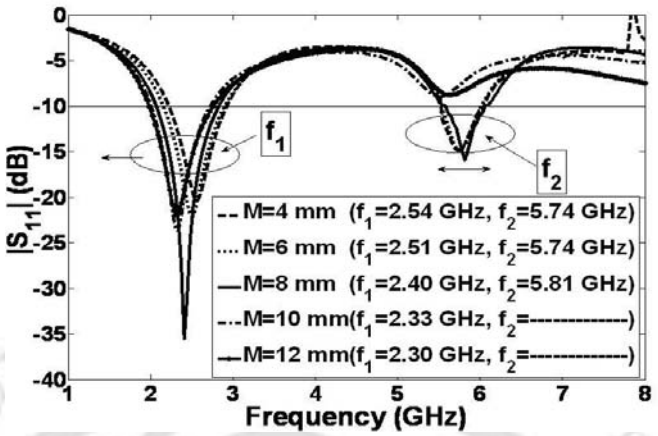

(a)

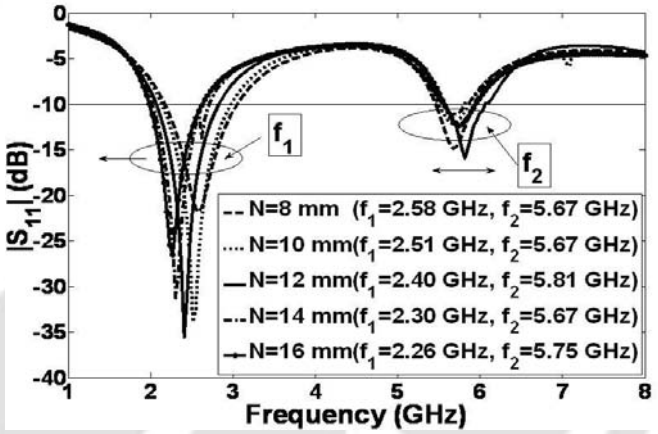

(b)

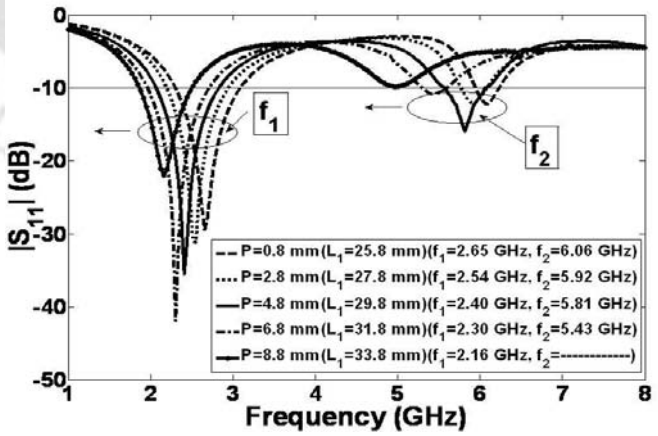

(c)

Figure 5.4: Simulated reflection coefficient ($|S_{11}|$) (dB) graphs, **(a)** M is a variable, N= 12 mm, P =4.8 mm, **(b)** N is a variable, M=8 mm, P=4.8 mm and **(c)** P is a variable, M=8 mm, N=12 mm.

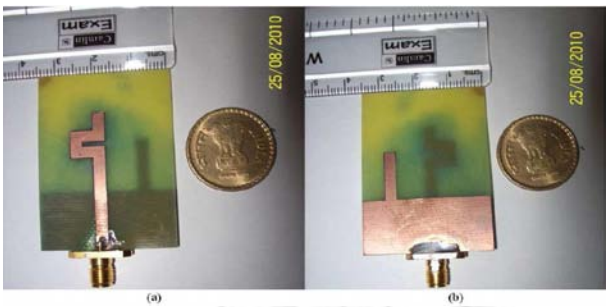

Figure 5.5: Fabricated folded strip monopole antenna with a protruding stub prototype (a) Top view and (b) Bottom view.

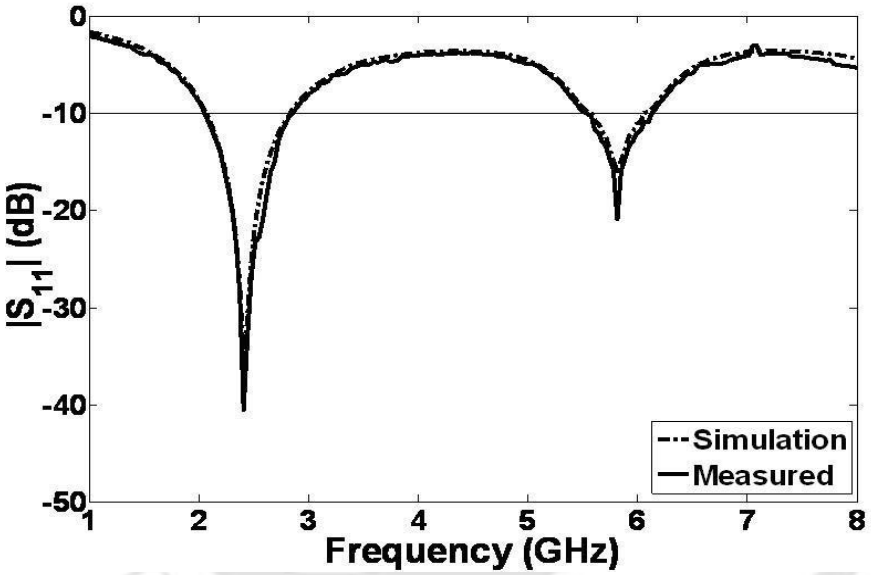

Figure 5.6: Comparison of the simulated and measured reflection coefficients ($|S_{11}|$) (dB) of the proposed dual-band monopole antenna for WLAN and RFID applications.

29.8 mm which is $0.23\lambda_1$ at the resonant frequency of 2.4 GHz.

With four 90^0 bends and in absence of protruding vertical stub in the ground plane shown in the Fig. 5.7(a), the radiating element resonates with the center frequency of f_x=2.58 GHz shown in the Fig. 5.8.

Now one of the 90^0 bend is unfolded and the radiating structure contains only three 90^0 bends shown in the Fig. 5.7(b) having the same length as before. On simulation, the radiating element produces resonance with the center frequency of f_{x3}=2.54 GHz shown in the Fig. 5.8.

Now the one of the 90^0 bend in the previous radiating structure is unfolded and the resonating path I contains only two 90^0 bends as shown in the Fig. 5.7(c). On simulation, the radiating structure

resonates with the center frequency of f_{x2}=2.23 GHz shown in the Fig. 5.8.

Now all the 90^0 bends in the resonating path I is unfolded and the radiating structure becomes linear (zero 90^0 bend) of same length as the resonating path with four 90^0 bends shown in the Fig. 5.7(d). On simulation there is no performance from the linear radiating element but there is a tendency of resonance at 1.94 GHz is visible in the Fig. 5.8 which can be denoted as f_{x0} for sake of analysis.

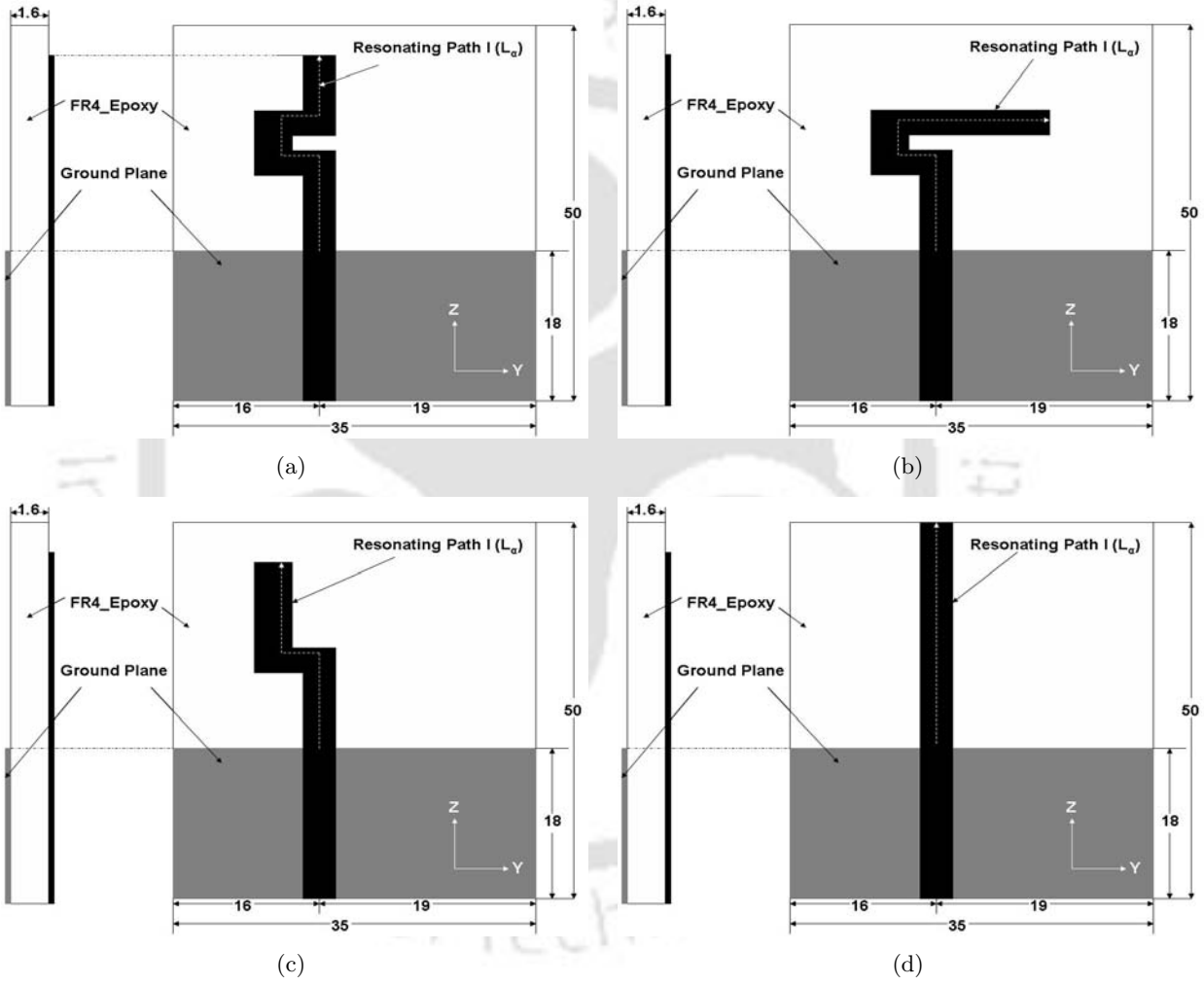

Figure 5.7: Geometry of radiating element in the absence of vertical stub in the ground plane with **(a)** four 90^0 bends, **(b)** three 90^0 bends, **(c)** two 90^0 bends and **(d)** zero 90^0 bend.

Hence from the above bending analysis on the resonating path I with four, three, two and zero 90^0 bends in the absence of protruding stub in ground plane, it is clear that the resonance frequency shifts right[110] of the reflection coefficient ($|S_{11}|$) on increase of bends in the resonating path. Apart from this, the quality of resonance and the bandwidth in the desired frequency band have improved with the increased number of 90^0 bends in the resonating path.

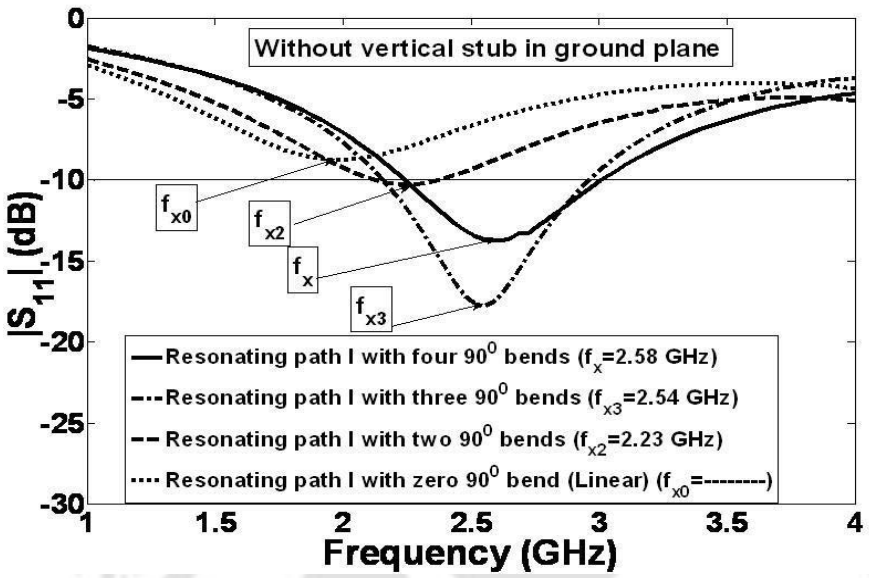

Figure 5.8: Comparison of simulated reflection coefficients ($|S_{11}|$) with four, three, two and zero (linear) 90^0 bends in resonating path I in the absence of vertical stub in ground plane.

5.4.2 Bending analysis on resonating path I with four, three, two and zero (linear) 90^0 bends in the presence of protruding stub in ground plane

Bending analysis is performed on the resonating path I (L_α) with four, three, two and zero (linear) 90^0 bends in the presence of protruding stub in the ground plane. The length of the resonant path is 29.8 mm which is $0.23\lambda_1$ at the resonant frequency of 2.4 GHz.

With four 90^0 bends and in presence of protruding vertical stub in the ground plane (proposed antenna) shown in the Fig. 5.1, the radiating element resonates with the center frequencies of f_1=2.40 GHz and f_2=5.81 GHz shown in the Fig. 5.10.

Now one of the 90^0 bend is unfolded and the radiating structure contains only three 90^0 bends shown in the Fig. 5.9(a) having the same length as before. On simulation, the radiating element produces resonance with the center frequency of f_{1b3}=2.23 GHz and there is no performance from the radiating element in the higher frequency range but there is a tendency of resonance at 5.32 GHz is visible in the Fig. 5.10 which can be denoted as f_{2b3} for sake of analysis.

Now the one of the 90^0 bend in the previous radiating structure is unfolded and the resonating path I contains only two 90^0 bends as shown in the Fig. 5.9(b). On simulation, the radiating element resonates with the center frequencies of f_{1b2}=2.16 GHz and f_{2b2}=5.01 GHz shown in the Fig. 5.10.

Now all the 90^0 bends in the resonating path I is unfolded and the radiating structure becomes

linear (zero 90^0 bend) of same length as the resonating path with four 90^0 bends shown in the Fig. 5.9(c). On simulation, the radiating element produces resonance with the center frequency of f_{1b0}=1.98 GHz and there is no performance from the radiating element in the higher frequency range but there is a tendency of resonance at 5.11 GHz is visible in the Fig. 5.10 which can be denoted as f_{2b0} for sake of analysis.

Hence from the above bending analysis on the resonating path I with four, three, two and zero 90^0 bends in the presence of protruding stub in ground plane, it is clear that the resonance frequency shifts right or increases [110] in the lower frequency region of the reflection coefficient ($|S_{11}|$) on the increase of bends in the resonating path. In the higher frequency region also, the resonant frequency shifts towards right or increases with the number in bends in the resonant path. The protruding vertical stub in the ground plane along with the with the four 90^0 bends in the resonating path tunes or helps in proper resonance in the lower and higher frequency ranges. Since the protruding vertical stub helps in producing proper resonance in the higher frequency region, it can be termed as the second resonant path (L_β) in the proposed antenna structure. Apart from this, the quality of resonance and the bandwidth in the desired frequency bands have improved with the increased number of 90^0 bends in the resonating path.

5.5 Gain of the proposed antenna

Fig 5.11 shows the measured gain in dBi of the proposed antenna. The measured gain at 2.4 GHz is 3.7 dBi, and the measured gain at 5.8 GHz is 3.57 dBi. The measured gain is almost consistent in the frequency range of 2.05 GHz to 2.86 GHz, and the average gain in this frequency range is 3.73 dBi. Similar situation can be seen in the frequency range of 5.55 GHz to 6.14 GHz. The average measured gain in this frequency range is approximately 3.59 dBi.

5.6 Surface current distribution of proposed antenna

At 2.4 GHz, the directions of currents in the feed-line and ground plane are opposite in nature. It can be observed that strong surface current flows from the top to bottom (downward direction) of the folded strip of length (L_α). Due to this heavy flow of surface current in the folded strip, strong resonance occurs at 2.4 GHz. Where as in the protruding stub (L_β) in the ground plane, a mild current is flowing in upward direction shown in Fig. 5.12 (a). This is the reason that the protruding

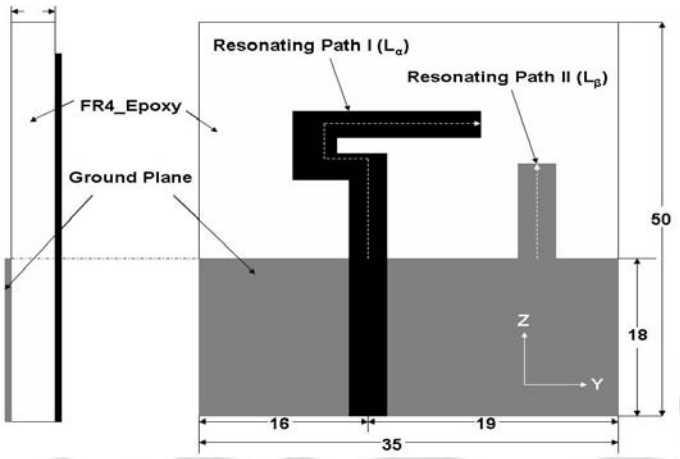

(a)

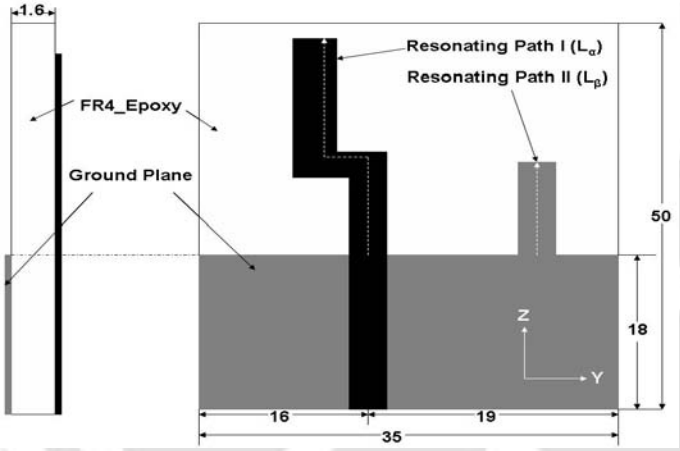

(b)

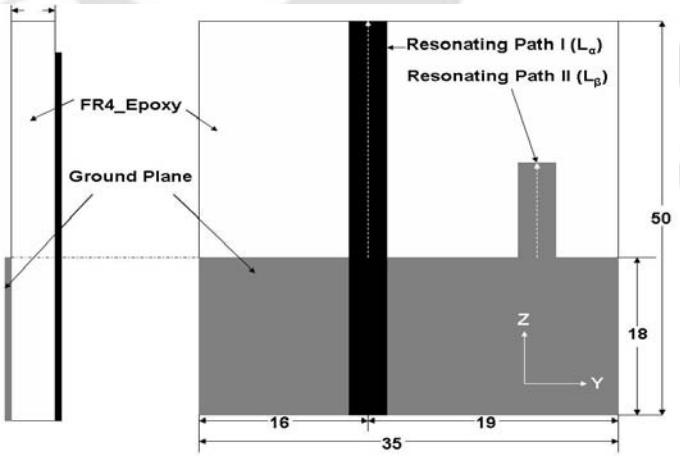

(c)

Figure 5.9: Geometry of radiating element in the presence of vertical stub in the ground plane with **(a)** three 90^0 bends, **(b)** two 90^0 bends and **(c)** zero 90^0 bend.

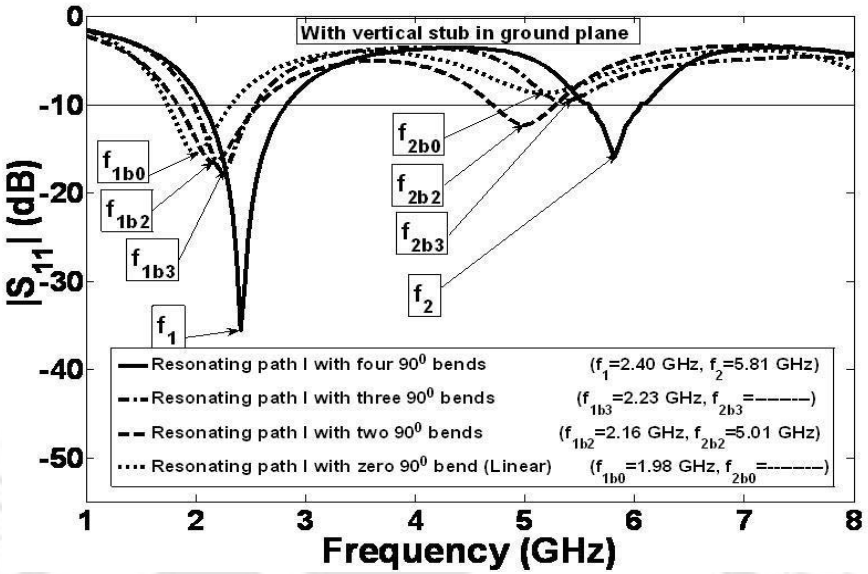

Figure 5.10: Comparison of simulated reflection coefficients ($|S_{11}|$) with four, three, two and zero (linear) 90^0 bends in resonating path I in the presence of vertical stub in ground plane.

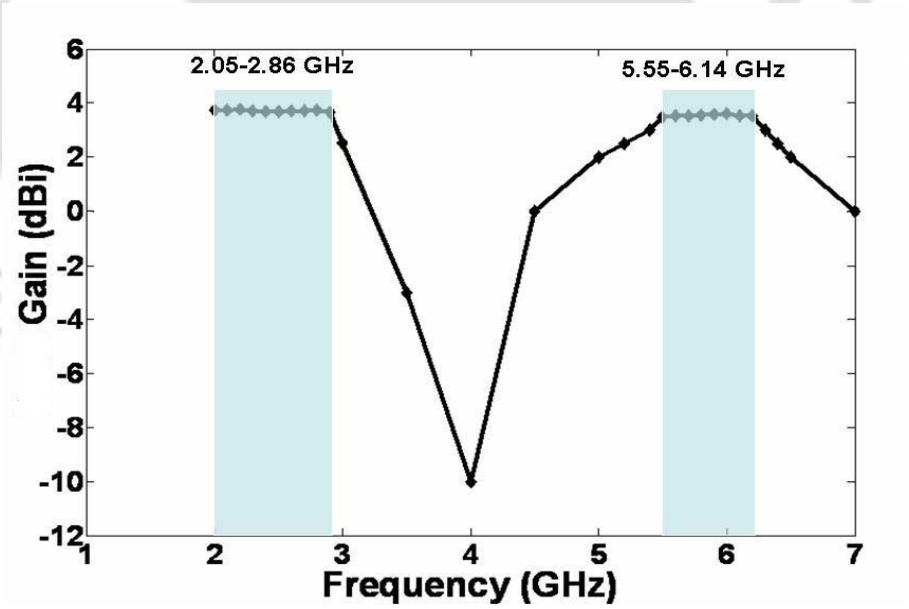

(a)

Figure 5.11: Measured gain (dBi) vs. frequency of the proposed antenna.

stub in the ground plane does not produce a good resonance at 5.8 GHz.

At 5.8 GHz, the current densities at the feed-line and ground plane are opposite in direction. The direction of current in the folded strip (L_α) is from the bottom to top (upward direction). A strong current is also available in the folded strip which gives strong resonance in 2.4 GHz at the simulation

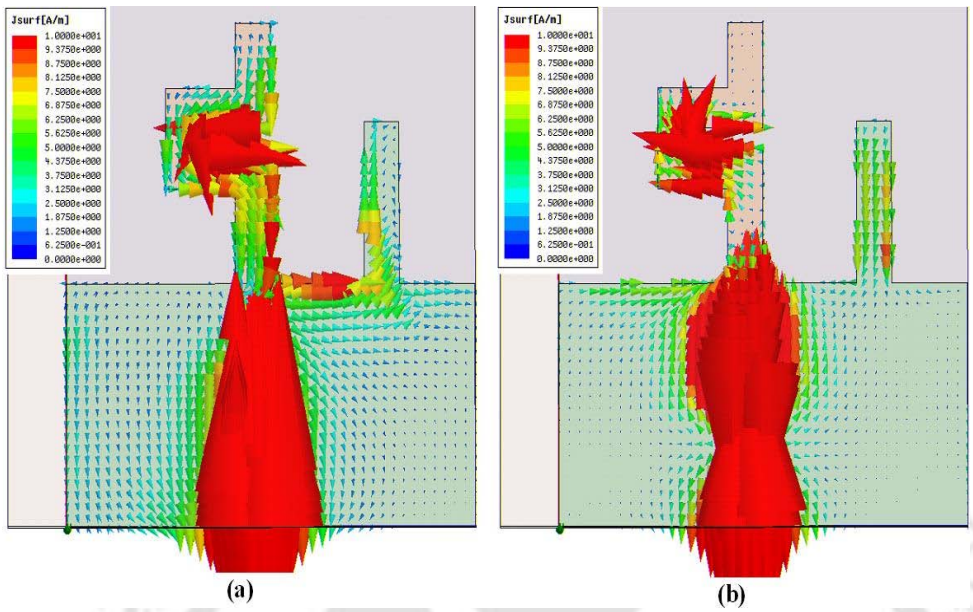

Figure 5.12: Direction and magnitude of the surface current distribution for quadruple bend PMA with a protruding stub in the ground plane **(a)** at 2.4 GHz and **(b)** at 5.8 GHz.

frequency of 5.8 GHz. At the same time in the protruding stub (L_β) in the ground plane, a very weak current flows from top to bottom (downward direction)shown in Fig. 5.12 (b). Hence, the protruding stub in the ground plane also does not produce a good resonance at 5.8 GHz.

5.7 Radiation pattern of the proposed antenna

Fig. 5.13 shows the measured normalized co-polar and cross-polar E-plane (yz-plane) radiation pattern of the proposed antenna at 2.4 and 5.8 GHz respectively and Fig. 5.14 shows the measured normalized co-polar and cross-polar H-plane (xy-plane) radiation pattern at 2.4 and 5.8 GHz respectively. The co-polar H-plane radiation pattern is purely omni-directional at all the measured frequencies. At 2.4 GHz, the cross-polar H-plane radiation is just around -30 dB and at 5.8 GHz, the cross-polar H-plane radiation is in between -10 dB to -20 dB. The co-polar E-plane radiation pattern is directional along 90^0 and 270^0 respectively. In the co-polar E-plane, the radiation patterns remain roughly a dumbbell shape like a small dipole leading to bidirectional patterns. The cross-polar E-lane radiation is just around -30 dB at 2.4 GHz and at 5.8 GHz, the cross-polar E-plane radiation is in between -10 dB to -20 dB. Cross-polarization for both E-plane and H-plane are comparable to that of the co-polar radiation pattern at some angles. So too many bends are not good idea in terms of radiation pattern purity even if it reduces the size significantly.

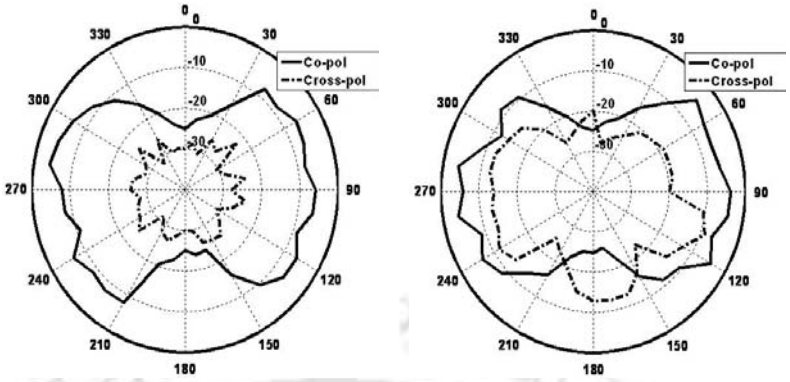

(a) (b)

Figure 5.13: Measured E-plane (yz-plane) radiation patterns of the proposed antenna at **(a)** 2.4 GHz and **(b)** 5.8 GHz.

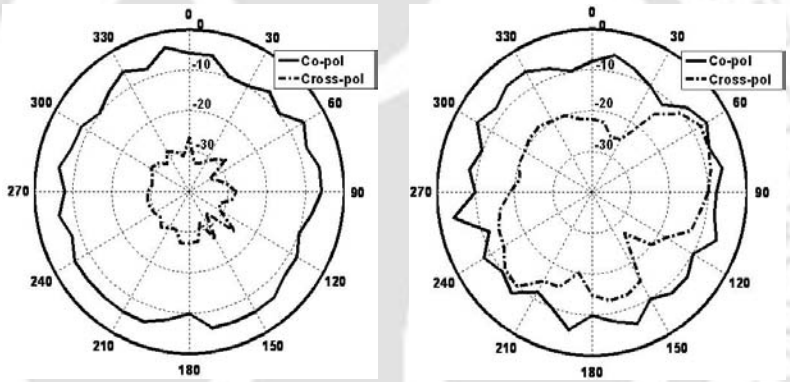

(a) (b)

Figure 5.14: Measured H-plane (xy-plane) radiation patterns of the proposed antenna at **(a)** 2.4 GHz and **(b)** 5.8 GHz.

5.8 Summary

The proposed antenna is a microstrip line fed folded strip dual-band monopole antenna with a straight protruding stub from the ground plane for application in RFID and WLAN is presented. The antenna is fabricated and all the antenna parameters such as reflection coefficient, gain and radiation pattern is measured. The measured results are in accordance with the simulated results. The antenna exhibits appropriate gain characteristics and consistent radiation pattern and can be usable in RFID and WLAN application in future. This new antenna attains 8.25 percent size reduction, 57.95 percent average bandwidth improvement and 16.19 percent average gain enhancement when compared to contemporary dual-band PMAs [141].

6

Rectangular UWB PMA with multiple bends in the feed region

Contents

6.1 Introduction 132
6.2 UWB PMA 138
6.3 Single notch UWB PMA 141
6.4 Double notch UWB PMA 146
6.5 Variability of UWB antenna parameters 152
6.6 Summary 162

6.1 Introduction

Usage of internet and mobile phones has rapidly increased in last two decades. Thus thirst for new technologies is also increasing. The rapid growth in technology and the successful commercial deployment of wireless communications are significantly affecting the daily lives. In this generation, consumers can access information around the globe from anywhere and at any time. It is due to the transforming of analog cellular communication to digital domain, the fast development of 3G and 4G radio systems and due to the replacement of wired connections with Wi-Fi and Bluetooth (wireless). Since consumers need high capacity, faster service and more secure wireless connections, these new technologies have to find place in this overcrowded and scarce radio frequency (RF) spectrum. Every radio technology occupies specific part of spectrum to avoid interference like signals for TV, radio, mobile phones are sent at different frequencies thus demanding the available RF spectrum with new services. Ultra-wideband communications is basically different from all other communication techniques because it uses extremely narrow RF pulses to communicate between transmitters and receivers. These narrow pulses directly give large bandwidth in frequency domain and offer many advantages such as large throughput, covertness, robustness to jamming, and coexistence with current radio services. This UWB communication was developed in 1960.

UWB technology had been used earlier only for the military purposes due to its ability to go beneath the ground. But in the recent years, it is being used for different applications due to its large bandwidth and high data rate[71]. UWB is different from the conventional narrow band technology. Instead of transmitting over different bands of frequencies, here we transmit over a wide frequency band. The main concept behind UWB radio systems as told earlier is that they transmit pulses of very short duration, as opposed to traditional communication schemes, which send sinusoidal waves. The role that UWB antennas play in all of this is that they have to be able to transmit these pulses as accurately and efficiently as possible.

The spectrum of UWB signal was a major problem for its commercial usage. All the radio communications have different rules and regulations for power output in certain frequency bands. Because of this, we can avoid interference with the users of the nearby frequency bands. But UWB occupies a very large spectrum thus interfering with the neighboring frequency bands. To minimize this problem, Federal Communications Commission (FCC) and other regulatory groups specified spectral masks for various applications which show the allowed power output for specific frequencies [166]. Fig. 6.1

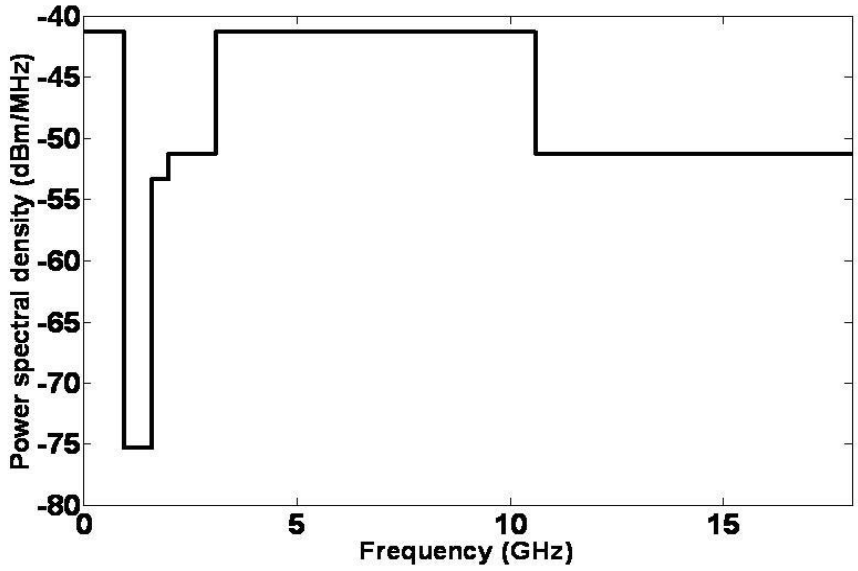

Figure 6.1: FCC mask for UWB indoor communications.

shows the FCC spectral mask for indoor UWB communication system. FCC defined the bandwidth of UWB as 7.5 GHz available between 3.1 GHz to 10.6 GHz with the maximum power output of -41.3 dBm/MHz or 75 nW/MHz.

The above spectrum was divided into 3 major categories by FCC regulations: communications, imaging, and vehicular radar. For indoor and outdoor UWB devices in communications devices category, different emission limits are allotted. Between 1.61 GHz and 3.1 GHz, the spectral mask for outdoor devices is 10 dB lower than that for indoor devices. For imaging devices, their operation is restricted to law enforcement and rescue teams.

Before knowing about the specifications of UWB systems or UWB signals, some of the properties of UWB signals should be known which is making the usage of UWB communication more and more elegant. UWB pulses are extremely short pulses (of order ns) with fast rise and fall time. So they have a very broad spectrum with low energy content. These short pulses avoid effects of multipath such as Inter- Symbol- Interference (ISI). Multipath is a phenomenon in which a signal reaches the receiver by traveling in various paths. This is due to reflection, diffraction, absorption and scattering of the electromagnetic energy between transmitter and receiver which occurs due to the presence of objects around it. The reflected signals reach the receiver with different path lengths and thus with different delays. UWB systems are immune to multipath. UWB pulses are separated by more

Table 6.1: UWB Specifications

Operation Band	3.1 GHz-10.6 GHz
Transmission Rate	100Mbps
Transmission Distance	10m
Spatial Capacity	318.3 Kbps
Spectral Capacity	0.013 bps/Hz
Power Consumption	30 mW

than one pulse width so that they do not overlap after multipath. As the pulse width decreases, the distance separating the multipath increases. By decreasing the duty cycle of the system, multipath interference can be decreased. Secondly, UWB pulses can easily penetrate through walls, doors and any environment. Thirdly, UWB systems have high spatial capacity measured in bits per second per square meter. Spatial capacity can be calculated as the maximum data rate of a system divided by the area over which that system can transmit. The speed of data transmission is very high in UWB systems with low system complexity and low cost [167]. The simplest UWB transmitter could be assumed to be a pulse generator, a timing circuit and an antenna. Now a days the UWB transmitters and receivers are produced with small size. This is due to the reduction of passive components such as modulators, demodulators and IF stages. This fact can reduce cost, size, weight and power consumption of UWB systems compared with conventional narrowband communication systems. Table 6.1 gives the UWB specifications.

An antenna plays a vital role in UWB system as antenna is a very important component in many conventional wireless systems. But there exist many critical challenges in designing a UWB antenna than a narrow band antenna [168].

(i) First of all frequency bandwidth is an important parameter for UWB antenna which distinguishes a UWB antenna from other antennas. According to the FCC ruling in 2002, the UWB antenna should have an absolute bandwidth no less than 500 MHz or a % fractional bandwidth at least 20%.

(ii) Secondly, the UWB antenna should exhibit consistent performance over the entire operational band from 3.1 GHz to 10.6 GHz. All the UWB antenna characteristics such as impedance bandwidth, gain and radiation pattern should be stable across the entire band. Sometimes it is needed that the UWB antenna should be designed for band-rejected characteristics to eliminate

the potential interference with other narrowband services occupying some operational band [169, 170].

(iii) Thirdly, the UWB antenna should exhibit omni-directional or directional radiation patterns depending on the practical applications. For mobile and hand-held systems, omni-directional radiation pattern are normally required. For radar, imaging and other directional applications where high gain is required, directional radiation pattern characteristics are preferred.

(iv) Fourthly, the compactness of UWB antenna is mostly desirable to accommodate in the small and hand-held devices. It is also highly desirable that the UWB antenna should be low profile and can be integrable with printed circuit board (PCB).

(v) Fifthly for the performance of overall system, the UWB antenna design should be optimal. For example, the antenna should be designed such that the overall device (antenna and RF front end) complies with the required power emission mask given by the FCC or other regulatory bodies.

(vi) Finally, a good time domain characteristics are necessary for the UWB antennas. Antennas used for the narrow band systems have consistent performances regarding the basic antenna parameters such as gain, reflection coefficient and have little variation across the operational band. In contrast very short pulses are used for the data transmission in UWB systems and a huge band is occupied by the UWB system. Hence, the UWB antenna can not be considered as the "spot filter" any more but a "band-pass filter". Hence, the UWB antenna provides more significant effect on the input signal. As a result the primary concerns for the UWB antenna is the minimum pulse distortion [171] because the signal is the carrier of useful information. That why the time domain characteristics of the UWB antenna is highly indispensable and important to investigate.

Shortly after the FCC's ruling in February 2002, research started throughout the world to design the various systems and components that will enhance the credibility of the UWB system and UWB antenna is one of them. Last ten years researchers all over the world designed and proposed many UWB antennas, which are compact, low cost, less fragile, light weight and easily incorporable in the portable and hand held devices in the UWB system. There are many challenges in the UWB

antenna design and the notable among them are broadband impedance matching, appropriate gain characteristics and stable radiation pattern.

But along with the vast operating bandwidth of the UWB antenna (3.1-10.6 GHz), there exist some narrowband wireless services, which occupy some of the frequency bands in the UWB bands. The most well known among them is wireless local area network (WLAN) IEEE802.11a and HIPERLAN/2 WLAN operating in 5-6 GHz band. Apart from WLAN, in some European and Asian countries, world interoperability for microwave access (WiMAX) service from 3.3-3.6 GHz also occupy in the UWB band. In some antenna designs, the UWB antenna uses filters to notch out the interfering bands. But the use of filters increases the complexity of the UWB system and also increases the weight and size. Hence, it is needed to design the UWB antenna with dual band-notched characteristics both in 3.3-3.6 GHz and 5-6 GHz to mitigate the interference between the narrowband wireless systems and UWB systems. Till now, many designs of the UWB band-notched antennas are proposed [172-188] to alleviate the disturbance caused by the WLAN with the UWB system.

The simple and most commonly used approach is to incorporate various shapes and sizes of slots into the main radiator. In [172], a bell shaped patch with stair case structure is proposed. Apart from two parasitic patches are printed on the substrate to provide the band-notch characteristics. An L-shaped slot [173] is cut in the edges of main radiator with a C-shaped main radiator. An arc shaped slot is cut in the elliptical shaped patch [174], with a rectangular slot is cut in the ground plane. A rectangular tuning stub [175] is embedded in the circular annular ring, which generates the band-notched characteristics in the UWB spectrum. A split ring resonator (SRR) [176] is used in the main patch for the band notched characteristics. A parasitic strip is used for the band notch function [177]. A ring shaped parasitic patch [178] is printed within the central circular slot. The central circular slot is cut from the bell shaped patch. A cutting pie with the flare angle θ is cut from the circular patch [179]. This antenna consists of two monopoles with a small strip bar located in between the two monopoles [180]. A new structure has been proposed [181] for UWB band notch function. A simple arc [182] cut in the circular radiating patch provides the band notch characteristic. An H-shaped structure is printed in the backside of the substrate and two rectangular slots are cut from the ground plane. The radiating patch is rectangular one and fed by a microstrip line [183]. A square shaped SRR is printed on a circular shaped radiating element [184]. Two L-shaped slots are cut from the ground plane with an arc is cut from the circular radiating patch [185]. A deep almost full shaped arc

is cut in the annular circular ring [186]. An E-shaped slot cut from the rectangular radiating patch with a notched ground plane [187]. In this antenna, the circular disc is used as the radiating element, which is fed by the tapered microstrip line. The ground plane is round cornered, which enhance the impedance bandwidth especially at the high frequency. In one structure, two L-shaped slot is cut from the ground plane and in another structure, a pair of square ring resonator is created in the ground plane, which provides the required band-notch characteristic to notch out the WLAN band from the UWB spectrum [188].

Based on the background of the structures of various UWB notch-antennas above, in this chapter a simple and compact microstrip line fed planar UWB antenna with dual band-notched characteristics in 3.48 GHz (3.03-4.04 GHz) and 5.59 GHz (4.76-6.29 GHz) is proposed. The dual band-notched characteristic in the proposed antenna can be achieved by introducing two open-circuited stubs from the two sides of the microstrip feed-line. It is observed that by adjusting the total length of each of the the two open circuited stubs to be to be approximately one quarter the guided wavelength (λ_g) of the required notch frequency, a destructive interference of the current distribution takes place causing the antenna non-radiating at that notch frequency. The tuning of the central notch frequency can be done by suitably adjusting the total length of the two open-circuited stubs. The optimization of the design and the subsequent simulation is done by IE3D software [191]. The proposed antenna provides an impedance bandwidth of 3.1-10.6 GHz with ,$VSWR \leq 2$ except the bandwidths of 3.03-4.04 GHz for WiMAX system and 4.76-6.29 GHz for IEEE802.11a and HIPERLAN/2 WLAN systems. The appropriate gain and stable radiation patterns are also obtained.

In this chapter, a compact UWB antenna of area $30 \times 35 mm^2$ is proposed. Simply by erecting one open-circuited stub on the one sides of the microstrip feed-line, a single band-notched characteristic from 4.76 GHz to 6.29 GHz is obtained. By introducing another open-circuited stub on the other side of the microstrip feed-line, a dual band-notched characteristics for the proposed antenna is created to reduce the potential interference between the narrowband system and the UWB system. Details of simulation results and the antenna designs are presented to demonstrate the performance of the proposed antenna.

6.2 UWB PMA

6.2.1 Antenna design

According to the Schantz [71], UWB PMA has three regions: feed-line, feed region and patch. We can optimize each of these regions for better antenna performance. In this chapter, we have introduced multiple bends in the feed region of the UWB PMA. These steps in the feed region introduce extra resonances in the bandwidth of the stair-cased antenna and hence enhance the bandwidth considerably.

Fig. 6.2 shows the geometry and configuration of an UWB PMA. The antenna (referred to as antenna 1 in this chapter) is fabricated on an h=1.6 mm FR4 epoxy substrate with the dielectric constant ε_r=4.4 and loss tangent tanδ=0.002. As shown in the figure, the shape of the radiating element is rectangular and there is a stair case structure symmetrically at the two bottom corners of the radiating element. The radiating element is fed by 50-Ω microstrip transmission line, which is terminated with a sub miniature A (SMA) connector for the measurement purpose. The electromagnetic software IE3D [191] is employed to perform the design and optimization process. The design parameters are given in the Fig. 6.2.

6.2.2 Results and discussion

The rectangular radiating element has a stair-cased geometry which has two steps at the two bottom corners of the rectangular radiating element. The stair case geometry is responsible for providing the wide operation bandwidth in the UWB (3.1-10.6 GHz) frequency range.

When there are no steps or no stair cased structure in the radiating element shown in the Fig. 6.3(a), the band extends from $f_{0S,LOW}$=3.74 GHz to $f_{0S,HIGH}$=11.13 GHz. The percentage bandwidth in this range is 99.83 as shown in the Fig. 6.4.

Now one more step is introduced at the two bottom corners of the radiating element as shown in the Fig. 6.3(b) and the radiating structure is simulated. After simulation, it is found that the band extends from $f_{1S,LOW}$=3.53 GHz to $f_{1S,HIGH}$=12.13 GHz, the percentage bandwidth in this range is 109.83 as shown in the Fig. 6.4. Hence appreciable bandwidth has been enhanced on the inclusion of one step as compared to previous case in the two bottom corners of the radiating element.

Now one more step is introduced in the two bottom corners of the rectangular radiating element. The total number of steps now has increased to two. This radiating structure is the UWB PMA shown in the Fig. 6.2. After simulation, it is found that the band extends from $f_{2S,LOW}$=3.48 GHz

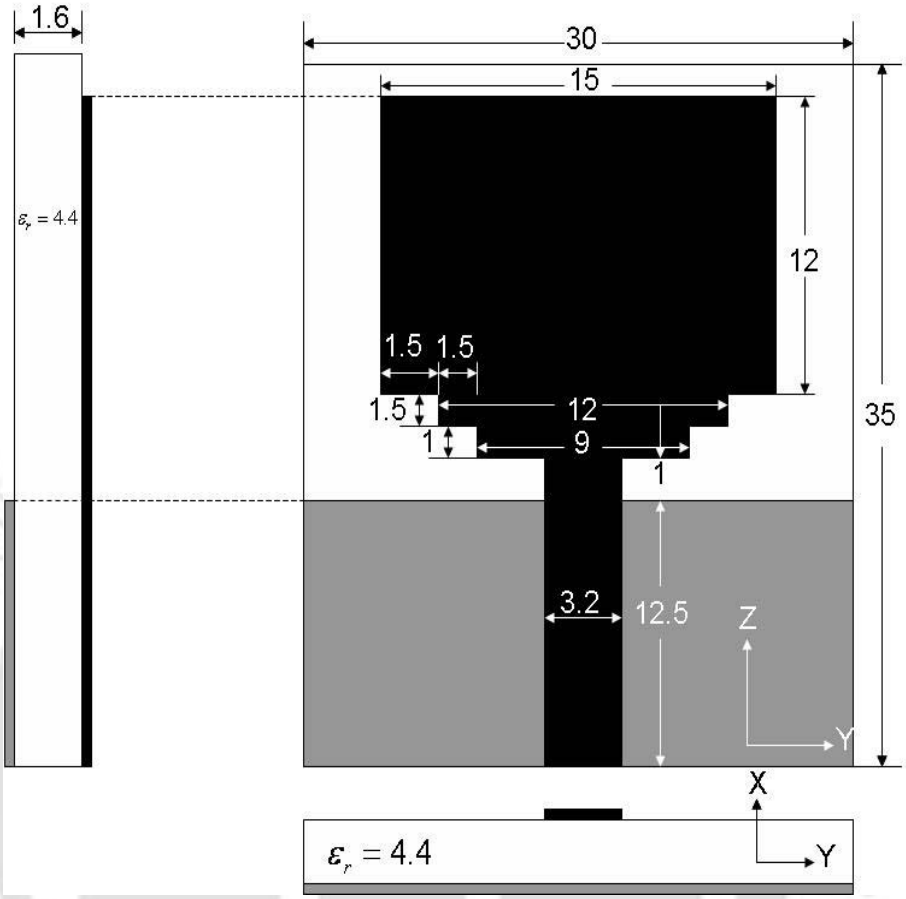

Figure 6.2: Geometry of antenna 1 (UWB PMA).

to $f_{2S,HIGH}$=13.38 GHz, the percentage bandwidth in this range is 117.43 as shown in the Fig. 6.4.

From the above study it is clear that as the number of steps in the stair case geometry increase, the bandwidth of the UWB PMA (antenna 1) enhances considerably. This is because the steps in the stair case geometry helps in proper impedance matching between the microstrip feed-line and the rectangular radiating element.

Fig. 6.5 shows the fabricated prototype of the UWB PMA (referred as the antenna 1). Fig. 6.6 shows the comparison between the simulated and measured VSWR of the antenna 1. The VSWR of the antenna 1 was measured by the Rohde and Schwarz ZVA 24 network analyzer. A good agreement of the measured and simulated VSWR is observed in case of antenna 1. The simulated VSWR graph cuts the VSWR=2 line at $f_{2S,LOW}$=3.48 GHz and remains below the line till $f_{2S,HIGH}$=13.38 GHz (% bandwidth=117.43) and the measured VSWR graph cuts the VSWR=2 line at 3.24 GHz and remains below the line till 13.83 GHz (% bandwidth=124.07). This depicts that there is good impedance

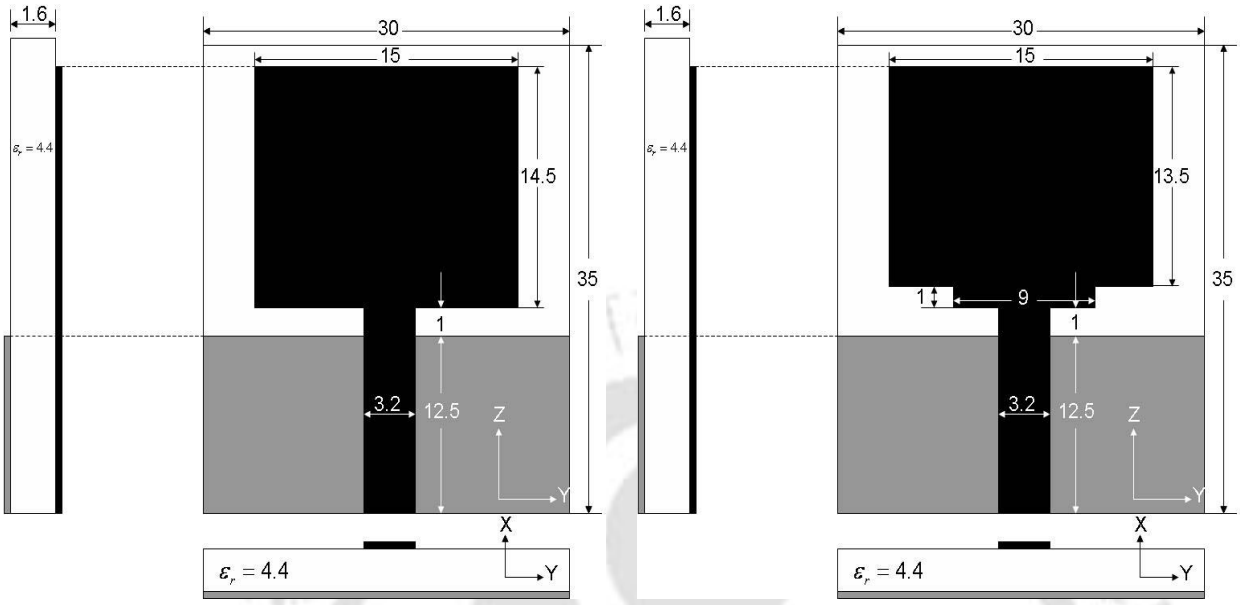

Figure 6.3: Geometry of radiating UWB antennas with **(a)** zero step and **(b)** one step in the stair-cased structures at the bottom corners of the rectangular radiating element.

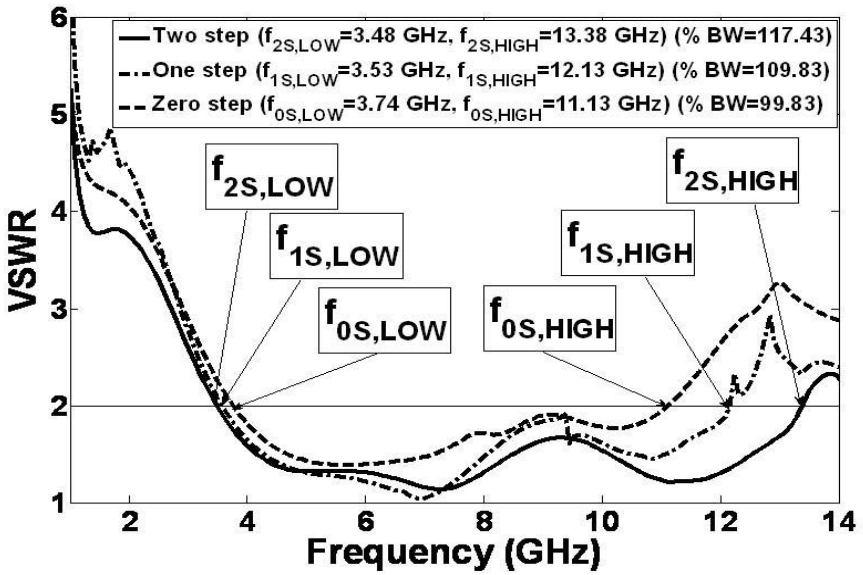

Figure 6.4: Comparison of VSWR graphs of radiating UWB antennas with zero step, one step and two steps in the stair-cased structures at the bottom corners of the rectangular radiating element.

matching between the microstrip transmission line and the stair cased rectangular radiating element. The staircase structure improves the impedance matching and the bandwidth of the antenna 1. Fig. 6.7 represents the comparison of simulated and measured gain in dBi versus frequency of the UWB

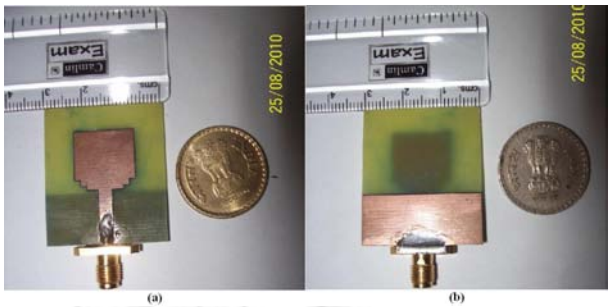

Figure 6.5: Fabricated prototype of the UWB PMA (antenna 1) **(a)** Top View **(b)** Bottom View.

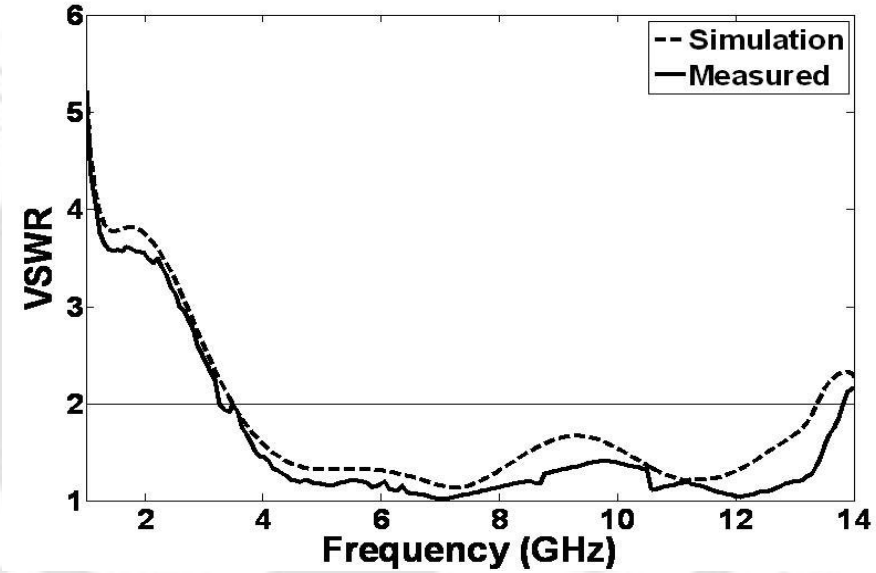

Figure 6.6: Comparison of simulated and measured VSWR of antenna 1.

PMA (antenna 1). The simulated and measured gains are flat and consistent throughout the UWB band. The range of simulated gain is from 3.51 dBi at 3 GHz to 4.5 dBi at 12 GHz. Similarly the range of measured gain is from 3.65 dBi at 3 GHz to 4.89 GHz at 12 GHz.

6.3 Single notch UWB PMA

6.3.1 Antenna design

Along with the UWB spectrum (3.1-10.6 GHz), some narrowband systems operate. Notable among them is IEEE 802.11a and HIPERLAN/2 WLAN system. Hence, to mitigate the interference from the above narrowband system, band-notch function is desirable in the UWB system.

Fig. 6.8 shows the geometry and dimension of the UWB PMA with band-notch characteristic in 5-6 GHz band (denoted as antenna 2) and Fig. 6.9 shows the fabricated prototype of the single notch

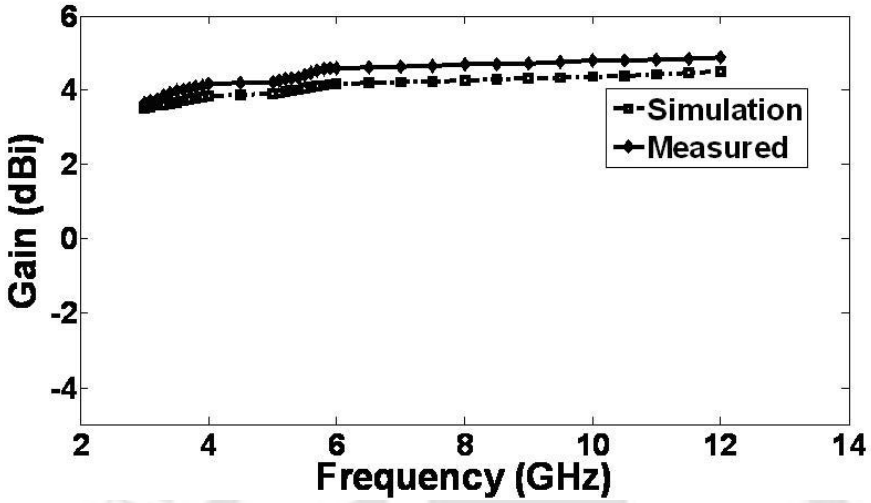

Figure 6.7: Comparison of simulated and measured gain (dBi) vs. frequency of antenna 1.

UWB PMA (referred to as the antenna 2). By introducing an open circuited stub on the right side of the microstrip fee-line, a band notch function is created. It is noteworthy that when the band-notched structure is applied to the antenna 1, there is no redesigning work needed for the previously taken dimensions. In general, the main aim behind the design methodology of the notch function is to tune the total length of the open circuited stub approximately equal to the quarter of the guided wavelength (λ_g) of the desired notch frequency. An open circuited ($\lambda_g/4$) line has an input impedance as short circuit. For a short circuit at the notch frequency, the reflection coefficient is -1. Hence, all the signals through the microstrip line get reflected back. They do not reach the antenna. Thereby, the antenna is non-responsive at the notch frequency.

The expression for the total length (L) of the open circuited stub for a given notch frequency (f_n) is given by

$$L = \frac{\lambda_g}{4} \tag{6.1}$$

where

$$\lambda_g = \frac{c}{f_n \sqrt{\varepsilon_{eff}}} \tag{6.2}$$

$$\varepsilon_{eff} = \sqrt{\frac{\varepsilon_r + 1}{2}} \tag{6.3}$$

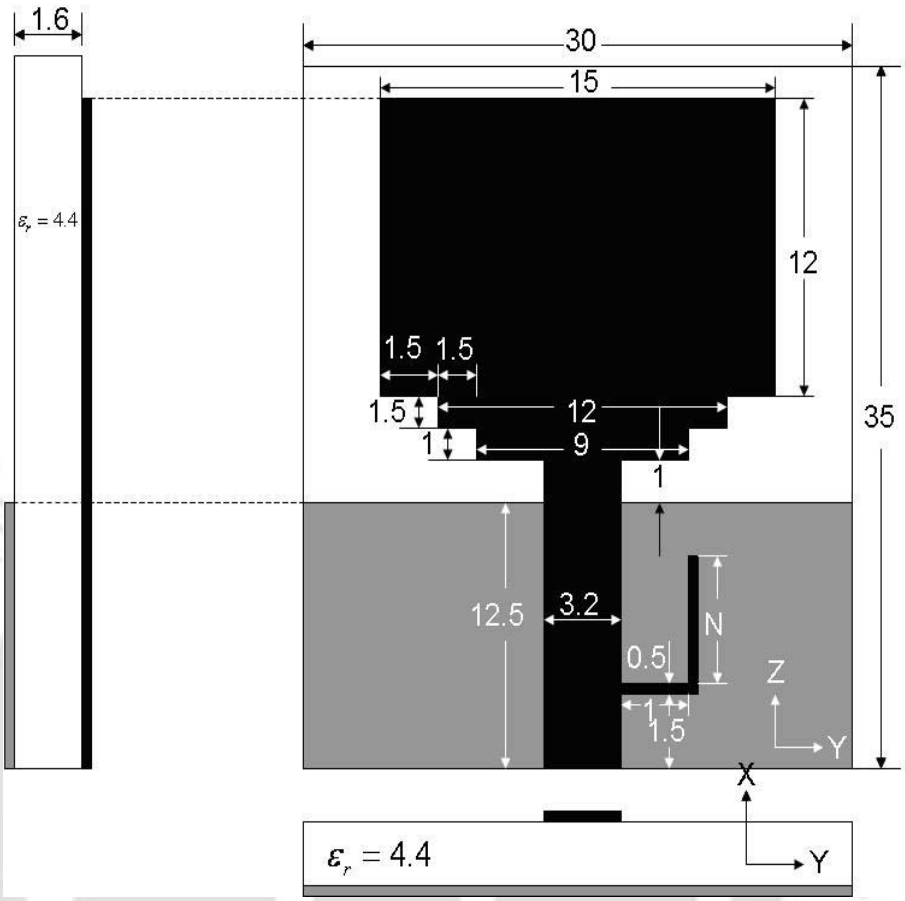

Figure 6.8: Geometry of antenna 2 (single notch UWB PMA).

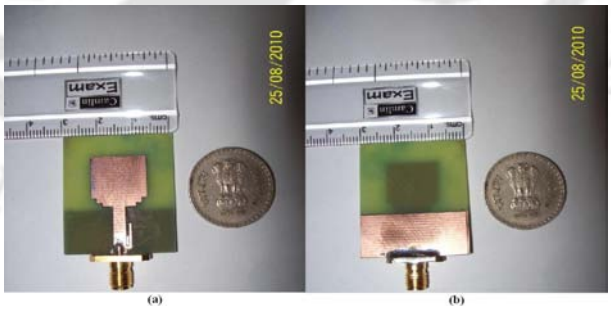

Figure 6.9: Fabricated prototype of the single notch UWB PMA (antenna 2) **(a)** Top View **(b)** Bottom View.

where L is the total length of the open circuited stub , λ_g is the guided wavelength of the microstrip feed line, ε_{eff} is the effective dielectric constant of the FR4 epoxy substrate , c is the speed of light in free space and ε_r is the relative dielectric constant of the substrate. The value of the relative dielectric constant ε_r =4.4. Using equation (6.3), the value of the ε_{eff} was found to be 1.6431. Using the equation (6.2), λ_g was found to be 33.95 mm. By simulation the total length of the open circuited

stub (L) was found to be L= (1+0.25+0.25+7) =8.5 mm. Hence the total length of the open circuited stub (L) is (8.5/33.95)= 0.25 times the guided wavelength (λ_g) of the desired notch frequency (f_n=5.5 GHz).

6.3.2 Results and discussion

The performance of the simulated VSWR of the antenna 2, which provides the desired center notch frequency of 5.5 GHz and measured VSWR by the Rohde and Schwarz ZVA 24 network analyzer of the antenna 2 along with the measured VSWR of the antenna 1, is shown in the Fig. 6.10. The measured VSWR of antenna 2 is in accordance with the simulation. From the figure, it is very clear that, the desired filtering property is achieved by introducing an open circuited stub on one side of the microstrip feed-line. The single notch UWB PMA effectively blocks out the 5-6 GHz and still performs excellent impedance matching at other frequencies of UWB band. The tip of the desired notch band is at 5.59 GHz with the simulated VSWR value of 10.63 and the tip of the notch band is at 5.67 GHz with the measured VSWR value of 10.19. The measured notch band stretches from 4.64 GHz to 6.51 GHz, in which whole of the WLAN band is immersed. The simulated VSWR for the antenna 2 extends from 3.08 GHz to 11.29 GHz (% bandwidth=114.26) with the notch band stretched from 4.64 GHz to 6.30 GHz having the VSWR notch peak value of 10.63 at 5.59 GHz. Similarly, the measured VSWR for the antenna 2 extends from 2.91 GHz to 13.37 GHz (% bandwidth=128.50) with the notch band stretched from 4.64 GHz to 6.51 GHz having the VSWR notch peak value of 10.19 at 5.67 GHz.

Fig. 6.11 depicts the simulated VSWR of the antenna 2 for the different values of N (in other words, it is the different values of total length of open circuited stub (L)). As observed, the adjustment of the band-notched frequency can be done by varying the length (N) (in other words, L) of the open circuited stub. By decreasing N from 8.1 to 6.4 mm, the tip of the notched band shifted from 5 GHz to 6 GHz. By simulation, the total length of the open circuited stub (L) was found to be L= (1+0.25+0.25+7) =8.5 mm.

The antenna gain of antenna 2, compared to antenna 1 in the entire UWB is presented in the Fig. 6.12, which shows a sharp decrease in gain at 5.5 GHz, which is the center frequency of the WLAN band and good performances at other frequencies of the UWB band. The range of simulated gain in dBi is 3.54 dBi at 3 GHz to 4 dBi at 12 GHz with a sharp drop of gain occurs at 5.5 GHz. The value of simulated gain at 5.5 GHz is -10.31 dBi. Similarly, the range of measured gain in dBi is 3.57 dBi

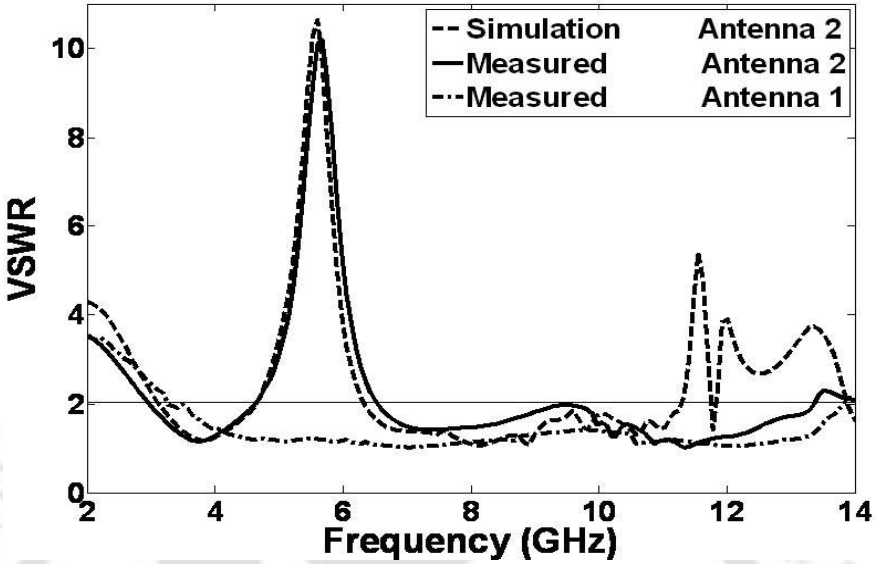

Figure 6.10: Measured and simulated VSWR of antenna 2, compared to antenna 1.

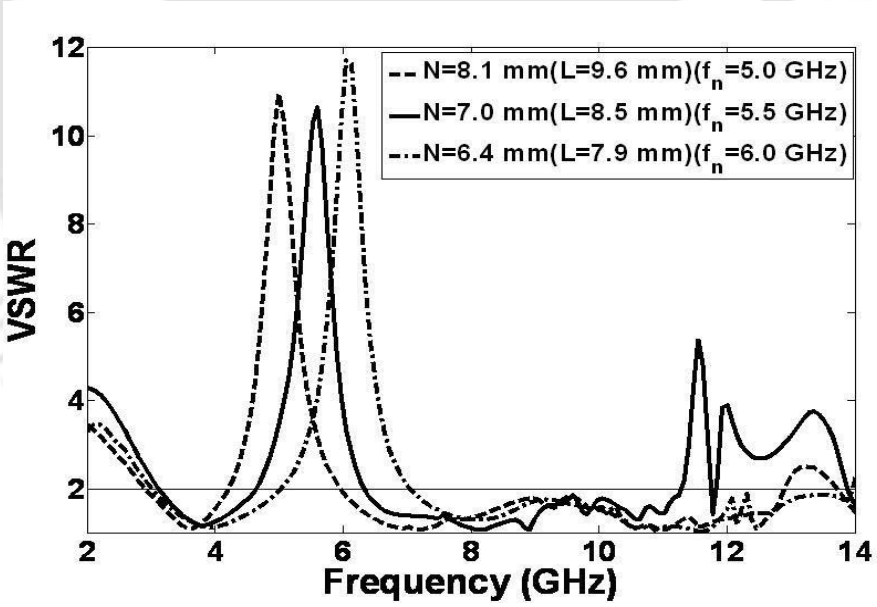

Figure 6.11: Effect of length (N) on the VSWR of the antenna 2.

at 3 GHz to 4.76 dBi at 12 GHz with a sharp drop of gain occurs at 5.6 GHz. The value of measured gain at 5.6 GHz is -10.13 dBi.

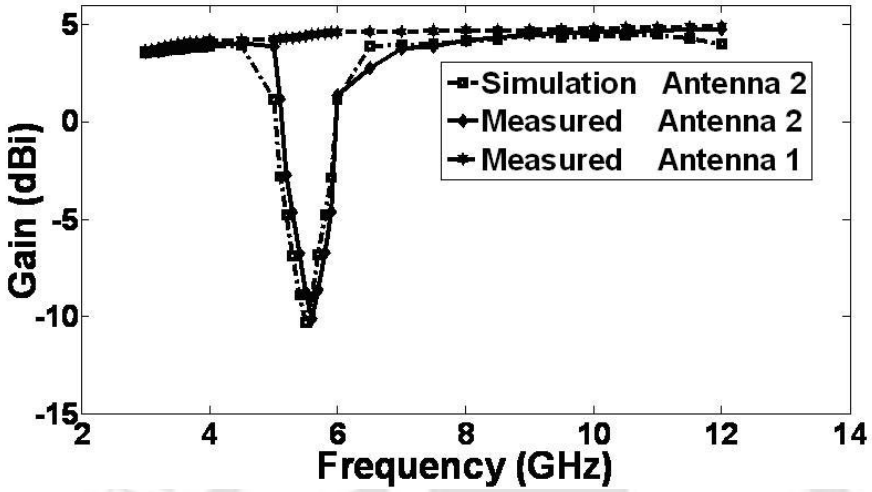

Figure 6.12: Simulated and measured gain (dBi) of antenna 2, compared with the measured gain of antenna 1.

6.4 Double notch UWB PMA

6.4.1 Antenna design

Apart from WLAN, WiMAX occupies band from 3.3-3.6 GHz, which is within the UWB frequency band of operation and this interferes with the operation of the UWB systems. Hence, to mitigate the potential interference between the narrow-band systems, in this chapter, a new design of double notch UWB PMA is presented. By introducing another open circuited stub on the left side of the microstrip feed-line, the appropriate dual band-notched functions both in 3.3-3.6 GHz and 5-6 GHz are achieved. Fig. 6.13 depicts the geometry of the double notch UWB PMA (referred to as antenna 3 in this chapter) in which two open circuited stubs are erected on both the sides of the microstrip feed line. Fig. 6.14 shows the fabricated prototype of the double notch UWB PMA (referred to as the antenna 3). The open circuited stub on the left side of the microstrip feed-line provides the notch band at center frequency of 3.4 GHz and the open circuited stub on the right side of the microstrip feed-line provides another one at center frequency of 5.5 GHz, each of the total length of the open circuited stub is obtained by using the expression (6.1). The optimized design parameters are shown in the Fig. 6.13.

The guided wavelength (λ_g) at 5.5 GHz was found to be 33.95 mm. By simulation, the total length of the right side open circuited stub (L) was found to be L= (1+0.25+0.25+7) =8.5 mm. Hence, the total length of the right side open circuited stub (L) is (8.5/33.95)= 0.25 times the guided wavelength

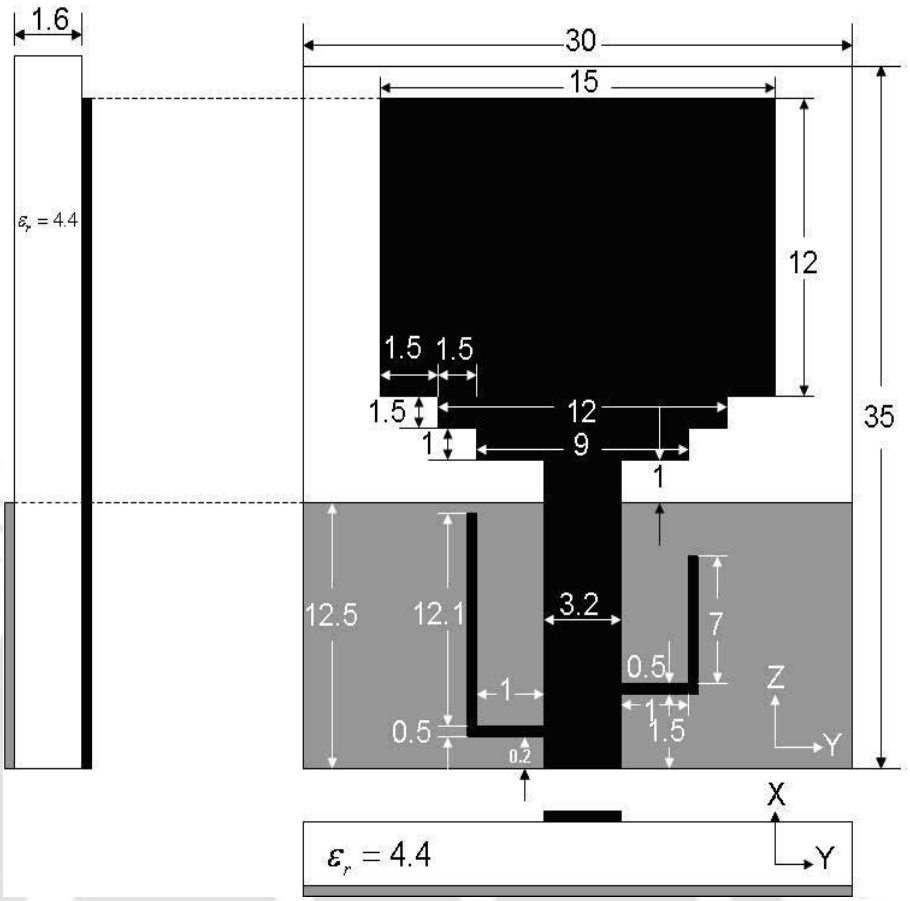

Figure 6.13: Geometry of antenna 3 (Double notch UWB PMA).

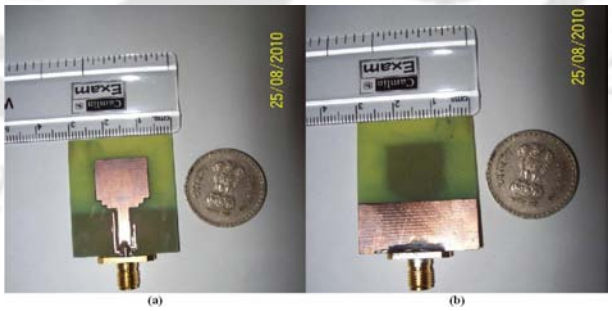

Figure 6.14: Fabricated prototype of the double notch UWB PMA (antenna 3) **(a)** Top View **(b)** Bottom View.

(λ_g) of the desired notch frequency (f_n=5.5 GHz). Similarly, λ_g at 3.48 GHz was found to be 67.25 mm. By simulation the total length of the left side open circuited stub (L_1) was found to be L_1= (1+0.25+0.25+12.1) =13.6 mm. Hence, the total length of the left side open circuited stub (L_1) is (13.6/67.25)= 0.20 times the guided wavelength (λ_g) of the desired notch frequency (f_n=3.48 GHz).

6.4.2 Results and discussion

Fig. 6.15 shows the measured and simulated VSWR of the antenna 3 compared to the measured VSWR of antenna 1. The simulated VSWR graph of the antenna 3 provides two notches centered at 3.48 GHz and 5.59 GHz respectively. The frequency band at center notch frequency of 3.48 GHz (VSWR=12.78) extends from 3.03 GHz to 4.04 GHz and the frequency band at center notch frequency of 5.59 GHz (VSWR=9.19) extends from 4.76 GHz to 6.29 GHz. Similarly the measured VSWR graph of the antenna 3 provides two notches centered of 3.63 GHz and 5.37 GHz. The frequency band at center notch frequency at 3.63 GHz (VSWR=13.15) extends from 3.15 GHz to 4.02 GHz and the frequency band of center notch frequency at 5.37 GHz (VSWR=8.81) extends from 4.58 GHz to 6.20 GHz. The measured UWB extends from 2.63 GHz to 13.1 GHz (% bandwidth=133.12).

Fig. 6.16 shows the variation of simulated and measured gain in dBi with the frequency for the double notch UWB PMA (antenna 3) compared with the measured gain values for UWB PMA (antenna 1). From the Figure, it is clear that there is sharp dip in the gain at around 3.5 GHz and 5.5 GHz, which confirms that double notch UWB PMA becomes non-responsive in the two-narrowband systems operating frequencies (WiMAX and WLAN). However, for the other frequencies outside the notched band, the antenna gain is appropriately consistent and almost stable in the whole of the UWB band. The range of simulated gain in dBi is 3.50 dBi at 3 GHz to 4.57 dBi at 12 GHz with a two sharp drops of gain occurs at 3.5 GHz and 5.5 GHz respectively. The value of simulated gain at 3.5 GHz is -15.15 dBi and 5.5 GHz is -10.32 dBi respectively. Similarly, the range of measured gain in dBi is 3.45 dBi at 3 GHz to 4.7 dBi at 12 GHz with a two sharp drops of gain occurs at 3.6 GHz and 5.4 GHz respectively. The value of measured gain at 3.6 GHz is -15.35 dBi and 5.4 GHz is -10.25 dBi respectively.

At 3.48 GHz and 5.5 GHz, the current is diverted to the respective open-circuited stubs elongated from the microstrip feed-line. Hence the concentration of current is very high at the microstrip feed-line and open ended stub junction. As the current is high, the input resistance is very low which is equal to almost zero input resistance at the feeding point as shown in the Fig. 6.17. On the other hand, the reactance value is very high at 3.48 GHz and 5.5 GHz respectively which is shown in Fig. 6.18. In other words, the microstrip feed-line behaves as the short circuited transmission line at 3.48 GHz as well as at 5.5 GHz due to the two quarter wave open circuited stubs on the two sides of the microstrip transmission line. In other words, the two open ended stubs put two shorts on the two

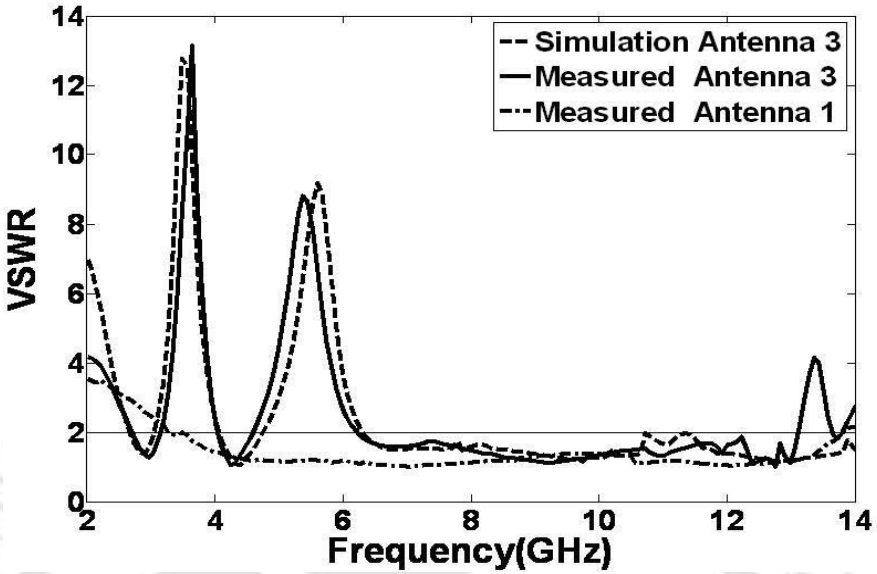

Figure 6.15: Simulated and measured VSWR of antenna 3, compared to antenna 1.

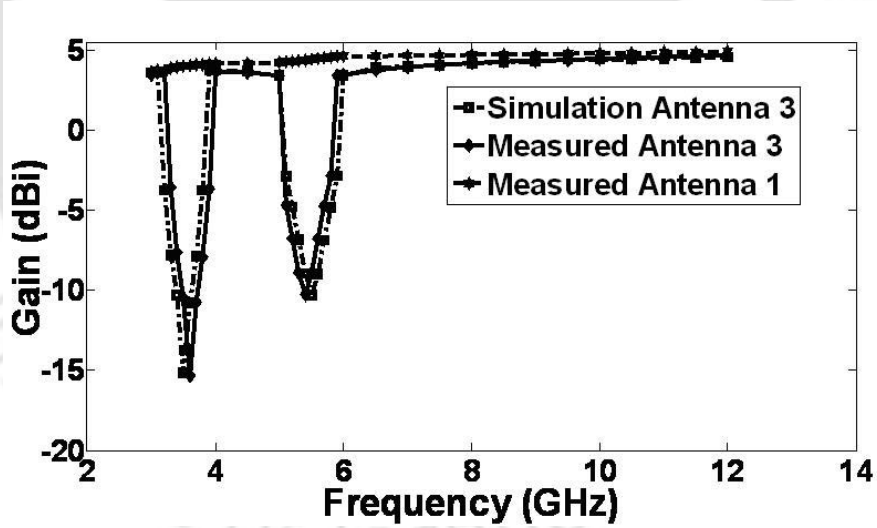

Figure 6.16: Simulated and measured gain (dBi) of antenna 3, compared with the measured gain of antenna 1.

side of the microstrip feed line. Due to the almost zero input impedance at the microstrip feed-line, there is huge impedance mismatch at the feeding point causing the antenna to be nonresponsive at the desired notch frequency bands i.e. at 3.48 GHz and 5.5 GHz.

At 3.4 GHz and 5.5 GHz, the current is diverted to the respective open-circuited stubs elongated from the microstrip feed-line is shown in Fig. 6.19 (a) and Fig. 6.19 (b). At 3.4 GHz and 5.5 GHz the current is flowing in one direction. Hence the concentration of current is very high at the microstrip

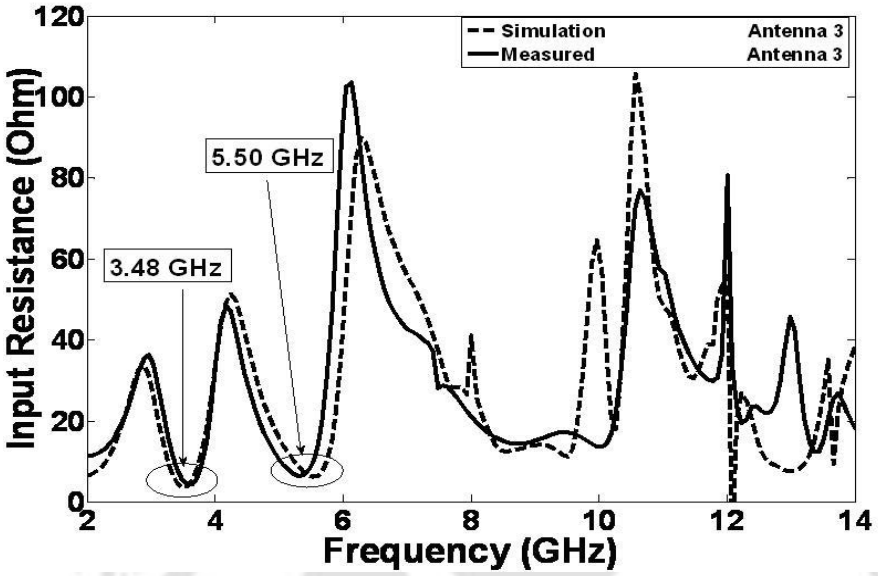

Figure 6.17: Comparison between the simulated and measured input resistance of antenna 3.

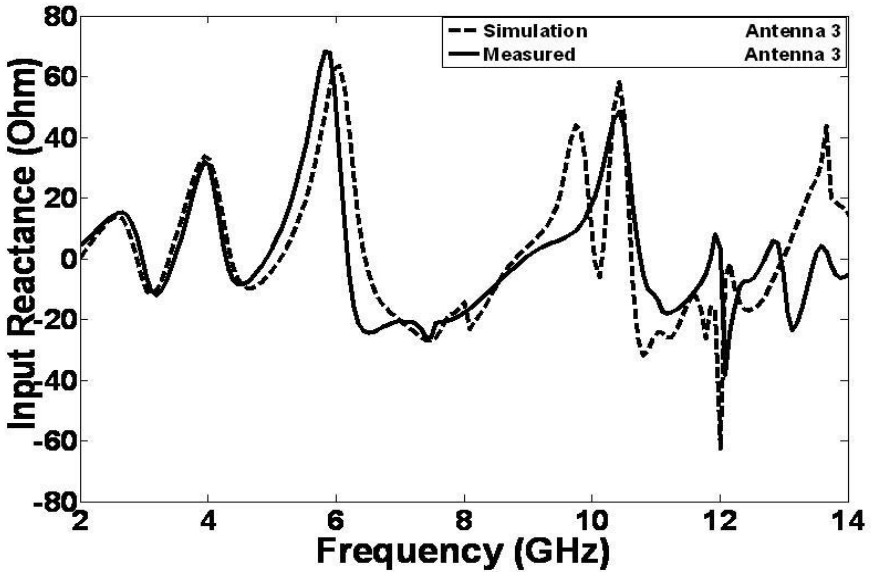

Figure 6.18: Comparison between the simulated and measured input reactance of antenna 3.

feed-line and open ended stub feed-line junction. As the current is high, the input resistance is very low which is equal to almost zero input resistance at the feeding point as shown in the Fig 5.14 (a). On the other hand the reactance value is very high at 3.4 GHz and 5.5 GHz respectively which is shown in Fig 5.14 (b). In other words, the microstrip feed-line behaves as the short circuited transmission line at 3.4 GHz as well as at 5.5 GHz due to the two quarter wave open circuited stubs on the two

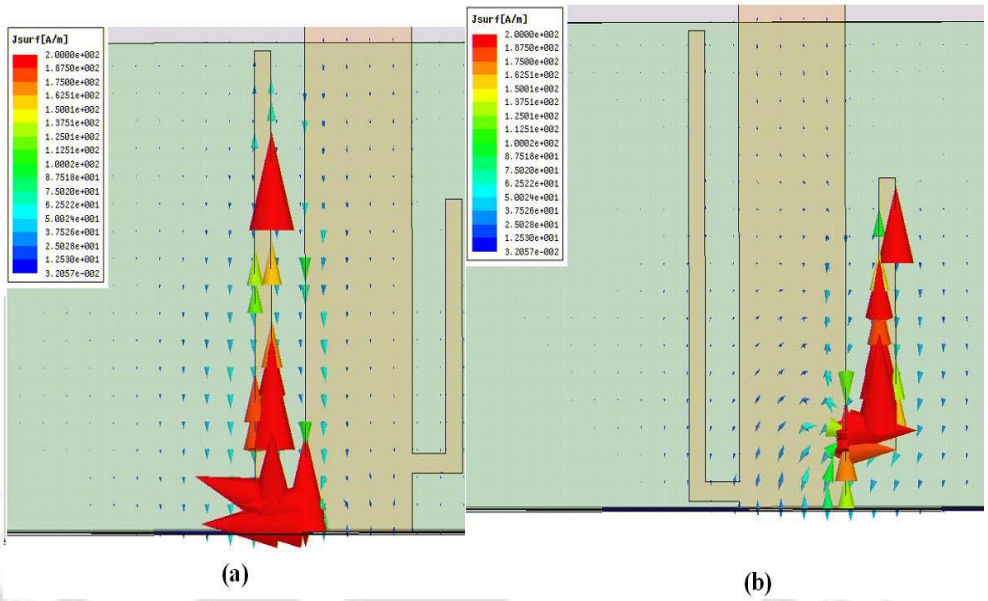

Figure 6.19: Direction and magnitude of the surface current distribution for double notch UWB PMA (antenna 3) **(a)** at 3.4 GHz and **(b)** at 5.5 GHz.

sides of the microstrip transmission line or the two open ended stubs put two shorts on the two side of the microstrip feed line. Due to the almost zero input impedance at the microstrip feed-line, there is huge impedance mismatch at the feeding point causing the antenna to be nonresponsive at the desired notch frequency bands i.e. at 3.4 GHz and 5.5 GHz.

Fig. 6.20 shows the measured normalized co-polar and cross-polar E-plane (yz-plane) radiation pattern of the antenna 3 at 4.5, 7.5, 9.5 and 12 GHz respectively and Fig. 6.21 shows measured normalized co-polar and cross-polar H-plane (xy-plane) radiation pattern of the antenna 3 at 4.5, 7.5, 9.5 and 12 GHz respectively. The co-polar H-plane radiation pattern is purely omni-directional at all the measured frequencies. At 4.5, 7.5, 9.5 and 12 GHz, the cross polar H-plane radiation pattern is in between -30 dB and -20 dB. Hence not much radiation occurs in the cross polar direction and more radiation occurs in the co-polar direction, making the proposed antenna an efficient radiator in the required direction. The co-polar E-plane radiation pattern is directional along 90^0 and 270^0 respectively. In the co-polar E-plane, the radiation patterns remain roughly a dumbbell shape like a small dipole leading to bidirectional patterns. Like cross-polar H-plane radiation pattern at 4.5, 7.5, 9.5 and 12 GHz, the cross-polar E-plane radiation pattern is in between -30 dB and -20 dB, showing not much energy radiation occurs in the cross-polar direction. The proposed band-notched structures including the single notch and double notch ones have little influence on the radiation patterns of the

UWB PMA. Hence, the antenna 3 exhibits stable and constant radiation pattern at all the frequencies.

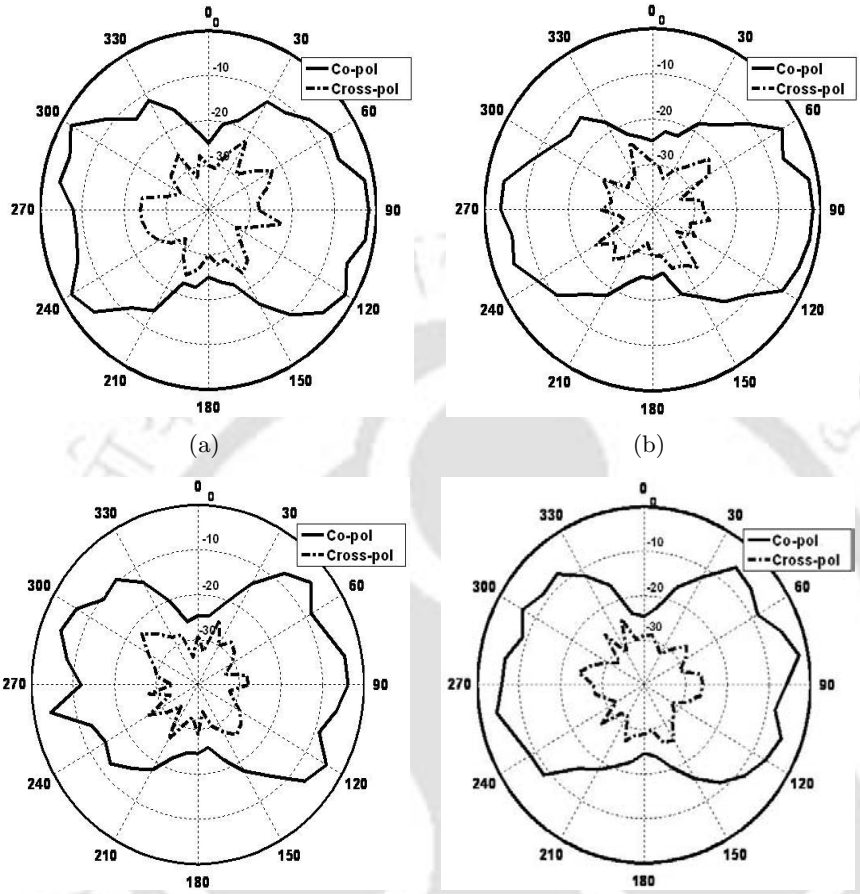

Figure 6.20: Measured E-plane (yz-plane) radiation patterns of double notch UWB PMA (antenna 3) at **(a)** 4.5 GHz, **(b)** 7.5 GHz, **(c)** 9.5 GHz and **(d)** 12 GHz.

6.5 Variability of UWB antenna parameters

6.5.1 Variability in frequency domain

6.5.1.1 Magnitude of transfer function

For an ideal UWB system, when a pulse is sent from a transmitting antenna, the receiving antenna should receive the undistorted version of the transmitted pulse. The function associated with the pulse transmitted and received in the frequency domain is known as the system transfer function $H(\omega)$. For accurate analysis of the system transfer function, a transmit-receive antenna system is to be used. Fig. 6.22 shows the basic schematic diagram for a typical transmit-receive antenna system in UWB communications [193].

To relate the output power of the receive antenna to the input power of the transmit antenna, the

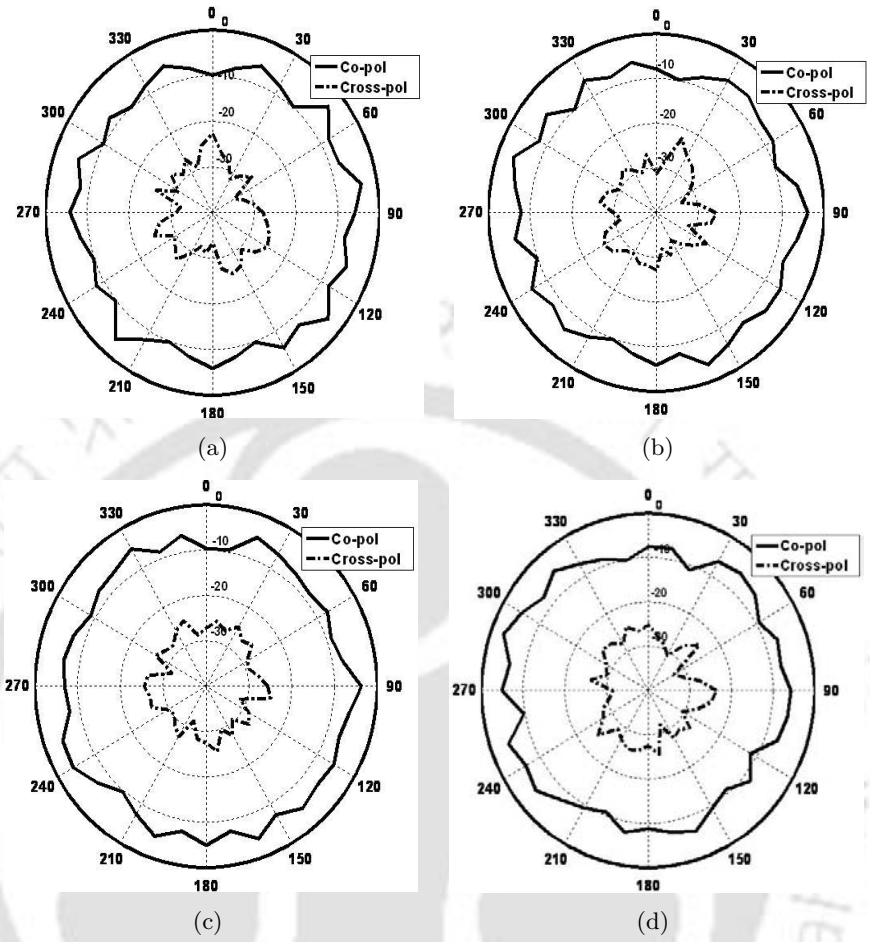

Figure 6.21: Measured H-plane (xy-plane) radiation patterns of double notch UWB PMA (antenna 3) at **(a)** 4.5 GHz, **(b)** 7.5 GHz, **(c)** 9.5 GHz and **(d)** 12 GHz.

Friis transmission formula can be used and it is given in equation 6.4, where it is assumed that each antenna such as transmit and receive antenna are in the far-field zone of each other. The expression in equation 6.4 is frequency dependent case when the parameters in equation vary within the operating frequency range of UWB system (3.1-10.6 GHz).

$$\frac{P_r(\omega)}{P_t(\omega)} = [1 - |\Gamma_t(\omega)|^2][1 - |\Gamma_r(\omega)|^2]G_r(\omega)G_t(\omega)|\hat{\rho}_t(\omega) \cdot \hat{\rho}_r(\omega)|^2\left(\frac{\lambda}{4\pi r}\right)^2 \tag{6.4}$$

where

P_r = Time average input power of the transmit antenna

P_t = Time average output power of the receive antenna

$\Gamma_t(\omega)$ = Reflection coefficient of the transmit antenna

$\Gamma_r(\omega)$ = Reflection coefficient of the receive antenna

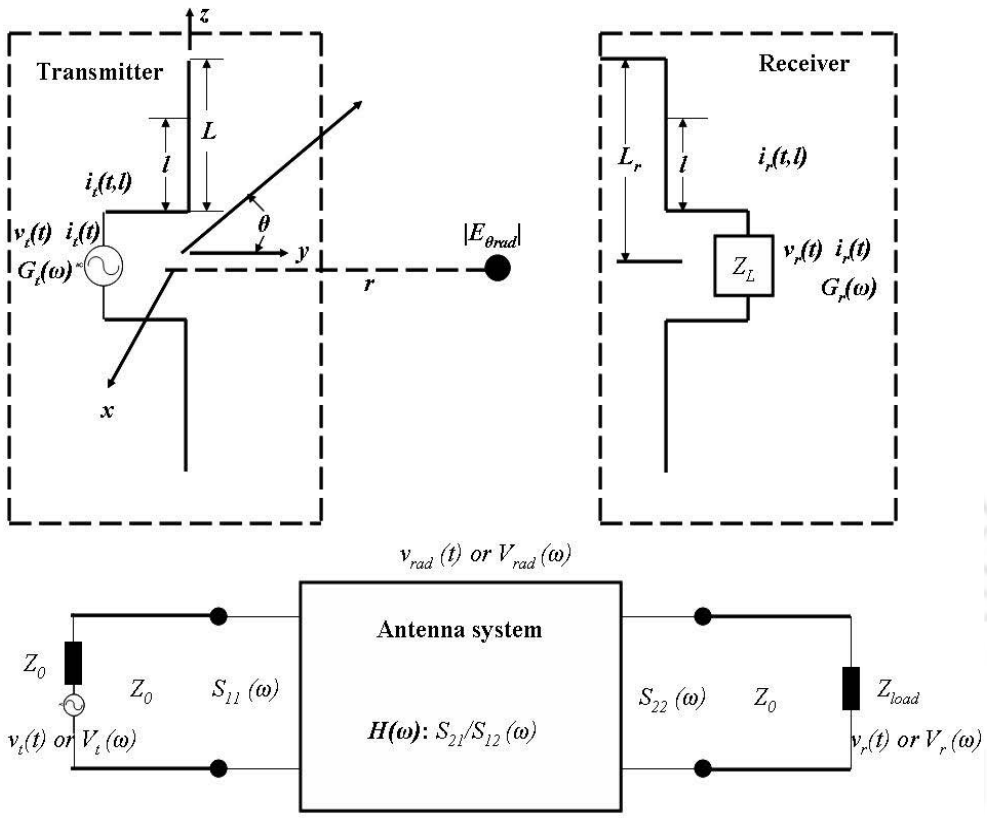

Figure 6.22: A transmit-receive antenna system.

G_t = Orientation dependent (θ, ϕ) gain of the transmit antenna

G_r = Orientation dependent (θ, ϕ) gain of the receive antenna

$|\hat{\rho}_t(\omega) \cdot \hat{\rho}_r(\omega)|$ = Polarization matching factors between transmit and receive antenna

λ =Operating wavelength at operating angular frequency ω

r = Distance between the transmit and receive antenna in the far-field.

If a transfer function $H(\omega)$ is defined to describe the relation between the source and output signal (voltage), equation 6.4 can be simplified as

$$H(\omega) = \frac{V_r(\omega)}{V_t(\omega)} = \left| \sqrt{\frac{P_r(\omega) Z_{load}}{P_t(\omega) 4 Z_0}} \right| e^{-j\phi(\omega)} = |H(\omega)|\, e^{-j\phi(\omega)} \tag{6.5}$$

$$\phi(\omega) = \phi_t(\omega) + \phi_r(\omega) + \frac{\omega r}{c} \tag{6.6}$$

where

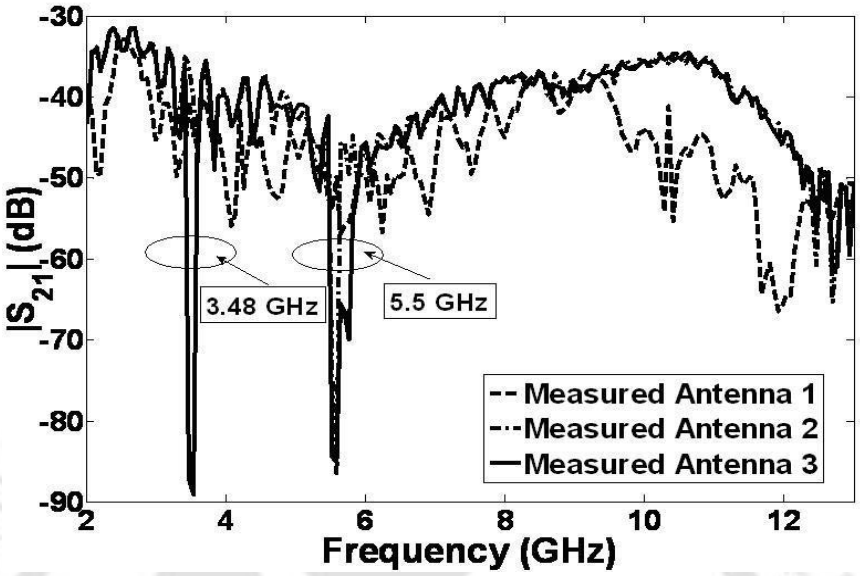

Figure 6.23: Measured transfer function ($|S_{21}|$) (face-to-face) of antenna 1, antenna 2 and antenna 3.

c=velocity of light in free space

$\phi_t(\omega)$=Phase variation caused by transmit antenna

$\phi_r(\omega)$=Phase variation caused by receive antenna

In UWB communication system domain, the variation of the transfer function magnitude should be as accurate as possible in the band-notched regions and need to be invariant in the un-notched bands to mitigate the potential interference between the UWB system and the existing narrowband systems (for instance, WiMAX and WLAN). A transmitting and receiving antenna configuration fulfilling these requirements will suppress interferences from the narrowband systems and impart little distortion on necessary and useful signals. The system transfer function, which is basically the $|S_{21}|$ transfer function of a two port network, is measured keeping the antenna pair face-to-face. The distance between the similar pair of antennas were 62 cm. Fig. 6.23 shows the measured $|S_{21}|$ transfer function of antenna 1, 2 and 3. For single notch UWB PMA (antenna 2) and double notch UWB PMA (antenna 3), it can be observed that there is a sharp drop in the system transfer function $|S_{21}|$ in the frequency band of 5-6 GHz (WLAN) for the antenna 2 and in the frequency ranges of 3.3-3.6 GHz (WiMAX) and 5-6 GHz (WLAN) for the antenna 3 respectively.

6.5.1.2 Transfer function phase : Group delay

When radiated at different frequencies, the stability of the magnitude of gain, radiation pattern, reflection coefficient and polarization do not take into account the phase difference. All the frequency components of the UWB system are radiated at the same time. Hence stability must take into account the phase difference for the different components in order to reconstruct the pulse on reception.

The group delay (GD) is considered as the figure of merit for studying the phase behavior of the transfer function and is calculated by using the expression given in equation 6.7.

$$GD(f) = -\frac{1}{2\pi}\frac{d\phi(f)}{df}||_{f=f_0} \tag{6.7}$$

where f_0 is the frequency of interest.

UWB pulse distortion by an antenna is an important issue in the UWB communication system as the UWB system uses pulse transmission. In true sense, a constant group delay (linear phase response) is needed in the UWB system. Fig. 6.24 depicts the measured group delay of antenna 1, antenna 2 and antenna 3. In case of antenna 1, the group delay variation over the UWB band is less than 1 ns. Considerable delay is occurring (more than 4 ns) in the antenna 2 at around 5-6 GHz band. Similarly for antenna 3, there are two huge delays occurring (more than 4 ns) at around 3.4- 3.6 GHz and 5-6 GHz respectively. These big delays deteriorate the phase linearity in the UWB system. However in the un-notched frequency part, the variations of group delays are small showing good linear phase characteristics. The above group delay characteristics demonstrate that the proposed antennas demonstrate phase linearity at desired UWB frequencies.

6.5.2 Variability in the time domain: Pulse distortion parameters

6.5.2.1 Fidelity Factor (F) and stretch ratio (SR)

In this section, the UWB signal presented in [189] is used to excite the proposed antennas, which fulfills the FCC spectral mask. The power spectral density (dBm/MHz) of the antenna input signal (5^{th} derivative of Gaussian pulse) combined the FCC spectral mask for indoor UWB communication systems as shown in Fig. 6.26. The UWB pulse, which is used to excite the antennas is a 5^{th} order derivative of the Gaussian pulse and is given by

$$z_1(t) = GM_5(t) = B(-\frac{t^5}{\sqrt{2\pi}\sigma^{11}} + \frac{10t^3}{\sqrt{2\pi}\sigma^9} - \frac{15t}{\sqrt{2\pi}\sigma^7}) \times \exp(-\frac{t^2}{2\sigma^2}) \tag{6.8}$$

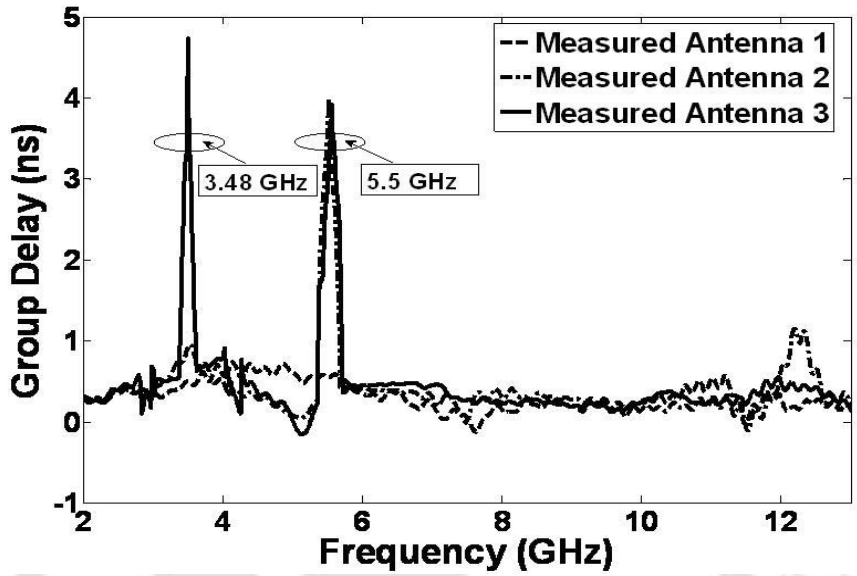

Figure 6.24: Measured group delay of antenna 1, antenna 2 and antenna 3.

where B=600, is a constant which can be chosen to make compatible with the peak power spectral density that the FCC permits and σ is the spread of Gaussian pulse, whose value is 51 ns to ensure that the size and shape of the spectrum fit with the FCC mask. The signal with single pulse is shown in the Fig. 6.25. The PSD of antenna input signal suitable fits the PSD of the FCC mask denoting the adequate compatibility of the 5^{th} order Gaussian pulse with the FCC indoor UWB communication system mask as shown in Fig. 6.26.

Fig. 6.29(b) shows the received pulse as the proposed antenna 3 acts as a received antenna. The transmit antenna is also a replica of the proposed antenna 3. That means the fifth order Gaussian pulse is transmitted from antenna 3 to antenna 3. The fifth order Gaussian pulse is generated in Tektronix AWG 7122B arbitrary signal generator and it is fed to the transmit antenna 3 (replica of proposed antenna). At 62 cm away the receiving antenna, which is the proposed antenna 3 is stationed face-to-face (θ=0^0) and the free air is considered as the medium of transmission of signal. The experimental set up for this experiment is shown in Fig. 6.27. The distance of 62 cm is approximately six times the wavelength of the lower frequency (3.1 GHz) of the UWB band of operation which is in the far field of the receiving antennas[190]. At the receiving side, the signal is received by the proposed antenna 3 and the received signal is captured by Tektronix DPO 70804 digital phosphor oscilloscope. As from the Fig. 6.29(b), there is ringing in the tail of the fifth order Gaussian pulse. Apart from this there is reduction

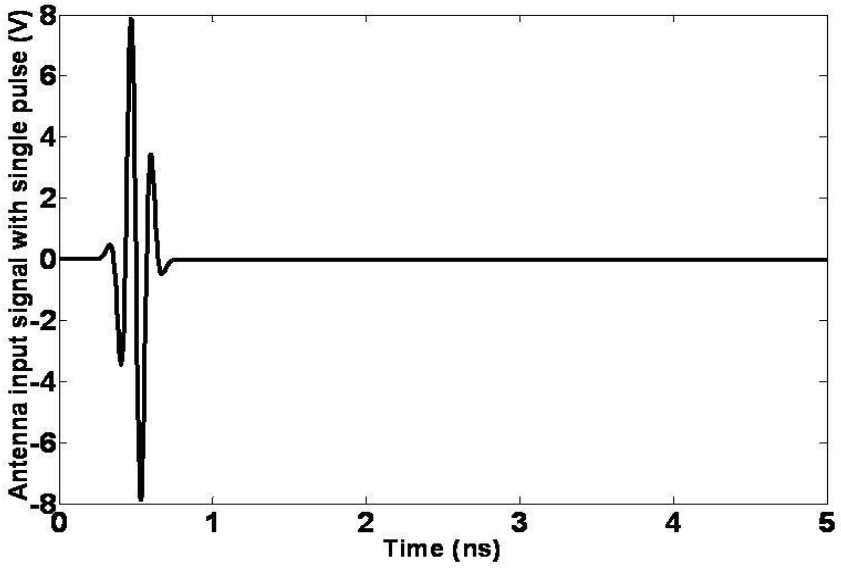

Figure 6.25: Antenna input signal (5^{th} derivative of Gaussian pulse) with single pulse.

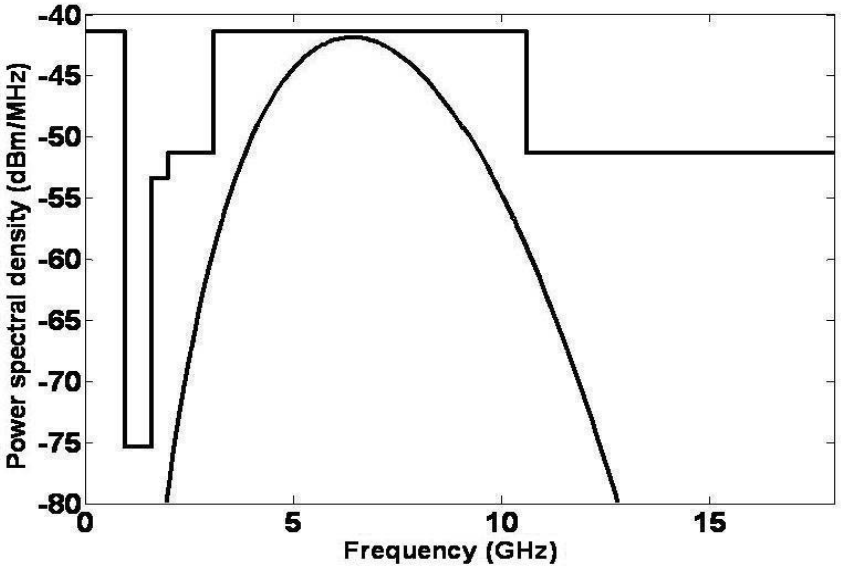

Figure 6.26: Power spectral density (dBm/MHz) of FCC spectral mask for indoor UWB communication system and power spectral density (dBm/MHz) of antenna input signal (5^{th} derivative of Gaussian pulse).

in the amplitude of the received pulse. The pulse is transmitted with the 8V peak-to-peak amplitude. But at the reception, the amplitude is reduced to 5V peak-to-peak. The reason for these two types of the disturbance (ringing and amplitude reduction) in the received signal may be due to the noise and other disturbances present in the air channel in between the two antennas. The measurements were done in a regular laboratory(not in anechoic chamber) where there are many equipments, computer

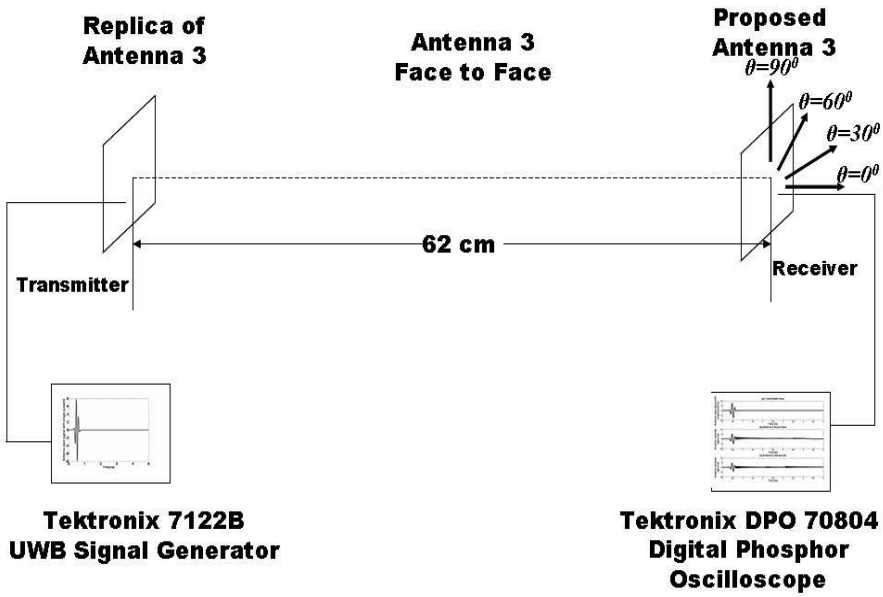

Figure 6.27: Experimental set-up for time domain transmission and reception characteristics for antenna 3 (face-to-face).

systems, etc are present. Besides, the cause of ringing for antenna 3 may be attributed to the highly non-linear phase characteristics of antenna 3 in the double notch regions(refer to Fig. 6.24). Similarly Fig. 6.29(c) shows the above environment when the two antennas are placed side-by-side (θ=0^0) and the experimental set up is shown in Fig. 6.28. From Fig. 6.29(b) and Fig. 6.29(c), one can see that the ringing in the tail of the received pulse is more in case of side-by-side (θ=0^0) as compared to the ringing present in the received signal when the antenna placed face-to-face (θ=0^0). This is because, when the antennas are stationed face-to-face (θ=0^0), the whole of the antenna surface is exposed to the receiving signal. Hence the signal reception is unobstructed in this situation. So the ringing is less rapid in this situation. But, when the antennas are placed side-by-side (θ=0^0), smooth signal reception is disrupted. So more ringing is present in the tail of the received signal.

The amount of shape distortion is necessary to be calculated for the quantitative analysis of the time domain characteristics of the antenna. Hence for the evaluation of the waveform distortion, the correlation or fidelity factor (F) has to be calculated between the input or transmit signal pulse at the transmitting antenna terminal and received signal at the receiving antenna. To determine the fidelity factor (F) between the received signal $z_2(t)$ and the input or transmit signal $z_1(t)$, the fidelity factor (F) is given by

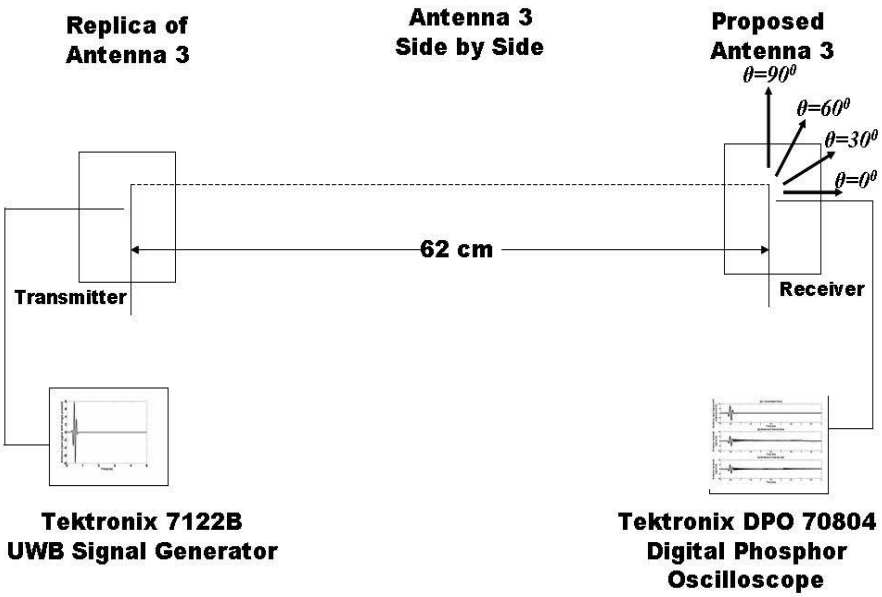

Figure 6.28: Experimental set-up for time domain transmission and reception characteristics for antenna 3 (side by side).

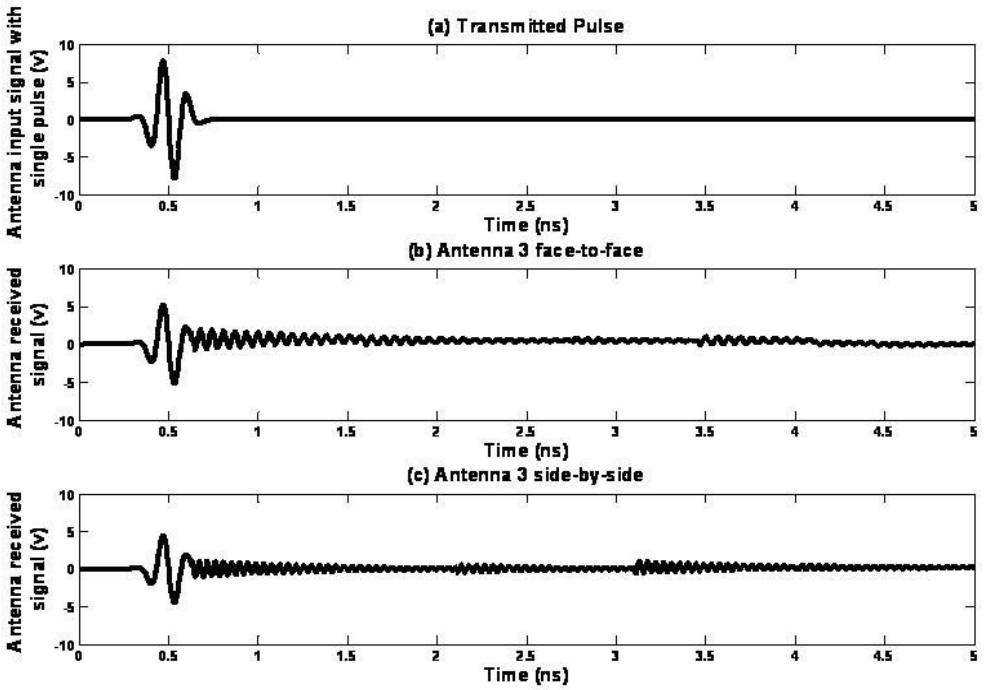

Figure 6.29: Measured received signals of antenna 3 **(a)** transmitted fifth derivative of Gaussian pulse, **(b)** face-to-face (θ=0^0), and **(c)** side-by-side (θ=0^0).

$$F = \max \frac{\int_{-\infty}^{\infty} z_1(t) z_2(t-\tau) dt}{\sqrt{\int_{-\infty}^{\infty} |z_1(t)^2|\, dt \cdot \int_{-\infty}^{\infty} |z_2(t)^2|\, dt}} \tag{6.9}$$

where τ is a suitable delay which is varied to make the numerator of equation 6.9 maximum [190].

In the UWB pulse radio technology, the temporal width of the transmitted pulses play a vital role to determine the energy content in the transmitted pulses. The amount of energy present at the peak of the pulse and the width of pulse can be determined as the width of the time window containing a certain percentage of the total energy [192]. The pulse width in terms of the stretch ratio (SR) or time spread can be evaluated by the ratio of the received signal waveform to the width of the source voltage waveform. For the signal $z(t)$, the normalized cumulative energy function $E_z(t)$ can be defined as

$$E_z(t) = \frac{\int_{-\infty}^{t} |z(t')|^2 dt'}{\int_{-\infty}^{\infty} |z(t')|^2 dt'} \tag{6.10}$$

After eliminating the first and the last 5% energy content in the time axis, the pulse width stretch ratio (SR) for 90% energy capture can be evaluated by

$$SR = \frac{E_{z_2}^{-1}(0.95) - E_{z_2}^{-1}(0.05)}{E_{z_1}^{-1}(0.95) - E_{z_1}^{-1}(0.05)} \tag{6.11}$$

From the analysis it is found that the value of the correlation or fidelity factor (F) between the transmitting/receiving UWB pulse for the antennas 3 is approximately 0.9 and 0.85 respectively when stationed face-to-face and side-by-side shown in the Fig. 6.29(b) and Fig. 6.29(c). This is because the amount of ringing is more in for side-to-side configuration in comparison of face-to-face positioning of antenna 3.

6.5.3 Variability in the space domain

Antenna is a very important component in the communication systems and it behaves more critically in the UWB communication environment. Since very short pulses are required for the impulse radio applications, the UWB notch antennas distort the emitted or received pulse shape. Measured received signals at various angle θ for the antenna 3 when positioned face-to-face and side-by-side are shown in Fig. 6.29, Fig. 6.30 and Fig. 6.31. The distance between the transmitting antenna and the electric field intensity signals is fixed at 62 cm and the experiment set-ups are shown in the Fig. 6.27 and Fig. 6.28 for face-to-face and side-by-side respectively.

From the graphs in Fig. 6.29(b) and Fig. 6.30 for the face-to-face condition, the received signals for the antenna 3 for various angle θ are distorted and rapid ringing starts before 1 ns. After some

cycles of repeatation, the ringing decays as the time increases. The amount of ringing is intense as the angular position between replica of antenna 3 and proposed antenna 3 is increased from θ=30^0 to 90^0 in the face-to-face condition as compared to the face-to-face positioning of the replica of antenna 3 and proposed antenna 3 at θ=0^0 shown in the Fig. 6.28(b). As per the previous case of θ=0^0 shown in the Fig. 6.29(b), the amplitude of the pulse in case of θ=30^0, 60^0 and 90^0 also decreases in comparison to the transmit pulse amplitude shown in the Fig. 6.30. The pulse is transmitted with the 8V peak-to-peak amplitude. But at the reception, the amplitude is reduced to around 4-5V peak-to-peak. The fidelity factor (F) or the correlation factor is approximately around 0.85 when the angle is θ=30^0. But the correlation factor decreases with the change of position of antenna 3 to various angles. This means more disturbances such as ringing is introduced when the angular position increases to 90^0.

The same situation is visible in the Fig. 6.31 when the replica of antenna 3 and proposed antenna 3 are stationed side-by-side. In this case also the amount of ringing is intense as the angular position between the replica of antenna 3 and proposed antenna 3 is increased from θ=30^0 to 90^0 in the side-by-side condition as compared to the side-by-side positioning of the replica of antenna 3 and proposed antenna 3 at θ=0^0 shown in the Fig. 6.29(c). At the same time the amplitude of the pulse decreases in comparison to the transmit pulse shown in the Fig. 6.31. The fidelity factor (F) or the correlation factor is approximately around 0.8 when the angle is θ=30^0. The correlation factor decreases with the change of position of antenna 3 to various angles in side-by-side condition.

6.6 Summary

In this chapter, the evolution of UWB system is introduced and the history related to UWB system is described. The UWB technology is described in brief and the various applications of the UWB antenna system is depicted. Apart from this, the technical specifications for the UWB system are provided. As the antenna is very crucial element in the UWB system, the challenges involved in the UWB antenna design are mentioned.

Finally in this chapter, a compact UWB PMA with dual band notch characteristic is proposed. Two open ended stubs are erected from the two lower end of the microstrip feed-line for the production of notch characteristics at the required frequency bands to eliminate the potential interference of UWB with WiMAX and WLAN. The use of two open ended stubs for creation of two band notch characteristics is new in the contemporary double notch UWB PMA design domain. Mathematical

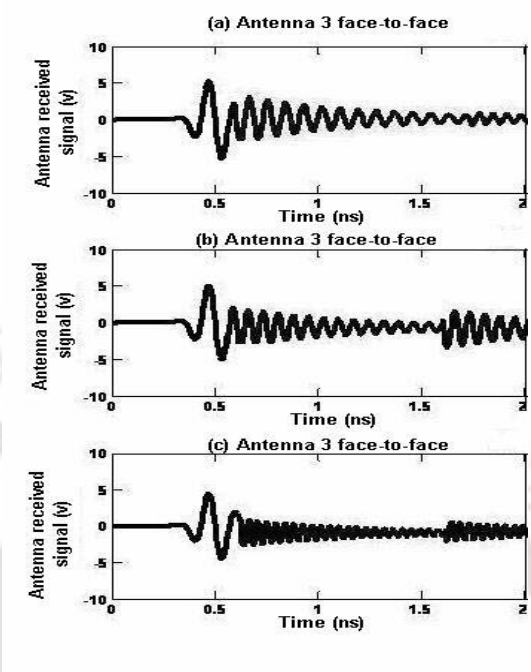

Figure 6.30: Measured received signals of antenna 3 stationed face-to-face for **(a)** θ=30^0 **(b)** θ=60^0 and **(c)** θ=90^0.

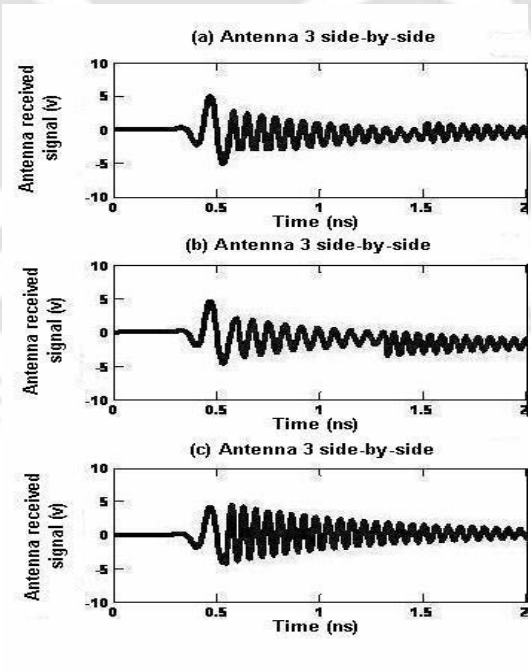

Figure 6.31: Measured received signals of antenna 3 stationed side-by-side for **(a)** θ=30^0 **(b)** θ=60^0 and **(c)** θ=90^0.

design expressions for the two open ended stubs are presented. Apart from this a stair case structure is embedded in the two lower corners of the rectangular radiating elements for the proper impedance

matching purpose. The double notch UWB PMA structure is simple and compact. The antenna exhibits consistent radiation pattern and appropriate gain characteristics. The proposed double notch UWB PMA is investigated in time domain also. In time domain, it has been observed experimentally that the received 5^{th} derivative of Gaussian pulse is not much distorted in the main waveform but some amount of ringing is observed in the tail of the pulse. The amplitude of the 5^{th} derivative of Gaussian pulse is slightly reduced due to the channel disturbances in both the cases. This antenna achieves a size reduction of 47.5 percent and gain enhancement of 9 percent when compared with the contemporary double notch UWB PMAs [182].

7

Conclusions and future work

Contents

7.1 Summary of the present work 166
7.2 Conclusions 167
7.3 Suggestions for future work 169

7.1 Summary of the present work

The objective of the thesis is to design, analyze and fabricate new compact printed monopole antennas with multiple bends for applications in wireless, RFID and UWB communication system. It has been observed that planar printed monopole antennas are superior from the existing planar antennas in terms of size compactness, bandwidth improvement, effective radiation characteristics and appropriate gain profile. Apart from this dual-band notch printed monopole antenna with compact size and appropriate time and frequency characteristic are essential for the successful application in UWB communication system.

During the course of study of the printed monopole antennas for dual-band and UWB applications, the design of erecting a resonating strip from the ground plane has been exploited which is new in the contemporary printed monopole antenna design for dual band wireless applications. In all the proposed antennas, 90^0 bends are present in either in the radiating element only or both in radiating element and protruding strips in the ground plane. The 90^0 bends play a vital role in the performance of the proposed antennas and effects in the miniaturization of proposed antennas. The resonance performance is improved considerably with the 90^0 bends either in resonating path or in both radiating path and protruding strips in the ground plane. Deep resonances result with the bending in resonating element or protruding stub in ground plane in comparison to their linear counterparts. 90^0 bends are responsible for the proper tuning of the resonance frequency in the desired band of operation such as WLAN and RFID systems. Proper bending analysis in all aspects is performed for all the proposed antennas and results are well documented in the respective chapters.

The multiple bend dual band printed monopole antennas are successfully designed, optimized, fabricated and tested for the dual-band applications. These antennas are easy to fabricate, compact in size with proper resonances occurred in the appropriate wireless frequency bands such as WLAN and RFID systems. These antennas provide consistent radiation pattern and appropriate gain characteristics in the respective wireless frequency bands.

A double notch UWB PMA has been successfully designed, optimized, fabricated and tested. The proposed double notch UWB PMA is evolved from a UWB PMA followed by single notch UWB PMA. Along with the proposed double notch UWB PMA, the UWB PMA and single notch UWB PMA are also designed, optimized, fabricated and tested. The proposed double notch UWB PMA has a rectangular radiating element and in the left and right extreme bottom corners of the rectangular

radiating element, there are two stair-cased structures each have two steps. These steps are like the multiple bends in the feed region of the UWB PMA. These steps help in the bandwidth enhancement of the proposed antenna by proving proper impedance matching between the feed-line and the radiating element. Apart from this, these steps introduce extra resonances in the UWB frequency range and hence the bandwidth is increased considerably. In the design of the double notch UWB PMA, two open ended stubs are erected from the microstip for the purpose of creating two notch bands to alleviate the potential interference of UWB system with other narrow band system such as WiMAX and WLAN. Usage of two open ended stubs in the microstrip feed-line for the creation of dual-band notch characteristic is new in the contemporary UWB band notch antenna design. The proposed UWB dual band notch antenna is simple in design and easy to fabricate. The double notch UWB PMA provides consistent radiation pattern and appropriate gain characteristic in the UWB domain. Apart from this, time domain analysis regarding the transmission, propagation and reception of the UWB pulses through the double notch UWB PMA is analyzed properly. In time domain, it has been observed experimentally that the ringing in introduced considerably in the tail of the received UWB pulse by double notch UWB PMA.

In nutshell, a detail study on the effect of multiple bends on the performance of PMAs has been carried so that the proposed PMAs can be used effectively in the wireless domain such as RFID, WLAN and UWB. Bends either in the radiating element or in the L-shaped protruding strips in the ground plane not only make the PMAs operate in the dual-band mode but also helps in tuning the resonance characteristics and resonance frequency to the desired frequency band effectively. Dual-mode operation of PMAs can be obtained by proving different resonating paths in the form of two arms or branches in main radiating element like that of F-shaped PMA.

7.2 Conclusions

It has been concluded that bends in the PMAs are a versatile and effective way of achieving dual-band antenna performance with size miniaturization. In order to achieve dual-band antenna performance L-strip can be introduced in the ground plane of the PMA. Another way of obtaining the dual-band antenna performance is to introduce two resonating paths in the PMA such as PMA with two arms or branches like that of the F-shaped PMA. Bends could also be introduced in the feed region of the PMA to obtain UWB antenna performance. Two open ended stubs are erected from the

microstrip feed-line which gives rise to band-notch characteristics in the UWB antenna. Some of the contributions of the thesis are:

(i) A new F-shaped dual-band PMA with a single 90^0 bend in each of the radiating element forming a "F" shape for RFID and WLAN application is proposed. The proposed antenna attains 12.5 percent size reduction, 43.16 percent bandwidth improvement and 3.10 percent average gain enhancement as compared to contemporary dual band PMAs [116].

(ii) A rectangular PMA with an inverted L-strip having one 90^0 bend in the ground plane is proposed for dual-band WLAN applications. This novel antenna attains 50.75 percent size reduction, 76.88 percent average bandwidth improvement and 15.17 percent average gain enhancement when compared to contemporary dual-band PMAs[113].

(iii) A compact PMA with having one 90^0 bend in the inverted L-shaped radiating element and an inverted L-strip with also one 90^0 bend in the ground plane for application in dual-band WLAN systems is proposed. This new antenna achieves 73.33 percent size reduction, 45.71 percent average bandwidth enhancement and 53.6 percent average gain improvement when compared to contemporary dual-band PMAs[121].

(iv) A novel compact PMA having two 90^0 bends in the reverse L-shaped radiating element with an inverted L-strip with one 90^0 bend in the ground plane is proposed for dual-band WLAN applications. This new antenna attains 5.71 percent size reduction, 64.53 percent average bandwidth improvement when compared to contemporary dual-band PMAs [133] but the improvement of gain is not considerable when compared to above PMA.

(v) A new 9-shaped dual-band PMA with three 90^0 bends for RFID and WLAN application is proposed. Size reduction of 18.57 percent, average bandwidth improvement of 37.08 percent and 16.45 percent average gain enhancement are achieved when compared to antenna[114].

(vi) A simple microstrip fed folded strip monopole antenna (FSMA) having four 90^0 bends in the radiating element with a protruding stub in the ground plane for simultaneous applications in the WLAN and RFID is presented. This new antenna attains 8.25 percent size reduction, 57.95 percent average bandwidth improvement and 16.19 percent average gain enhancement when compared to contemporary dual-band PMAs[141].

(vii) A compact double notch UWB PMA is proposed. Two open circuited stubs at two sides of the microstrip feed line achieves the dual band notch characteristics. This antenna achieves a size reduction of 47.5 percent and gain enhancement of 9 percent when compared with the contemporary double notch UWB PMAs[182].

7.3 Suggestions for future work

- **Equivalent circuit analysis for the printed monopole antenna**:- As the antennas are the resonant devices, all the components such as feed-line, ground plane and the radiating element can be demonstrated in the form of equivalent circuit containing either RLC series or parallel circuit. If the circuit parameters such as R, L and C can be extracted correctly, then all the antenna parameters such as scattering parameters ($|S_{11}|$) and input impedance characteristics can be validated properly along with the simulated and measured antenna characteristics. Hence the accurate equivalent circuit analysis and mathematical or analytical extraction of circuit parameters of the printed monopole antennas are needed to have another confirmation test along with the simulated and measured parameters.

- **Miniaturization of printed monopole antennas**:- The radiation element of the printed monopole antennas (PMA) can be designed in the form of fractals instead of traditional rectangular or strip shape to achieve the size reduction of the PMAs. Hence the effect of applying fractal technique, in reducing the size of PMAs can be further investigated. Major problem for each antennas will be enhanced ringing effects.

- **Further studies on the protruded stubs from the ground plane**:- Traditionally, the dual-band characteristics in the PMAs are achieved by creating two independent branches from the prime radiating element. But to create dual-band characteristics by erecting protruding stubs from the ground plane is new and not much research is carried out so far in this regard till now. More detail and extensive study of the behavior of the protruding stubs in the ground plane and its effect on the antenna parameters should be carried out.

- **Detail understanding of wide band mechanism in the UWB antennas**:- Stair-case structures are created as multiple bends in the feed region of the UWB PMA and it is shown that as the number of steps or bends in the feed region increases, the bandwidth enhances

considerably by providing extra resonances. As we all know that the UWB characteristics are the outcome of the suitable overlapping of closely spaced resonances from the radiating elements and feed region but the detail exact mathematical and analytical investigations are needed for the proper understanding of the bandwidth improvement mechanism in UWB PMAs.

- **Studies on the interaction of the UWB PMAs with the human body (Body area networks)**:- As some of the UWB PMAs are embedded in the laptop or other hand held portable devices, the device effect on the antenna performance should be studied. As UWB PMAs are also incorporated in many devices that come in contact with the human body, the impact from the human body on the UWB PMA performances should be studied extensively.

A

Antenna Measurement

Contents

A.1 Antenna Measurement 172

A.1 Antenna Measurement

A.1.1 Antenna measurement methodology

A brief illustration of methodologies, facilities and equipments needed for the measurement of antenna characteristics is presented in this section.

A.1.1.1 Rohde and Schwarz ZVA 24 vector network analyzer based measurement set up

The Rohde and Schwarz ZVA 24 vector network analyzer (VNA) is a member of ZVA series of VNA platform and provides the combination of precision and speed for the challenging and demanding needs for today's high performance and high frequency component test requirements. The Rohde and Schwarz ZVA series VNA attains these testing challenges by providing the accurate combination of flexible connectivity, low trace noise, wide dynamic range and first sweep speeds. The picture of the Rohde and Schwarz ZVA 24 vector network analyzer (VNA) is Fig. A.1 is shown below.

The operating frequency range of the Rohde and Schwarz ZVA 24 VNA is 10 MHz to 24 GHz. With static frequency accuracy of 1x10-7 and the number of measurement points (user-selectable) is 1 to 60001. Some detail characteristics of the Rohde and Schwarz ZVA 24 VNA is given below in a tabular form.

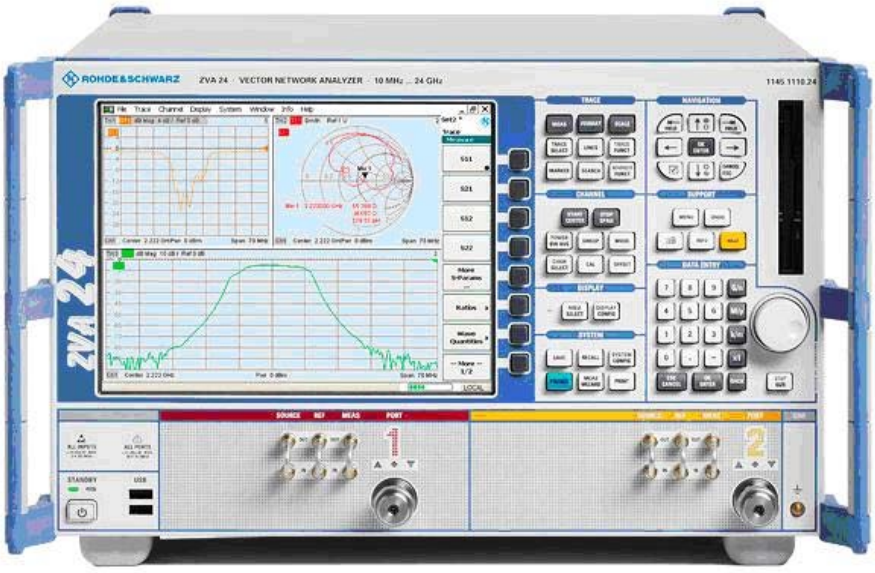

Figure A.1: Front face of the Rohde and Schwarz ZVA 24 vector network analyzer.

Table A.1: Some specifications of the Rohde and Schwarz ZVA 24 vector network analyzer

Impedance	50-Ω
Test port connector	3. mm, Male
Number of test ports	2
Frequency resolution	1 Hz
Number of measurement points	1 to 60001
Measurement bandwidth	1 Hz to 1 MHz
I/O port	USB, LAN, GPIB
O/S	Windows xp

A.1.1.2 Reflection coefficient ($|S_{11}|$) measurement by Rohde and Schwarz ZVA 24 vector network analyzer

To measure the reflection coefficient ($|S_{11}|$) of the antenna under test (AUT), the antenna is connected to any one of the port through the testing cable and the VNA is operated in the ($|S_{11}|$) mode. Prior to the measurement, the specific port of the VNA is calibrated carefully and accurately so that the measurement error will be minimal. The measured the reflection coefficient ($|S_{11}|$) data of AUT is stored in the VNA database as comma separated variable (CSV) format and later on these data are transferred to a computer through a USB drive. The measured the reflection coefficient ($|S_{11}|$) graph is plotted in the computer and compared with the simulated reflection coefficient ($|S_{11}|$) graph.

A.1.2 Agilent PNA (N5230A) based radiation pattern measurement set up

Fig. A.2 represents the measurement set up for the radiation pattern of any antenna

A.1.2.1 Anechoic chamber

Anechoic chamber is widely used for the radiation pattern measurement throughout the world, which consist of an acoustic free room with microwave absorbers fixed on the walls, floor and roof of the chamber to protect EM reflections. The microwave absorbers are mad up of high quality low foam embedded with dielectrically/magnetically lossy medium. Good impedance matching is provided by tapered shape of the absorbers when the microwave power impinges on it. To shield from

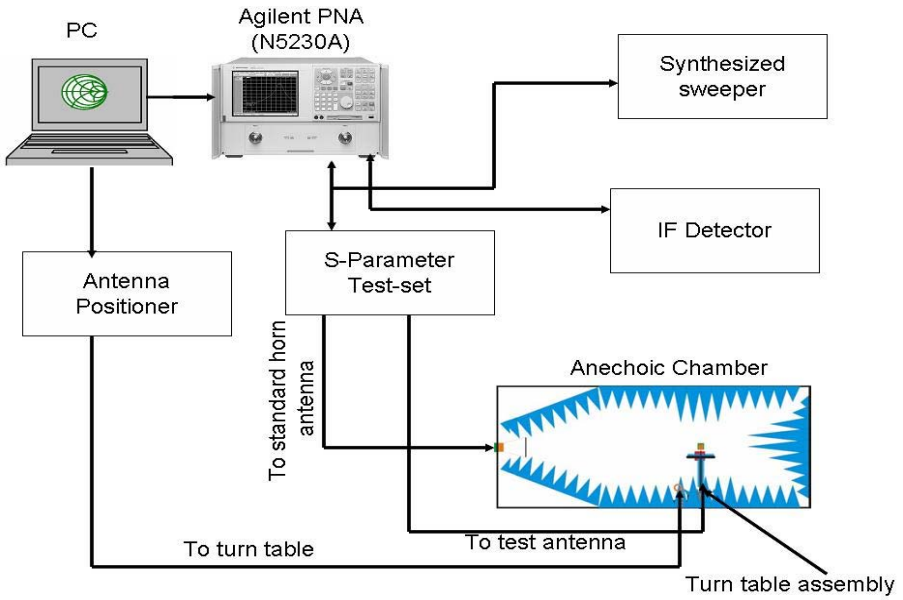

Figure A.2: Radiation pattern measurement set up.

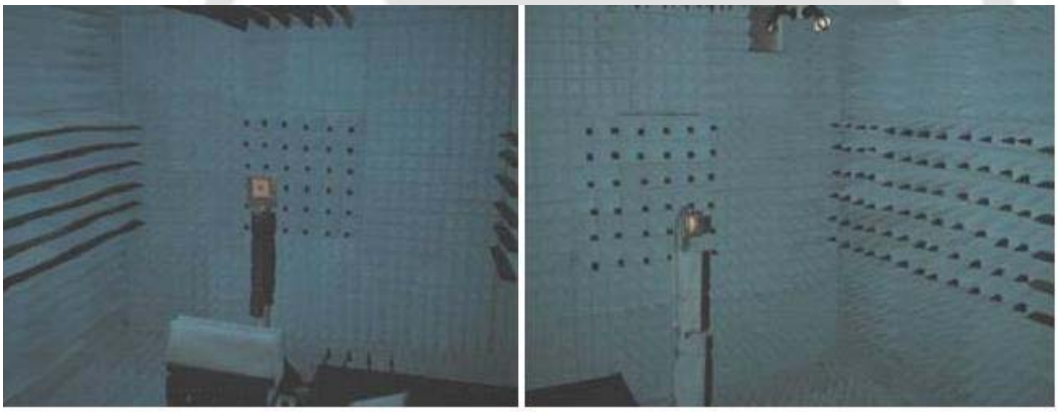

Figure A.3: Photographs of anechoic chamber used for the measurement of radiation pattern for proposed antennas in Microwave Laboratory of department of Electrical Communication Engineering, Indian Institute of Science, Bangalore, INDIA.

electromagnetic interference from surroundings, aluminum sheets are used in anechoic chamber. Fig. A.3 shows the interior of an anechoic chamber used for the measurement of radiation pattern of all proposed antennas in Microwave Laboratory of department of Electrical Communication Engineering, Indian Institute of Science, Bangalore, INDIA.

A.1.2.2 Turn table assembly for the far-field radiation pattern measurement

A turn table arrangement inside the anechoic chamber is consist of a microcontroller based antenna positioner interfaced with a PC for the radiation pattern measurement. The antenna under test (AUT) is fixed over the turn table assembly and a linearly polarized; wideband calibrated standard horn antenna is used as the transmitter for the radiation pattern measurement. The Matlab based graphical user interface (GUI) manages the antenna characterization by synchronizing each component of the system.

A.1.2.3 Radiation pattern measurement

Radiation pattern measurement is accomplished with the help of Agilent PNA (N230A) network analyzer inside the anechoic chamber. The AUT is configured in the receiver mode which is mounted on a turn table assembly in the anechoic chamber and is connected to one port of the network analyzer. A wide band pre-calibrated horn antenna acts as a transmitter. The turn table controller and network analyzer are interfaced to a computer which runs the measurement automation software. The measurement automation software requires the file name, angular step size and the measurement band. Prior to the measurement, the system automatically undergoes through calibration and performs the transmission measurement for each step angle and records the angular transmission characteristics in a data file specified by the file name.

A.1.3 Antenna gain measurement

The common way to measure antenna gain is by the Gain transfer method. The different steps for the measurement of gain of an antenna are (1) a calibrated horn antenna is placed against another identical horn antenna in a anechoic chamber in the far field of each other and S21 is measured which is known as S21(calibrated), (2) Now the calibrated horn antenna is replaced with antenna under test (AUT) and S21 is measured which is known as S21(test), (3) The calibrated horn antenna gain should be known prior to the measurement process, and (4) finally using the above measured S21 data and the gain of the standard calibrated antenna, on can derive the antenna gain at different frequencies. The expression for the measured gain of AUT is "Gain (test) = [S21 (test) - S21 (calibrated)] + G (calibrated)". The meaning of this method of gain measurement is the difference of S21 terms gives us the gain difference of the antennas and when added to the known calibration gain of horn antenna yields the wanted result.

B

Electromagnetic Simulation Software IE3D

Contents

B.1 Electromagnetic Simulation Software IE3D 178
B.2 IE3D 178
B.3 Basics of method of moments (MoM) 178
B.4 Features of IE3D 181
B.5 Advantages of IE3D 182
B.6 Disadvantages of IE3D 182

B.1 Electromagnetic Simulation Software IE3D

The technology of wireless communication is based on the principle of waves and electromagnetic (EM) fields. Hence to solve the EM field problems numerical techniques play a vital role when the problem complexity increases.

Now-a-days many numerical techniques are available to solve the complex EM problems, such as finite element method (FEM), finite difference time domain method (FDTD), finite integration technique (FIT) and method of moments (MoM). The MoM and finite element method of solving the EM solutions are in frequency domain. On the other hand FIT and FDTD techniques for solving the EM problem are in time domain. A particular electromagnetic problem solving technique is appropriate for analysis of definite type of problem. Analyses have shown that method of moment based numerical technique is accurate as well as fast in computation. The precision and resolution of MoM based numerical technique is better than the other available electromagnetic simulation software package. The IE3D which is based on the MoM numerical method has been used as the simulation tool in the thesis.

B.2 IE3D

IE3D considered as the de facto standard EM simulation design tool in the industry which is built upon the method of moments (MoM) based full wave 3D platform. IE3D is appropriately developed for design of patch antennas, slot antennas, wire antennas, RFID antennas, high temperature superconducting (HTS) circuit, low temperature co-fired ceramic structure (LTCC) circuits, microwave monolithic integrated circuits (MMIC) and radio frequency integrated circuits (RFIC). Based on the proven flexibility, speed, capacity and accuracy, IE3D helps designer's quickly turn ideas into design and design products.

B.3 Basics of method of moments (MoM)

The simulation software IE3D is a full-wave EM solver. To govern the micro electromagnetic phenomenon, IE3D solves the Maxwell's equation. Because of the numerical nature of method, there is no much assumption involved and the solution is extremely accurate.

The original Maxwell's equations are in the differential form and the electric field (E) and magnetic field (H) which are the solutions of the Maxwell's equation are in the whole space. There is need to solve

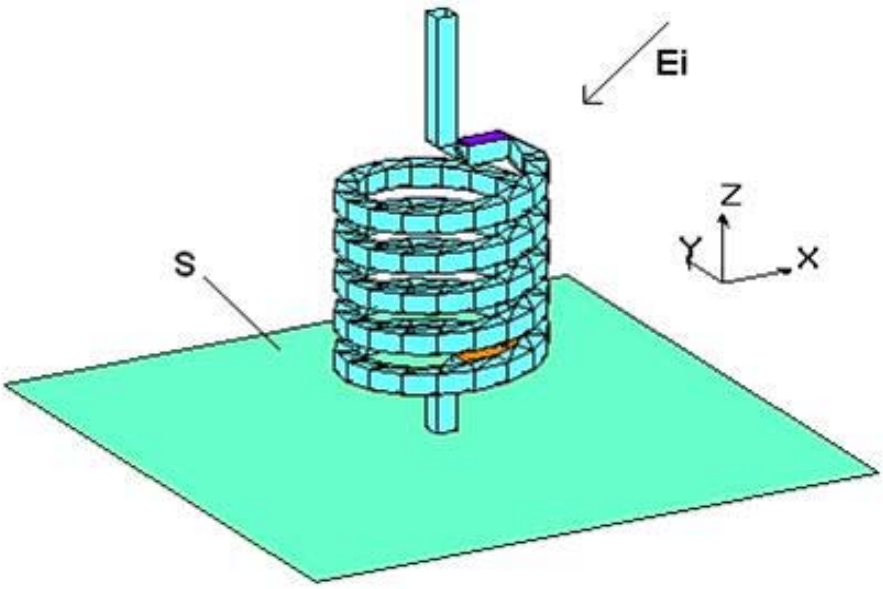

Figure B.1: An incident field E_i is applied to the metallic structure S.

the E and H field numerically to solve the various EM problems. The E- and H- field involves many unknowns which are the numerical solution of original Maxwell's equation. Instead IE3D through the use of Green's function solves the Maxwell's equation in the integral form. In IE3D, E- and H-fields on metallic structures are represented as some weighted integrals of electric current and on a metallic aperture; the magnetic current is derived from the electric field distribution. For most antenna structures and other passive structures, the metallic domain is limited and the solution of IE3D is very limited. Microstrip circuit is a typical example. The surface of the printed strip contains the solution domain. Its solution domain is significantly smaller than that of the original Maxwell's equation.

IE3D efficiently solve the 3D finite dielectric problems as well as the magnetic and electric current problems. To solve the equivalent circuit distribution inside the 3D finite dielectric, IE3D needs the mesh the 3D dielectrics. IE3D assumes a conducting structure in a stratified dielectric environment for a general EM scattering problem. To induce current distribution, an incident field is imposed to the structure as shown in Fig B.1.

To satisfy the boundary condition on the metallic structure, the induce current will create the secondary field. The induce current is flowing on the conducting surface for a typical highly conducting surface and the boundary condition is

$$E(r) = Z_s(r)J(r), r \in S \tag{B.1}$$

Where S is the conducting surface, $E(r)$ is the total tangential field on the surface, $J(r)$ is the current distribution on the surface and $Z(r)$ is the surface impedance of the conductor.

The total field can be written when the structure is in layered dielectric environment as

$$E(r) = E_i(r) + \int_s G(r/r').J(r')ds' \tag{B.2}$$

Where E_i(r) is the incident field on the conducting surface, $G(r/r')$ is the dyadic Green's function for the electric environment. On the stratified dielectrics $G(r/r')$ satisfied boundary condition except the boundary condition on the conductor S.

Substituting (B.2) into (B.1) provides the integral equation

$$Z_s(r)J(r) = E_i(r) + \int_s G(r/r').J(r')ds' \tag{B.3}$$

The surface impedance and the incident field are provided the Green's function can be derived. The only unknown is the current distribution $J(r)$.

The current distribution on assumption can be represented by a set of complete basis function

$$J(r) = \sum_n I_n B_n(r), n = 1, 2, ... \tag{B.4}$$

We obtain

$$Z_s(r)\sum_n I_n B_n(r) = E_i(r) + \sum_n I_n \int_s G(r/r').B_n(r')ds' \tag{B.5}$$

We can convert (B.5) into a matrix equation by taking the Galerkin's procedure

$$\int_s dsE_i(r)B_n(r) = S_n I_n\{\int_s dsB_n Z_s(r)B_m(r)B_n(r) - \int_s ds \int_s ds'B_m(r).G(r/r')B_n(r')\}, n = 1, 2, ... \tag{B.6}$$

To enforce (B.5), the Galerkin's procedure requires a complete set of test functions and the test function are the same as the basis function. The basis function with complete consist of infinite number of terms. Hence the equation (B.6) is an infinite dimension problem. When the basis function in

equation (B.4) are a complete set, the equation (B.6) is exact. But unfortunately, IE3D unable to solve equation (B.6) analytically except some vary specific structure. Hence IE3D, by truncating the infinite series with finite number of terms can get only an approximate solution numerically. Mathematically truncation is a projection process. IE3D project the actual solution in infinite dimensions to that of the finite dimensions. After the projection the equation (B.6) becomes an N by N matrix equation.

$$[Z_{mn}][I_m] = [V_m] \tag{B.7}$$

Where N is a number of finite terms.

$$Z_{mn} = \int_s dsZ_s(r)B_m(r).B_n(r) - \int_s ds \int_s ds' B_m(r).G(r/r')B_n(r') \tag{B.8}$$

$$V_m = \int_s dsE_i(r).B_n(r) \tag{B.9}$$

The solutions of equation (B.7) are the coefficients of the expanded current distribution in equation (B.4). IE3D can calculate the S-parameter, radiation pattern, near field distribution, after the current distribution is solved.

The above method is known as moment method. All method moment (or method-of-moments, MoM) formulation take the form of equation (B.7) and (B.9) no matter simple or complex. The differences are on the choice of basis functions and the Green's function.

For a dyadic Green's function and basis function, there are many choices. Considerations on the dyadic Green's function and basis function is mainly depends on accurate and efficient evaluation of the double surface integrals in (B.8).

B.4 Features of IE3D

Industry's only full-wave 3D method-of-moment (MoM) EM simulation is IE3D. MoM treating both 3D and planar high frequency structure in a multilayer environment provides full 3D capability in the frequency domain. In both 2D and 3D, the built in powerful EM structure editor has a flexible input mode. The editor also provides full support for major CADD formats such as ACIS, DXF and GDS.

The other important features related to IE3D full-wave simulation software are

- Turn S-parameter into time domain response using MD-spice.
- Finite dielectric or different dielectric portions within the same layer.
- Unlimited number of layers and ports.
- Automatic magnetic current formulation enhances usability.
- Built-in optimization and parameterization/fast EM schemes.

Apart from these features many application benefit from using IE3D including

- Antennas-Simulate a number of antenna geometries including optical frequency antenna, RFID tag antenna, dielectric resonator antenna, planar inverted F- and L-antenna (PIFA and PILA), wire antenna, horn antenna, slot antenna and patch antenna.
- RF/Microwave circuits-Simulate passive components, high temperature superconducting structures, LTCC circuits, even active components

B.5 Advantages of IE3D

- **Fast throughput**:- Leverage the 50x-100x run time advantage over other solutions on a single processor computer, or use any combination of multi-core/multi-mode distributed processing to return on challenging design in hours instead of days.
- **High capacity**:- EM solution and modeling limit have been extended. Full package, PCB and IC/MMIC circuits can be solved within a compact memory footprint.
- **High Accuracy**:- Based on production proven IE3D EM simulation technology, yields reliable, predictable results.

B.6 Disadvantages of IE3D

IE3D or method of moment codes have some rooter disadvantages in modeling 3D dielectric structures, waveguide structures and structures emphasizing near field distributions.

Bibliography

[1] J. C. Maxwell, *A Treatise on Electricity and Magnetism*, London, England: Oxford University Press, 1873, 1904.

[2] W. J. G. Beynon, "Marconi, radio waves and the ionosphere," *Radio Science*, vol.10, no.7, pp 657-664, Jul. 1975.

[3] J. D. Kraus, "Antennas since Hertz and Marconi," *IEEE Trans. Antennas and Propagat.*, vol.33, no.2, pp 131-136, Feb. 1985.

[4] G. R. M. Garratt, "The Early History of Radio from Faraday to Marconi," *Institution of Electrical Engineers*, London, 1994.

[5] N. J. Warren, *Events in Telecommunications History*, AT and T Archives, 1992.

[6] G. P. Oslin, *The Story of Telecommunications*, Mercer University Press, 1992.

[7] G. G. Blake, *History of Radio Telegraphy and Telephony*, London: Chapman and Hall, 1928 (Reprinted by Arno Press, 1974).

[8] R. Bowers, A. M. Lee, and C. Hershey, *Communications for a Mobile Society: An Assessment of New Technology*, Beverly Hills, CA: Sage Publications, 1978.

[9] S. Haykin and M. Moher, *Modern Wireless Communications*, Prentice Hall, 2005.

[10] *IEEE standard definitions of terms for antennas*, IEEE Std 145-1983, June 1983.

[11] O. M. Bucci, G. Pelosi and G. Selleri, "The work of Marconi in microwave communications," *IEEE Antennas and Propagat. Magazine*, vol.45, no.5, pp 46-53, Oct. 2003.

[12] C. Sterling and G. Shiers (Eds), *History of Telecommunications Technology: An Annotated Bibliography*, Lanham, MD: Scarecrow, 2000.

[13] B. M. Kolundzija and A. R. Djordjevic, *Electromagnetic modeling of composite metallic and dielectric structures*, Artech house, Inc., Norwood, MA, 2002.

[14] T. K. Sarkar, *History of Wireless*, Wiley-IEEE Press, 2006.

[15] W. H. Chen, J. W. Sun, X. Wang, Z. H. Feng, F. L. Chen, Y. Furuya and A. Kuramoto, "A novel planar switched parasitic array antenna with steered conical pattern," *IEEE Trans. Antennas and Propagat.*, vol. 55, no. 6, pp. 1883-1887, Jun. 2007.

[16] K. -L. Wong, F. -R. Hsiao and T. -W. Chiou, "Omnidirectional planar dipole array antenna," *IEEE Trans. Antennas and Propagat.*, vol. 52, no. 2, pp. 624-628, Feb. 2004.

[17] W. P. M. N. Keizer, "Fast low-sidelobe synthesis for large planar array antennas utilizing successive fast Fourier transforms of the array factor," *IEEE Trans. Antennas and Propagat.*, vol.55, no. 3, pp. 715-722, Mar. 2007.

[18] J. -F. Frigon, A. M. Eltawil, E. Grayver, "Design and implementation of a baseband WCDMA dual-antenna mobile terminal," *IEEE Trans. Circuits and Systems*, vol. 54, no. 3, pp. 518-529, Mar. 2007.

[19] J. -S. Row, "Dual-frequency triangular planar inverted-F antenna," *IEEE Trans. Antennas and Propagat.*, vol.53, no. 2, pp. 874-876, Feb. 2005.

[20] J. R. James and P. S. Hall, *Handbook of microstrip antennas-vol.1*, Edited, Peter Peregrinus Ltd., U.K.

[21] D. M. Pozar, "Microstrip Antennas," *Proc. IEEE*,vol. 80, no. 1, pp. 79-91, Jan. 1992.

[22] K. -L. Wong, *Planar Antennas for Wireless Communications*, John Wiley and Sons, 2002.

[23] W. Cho, M. Kanda, H. Hwang and M. Howard, "A disk-loaded thick cylindrical dipole antenna for validation of an EMC test site from 30 to 300 MHz," *IEEE Tran. on Electromag. Compatibility*, vol. 42, no. 2, pp. 172-180, 2000.

[24] S. D. Rogers and C. M. Butler, "Cage antennas optimized for bandwidth," *IEE Electron. Lett.*, vol. 36, no. 11, pp. 932-933, 2000.

[25] S. -Y. Suh, W. L. Stutzman and W. A. Davis, "Realization of dual-frequency and wide-band VSWR performances using normal-mode helical and inverted-F antennas," *IEEE Trans. Antennas and Propagat.*, vol. 46, no. 6, pp. 788-793, Jun. 1998.

[26] H. Kawakami and G. Sato, "Broadband characteristics of rotationally symmetric antennas and thin wire constructs," *IEEE Trans. Antennas and Propagat.*, vol. 35, no. 1, pp. 26-32, Jan. 1987.

[27] M. J. Ammann and Z. N. Chen, "Wideband monopole antennas for multi-band wireless systems," *IEEE Antennas and Propag. Mag.*, vol. 45, no. 2, pp. 146-150, 2003.

[28] Z. N. Chen, "Impedance characteristics of planar bow-tie-like monopole antennas," *IEE Electron. Lett.*, vol. 36, no. 13, pp. 1100-1101, 2000.

[29] M. J. Ammann, "Square planar monopole antenna," *IEE National Conf. on Antennas and Propag.*, vol. 1, pp. 37-40, 1999.

[30] Y. S. Li, X. D. Yang, C. Y. Liu, and T. Jiang, "A sleeve monopole antenna with wide impedance bandwidth for indoor base station applications," *Progress In Electromagnetics Research C*, vol. 16, pp. 223-232, 2010.

[31] S. Honda, M. Ito, H. Seki and Y. Jinbo, "A disk monopole antenna with 1:8 impedance bandwidth and omnidirectional radiation pattern," *Int. Symp. on Antennas and Propag.*, pp. 1145-1148, 1992.

[32] S. -S. Zhong, X. -L. Liang and W. Wang, "Compact elliptical monopole antenna with impedance bandwidth in excess of 21:1," *IEEE Trans. Antennas and Propagat.*, vol. 55, no. 11, pp. 3082-3085, Nov. 2007.

[33] E. C. Jordan and K. G. Balmain, *Electromagnetic Waves and Radiating Systems*, pp. 548, 2nd ed., Englewood Cliffs. NJ: Prentice-1968.

[34] L. J. Chu, "Physical limitations of omnidirectional antennas," *J. Appl. Phys.*, vol. 19, pp. 1163-1175, Dec. 1948.

[35] R. F. Harrington, "Effect of antenna size on gain, bandwidth and efficiency," *J. Res. Nat. Bur. Stans.*, vol. 64D, pp. 1-12, Jan.-Feb. 1960.

[36] R. E. Collin and S. Rothschild, "Evaluation of antenna Q," *IEEE Trans. Antennas and Propagat.*, vol. 12, no. 1, pp. 23-27, Jan. 1964.

[37] H. Wheeler, "Small antennas," *IEEE Trans. Antennas and Propagat.*, vol. AP-23, no. 4, pp. 462-469, Jul. 1975.

[38] R. C. Hansen, "Fundamental limitations in antennas," *Proceedings of IEEE*, vol. 69, no. 2, pp. 170-182, Feb. 1981.

[39] J. S. McLean, "A re-examination of the fundamental limits on the radiation Q of electrically small antennas," *IEEE Trans. Antennas and Propagat.*, vol. 44, no. 5, pp. 672-676, May 1996.

[40] W. Geyi, "A method for the evaluation of small antenna Q," *IEEE Trans. Antennas and Propagat.*, vol. 51, no. 8, pp. 2124-2129, Aug. 2003.

[41] R. C. Hansen and R. E. Collin, "A new Chu formula for Q," *IEEE Antennas and Propag. Mag.*, vol. 51, no. 5, pp. 38-41, Oct. 2009.

[42] O. S. Kim and O. Breinbjerg, "Lower bound for the radiation Q of electrically small magnetic dipole antennas with solid magnetodielectric core," *IEEE Trans. Antennas and Propagat.*, vol. 59, no. 2, pp. 679-681, Feb. 2011.

[43] O. S. Kim and O. Breinbjerg, "Reaching the Chu lower bound on Q with magnetic dipole antennas using a magnetic-coated PEC core," *IEEE Trans. Antennas and Propagat.*, vol. 59, no. 8, pp. 2799-2805, Aug. 2011.

[44] M. J. Ammann and Z. -N. Chen, "Wideband monopole antennas for multi-band wireless systems" *IEEE Antennas Propag. Mag.*, vol. 45, no.2, pp. 146-150, April 2003.

[45] G. Dubost and S. Zisler, *Antennas a Large Bande*, pp.128-129, Masson, Paris, New York, 1976.

[46] N. P. Agrawall, G. Kumar and K. P. Ray, "Wide-band planar monopole antenna," *IEEE Trans. Antennas and Propagat.*, vol. 46, no. 2, pp. 294 -295, Feb. 1998.

[47] E. Lee, P. S. Hall and P. Gardner, "Compact wideband planar monopole antenna," *IEE Electron. Lett.*, vol. 35, no. 25, pp. 2157-2159, 1999.

[48] G. Kumar and K. P. Ray, *Broad Band Microstrip Antennas*, Boston, MA: Artech House, 2003.

[49] S. Honda, M. Ito, H. Seki and Y. Jingo, "A Disc Monopole Antenna with 1:8 Impedance Bandwidth and Omnidirectional Radiation Pattern," *Proc. ISAP, Sapporo, Japan*, pp. 1145-1148, 1992.

[50] P. P. Hammoud and F. Colomel, "Matching the Input Impedance of a Broadband Disc Monopole," *IEE Electron. Lett.*, vol. 29, no. 4, pp. 406-407, Feb. 1993.

[51] K. P. Ray, P. V. Anob, R. Kapur and G. Kumar, "Broadband Planar Rectangular Monopole Antennas," *Microwave Opt. Technol. Lett.*, vol. 28, no. 1, pp. 55-59, 2001.

[52] A. Kerkhoff and H. Ling, "Design of a Planar Monopole Antenna for use with Ultra Wide Band having Band Notched Characteristics," *IEEE Antennas and Propagation Society International Symposium*, vol. 1, pp. 830-833, 2003.

[53] S. -Y. Lin, "Multi-band Planar Monopole Antenna for Handset," *IEEE Antennas and Propagation Society International Symposium*, vol. 3, pp. 56-59, 2003.

[54] N. Herscovici and C. Christodouloc, "Wideband monopole antennas for multi-band wireless systems," *IEEE Antennas Propag. Mag.*, vol. 45, no.2, Apr. 2003.

[55] G. Ruvio, M. J. Ammann and Z. N. Chen, "Wideband reconfigurable rolled planar monopole antenna," *IEEE Trans. Antennas and Propagat.*, vol. 55, no. 6, pp. 1760-1767, Jun. 2007.

[56] Z. -N. Chen, M. J. Amman, M. Y. W. Chia and T. S. P. See, "Annular Planar Monopole Antennas," *IEE Proc-Microw, Antenna Propag.*, vol, 149, no. 4, pp. 200-203, Aug. 2002.

[57] A. W. Rudge, K. Milne, A. D. Oliver and P. Knight, *The Handbook of Antenna Design, vol. 2*, Peter Peregrinus Ltd., Lindon, UK, 1982.

[58] M. J. Ammann, "Square planar monopole antenna," *IEE National Conference on Antennas and Propagation*, pp. 37-40. 30 March-1 April 1999.

[59] M. J. Ammann, "Experiments on input impedance of tilted planar monopole antenna," *Microwave Optical Tech. Lett.*, vol. 26, no. 3, pp. 202-204, Aug. 2000.

[60] Z. -N. Chen and Y. W. M. Chia, "Impedance Characteristics of Trapezoidal Planar Monopole Antennas," *Microwave Optical Tech. Lett.*, vol. 27, no. 2, pp. 120-122, Oct. 2000.

[61] L. Smith, T. Starkie and J. Lang, "Measurements of Artimi's Antenna Designs," *2004 International Workshop on Ultrawideband Systems, Joint with Conference on Ultrawideband Systems and Technologies*, pp. 304-306, 18-21 May, 2004.

[62] G. Ruvio and M. J. Ammann, "A Compact Wide-Band Shorted Folded Antenna," *2006 IEEE International Workshop on Antenna Technology Small Antennas and Novel Metamaterials*, pp. 84-87, March 6-8, 2006.

[63] M. John, J. A. Evans, M. J. Ammann, J. C. Modro and Z. N. Chen, "Reduction of ground-plane-dependent effects on microstrip-fed printed rectangular monopoles," *IET Microw. Antennas Propag.*, vol, 2, no. 1, pp. 42-47, Jan. 2008.

[64] M. J. Ammann and Z. -N. Chen, "A Wide-Band Shorted Planar Monopole with Bevel," *IEEE Trans. Antennas and Propagat.*, vol. 51, no. 4, pp. 901-903, Apr. 2003.

[65] M. J. Ammann, "A wideband monopole for reconfigurable multiband radio terminals," *2001 IEEE AP-S International Symposium on Antennas and Propagation*, vol. 1, pp. 170-173, 8-13 July 2001.

[66] E. Antonino-Daviu, M. Cabedo-Fabres, M. Ferrando-Bataller and A. Valero-Nogueira, "Wideband double-fed planar monopole antennas," *IEE Electron. Lett.*, vol. 39, no. 23, pp. 1635-1636, Nov. 2003.

[67] M. J. Ammann and Z. -N. Chen, "An Asymmetrical Feed Arrangement for Improved Impedance Bandwidth of Planar Monopole Antennas," *Microwave Optical Tech. Lett.*, vol. 40, no. 2, pp. 156-158, Jan. 2004.

[68] K. -L. Wong, C. -H. Wu and S. -W. (Stephen) Su, "Ultrawide-Band Square Planar Metal-Plate Monopole Antenna With a Trident-Shaped Feeding Strip," *IEEE Trans. Antennas and Propagat.*, vol. 53, no. 4, pp. 1262-1269, Apr. 2004.

[69] M. J. Ammann, R. Sierra Cordoba, M. Uzelac, J. A. Evans and A. T. Schwarzbacher, "On Pattern Stability of The Crossed Planar Monopole," *Microwave Optical Tech. Lett.*, vol. 40, no. 4, pp. 294-296, Feb. 2004.

[70] M. J. Ammann, "Improved pattern stability for monopole antennas with ultra- wideband impedance characteristics," *2003 IEEE AP-S International Symposium on Antennas and Propagation*, vol. 1, pp. 818-821, 22-27 June 2003.

[71] H. Schantz, *The Art and Science of Ultrawideband Antennas*, Artech House, Inc, 2005.

[72] H. Schantz, "Planar elliptical element ultra-wideband dipole antennas," *IEEE Antennas and Propagation Society International Symposium*, vol. 3, pp. 44-47, 16-21 June 2002.

[73] G. Lu, S. von der Mark, I. Korisch, L. J. Greenstein and P. Spasojevic, "Diamond and Rounded Diamond Antennas for Ultrawide-Band Communications," *IEEE Antennas Wireless Propag. Lett.*, vol. 3, pp. 249-252, 2004.

[74] K. Kiminami, A. Hirata and T. Shiozawa, "Double-Sided Printed Bow-Tie Antenna for UWB Communications," *IEEE Antennas Wireless Propag. Lett.*, vol. 3, no. 1, pp. 152-153, 2004.

[75] Y. -L. Kuo, and K. -L. Wong, "Printed Double-T Monopole Antenna for 2.4/5.2 GHz Dual-Band WLAN Operations," *IEEE Trans. Antennas and Propagat.*, vol. 51, no. 9, pp. 2187-2191, Sep. 2003.

[76] J. Jung, K. Seol, W. Choi and J. Choi, "Wideband monopole antenna for various mobile communication applications," *IEE Electron. Lett.*, vol. 41, no. 24, pp. 1313-1314, Nov. 2005.

[77] K. Chung, J. Kim and J. Choi, "Wideband Microstrip-Fed Monopole Antenna Having Frequency Band-Notch Function," *IEEE Microw. Wireless Comp. Lett.*, vol. 15, no. 11, pp. 766-768, Nov. 2005.

[78] Y. -J. Cho, K. -H. Kim, S. -H. Hwang and S. -O. Park, "A Miniature UWB Planar Monopole Antenna with 5GHz Band-Rejection Filter," *35th European Microwave Conference, Paris, France*, pp. 1911-1914, October 3-7, 2005.

[79] J. Liang, C. Chiau, X. Chen and C.G. Parini, "Study of a Printed Circular Disc Monopole Antenna for UWB Systems," *IEEE Trans. Antennas and Propagat.*, vol. 53, no. 11, pp.3500-3504, Nov. 2005.

[80] J. Liang, C Chiau and X. Chen, "Printed circular ring monopole antennas," *Microwave Optical Tech. Lett.*, vol. 45, no. 5, pp. 372-375, Jun. 2005.

[81] H. -D. Chen and H. -T. Chen, "A CPW-Fed Dual-Frequency Monopole Antenna," *IEEE Trans. Antennas and Propagat.*, vol. 52, no. 4, pp. 978-982, April 2004.

[82] J. -Y. Jan and T. -M. Kuo, "CPW-fed wideband planar monopole antenna for operations in DCS, PCS, 3G, and Bluetooth bands," *IEE Electron. Lett.*, vol. 41, no. 18, pp. 991-993, Sep. 2005.

[83] Y. Kim and D. -H. Kwon, "CPW-fed planar ultra wideband antenna having a frequency band notch function," *IEE Electron. Lett.*, vol. 40, no. 7, pp. 403-405, Apr. 2004.

[84] W. Wang, S. S. Zhong and S. -B. Chen, "A Novel Wideband Coplanar-Fed Monopole Antenna," *Microwave Optical Tech. Lett.*, vol. 43, no. 1, pp. 50-52, Oct. 2004.

[85] S. -H. Lee, J. -K. Park and J. -N. Lee, "A Novel CPW-Fed Ultra-Wideband Antenna Design," *Microwave Optical Tech. Lett.*, vol. 44, no. 5, pp. 393-396, Mar. 2005.

[86] J. Liang, L. Guo, C. C. Chiau, X. Chen and C. G. Parini, "Study of CPW-Fed circular disc monopole antenna," *IEE Proc.-Microw. Antennas Propag.*, vol. 152, no. 6, pp. 520-526, Dec. 2005.

[87] J. -S. Kuo and C. -Y. Huang, "Triple-frequency planar monopole antenna for side-feed communication device on GSM/DCS/PCS operation," *IEE Electron. Lett.*, vol. 42, no. 5, pp. 268-270, 2006.

[88] X. -L. Liang, S. -S. Zhong and W. Wang, "Elliptical planar monopole antenna with extremely wide bandwidth," *IEE Electron. Lett.*, vol. 42, no.8, pp. 441-442, 2006.

[89] C. A. Balanis, *Antenna Theory Analysis and Design*, John Wiley and Sons, 2005.

[90] R. N. Simons, *Coplanar Waveguide Circuits, Components, and Systems*, Wiley-Interscience, 2001.

[91] H. Yang and S. Yan, "A novel P-shaped printed monopole antenna for RFID applications," *Microwave Opt. Technol. Lett.*, vol. 51, no. 2, pp. 554-556, Feb. 2009.

[92] I. -F. Chen and C. -M. Peng, "Microstrip-fed dual-U-shaped printed monopole antenna for dual-band wireless communication applications," *IEE Electron. Lett.*, vol. 39, no. 13, pp. 955-956, 2003.

[93] S. -Y. Suh, W. L. Stutzman and W. A. Davis, "A new ultrawideband printed monopole antenna: the planar inverted cone antenna (PICA)," *IEEE Trans. Antennas and Propagat.*, vol. 52, no. 5, pp. 1361-1364, May 2004.

[94] W. -S. Chen and Y. -C. Chang, "CPW-fed printed monopole antenna with branch slits for WiMAX applications," *Microwave Opt. Technol. Lett.*, vol. 50, no. 4, pp. 952-954, Apr. 2008.

[95] S. -Y. Lin and K. -C. Huang, "Printed pentagon monopole antenna with a band-notched function," *Microwave Opt. Technol. Lett.*, vol. 48, no. 10, pp. 2016-2018, Oct. 2006.

[96] C. Lin, F. -S. Zhang, G. Zhao, F. Zhang, and Y. Song, "A novel symmetrical monopole antenna for dual-broadband operation," *Microwave Opt. Technol. Lett.*, vol. 51, no. 4, pp. 976-979, Apr. 2009.

[97] W. -C. Liu, "Optimal design of dual-band CPW-fed G-shaped monopole antenna for WALN application," *Progress In Electromagnetics Research, PIER*, vol. 74, pp. 21-38, 2007.

[98] S. C. Basaran and Y. E. Erdemli, "A dual-band split-ring monopole antenna for WLAN applications," *Microwave Opt. Technol. Lett.*, vol. 51, no. 11, pp.2685-2688. Nov. 2009.

[99] S. Jing, Y. Yin, A. Sun, Y. Wei and Y. Yang, "Compact E-shaped monopole antenna for dual-band WLAN applications," in Proc. *IEEE International Conference on Microwave Technology and Computational Electromagnetics (ICMTCE)*, pp. 305-308, 2011.

[100] A. Khaleghi, "Dual band meander line antenna for Wireless LAN communication," *IEEE Trans. Antenna Propag.*, vol. 55, no. 3, pp. 1004-1008, Mar. 2007.

[101] Z. -H. Xiao, Z. -Q. Guan, and Z. -H. Zheng, "The research and development of the highway's electronic toll collection system," *Knowledge Discovery Data Mining*, vol. 3, pp. 359-362, 2008.

[102] S. -Y. Chen and P. Hsu, "CPW-fed folded-slot antenna for 5.8 GHz RFID tags," *Electron.Lett.*, vol. 40, no. 24, pp. 1516-1517, Jul. 2004.

[103] M. Keskilammi and M. Kivikoski, "Using text as a meander line for RFID application," *IEEE Antenn. Wireless. Propag.Lett.*, vol. 3, pp. 372-374, 2004.

[104] W. -C. Liu and Z. -K. Hu, "Broadband CPW-fed folded-slot monopole antenna for 5.8 GHz RFID application," *Electron. Lett.*, vol. 41, no. 17, pp. 937-939, Aug 18, 2005.

[105] S. K. Padhi, N. C. Karmakar and C. L. Law, "An EM-coupled dual-polarized microstrip patch antenna for RFID application," *Microwave Opt. Technol. Lett.*, vol. 39, pp. 354-360, 2003.

[106] G. Morrocco, "Gain-optimized self-resonant meander line antenna for RFID application," *IEEE Antenn. Wireless. Propag. Lett.*, vol. 2, pp. 302-305, 2003.

[107] W. -C. Liu, "A coplanar waveguide-fed folded-slot monopole antenna for 5.8 GHz radio frequency identification application," *Microwave Opt. Technol. Lett.*, vol. 49, no. 1, pp. 71-74, Jan. 2007.

[108] W. -C Liu and C. -M. Wu, "CPW-fed shorted F-shaped monopole antenna for 5.8-GHz RFID applications," *Microwave Opt. Technol. Lett.*, vol. 48, no. 3, pp. 573-575, Mar. 2006.

[109] D. Ma and W. -X. Zhang, "Broadband CPW-fed RFID antenna at 5.8 GHz," *Electron. Lett.*, vol. 42, no. 22, pp. 1258-1259, Oct 26, 2006.

[110] A. Sabban and K. C. Gupra, "Characterization of radiation loss from microstrip discontinuities using a multiport network modeling approach," *IEEE Trans. Microwave Theory Tech.*, vol. 39, no. 4, pp. 705-712, Apr. 1991.

[111] K. P. Ray and Y. Ranga, "Printed rectangular monopole antennas," in *Proc. IEEE Antennas and Propagation Society Symposium*, New Mexico, pp. 1693-1696, 2006.

[112] K. P. Ray, "Design aspects of printed monopole antennas for Ultra-Wide band applications," *International Journal of Antennas and Propagation*, pp, 1-8, 2008.

[113] H. Ma, Q. -X. Chu and Q. Zhang, "Compact dual-band printed monopole antenna for WLAN application," *Electron.Lett.*, vol. 44, no. 14, pp. 834-835, Jul. 2008.

[114] Y. Song, Y. -C. Jiao, H. Zhao, Z. Zhang, Z. -B. Weng, and F. -S. Zhang, "Compact printed monopole antenna for multiband WLAN applications," *Microwave Opt. Technol. Lett.*, 50, no. 2, pp. 365-367, Feb. 2008.

[115] J. -H. Gu, S. -S. Zhong, L. -L. Xue, and Z. Sun, "Dual-band monopole antenna with L-shaped strips for 2.4/5 GHz WLAN applications," *Microwave Opt. Technol. Lett.*, vol. 50, no. 11, pp. 2830-2833, Nov. 2008.

[116] W. Ren, "Compact 2.4/5-GHz dual-band annular-ring slot antenna with circular polarization," *Microwave Opt. Technol. Lett.*, vol. 51, no. 8, pp. 1848-1852, Aug. 2009.

[117] X. He, S. Hong, H. Xiong, Q. Zhang and E. M. M. Tentzeris, "Design of a Novel High-Gain Dual-Band Antenna for WLAN Applications," *IEEE Antennas Wireless Propag. Lett.*, vol. 8, pp. 798-801, 2009.

[118] G. Zhao, F. -S. Zhang, Y. Song, Z. -B. Weng and Y. -C. Jiao, "Compact ring monopole antenna with double meander lines for 2.4/5 GHz dual-band operation," *Prog. In Electromag. Research*, vol. 8, pp. 798-801, 2009.

[119] C. Lin, F. -S. Zhang, G. Zhao, F. Zhang, and Y. Song, "A novel symmetrical monopole antenna for dual-broadband operation," *Microwave Opt. Technol. Lett.*, vol. 51, no. 4, pp. 976-979, Apr. 2009.

[120] L. Han, W. Zhang, G. Han, R. Ma, and L. Li, "Differential Dual-Frequency Antenna for Wireless Communication," *ETRI Journal*, vol. 30, no. 6, pp. 877-879, Dec. 2008.

[121] M. Midrio, S. Boscolo, F. Sacchetto, C. G. Someda, A. D. Capobianco, and F. M. Pigozzo, "Planar, Compact Dual-Band Antenna for Wireless LAN Applications," *IEEE Antennas Wireless Propag. Lett.*, vol. 8, pp. 1234-1237, 2009.

[122] Y. L. Kuo, T. W. Chiou and K. -L. Wong, "A novel dual-band printed inverted-F antenna," *Microwave Opt. Technol. Lett.*, vol. 31, no. 5, pp. 353-355, Dec. 2001.

[123] C. -Y. Pan, T. -S. Horng, W. -S. Chen and C.-H. Huang, "Dual wideband printed monopole antenna for WLAN/WiMAX applications," *IEEE Antennas Wireless Propag. Lett.*, vol. 6, pp. 149-151, 2007.

[124] G. Zhao, F. -S. Zhang, Y. Song, Z. -B. Weng, and Y. -C. Jiao, "Compact ring monopole antenna with double meander lines for 2.4/5 GHz dual-band operation," *Prog. In Electromag. Research*, vol. 72, pp. 187-194, 2007.

[125] M. R. Khan, M. M. Morsy, M. Z. Khan and F. J. Harackiewicz, "Dual band antenna for wireless network (WLAN) applications," in Proc.*IEEE International Symposium on Antennas and Propagation (APSURSI)*, pp. 1397-1400, 2011.

[126] K. -H. Chiang and K. -W. Tan, "Microstrip monopole antenna with enhanced bandwidth using defected ground structure," *IEEE Antennas Wireless Propag. Lett.*, vol. 7, pp. 532-535, 2008.

[127] H. -D. Chenn, "Compact broadband microstrip-line fed sleeve monopole antenna for DTV application and ground plane effect," *IEEE Antennas Wireless Propag. Lett.*, vol. 7, pp. 497-500, 2008.

[128] X. L. Bao and M. J. Ammannn, "Microstrip line fed dual-frequency annular-slot antenna loaded by split-ring slot," *IET Microw. Antennas Propag.*, vol. 3, no. 5, pp. 757-764, 2009.

[129] X. Yang, Y. Z. Yin, W. Hu and K. Song, "Dual-band planar monopole antenna loaded with pair of edge resonators," *Electron. Lett.*, vol. 46, no. 21, pp. 1419-1421, Oct. 2010.

[130] P. Xu, Z. -H. Yan and C. Wang, "Multiband modified fork-shaped monopole antenna with dual L-shaped parasitic planes," *Electron. Lett.*, vol. 47, no. 6, pp. 364-365, Mar. 2011.

[131] Z. -H. Song, Y. Ding and K. Huang, "A compact multiband monopole antenna for WLAN/WiMAX application," *Prog. Eectromag. Research Lett.*, vol. 23, pp. 147-155, 2011.

[132] J. Pei, A. -G, Wang, S. Gao and W. Leng, "Miniaturized triple band antenna with a defected ground plane for WLAN/WiMAX application," *IEEE Antennas Wireless Propag. Lett.*, vol. 10, pp. 298-301, 2011.

[133] W. Hu, Y. Z. Yin, X. Yang and X. S. Ren, "Compact printed antenna with h-shaped stub for dual-band operation," *Electron.Lett.*, vol. 46, no. 25, pp. 1644-1645, Dec. 2010.

[134] C. -Y. -D. Sim, "Dual band CPW-fed monopole antenna with asymmetrical ground plane for bandwidth enhancement," *Microwave Opt. Technol. Lett.*, vol. 50, no. 11, pp. 3001-3004, Nov. 2008.

[135] C. -Y. -D. Sim, "Compact dual- and wide-band CPW-fed slot antenna for wireless applications," *Microwave Opt. Technol. Lett.*,vol. 50, no. 3, pp. 574-575, Mar. 2008.

[136] C. -C. Lin, "Dual-band folded monopole antenna with slotted ground plane for WLAN application," *Progress In Electromagnetics Research Lett.,*, vol. 15, pp. 53-60, 2010.

[137] W. -C. Liu, C. -M. Wu, S. -H. Chung, and J. -L. Jaw, "Notched CPW-fed pentagonal monopole antenna for dual wideband operation," *Microwave Opt. Technol. Lett.*, vol. 50, no. 12, pp. 3104-3108, Dec. 2008.

[138] K. G. Thomas and M. Sreenivasan, "A simple dual-band microstrip-fed printed antenna for WLAN applications," *IET Microw. Antennas Propag.*, vol. 3, no. 4, pp. 687-694, 2009.

[139] W. -C. Liu and J. -K. Chen, "Dual-band twin stepped-patch monopole antenna for WLAN application," *Electron.Lett.*, vol. 45, no. 18, pp. 929-931, Aug. 2009.

[140] H. -D. Chen, J. -S. Chen and Y. -T. Cheng, "Modified inverted-L monopole antenna for 2.4/5 GHz dual-band operations," *Electron.Lett.*, vol. 39, no. 22, pp.1567-1568, Oct. 2003.

[141] C. -M. Wu, "Dual-band CPW-fed cross-slot monopole antenna for WLAN operation," *IET Microw. Antennas Propag.*, vol. 1, no. 2, pp. 542-546, 2007.

[142] C. Wang, Z. -H. Yan, P. Xu, J. -B. Jiang and B. Li, "Trident-shaped dual-band CPW-fed monopole antenna for PCS/WLAN applications," *Electron.Lett.*, vol. 47, no. 4, pp. 231-232, Feb. 2011.

[143] H. -D. Chen and H. -T. Chen, "A CPW-fed dual-frequency monopole antenna," *IEEE Trans. Antennas Propagat.*, vol. 52, no. 4, pp. 978-982, Apr. 2004.

[144] C. -H. Cheng, W. -J. Lv, Y. Chen and H. -B. Zhu, "A dual-band strip-sleeve monopole antenna fed by CPW," *Microwave Opt. Technol. Lett.*, vol. 42, no. 1, pp. 70-73, Jul. 2004.

[145] W. -C. Liu, and C. -C. Huang, "A CPW-fed L-shaped slot planar monopole antenna for triple-band operations," *Microwave Opt. Technol. Lett.*, vol. 44, no. 6, pp. 510-512, Mar, 2005.

[146] C. -A. Shen, and K. -H. Lin, "A broadband internal planar monopole antenna for mobile phone," *Microwave Opt. Technol. Lett.*, vol. 48, no. 4, pp. 768-769, Apr. 2006.

[147] M. N. Suma, R. K. Raj, M. Joseph, P. C. Bybi and P. Mohanan , "A compact dual band planar branched monopole antenna for DCS/2.4-GHz WLAN applications," *IEEE Microw. Wireless Comp. Lett.*, vol. 16, no. 5, pp. 275-277, May 2006.

[148] W. -C. Liu and P. -C. Kao, "Compact CPW-fed dual folded-strip monopole antenna for 5.8-GHz RFID application," *Microwave Opt. Technol. Lett.*, vol. 48 ,no. 8, pp. 1614-1615, Aug. 2006.

[149] J. C. Ammann and R. Farrel, "Dual-band monopole antenna with stagger-tuned arms for broad-banding," In *IEEE International Workshop on Antenna Technology: Small Antennas and Novel Metamaterials (IWAT-2005)*, 2005, pp. 278-281.

[150] K. M. Z. Shams, M. Ali, and H.-S. Hwang, "A planar inductively coupled bow-tie slot antenna for WLAN application," *Journal of Electromagnetic Waves and Applications*, vol. 20, no. 7, pp. 861-871, 2006.

[151] T. -L. Zhang, Z. -H. Yan, L. Chen, and Y. Song, "A compact dual-band CPW-fed planar monopole antenna for WLAN applications," *Journal of Electromagnetic Waves and Applications*, vol. 22, nos. 14-15, pp. 2097-2104, 2008.

[152] J. -L. Jaw, F. -S. Chen, and D. -F. Chen, "Compact dual-band CPW-fed slotted patch antenna for 2.4/5 GHz WLAN operation," *Journal of Electromagnetic Waves and Applications*, vol. 23, Nos. 14-15, pp. 1947-1955, 2009.

[153] W. -C. Liu, P. -W. Chen, and C. -C. Liu, "Triple-band planar monopole antenna for DMB/WLAN applications," *Journal of Electromagnetic Waves and Applications*, vol. 24, nos. 5-6, pp. 653-661, 2010.

[154] K. Zhao, S. Zhang, and S. L. He, "Closely-located MIMO antennas of tri-band for WLAN mobile terminal applications," *Journal of Electromagnetic Waves and Applications*, vol. 24, nos. 2-3, pp. 363-371, 2010.

[155] W. S. Chen and Y. -H. Yu, "Dual-band printed dipole antenna with parasitic element for WIMAX applications," *IEE Electron. Lett.*, vol. 44, no. 23, pp. 1338-1339, Nov. 2008.

[156] T. -N. Chang, G.-Y. Shen, and J. -M. Lin, "CPW-fed antenna covering WiMAX 2.5/3.5/5.7 GHz bands," *Journal of Electromagnetic Waves and Applications*, vol. 24, nos. 2-3, pp. 189-197, 2010.

[157] Y. -L. Kuo and K. L. Wong, "Printed double-T monopole antenna for 2.4/5.2 GHz dual-band WLAN operation," *IEEE Trans. Antennas Propag.*, vol. 51, no. 9, pp. 2187-2191, Sept. 2003.

[158] W. -C. Liu, W. R. Chen, and C. M.Wu, "Printed double S-shaped monopole antenna for wide-band and multiband operation of wireless communication," *IEE Proc. Microw. Antennas Propag.*, vol. 151, no. 6, pp. 473-476, 2004.

[159] W.-C. Liu, "Optimal design of dualband CPW-fed G-shaped monopole antenna for WLAN application," *Progress In Electromagnetics Research*, vol. 74, pp. 21-38, 2007.

[160] Z. -Y. Liu, Y. -Z. Yin, L. -H. Wen, W. -C. Xiao, Y. Wang, and S. -L. Zuo, "A Y-shaped tri-band monopole antenna with a parasitic M-strip for PCS and WLAN applications," *Journal of Electromagnetic Waves and Applications*, vol. 24, Nos. 8-9, pp. 1219-1227, 2010.

[161] W. C. Liu and C. -F. Hsu, "Dual-band CPW-fed Y-shaped monopole antenna for PCS/WLAN application," *IEE Electron. Lett.*, vol. 41, no. 7, pp. 390-391, 2005.

[162] Y. Wei, Y. Yin, Y. Yang, S. Jing and W. Hu, "Compact dual-band antenna with modified open U-shaped slot for WLAN applications," in Proc. *IEEE International Conference on Microwave Technology and Computational Electromagnetics (ICMTCE)*, pp. 35-37, 2011.

[163] F. -G. Bian, F. -S. Zhang, Y. -B. Yang, Q. Zhang and J. -X. Huang, "A compact dual band printed monopole antenna for WLAN applications," in Proc. *IEEE International Symposium on Signals Systems and Electronics (ISSSE)*, pp. 1-4, 2010.

[164] W. -C. Liu, C.-M. Wu, and N. -C. Chu, "A compact CPW-fed slotted patch antenna for dual-band operation," *IEEE Antennas Wireless Propag. Lett.*, vol. 9, pp. 110-113, 2010.

[165] C. Hsieh, T. Chiu, and C. Lai, "Compact dual-band slot antenna at the corner of the ground plane," *IEEE Trans. Antennas Propag.*, vol. 57, no. 10, pp. 3423-3426, 2009.

[166] First Report and Order, "Revision of Part 15 of the Commission's Rule Regarding Ultra-Wideband Transmission systems FCC 02-48," Federal Communication Commission, 2002.

[167] M. Ghavami, L. B. Michael and R. Kohno, *Ultra Wideband Signals and Systems in Communication Engineering*, John Wiley and Sons, 2007.

[168] K. Y. Yazdandoost and R. Konho, "Ultra wideband antenna," *IEEE Communication Magazine*, vol. 42, no. 6, pp. S29-S32, Jun. 2004.

[169] W. Choi, K. Chung, J. Jung and J. Choi, "Compact ultra-wideband printed antenna with band-rejection characteristic," *IEE Electron. Lett.*, vol. 41, no. 18, pp. 990-991, Sep.2005.

[170] K. -L. Wong, Y. -W. Chi, C. -M. Su and F. -S. Chang, "Band-notched ultra-wideband circular-disc monopole antenna with an arc-shaped slot," *Microwave Opt. Technol. Lett.*, vol. 45, no. 3, pp. 188-191, May 2005.

[171] S. Licul, J. A. N. Noronha, W. A. Davis, D. G. Sweeney, C. R. Anderson and T. M. Bielawa, "A parametric study of time-domain characteristics of possible UWB antenna architectures," in Proc. *IEEE 58th Vehicular Technology Conference, VTC 2003-Fall*, vol. 5, pp. 3110-3114, 6-9 Oct. 2003.

[172] K. -H. Kim, Y. -J. Cho, S. -H. Hwang and S. -O. Park, "Band-notched UWB planar monopole antenna with two parasitic patches," *Electron.Lett.*, vol. 41, no. 14, pp. 783-785, Jul, 2005.

[173] W. Choi, K. Chung, J. Chung and J. Choi, "Compact ultra-wideband printed antenna with band-rejection characteristics," *Electron.Lett.*, vol. 41, no. 18, pp. 990-991, Sep, 2005.

[174] C. -Y. Huang.,W. -C. Hsia and J. -S. Kuo, "Planar ultra-wideband antenna with a band-notched characteristics," *Microwave Opt. Technol. Lett.*, vol. 48, no. 1, pp. 99-101, Jan. 2006.

[175] Y. Gao, B. -L. Ooi and A. P. Popov, "Band-notched ultra-wideband ring-monopole antenna," *Microwave Opt. Technol. Lett.*, vol. 48, no. 1, pp. 125-126, Jun. 2006.

[176] J. Kim, C. S. Cho and J. W. Lee, "A novel compact printed circular antenna for very ultraw-ideband applications," *Electron.Lett.*, vol. 42, no. 6, pp. 315-316, Mar, 2006.

[177] K. -H. Kim and S. -O. Park, "Analysis of the small band-rejected antenna with the parasitic strip for UWB," *IEEE Trans. Antennas Propag.*, vol. 54, no. 6, pp. 1688-1692, Jun. 2006.

[178] K. -H. Kim and S. -O. Park, "Design of the band-rejected UWB antenna with the ring-shaped parasitic patch," *Microwave Opt. Technol. Lett.*, vol. 48 , no. 7, pp. 1310-1313, Jul. 2006.

[179] C. -Y. Huang and W. -C. Hsia, "Planar ultra-wideband antenna with a frequency notch char-acteristic," *Microwave Opt. Technol. Lett.*, vol. 49 , no. 2, pp. 316-320, Feb. 2007.

[180] K. Chung, S. Hong and J. Choi, "Ultrawide-band printed monopole antenna with band-notch filter ," *IET Microw. Antennas Propag.*, vol. 1 , no. 2, pp. 518-522, Apr. 2007.

[181] C. -Y. Hong, C. -W.Ling, I. -Y.Tarn and S. -J. Chung, "Design of a planar ultrawideband antenna with a new band-notch structure ," *IEEE Trans. Antennas Propag.*, vol. 55, no. 12, pp. 3391-3397, Dec. 2007.

[182] S. N. Khan, J. X. Xiong and S. He, "Low profile and small size frequency notched planar monopole antenna from 3.5 to 23.64 GHz , " *Microwave Opt. Technol. Lett.*, vol. 50 , no. 11, pp. 235-236, Jan. 2008.

[183] R. Zaker, C. Ghobadi and J. Nourinia, "Novel modified UWB planar monopole antenna with variable frequency band-notch function, " *IEEE Antenna Wireless Propag Lett.*, vol. 7, pp. 112-114, 2008.

[184] J. Liu, S. Gong, Y. Ku, X. Zhang, C. Feng and N. Qi, "Compact printed ultra-wideband monopole antenna with dual band-notched characteristics, " *Electron.Lett.*, vol. 44, no. 12, pp. 710-711, Jun, 2008.

[185] H. Lee, Y. Jang, J. Kim and J. Choi, "Wideband monopole antenna with WLAN (2.4 GHz/ 5 GHz) dual band-stop function," *Microwave Opt. Technol. Lett.*, vol. 50, no. 6, pp. 1646-1649, Jun. 2008.

[186] F. -J. Wang, X. -X. Yang, J. -S. Zhang, G. -P. Guo and J. -X. Xiao, "A band-notched ring monopole antenna," *Microwave Opt. Technol. Lett.*, vol. 50, no. 7, pp. 1882-1884, Jul. 2008.

[187] Z. Cui, Y. -C. Jiao, L. Zhang and F. -S. Zhang., "The band-notch function for a printed ultra-wideband monopole antenna with E-shaped slot," *Microwave Opt. Technol. Lett.*, vol. 50, no. 8, pp. 2048-2052, Aug. 2008.

[188] Y. -D. Dong, W. Hong, Z -Q. Kuai and J. -X. Chen, "Analysis of planar ultrawideband antennas with on-ground slot band-notched structures," *IEEE Trans. Antennas Propag.*, vol. 57, no. 7, pp. 1886-1892, Jul. 2009.

[189] H. Kim, D. Park and Y. Joo, "All-digital low power CMOS pulse generator for UWB signals," *Electron. Lett.*, vol. 40, no. 24, pp. 1534-1535, Nov. 2004.

[190] N. Telzhensky and Y. Leviatan, "Novel method of UWB antenna optimization for specified input signal form by means of genetic algorithm," *IEEE Trans Antennas Propag.*, vol. 54, no. 8, pp. 2216-2225, Aug. 2006.

[191] IE3D version 10.2, Zeland Corp, *Freemont, CA, USA.*

[192] D. H. Kwon, "Effect of antenna gain and group delay variations on pulse-preserving capabilities of ultrawideband antennas," *IEEE Trans Antennas Propag.*, vol. 54, no. 8, pp. 2208-2215, Aug. 2006.

[193] Z. -N. Chen, X. -H. Wu, H. -F. Li, N. Yang and M. Y. W, Chia, "Considerations for source pulses and antennas in UWB radio systems," *IEEE Trans Antennas Propag.*, vol. 52, no. 7, pp. 1739-1748, Jul. 2004.

[194] Ansys HFSS V.14.

Publications

Journal Publications

1. J. R. Panda and R. S. Kshetrimayum, "A 3.4/5.5 GHz dual-band notched UWB printed monopole antenna with two open-circuited stubs in the microstrip feedline," *Microwave and Optical Technology Letters*, vol. 53, no. 12, pp. 2973-2978, December 2011.

2. J. R. Panda and R. S. Kshetrimayum, "An F-shaped printed monopole antenna for dual-band RFID and WLAN applications," *Microwave and Optical Technology Letters*, vol. 53, no. 7, pp. 1478-1481, July 2011.

3. J. R. Panda and R. S. Kshetrimayum, "A printed 2.4 GHz/5.8 GHz dual-band monopole antenna with a protruding stub in the ground plane for WLAN and RFID applications," *Progress In Electromagnetics Research (PIER)*, vol. 117, pp. 425-434, 2011.

4. J. R. Panda, A. S. R. Saladi and R. S. Kshetrimayum, "A compact printed monopole antenna for dual-band RFID and WLAN applications," *Radioengineering*, vol. 20, no. 2, pp. 464-467, June 2011.

Conference Publications

1. J. R. Panda and R. S. Kshetrimayum, "A printed 2.4 GHz/5.8 GHz dual-band monopole antenna for WLAN and RFID applications with a protruding stub in the ground plane," in *Proc. IEEE Seventeenth National Conference on Communications (NCC 2011)*, 28-30 January, Bangalore, India, 2011.

2. J. R. Panda and R. S. Kshetrimayum, "A printed F-shaped dual-band monopole antenna for RFID and WLAN applications," in *Proc. IEEE International Conference on Computer and Communication Technology (ICCCT 2010)*, pp. 789-791, 17-19 September, Allahabad, India, 2010.

3. J. R. Panda, A. S. R. Saladi and R. S. Kshetrimayum, "A compact 3.4/5.5 GHz dual band-notched UWB monopole antenna with nested U-shaped slots," in *Proc. IEEE International Conference on Computing, Communication and Networking Technologies (ICCCNT 2010)*, 29 -31 July, Karur, India, 2010.

4. A. S. R. Saladi, J. R. Panda and R. S. Kshetrimayum, "A compact printed 9-shaped dual-band monopole antenna for WLAN and RFID applications," in *Proc. IEEE International Conference on Computing, Communication and Networking Technologies (ICCCNT 2010)*, 29 -31 July, Karur, India, 2010.

5. J. R. Panda and R. S. Kshetrimayum, "A compact CPW-fed hexagonal 5 GHz/6 GHz band-notched antenna with an U-shaped slot for ultrawideband communication system," in *Proc. IEEE International Conference on Signal Processing and Communications (SPCOM 2010)*, Bangalore, 18-21 July, India, 2010.

6. J. R. Panda and R. S. Kshetrimayum, "A compact 3.5/5.5 GHz dual band-notched monopole antenna for application in UWB communication systems with defected ground structure," in *Proc. IEEE Indian Antenna Week (IAW 2010)*,Puri, India, 31 May-4 June 2010. **(Student Participation Award)**

7. J. R. Panda and R. S. Kshetrimayum, "A compact printed U-shaped dual-band monopole antenna for wireless and RFID applications," in *Proc. IEEE Applied Electromagnetics Conference (AEMC 2009)*, Kolkata, India, 14-16 Dec. 2009.

8. J. R. Panda and R. S. Kshetrimayum, "A printed inverted double L-shaped dual-band monopole antenna for RFID applications," in *Proc. IEEE Applied Electromagnetics Conference (AEMC 2009)*, Kolkata, India, 14-16 Dec. 2009.

9. J. R. Panda and R. S. Kshetrimayum, "A printed C-shaped dual-band monopole antenna for RFID applications," in *Proc. IEEE Applied Electromagnetics Conference (AEMC 2009)*, Kolkata, India, 14-16 Dec. 2009.